The influence of boundary configurations on the dissipation and stability in fluids at low Reynolds numbers

M.Sc. Michael Eigenbrod

TECHNISCHE
UNIVERSITÄT
DARMSTADT

Nano- and
Microfluidics

The influence of boundary configurations on the dissipation and stability in fluids at low Reynolds numbers

Vom Fachbereich Maschinenbau

der Technischen Universität Darmstadt

zur Erlangung des Grades

Doktor-Ingenieur (Dr.-Ing.)

genehmigte

Dissertation

von

Michael Eigenbrod

Erstgutachter: Prof. Dr. rer. nat. Steffen Hardt
Zweitgutachter: Prof. Dr. Benoit Scheid

Tag der Einreichung: 07. Mai 2020
Tag der mündlichen Prüfung: 15. Juli 2020

Darmstadt 2020
D17

Eigenbrod, Michael: The influence of boundary configurations on the dissipation and stability in fluids at low Reynolds numbers
Darmstadt, Technische Universität Darmstadt
Jahr der Veröffentlichung der Dissertation auf TUprints: 2021
Tag der mündlichen Prüfung: 15.07.2020

Erklärung

Hiermit erkläre ich, dass ich die vorliegende Arbeit, abgesehen von den in ihr ausdrücklich genannten Hilfen, selbständig verfasst habe.

Michael Eigenbrod

Darmstadt, 07. Mai 2020

Abstract

The physical nature of boundaries that restrict the spreading of fluids or appear as interfaces between two immiscible fluids can have a significant influence on the static and dynamic properties of a fluidmechanical system. The aim of the present work is to investigate the influence of different boundary configurations on the energy dissipation and stability of fluid systems in the case of creeping flows, as they typically occur in microfluidic devices.

The motion of charged interfacial microparticles induced by an applied electric field is theoretically investigated in this work. In addition to the functional relationship, which relates the velocity of the particle with the strength of the electric field and depends, among others, on the wetting properties of the particle, the deformation of the fluid interface is also determined, which results as a consequence of the charge of the particle and the resulting electric double layer, which is different in both bulk phases.

The presence of multiple interfacial particles can effectively be described by a change in the rheological properties of the fluid interface. The theoretical model developed in this work is suitable for determining the effective shear and dilatation viscosity of the interface, which can be expressed as a function of the particle concentration and the contact angle of the particles.

Microfluidic systems are typically characterized by a small volume-to-surface ratio, whereby the influence of the boundary conditions on the global properties of a flow increases dramatically. A charged, weakly deformed circular obstacle subjected to a pressure-driven flow can be isolated by a locally restricted electro-osmotic flow induced on the walls of the channel such that the hydrodynamic force on the body vanishes. The exact charge distribution that encloses the solid at the walls of the channel and provides hydrodynamic isolation, is determined theoretically and validated with the help of numerical simulations.

The aim of many technical applications is to create an uniform liquid film on a flat surface. However, under certain external conditions, defects or holes can form which, if they are stable, may even lead to component failure. In the course of this work, a stability criterion is determined that predicts under which conditions the defects in spatially limited liquid films will self-heal. In addition, the dynamics of the closure of single circular defects is investigated theoretically and compared with experiments on different substrates.

As an extension of the investigation on single defects in liquid films, a model is developed which predicts the temporal evolution of multiple defects. The theoretical results are validated by a comparison with experiments.

Kurzfassung

Die physikalische Beschaffenheit von Rändern, die Fluide in ihrer geometrischen Ausbreitung einschränken oder sich als Grenzfläche zwischen zwei nicht mischbaren Fluiden bilden, können signifikanten Einfluss auf die statischen und dynamischen Eigenschaften eines fluidmechanischen Systems haben. Das Ziel der vorliegenden Arbeit ist die Untersuchung des Einflusses verschiedener Randkonfigurationen auf die Energiedissipation und Stabilität von Flüssigkeitssystemen im Fall schleichender Strömungen, wie sie typischerweise in mikrofluidischen Systemen auftreten.

Die durch ein angelegtes elektrisches Feld induzierte Bewegung von geladenen, an Fluidgrenzflächen absorbierten Mikropartikeln wird im Rahmen dieser Arbeit theoretisch untersucht. Neben dem funktionalen Zusammenhang, der die Geschwindigkeit des Partikels mit der Stärke des elektrischen Feldes verknüpft und unter anderem von den Benetzungseigenschaften des Partikels abhängt, wird ebenfalls die Deformation der Grenzfläche bestimmt, die sich als Konsequenz der Ladung des Partikels und der sich in beiden Phasen unterschiedlich einstellenden elektrischen Doppelschicht ergibt.

Die Präsenz von mehreren Grenzflächenpartikeln lässt sich effektiv durch eine Änderung der rheologischen Eigenschaften der fluiden Grenzfläche beschreiben. Das im Rahmen dieser Arbeit entwickelte theoretische Modell eignet sich zur Bestimmung der effektiven Scher- und Dilatationsviskosität der Grenzfläche, welche sich als Funktion der Partikelkonzentration und des Kontaktwinkels der Partikel ausdrücken lässt.

Mikrofluidische Systeme sind typischerweise durch ein geringes Volumen-zu-Oberflächen-Verhältnis charakterisiert, wodurch der Einfluss der Randbedingungen auf die globalen Eigenschaften einer Strömung drastisch zunimmt. Ein geladener, schwach deformierter und in einer durckgetriebenen Strömung eingebrachter Festkörper kann durch einen, an den Wänden des Kanals induzierten, örtlich beschränkten elektoosmotischen Fluss derart isoliert werden, sodass die hydrodynamische Kraft auf den Körper verschwindet. Die exakte Ladungsverteilung, die den Festkörper an der Wand des Kanals umschließt und für eine hydrodynamische Isolierung sorgt, wird theoretisch bestimmt und mit Hilfe von numerischen Simulationen validiert.

Das Ziel vieler technischer Anwendungen ist die Erzeugung eines gleichmäßigen Flüssigkeitsfilms auf einer ebenen Fläche. Unter bestimmten äußeren Bedingungen jedoch, bilden sich Defekte oder Löcher, die, sofern sie stabil sind, womöglich sogar zu Bauteilversagen führen können. Im Rahmen dieser Arbeit wird ein Stabilitätskriterium bestimmt, welches vorhersagt, unter welchen Umständen sich die Defekte in räumlich begrenzten Flüssigkeitsfilmen selbst heilen. Außerdem wird die Dynamik der Lochschließung einzelner runder Defekte theoretisch untersucht und mit Experimenten auf unterschiedlichen Substraten verglichen.

Als Erweiterung der Untersuchung zu einzelnen Defekten in Flüssigkeitsfilmen, wird ein Modell entwickelt, welches die Vorhersage von mehreren Defekten in ihrer zeitlichen Entwicklung vorhersagt. Durch einen Vergleich mit Experimenten werden die theoretischen Resultate validiert.

Danksagung

Die vorliegende Arbeit entstand während meiner Tätigkeit als wissenschaftlicher Mitarbeiter am Institut für Nano- und Mikrofluidik der Technischen Universität Darmstadt unter der Leitung von Herrn Prof. Dr. rer. nat. Steffen Hardt. Ich hatte das große Glück vielseitig und umfassend unterstützt zu werden, wodurch mir die Erstellung dieser Arbeit erst ermöglicht wurde.

Zunächst möchte ich mich besonders bei Prof. Dr. rer. nat. Steffen Hardt bedanken. Neben den hilfreichen Diskussionen bedanke ich mich vor allem für die Freiheit die mir bei der Auswahl und Bearbeitung meiner Forschungsfragen entgegengebracht wurde. Je tiens également à remercier mon deuxième évaluateur, le professeur Benoit Scheid, pour l'intérêt qu'il porte à mes travaux.

Ferner möchte ich mich bei allen Kolleginnen und Kollegen des Instituts für das tolle Arbeitsklima bedanken. Besonderer Dank gilt Prof. Dr. Cunjing Lv, der mich insbesondere zu Beginn meiner Promotionsphase unterstützt hat und mit dem ich viele Stunden gemeinsam im Labor verbracht habe. Weiterhin möchte ich mich besonders bei Dr. Tobias Baier, Dr. Mathias Dietzel, Maximilian Hartmann und Dr. Sicheng Zhao für die zahlreichen wissenschaftlichen und nichtwissenschaftlichen Diskussionen bedanken. Jörg Bültemann, Frank Plückebaum und Lidia Querling danke ich für den technischen und administrativen Support. Außerdem möchte ich mich besonders bei Corinna Neumann für die Unterstützung bei den vielen organisatorischen Fragen bedanken.

Danken möchte ich ebenfalls allen Kollegen vom KIT in Karlsruhe, sowie den Kollegen vom Technion - Israel Institute of Technology, mit denen ich im Rahmen von Kooperationsprojekten zusammengearbeitet habe. Den studentischen Hilfskräften, sowie Bacheloranden und Masteranden, die ich im Laufe der Jahre betreut habe, danke ich ebenfalls.

Last but not least, möchte ich mich bei meinen Eltern, meinem Bruder und meinen Freunden für die Rücksichtnahme und das Verständnis, welches mir die letzten vier Jahre entgegengebracht wurde, bedanken. Ohne eure selbstlose Unterstützung wäre das Verfassen dieser Arbeit nicht möglich gewesen.

Author's contribution

All results presented in chapter 3 - 7 were elaborated under the supervision of Prof. Dr. rer. nat. Steffen Hardt.

Contributions to chapter 3

Most of the results presented in chapter 3 have been published in Eigenbrod et al. (2018). With the exception of the numerical simulations performed by Florian Bihler (student assistant), the entire content of this chapter was worked out by me.

Contributions to chapter 4

Most of the results presented in chapter 4 have been published in Eigenbrod and Hardt (2020). The whole content of this chapter was elaborated by me.

Contributions to chapter 5

The results presented in chapter 5 are part of a cooperation project with the Faculty of Mechanical Engineering, Israel Institute of Technology (Prof. Moran Bercovici, Prof. Amir D. Gat, Evgeniy Boyko, Vesna Bacheva) and IBM Research - Zurich (Federico Paradore). My contribution was the theoretical modeling of the hydrodynamic shielding of non-circular obstacles through spatially dependent electro-osmotic flow and a validation of the results in form of 2D numerical simulations. The theoretical modeling of the shielding of circular obstacles was contributed by Evgeniy Boyko. Chapter 5 essentially contains my contribution to the project.

Contributions to chapter 6

Most of the results presented in chapter 6 have been published in Lv et al. (2018) (co-first-authorship with C. Lv). My contributions are:

- Performance of the experiments (together with C. Lv);
- Experimental post-processing with a custom-made MATLAB® code;
- Numerical simulations with SURFACE EVOLVER and a custom-made MATLAB® code;
- Modeling of the statics (asymptotic model);
- Modeling of the dynamics;
- Writing the manuscript (together with C. Lv).

C. Lv co-supervised the work and contributed the scaling law analysis for the growth of the liquid column.

Contributions to chapter 7

The whole content of this chapter was elaborated by me.

Inhaltsverzeichnis

1 Introduction

In almost any hydrostatic or hydrodynamic system, boundaries not only limit the volumetric confinement of a fluid but also bring along extensive influences on the mechanical properties of a single or multiphase system. The influence of differently constituted boundaries on the motion, dissipation and stability of fluid systems is the subject of this thesis. In particular, the influence of fluid interfaces separating two immiscible fluids, moving particles attached to fluid interfaces, either convected by a flow or relative to the motion of a fluid, and spatially confined channels and their influence on global flow properties, such as the force acting on an obstacle located in the center of the channel, are of major interest throughout this work.

Free surface flows are ubiquitous in our daily life. In nearly every situation where liquids are involved, fluid interfaces are present or can appear due to different mechanisms such as cavitation or chemical reactions. Consequently, the characteristic length and time scales vary in a very wide range from nanometers to kilometers and from nanoseconds to hours. Examples that reveal the huge length and time scales are ranging from bursting nanobubbles (Zhang et al., 2014) towards lava flows (e.g., Belousov and Belousova, 2018). Multiphase flows are complex due to additional physical effects induced by the presence of a fluid interface (e.g., surface tension). However, the specific properties of fluid interfaces also induce a wide range of possible applications, ranging from medical applications [e.g., cavitation induced damage of kidney stones (Pishchalnikov et al., 2003) or lab-on-a-chip technologies for drug delivery (Neužil et al., 2012)] to ink-jet printing (Singh et al., 2010) and controlling the patterning of surfaces for applications in photolithography (Nejati et al., 2016). Some practical applications are probably inspired by nature. Animals such as the 'snapping shrimp' uses cavitation, induced by a rapid closure of its snapper claw, to stun or kill prey animals (Versluis et al., 2000), whereas some insects predominantly use fluid interfaces for locomotion, in order to avoid predators (Bush and Hu, 2006). The diversity of the animals thereby leads to various different transportation mechanisms, such as inertia or curvature driven motion as well as a motion induced by a nonuniform surface tension (Marangoni effect) due to surfactants, created by the insect (Bush and Hu, 2006).

Probably one of the oldest questions scientists have asked themselves in connection with fluid motion is: What force is applied on a particle moving through a quiescent liquid? This question is of practical relevance, since particles are often dispersed in the bulk of a fluid. Familiar examples are blood, sand in sea water, orange juice or magma flows. The complexity of these flows results from the complex shape of the suspended matter, its deformability [e.g., red blood cells in blood flow (Freund, 2014)] and, probably most important, from the hydrodynamic interactions between the suspended matter. Furthermore, the self-movement of the dispersed substances relative to the flow influences the global flow properties (Guazzelli and Morris, 2011). The constitution of the boundaries, influences the alignment of the dispersed matter significantly. Exemplarily, it was found that biofilms (colonies of microorganisms) build a close formation while streaming through a curved (zigzag) microchannel, due to secondary flow induced at the lower and the upper wall of the channel (Rusconi et al., 2011). Microparticles translating along liquid-air interfaces due to an external applied force acting at the center of the particle have been

studied theoretically (Dörr and Hardt, 2015; Dörr et al., 2016) and experimentally (Petkov et al., 1995). It has been found that the resistance force increases the more the particle is immersed into the liquid phase. If, however, the driving force also depends on the depth of immersion, e.g., through electrostatic forces due to an externally applied electric field inside the liquid phase, the exact relationship between the velocity of the particle and the applied force has remained largely obscure.

Microfluidic devices are characterized through a small volume-to-surface ratio. To emphasize the relevance of the boundary conditions on the global properties of a flow in microfluidic devices, we exemplarily consider a fluid with a viscosity μ enclosed between two parallel walls having a distance H, where the upper wall is moving with a velocity U while the lower wall is at rest. Furthermore, we assume the existence of a pressure difference of Δp over a length L in the opposite direction of U. The flow rate $\mathfrak{Q}$ per area of the walls $\mathscr{A}_\mathrm{w}$ is found to read $\mathfrak{Q}/\mathscr{A}_\mathrm{w} = HU/2 - H^3\Delta p/(12\mu L)$. For sufficiently large channel heights, the last term becomes dominant leading to a pressure induced backflow with respect to the direction of wall motion. Consequently, the motion of the upper wall is insufficient for pumping the fluid against a pressure gradient. In opposite, for sufficiently small heights, the first term becomes dominant leading to a nearly pressure-independent flow rate along the direction of the translating upper wall. In this case, the effect of the boundary condition dominates over the pressure gradient. However, for very small heights less liquid is transported. To increase the overall pumping rate, an array of multiple channels could be employed that increases the volumetric flow rate and the pumping efficiency. Besides the motivation of the significant influence of boundary conditions on small devices, the preceding example also serves as a general motivation for the application of microfluidic systems.

Due to the small length scales in microfluidics, the fluid motion is often described as creeping motion or Stokes motion. In these cases, the Reynolds number is typically very small $\mathrm{Re} = \rho UL/\mu \ll 1$, in which ρ and L are the density of the fluid and a characteristic length scale, respectively. The small Reynolds number assumption is also often applied to fluid-particle systems due to the commonly small characteristic length scales of particles or bacteria in numerous practical applications (e.g., Happel and Brenner, 2012; Kim and Karrila, 2013). However, our physical intuition is mainly based on daily life experiences with large Reynolds numbers, e.g., when cycling, and could therefore lead us astray in the case of small Reynolds number flows as shown with the following examples.

We know from everyday experience that cycling in a lowered posture is associated with a reduction in the force exerted on the cyclist and that higher velocities can therefore be achieved at the same cadence and transmission ratio. Professional cyclists form a group (a so-called Peloton) which allows all cyclists to save their resources. It has been experimentally and numerically proven that the drag force acting on the cyclists in a Peloton can be reduced by more than 90% compared to an isolated cyclist moving at the same velocity (Blocken et al., 2018). The typical Reynolds number in bicycle races is of the order $\mathrm{Re} \approx O(10^5 - 10^6)$. At high Reynolds numbers, the presence of other objects moving at the same velocity can lead to a significant reduction of the drag force on a single object. Another insightful example is given through the drag resistance of convertible cars, as sketched in figure 1.1. It is known that the top-open car experiences an increase in drag of about $10\% - 25\%$ compared to the same car having the top closed (Cogotti, 1992). If the top of the car is open, a big pressure drop before and right after the windshield

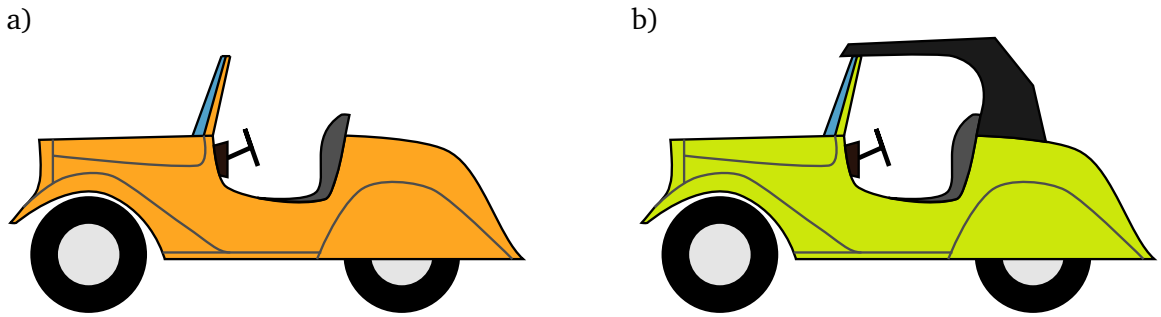

Abbildung 1.1.: Sketch of a convertible car with: a) an open top and b) a closed top.

goes along with vortices located in the passenger cabin leading to a high energy dissipation and consequently to a larger drag force (Cogotti, 1992). At typical traveling speed, the Reynolds number is about $\mathrm{Re} \approx O(10^6 - 10^7)$. In summary, a top-open car experiences a higher drag than a top-closed car at large Reynolds numbers. But how does the physical picture change at small Reynolds numbers?

The theorem formulated by Hill and Power (1956) helps answering this question. In the case of creeping flows ($\mathrm{Re} \ll 1$), the authors found with the help of the minimum energy dissipation theorem by von Helmholtz (1882):

1. The drag force on a body $\mathscr{B}_1$ translating through a quiescent fluid is smaller or equal to the drag on a different body $\mathscr{B}_2$ completely enclosing $\mathscr{B}_1$, i.e., $\mathscr{B}_1 \subset \mathscr{B}_2$;
2. The drag on a body $\mathscr{B}_1$ tends to increase by the presence of other bodies $\mathscr{B}_2, \ldots, \mathscr{B}_n$. The bodies $\mathscr{B}_2, \ldots, \mathscr{B}_n$ can be either fixed in position or free to move relative to $\mathscr{B}_1$.

At small Reynolds numbers the presence of other cyclists in the Peloton would increase the drag on an individual cyclist in contradiction to high Reynolds numbers (following result 2). Clearly, small Reynolds numbers are not present in bicycle races and one should probably think of bacteria instead of cyclists to reveal more reference to reality. In view of this example, however, our physical intuition does not agree with the results by Hill and Power (1956). Moreover, result 1 states that a convertible car as shown in figure 1.1 would experience a lower drag force if the top is opened, since it is a geometrical subset of the top-closed convertible car. The presence of aerodynamic components such as rear wings in microfluidic devices would therefore have an opposite effect and cause an increase of the drag force. In summary, it can therefore be stated that findings obtained for flows of large Reynolds numbers are not easily transferable to flows of small Reynolds numbers and vice versa.

This work is organized as follows:

Chapter 2 serves as an introduction of the underlying modeling concepts, the governing equations, the boundary conditions at fluid interfaces for a static and dynamic configuration, as well as other relevant principles and theorems that are applied in the course of this work. Chapter 2 therefore mainly summarizes results from the literature, whereas the main focus is on a phenomenological introduction of the underlying basic concepts.

Chapter 3 describes the transport of a single mircoparticle attached to a fluid interface driven by an externally applied electric field. Throughout this theoretical work, the influence of the contact angle between the surface of the particle and the fluid interface and its effect on the particle

motion as well as on the interfacial deformation is of major interest.

The influence of multiple spherical interfacial particles on global rheological properties of a fluid interface is studied theoretically in chapter 4. In the absence of external fields that induce a relative motion of the particle with respect to the fluid, the convective particle transport leads to an increase in energy dissipation which can effectively be related to an increase of the effective interfacial viscosities.

Chapter 5 describes a novel method to hydrodynamically isolate an obstacle from an applied flow in a shallow channel. Due to the small volume-to-surface ratio in narrow channels, an electro-osmotic flow (EOF), induced in a spatially controlled region at the walls perpendicular to the surface of the obstacle, is sufficient to significantly reduce the hydrodynamic force acting on the obstacle. A theoretical model is derived which determines the strength of the EOF and the geometrical shape of the charged region, which allows the shielding of a broad class of differently shaped obstacles.

The stability and collapse of a finitely extended liquid film with a single circular defect/hole is studied experimentally, theoretically and numerically in chapter 6. The influence of the wettability of the liquid layer as well as its lateral extension is the focus of the observation.

On the basis of chapter 6, the collapse of multiple circular holes is studied in chapter 7. By making use of the results of a single circular hole, a theoretical model is derived that allows the prediction of the collapse dynamics of multiple holes.

Every chapter contains a separate, more detailed introduction to its content, including a summary of previous work and possible applications. In addition, a summary of the most important results and an outlook on further studies are provided separately in every chapter. Chapter 8 therefore summarizes the main results of this work in a wider sense.

2 Theoretical background

This chapter introduces the underlying theoretical principles and the relevant governing equations of this work. The focus of this chapter lies in a more physically or phenomenologically motivated introduction of the mathematical framework of this study and does not contain a complete mathematical deduction as it can be found in many textbooks. Since a large part of this work deals with fluid-fluid interfaces, special attention is given on the derivation of the corresponding boundary conditions. Furthermore, the analytical solution of the linearized equation of fluid motion is discussed and the underlying mathematical framework is introduced. Subsequently, the reader is introduced to the domain perturbation method. After that, the so-called Lorentz reciprocal theorem is derived which will prove to be very useful in the course of this work. This chapter closes with the introduction of the physical concept of electric double layers and its properties.

2.1 Governing equations

Throughout this study, all physical effects are described on the basis of the continuum hypothesis. It is therefore assumed that it is always possible to define a representative volume element that contains a statistically significant number of fluid particles (or molecules) but is small enough to exclude the scale of variations of interest in a macroscopic point-of-view (Kim and Karrila, 2013). Consequently, macroscopic material properties, such as density or viscosity, can be attributed to the volume elements. The underlying physical perspective is often described as phenomenological (Giesekus, 2011; Altenbach, 2012).

The flow of a viscous liquid is closely related to a viscous dissipation that is accompanied with an increase of the temperature inside the liquid. The temperature inside a liquid strongly influences the macroscopic material parameters such as viscosity or surface tension. Throughout this study, we follow the general train-of-thought in microfluidics and assume isothermal conditions. By employing scaling arguments, Kim and Karrila (2013) have shown that isothermal conditions are fairly well satisfied as long as the flow is sufficiently slow.

Whenever the flow configuration consists of more than a single phase of a fluid, we assume that the fluids are immiscible. Fluid interfaces in that sense correspond to mathematical sharp interfaces, whereas in case of miscible liquids, fluid interfaces are more or less of diffusive character in which a clear definition of surface properties, such as surface tension, cannot be established (Gatignol and Prud'homme, 2001).

2.1.1 Equations of fluid motion

The balance equations for mass, momentum and angular momentum can be derived on the basis of the continuum hypothesis. The energy balance equation is of minor interest in large parts of this work, since we consider isothermal conditions. We may start our observation with the mass balance equation and consider a spatially fixed volume element $\mathrm{d}\mathcal{V}$ inside a flow field of a homogeneous fluid. In absence of sources and sinks inside $\mathrm{d}\mathcal{V}$, the temporal change of

the mass inside $\mathrm{d}\mathcal{V}$ is solely determined through the flux of mass in- and outwards across the boundaries of the volume element. Mathematically, the mass balance reads (e.g., Happel and Brenner, 2012)

$$\frac{\partial \rho}{\partial t} + \boldsymbol{\nabla} \cdot (\rho \boldsymbol{u}) = 0, \tag{2.1}$$

in which ρ, $\boldsymbol{u}$, t and $\boldsymbol{\nabla}$ denote the density, the velocity vector, the time and the Nabla operator, respectively. For liquids it is widely assumed that the density is constant in time and space. Exemplarily, water at $T = 20°\mathrm{C}$ exhibits a volume compression of 0.1% if the applied pressure is increased by 20 bar (Böhme, 2013). For gases on the other hand, the compressibility is typically related to the Mach number $\mathrm{Ma} = U/c \ll 1$ (Landau and Lifschitz, 1987), in which U and c denote a typical flow velocity and the speed of sound, respectively. For air at $T = 15°\mathrm{C}$, the speed of sound is $c \approx 340$ m/s (Batchelor, 2000), which is much faster than the typical velocities expected in the present study. Consequently, we assume $\rho = \text{const.}$ throughout this work. Equation (2.1) then simplifies to

$$\boldsymbol{\nabla} \cdot \boldsymbol{u} = 0. \tag{2.2}$$

Equation (2.2) is the so-called continuity equation.

The temporal change of the momentum inside a volume element $\mathrm{d}\mathcal{V}$ is equal to the convective transport of momentum over the boundaries $\mathrm{d}(\partial\mathcal{V})$ of $\mathrm{d}\mathcal{V}$ and momentum transported with forces acting on $\mathrm{d}\mathcal{V}$. The forces are typically divided into forces acting on the surface of $\mathrm{d}\mathcal{V}$ as well as inner forces (so-called volume forces), such as gravity. Mathematically, the momentum balance can be written as (e.g., Happel and Brenner, 2012)

$$\rho \left(\frac{\partial \boldsymbol{u}}{\partial t} + \boldsymbol{u} \cdot (\boldsymbol{\nabla} \boldsymbol{u}) \right) = \boldsymbol{\nabla} \cdot \boldsymbol{\Pi} + \boldsymbol{f}, \tag{2.3}$$

with $\boldsymbol{\Pi}$ and $\boldsymbol{f}$ denoting the total stress tensor and the total volume force density, respectively. In some parts of this work, the total stress tensor $\boldsymbol{\Pi}$ does not solely consist of hydrodynamic stresses $\boldsymbol{\sigma}$, but can be written as a superposition of hydrodynamic and Maxwell stresses $\boldsymbol{\sigma}_{\mathrm{M}}$, such that

$$\boldsymbol{\Pi} = \boldsymbol{\sigma} + \boldsymbol{\sigma}_{\mathrm{M}}. \tag{2.4}$$

However, equation (2.3) holds regardless of the rheological properties of the fluid. In this study, all fluids are Newtonian and therefore the viscosity of the liquid is independent on the deformation rate of the fluid (Giesekus, 2011). Prominent examples of incompressible Newtonian fluids are water or silicone oil under typical laboratory conditions (Böhme, 2013). For incompressible Newtonian fluids the hydrodynamic stress tensor can be written as

$$\boldsymbol{\sigma} = -p\boldsymbol{I} + \mu \left(\boldsymbol{\nabla} \boldsymbol{u} + (\boldsymbol{\nabla} \boldsymbol{u})^{\mathscr{T}} \right), \tag{2.5}$$

in which p, $\boldsymbol{I}$, μ and the superscript $\mathscr{T}$ denote the thermodynamic pressure, the identity matrix, the shear viscosity and the transpose of a tensor, respectively. Mathematically, equation (2.5) describes the decomposition of the hydrodynamic stresses into an isotropic $\boldsymbol{\sigma}_{\mathscr{I}}$ and a deviatoric

part $\boldsymbol{\sigma}_{\mathscr{D}}$, proportional to the thermodynamic pressure and the gradient of the velocity field, respectively. Inserting equations (2.4) and (2.5) into (2.3), one obtains

$$\rho\left(\frac{\partial \boldsymbol{u}}{\partial t}+\boldsymbol{u}\cdot(\boldsymbol{\nabla}\boldsymbol{u})\right)=-\boldsymbol{\nabla}p+\mu\boldsymbol{\nabla}^2\boldsymbol{u}+\boldsymbol{\nabla}\cdot\boldsymbol{\sigma}_M+\boldsymbol{f}, \tag{2.6}$$

in which $\boldsymbol{\nabla}^2=\boldsymbol{\nabla}\cdot\boldsymbol{\nabla}$ denotes the Laplace operator. An alternative form of the latter equation can be achieved when defining $\boldsymbol{f}_{\mathrm{M}}=\boldsymbol{\nabla}\cdot\boldsymbol{\sigma}_{\mathrm{M}}$. However, the probably most prominent body force is induced by gravity and reads $\boldsymbol{f}_{\mathrm{g}}=\rho\boldsymbol{g}$, with $\boldsymbol{g}=-g\boldsymbol{e}_z$, whereas g is the gravitational constant, hereby working in negative z-direction. $\boldsymbol{e}_z$ is the Cartesian unit vector in z-direction. It should be noted that the gravitational body force can alternatively be written as $\boldsymbol{f}_{\mathrm{g}}=-\boldsymbol{\nabla}(-\rho\boldsymbol{g}\cdot\boldsymbol{r})$ ($\boldsymbol{r}$ is the position vector), which means that the term $(-\rho\boldsymbol{g}\cdot\boldsymbol{r})$ is the potential of $\boldsymbol{f}_{\mathrm{g}}$. If, however, the gravitational body force is the only volume force that acts on the system, we may rewrite equation (2.6) into

$$\begin{aligned}\rho\left(\frac{\partial \boldsymbol{u}}{\partial t}+\boldsymbol{u}\cdot(\boldsymbol{\nabla}\boldsymbol{u})\right) &= -\boldsymbol{\nabla}p^\star+\mu\boldsymbol{\nabla}^2\boldsymbol{u}+\boldsymbol{\nabla}\cdot\boldsymbol{\sigma}_M, &(2.7)\\ \text{with } p^\star &= p-\rho\boldsymbol{g}\cdot\boldsymbol{r}. &(2.8)\end{aligned}$$

Consequently, it is possible to include the effect of gravity, or any other volume force that can be expressed through a potential, into the pressure, while $p^\star$ is often referred to as dynamic pressure. From now on, we suppress to carry the superscript * in the notation, keeping in mind that the pressure includes the gravitational term, if needed.

To reveal the relevance of the Reynolds number Re in the theoretical description of flow processes, the momentum balance is written in dimensionless form. The following dimensionless quantities are introduced

$$\tilde{\boldsymbol{u}}=\boldsymbol{u}/U,\quad \tilde{t}=tU/L,\quad \tilde{p}=pL/(\mu U),\quad \tilde{\boldsymbol{\nabla}}=L\boldsymbol{\nabla}. \tag{2.9}$$

U and L represent a characteristic flow velocity and a characteristic length scale, respectively. The Maxwell stresses are not written in non-dimensional form, since they have not yet been introduced. Equation (2.7) then evolves into

$$\mathrm{Re}\left(\frac{\partial \tilde{\boldsymbol{u}}}{\partial \tilde{t}}+\tilde{\boldsymbol{u}}\cdot(\tilde{\boldsymbol{\nabla}}\tilde{\boldsymbol{u}})\right)=-\tilde{\boldsymbol{\nabla}}\tilde{p}+\tilde{\boldsymbol{\nabla}}^2\tilde{\boldsymbol{u}}+\frac{L^2}{\mu U}\boldsymbol{\nabla}\cdot\boldsymbol{\sigma}_M. \tag{2.10}$$

$\mathrm{Re}=\rho UL/\mu$ is the Reynolds number, i.e., the ratio of inertial and viscous forces within the flow. Due to the small length scales in microfluidics, the Reynolds number is typically small enough to neglect the left-hand side in equation (2.10) (Kim and Karrila, 2013). However, the non-dimensional form of the Maxwell stresses together with the prefactor in equation (2.10) should be of order $O(1)$ (referring to the Reynolds number) to preserve the electrostatic effects in the momentum equation. In dimensional form, we therefore have

$$0=-\boldsymbol{\nabla}p+\mu\boldsymbol{\nabla}^2\boldsymbol{u}+\boldsymbol{\nabla}\cdot\boldsymbol{\sigma}_M. \tag{2.11}$$

In absence of Maxwell stresses $\boldsymbol{\sigma}_M = 0$, the combination of equations (2.2) and (2.11) is often referred as Stokes' equations (e.g., Happel and Brenner, 2012; Kim and Karrila, 2013).

The balance equation of the angular momentum trivially leads to $\mathbf{\Pi} = \mathbf{\Pi}^{\mathscr{T}}$ and therefore states that the stress tensor is symmetric (Giesekus, 2011; Altenbach, 2012). Implicitly, we have already made use of this result when introducing the constitutive equation for incompressible Newtonian fluids [see equation (2.5)].

2.1.2 Equations of electrostatics

The essential basis for the derivation of the governing equations of electrostatics is Coulomb's law (Jackson, 2007; Masliyah and Bhattacharjee, 2006) that determines the force between two point charges Q_1 and Q_2. More specifically, the force between two point charges has been postulated proportional to the product of both charges, decaying with the squared distance between the charges. In a linear and isotropic dielectric medium [no free or mobile charges (Masliyah and Bhattacharjee, 2006)], Coulomb's law states that the force on Q_2 due to the presence of Q_1 is

$$\mathscr{F}_{\mathrm{c}} = \frac{Q_1 Q_2 \boldsymbol{r}_{12}}{4\pi\epsilon\,|\boldsymbol{r}_{12}|^3}. \tag{2.12}$$

$\boldsymbol{r}_{12}$, $|\boldsymbol{r}_{12}|$ and ϵ denote the position vector directing from Q_1 to Q_2, the distance between both charges and the permittivity of the surrounding medium, respectively. Without loss of generality, we assume that the origin of the coordinate system $\mathscr{O}$ is located at the position of the charge Q_1. The electric field strength $\boldsymbol{E}$ at the second charge is defined as the term proportional to Q_2 in equation (2.12). Consequently, the electric field strength $\boldsymbol{E}$ induced by a point charge $Q = Q_1$, aligned with the coordinate origin, reads

$$\boldsymbol{E} = \frac{Q}{4\pi\epsilon r^2}\boldsymbol{e}_r. \tag{2.13}$$

When assuming that Q is located at the center of a control volume $\mathrm{d}\mathscr{V}$ enclosed by a surface $\mathrm{d}(\partial\mathscr{V})$ with a surface normal vector $\boldsymbol{n}$ pointing in outward direction, we find after integrating the normal electric field strength $\boldsymbol{E}\cdot\boldsymbol{n}$ over the surface $\mathrm{d}(\partial\mathscr{V})$

$$\int\limits_{\mathrm{d}(\partial\mathscr{V})} \boldsymbol{E}\cdot\boldsymbol{n}\;\mathrm{d}\mathscr{A} = \frac{Q}{\epsilon}. \tag{2.14}$$

The charge Q is now expressed through a volume integral of the charge density q, i.e., $Q = \int q\;\mathrm{d}\mathscr{V}$, by making use of the superposition principle for point charges (Jackson, 2007). When employing the divergence theorem, the left-hand side of equation (2.14) can be transferred into a volume integral. Since $\mathrm{d}\mathscr{V}$ is chosen arbitrarily, the integrand itself has to coincide and we obtain

$$\epsilon\boldsymbol{\nabla}\cdot\boldsymbol{E} = q. \tag{2.15}$$

Equation (2.15) is known as Gauss's law (e.g., Jackson, 2007).

Equation (2.13) serves as the basis of another important relationship for the electric field. Computing the curl of the electric field strength defined as $\boldsymbol{\nabla} \times \boldsymbol{E}$, we obtain

$$\boldsymbol{\nabla} \times \boldsymbol{E} = 0, \tag{2.16}$$

which is easily verified with index notation. The latter equation motivates introducing the electrostatic potential Ψ via $\boldsymbol{E} = -\boldsymbol{\nabla}\Psi$. For mathematical purposes, it is helpful to replace the electric field in equation (2.15) with the potential Ψ, leading to the Poisson equation (e.g., Jackson, 2007)

$$\epsilon \boldsymbol{\nabla}^2 \Psi = -q, \tag{2.17}$$

relating the electrostatic potential with the charge density. The volume force density related to the Maxwell stresses $\boldsymbol{f}_{\mathrm{M}} = \boldsymbol{\nabla} \cdot \boldsymbol{\sigma}_{\mathrm{M}}$ then reads

$$\boldsymbol{f}_{\mathrm{M}} = q\boldsymbol{E} = \epsilon \boldsymbol{\nabla}^2 \Psi \boldsymbol{\nabla} \Psi. \tag{2.18}$$

2.1.3 Equations of species transport

In agreement with section 2.1.1, in which the simplification of the momentum balance equation led to the Stokes equations, the derivation of the governing equations of species transport underlies the assumption of time independent transport in which chemical reactions are excluded. All electrolytes that are considered in this work are symmetric $(\mathfrak{z}, -\mathfrak{z})$. In symmetric electrolytes, the cations and anions have the same valency $|\mathfrak{z}|$ (Masliyah and Bhattacharjee, 2006). The probably most prominent example of a symmetric electrolyte is NaCl $(\mathfrak{z} = 1)$ dissolved in water. We may denote the cations with the subscript $+$, whereas the anions carry the subscript $-$. Under the given assumptions, the equation of species transport reads

$$\boldsymbol{\nabla} \cdot \boldsymbol{j}_i = 0, \qquad \boldsymbol{j}_i = n_i \boldsymbol{u}_i, \qquad i = +, -, \tag{2.19}$$

in which n_i and $\boldsymbol{u}_i$ denote the number density of species i and the velocity of species i, respectively. $\boldsymbol{j}_i$ is the ionic flux of the cations and anions. For convenience, the ionic flux $\boldsymbol{j}_i$ can be rewritten into

$$\boldsymbol{j}_i = n_i \boldsymbol{u} + n_i (\boldsymbol{u}_i - \boldsymbol{u}), \tag{2.20}$$

which can be interpreted as a superposition of a purely convective ion transport (the ions follow the flow of the surrounding fluid with the same velocity $\boldsymbol{u}$) and additional transport processes that describe an ionic motion relative to the surrounding fluid. Obviously, even in the absence of fluid motion $(\boldsymbol{u} = 0)$ ions can be transported throughout the medium depending on the presence of additional fluxes.

The first additional flux to be taken into account is due to the diffusive properties of dissolved salt in water, typically described with Fick's law (Masliyah and Bhattacharjee, 2006)

$$\boldsymbol{j}_i^d = -D_i \boldsymbol{\nabla} n_i, \tag{2.21}$$

with D_i denoting the diffusion coefficient of species i. For convenience, we assume that the diffusion coefficients of the cations and anions coincide $D_+ = D_- = D$. Equation (2.21) states that dissolved ions tend to move towards the region of lower concentration gradients in order to achieve a homogeneous concentration inside the fluid.

The second additional ion flux considered in the course of this work is induced by the presence of an electric field. Due to the small size of the ions, they might be considered as point charges, with charges $\mathfrak{z}_+ e$ (cation) and $\mathfrak{z}_- e$ (anion), with $\mathfrak{z}_+ = -\mathfrak{z}_- = \mathfrak{z}$ and $e = 1.60217662 \times 10^{-19}$ A s denoting the elementary charge. Due to the charge of the ions and the presence of an electric field, an electrostatic force is induced (see section 2.1.2) that leads to a relative motion of the ions through the fluid. In steady state, the electrostatic force is balanced by the hydrodynamic force, leading to

$$6\pi\mu\mathfrak{a}(\boldsymbol{u}_i - \boldsymbol{u}) = -\mathfrak{z}_i e \boldsymbol{\nabla}\Psi, \tag{2.22}$$

where $\mathfrak{a}$ is the radius of an ion. The left-hand side is known as the Stokes force, i.e., the hydrodynamic force acting on a spherical particle in a constant flow field at low Reynolds numbers $\mathrm{Re} \ll 1$. With the Einstein-Stokes relation (Masliyah and Bhattacharjee, 2006)

$$D = \frac{k_B T}{6\pi\mu\mathfrak{a}}, \tag{2.23}$$

with $k_B = 1.38064852 \times 10^{-23}$ m^{2}kg/(s^{2}K) and T being the Boltzmann constant and the temperature of the medium, the electrostatic migration flux can be written as

$$\boldsymbol{j}_i^m = -n_i \frac{\mathfrak{z}_i e D}{k_B T} \boldsymbol{\nabla}\Psi. \tag{2.24}$$

Inserting equations (2.24), (2.21) and (2.20) into (2.19), we arrive at

$$\boldsymbol{\nabla} \cdot \left[n_i \boldsymbol{u} - D\left(\boldsymbol{\nabla} n_i + n_i \frac{\mathfrak{z}_i e}{k_B T} \boldsymbol{\nabla}\Psi \right) \right] = 0, \qquad i = +, -. \tag{2.25}$$

Equation (2.25) is often referred as the stationary Nernst-Planck equation for symmetric $(\mathfrak{z}, \mathfrak{z})$-electrolytes.

The charge density q from equation (2.17) is related to the difference of the number concentrations of cations and anions as follows

$$q = \mathfrak{z} e (n_+ - n_-). \tag{2.26}$$

2.2 Boundary conditions at free interfaces

In this section, we derive the boundary conditions on a fluid-fluid interface corresponding to the governing equations introduced in the foregoing sections. To start with, we define the term 'free interface' and discuss its associated physical properties.

In agreement with previous sections, the physics of multiphase flows underlies the continuum

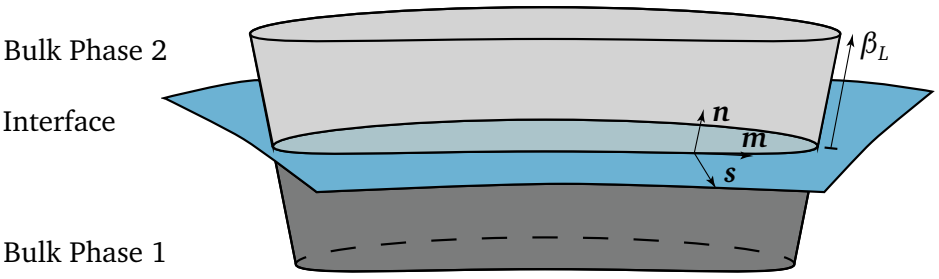

Abbildung 2.1.: Sketch of a control volume $\mathscr{V}$ consisting of two fluid portions $\mathscr{V}_1$ and $\mathscr{V}_2$ divided by an ideal interface $\mathscr{A}$. A control volume of this type is often referred as a Gaussian pillbox (Jackson, 2007). The vector $\boldsymbol{n}$ is the normal vector on the ideal interface at the intersecting curve between $\mathscr{V}_i$ and $\mathscr{A}$, pointing from $\mathscr{V}_1$ towards $\mathscr{V}_2$. $\boldsymbol{m}$ is the vector pointing in tangential direction along the intersection curve and $\boldsymbol{s}$ corresponds to the second tangential vector on $\mathscr{A}$ but orthogonal to $\boldsymbol{m}$. β_L is the height of each bulk portion.

hypothesis. Therefore, we describe the interface from a macroscopic point-of-view, i.e., a two-dimensional singular boundary separating two bulk phases (Brenner, 1991). Consequently, the physical properties experience a jump across the interface. It is also possible that the interface carries own physical quantities deviating from the bulk quantities such as a surface mass density or surface concentration. In this case, additional interfacial conservation equations have to be taken into account. For more details, the reader is referred to Brenner (1991); Slattery et al. (2007); Wang and Oberlack (2011). If not stated otherwise, we may limit ourselves to 'ideal' interfaces defined as massless, incompressible, concentration-free and chargeless. As one important consequence, the interface is convectively transported with the bulk phases.

The boundary conditions at the fluid interface are derived by integrating the governing equations over the interface, while taking additional interfacial properties such as surface/interfacial tensions into account. In figure 2.1, a sketch of a control volume $\mathscr{V}$ consisting of two fluid portions with volume $\mathscr{V}_1$ and $\mathscr{V}_2$ separated by an ideal interface $\mathscr{A}$ is shown. It is assumed that the control volume $\mathscr{V}$ has a height $2\beta_L$ and that the upper and lower surface is parallel with the interface $\mathscr{A}$. We may therefore denote the top and bottom portion of the enclosing surface of $\mathscr{V}$ as $\partial\mathscr{V}_{1,\parallel}$ and $\partial\mathscr{V}_{2,\parallel}$, whereas the perpendicular portions of the surrounding surface are denoted by $\partial\mathscr{V}_{1,\perp}$ and $\partial\mathscr{V}_{2,\perp}$, respectively.

When integrating the continuity equation over the control volume $\mathscr{V}$, we find

$$\sum_{i=1}^{2} \int_{\mathscr{V}_i} \boldsymbol{\nabla} \cdot \boldsymbol{u}_i \, \mathrm{d}\mathscr{V} = 0. \tag{2.27}$$

Employing the divergence theorem, the volume integrals are transferred into surface integrals as follows

$$\sum_{i=1}^{2} \left[\int_{\partial\mathscr{V}_{i,\parallel}} \boldsymbol{u}_i \cdot \boldsymbol{n}_{i,\parallel} \, \mathrm{d}\mathscr{A} + \int_{\partial\mathscr{V}_{i,\perp}} \boldsymbol{u}_i \cdot \boldsymbol{n}_{i,\perp} \, \mathrm{d}\mathscr{A} \right] = 0, \tag{2.28}$$

in which $\boldsymbol{n}_{i,\parallel}$ and $\boldsymbol{n}_{i,\perp}$ are the outwards directed normal vectors on $\partial\mathscr{V}_{i,\parallel}$ and $\partial\mathscr{V}_{i,\perp}$, respectively. To achieve boundary conditions for the fluid interface, we set $\beta_L \to 0$ and find $\partial\mathscr{V}_{i,\perp} \to 0$, $\partial\mathscr{V}_{i,\parallel} \to \mathscr{A}$, for $i = 1,2$ and $\boldsymbol{n}_{1,\parallel} = -\boldsymbol{n}_{2,\parallel} = -\boldsymbol{n}$, while $\boldsymbol{n}$ is the normal vector on $\mathscr{A}$ pointing from phase 1 into phase 2. Equation (2.28) consequently leads to

$$\int_{\mathscr{A}} (\boldsymbol{u}_2 - \boldsymbol{u}_1) \cdot \boldsymbol{n} \, \mathrm{d}\mathscr{A} = 0. \tag{2.29}$$

Since the control volume is chosen arbitrarily, the previous equation holds for all portions of the fluid interface. Therefore, the integrand has to vanish, i.e.,

$$(\boldsymbol{u}_2 - \boldsymbol{u}_1) \cdot \boldsymbol{n} = [\![\boldsymbol{u}]\!] \cdot \boldsymbol{n} = 0. \tag{2.30}$$

The notation $[\![.]\!]$ is commonly referred as jump-bracket notation (e.g., Brenner, 1991; Wang and Oberlack, 2011).

Whenever a viscous fluid is in contact with a moving wall it is often assumed that the velocity of the fluid coincides to the velocity of the wall. This boundary condition is called 'no-slip' boundary condition. Inspired by the no-slip boundary condition, it is also often assumed that the tangential velocities of both fluids coincide at the fluid interface (Castellanos, 1998; Ramos, 2011). Consequently, we may extend equation (2.30) leading to

$$[\![\boldsymbol{u}]\!] = 0. \tag{2.31}$$

Mathematically, equation (2.31) states that the velocity vector is continuous across a fluid interface.

It is known from daily life experience, that buoyant objects (e.g., a paper-clip) can float on water. This phenomena is attributed to the surface tension γ_{12} from which a fluid-fluid interface shows a membrane-like elastic behavior. The surface tension (in general space and time dependent) enables fluids to minimize their surface area and to form various morphologies under external forces or geometrical constraints, e.g., induced by a floating paper-clip. The surface tension force is modeled as a line integration of the surface tension along the intersection curve between $\mathscr{V}_i$ and $\mathscr{A}$ (see figure 2.1), as follows (e.g., Leal, 2007)

$$\mathscr{F}_{\mathrm{SF}} = \oint_{\partial\mathscr{A}} \gamma_{12} \boldsymbol{s} \, \mathrm{d}(\partial\mathscr{A}), \tag{2.32}$$

The latter equation can be transferred into an integral over an area portion of the interface $\mathscr{A}$ with the help of the Stokes theorem (e.g., Leal, 2007). We obtain

$$\mathscr{F}_{\mathrm{SF}} = \int_{\mathscr{A}} \boldsymbol{\nabla}_{\mathscr{S}} \gamma_{12} - \gamma_{12} \boldsymbol{n} (\boldsymbol{\nabla}_{\mathscr{S}} \cdot \boldsymbol{n}) \, \mathrm{d}\mathscr{A}, \tag{2.33}$$

with $\boldsymbol{\nabla}_{\mathscr{S}}$ denoting the Nabla operator defined on the interface $\mathscr{A}$. The term $\boldsymbol{\nabla}_{\mathscr{S}}\gamma_{12}$ takes so-called Marangoni effects, i.e., a spatial depending interfacial tension due to temperature or concentration gradients, into account (e.g., Brenner, 1991; Leal, 2007).

Similar to the integration of the continuity equation, we integrate the momentum equation over the total volume consisting of both volume portions. We may therefore assume that all volume forces that can be expressed with a potential are included in the total stress tensor $\boldsymbol{\Pi}$ as already discussed in section 2.1.1. We then find

$$\sum_{i=1}^{2}\left[\int_{\mathscr{V}_i}\rho_i\left(\frac{\partial \boldsymbol{u}_i}{\partial t}+\boldsymbol{u}_i\cdot\boldsymbol{\nabla}\boldsymbol{u}_i\right)\mathrm{d}\mathscr{V}+\int_{\partial\mathscr{V}_{i,\parallel}}\boldsymbol{\Pi}_i\cdot\boldsymbol{n}_{i,\parallel}\,\mathrm{d}\mathscr{A}+\int_{\partial\mathscr{V}_{i,\perp}}\boldsymbol{\Pi}_i\cdot\boldsymbol{n}_{i,\perp}\,\mathrm{d}\mathscr{A}\right]=-\mathscr{F}_{\mathrm{SF}}. \quad (2.34)$$

Here, $\boldsymbol{\Pi}$ is the overall stress tensor, defined in equation (2.4). Again, we set $\beta_L \to 0$ and the volume integrals as well as the contributions perpendicular to the fluid interface vanish asymptotically, whereas we are left with

$$\int_{\mathscr{A}}[\![\boldsymbol{\Pi}]\!]\cdot\boldsymbol{n}\mathrm{d}\mathscr{A}=-\mathscr{F}_{\mathrm{SF}}. \quad (2.35)$$

Since the area portion $\mathscr{A}$ has been chosen arbitrarily, the integrand on both sides of the latter equation has to coincide, leading to

$$[\![\boldsymbol{\Pi}]\!]\cdot\boldsymbol{n}=\gamma_{12}\boldsymbol{n}(\boldsymbol{\nabla}_{\mathscr{S}}\cdot\boldsymbol{n})-\boldsymbol{\nabla}_{\mathscr{S}}\gamma_{12}. \quad (2.36)$$

For convenience, we compute the scalar product of the latter equation with the normal $\boldsymbol{n}$ and tangential vectors $\boldsymbol{m}$ & $\boldsymbol{s}$ of the fluid interface and obtain

$$\boldsymbol{n}\cdot[\![\boldsymbol{\Pi}]\!]\cdot\boldsymbol{n} = \gamma_{12}(\boldsymbol{\nabla}_{\mathscr{S}}\cdot\boldsymbol{n}), \quad (2.37)$$
$$\boldsymbol{t}_i\cdot[\![\boldsymbol{\Pi}]\!]\cdot\boldsymbol{n} = -\boldsymbol{\nabla}_{i,\mathscr{S}}\gamma_{12},\quad i=1,2, \quad (2.38)$$

where we have employed the notation $\boldsymbol{t}_1=\boldsymbol{m}$ and $\boldsymbol{t}_2=\boldsymbol{s}$. In absence of Maxwell stresses and in case of a static configuration, equation (2.37) leads to the Young-Laplace equation, discussed in more detail in section 2.2.1. Equations (2.37) and (2.38) are often referred as the normal and tangential stress-jump equations of a fluid interface.

Following the general train of thought of this chapter, we integrate the Poisson equation (2.17) over the volume element depicted in figure 2.1, to find

$$\sum_{i=1}^{2}\left[\int_{\partial\mathscr{V}_{i,\parallel}}\epsilon_i\boldsymbol{\nabla}\Psi_i\cdot\boldsymbol{n}_{i,\parallel}\mathrm{d}\mathscr{A}+\int_{\partial\mathscr{V}_{i,\perp}}\epsilon_i\boldsymbol{\nabla}\Psi_i\cdot\boldsymbol{n}_{i,\perp}\mathrm{d}\mathscr{A}\right]=-\sum_{i=1}^{2}\left[\int_{\mathscr{V}_i}q_i\mathrm{d}\mathscr{V}\right]-\int_{\mathscr{A}}q_{\mathscr{S}}\mathrm{d}\mathscr{A}. \quad (2.39)$$

For $\beta_L \to 0$, the left-hand side of the latter equation transforms in agreement to the previous equations. However, the volume integrals on the right-hand side of equation (2.39) converge to

zero whereas the surface integral of the interfacial charge $q_{\mathscr{S}}$ over the fluid interface remains (Jackson, 2007). It is worth mentioning that in case of mobile interfacial charges (depending on time and space), an additional conservation equation for the interfacial charges has to be taken into account, as discussed in Castellanos (1998). However, equation (2.39) leads to

$$[\![\epsilon \boldsymbol{\nabla}\Psi]\!] \cdot \boldsymbol{n} = -q_{\mathscr{S}}. \tag{2.40}$$

Finally, we are left with the integration of the stationary Nernst-Planck equation from equation (2.25) over the volume element $\mathscr{V}$ containing the singular surface $\mathscr{A}$. For a reason that become clear later, we assume that volume $\mathscr{V}_2$ is free of ions. Then, following the same strategy as before, we obtain

$$\boldsymbol{\nabla} n_i \cdot \boldsymbol{n} = \frac{n_i}{D}\boldsymbol{u} \cdot \boldsymbol{n} - n_i \frac{\mathfrak{z}_i e}{k_B T}\boldsymbol{\nabla}\Psi \cdot \boldsymbol{n}, \qquad i = +,-, \tag{2.41}$$

where all variables and constants refer to volume $\mathscr{V}_1$.

2.2.1 The Young-Laplace equation

Whenever a two-phase configuration is at rest, the shape of the fluid interface is controlled through the Young-Laplace equation (de Gennes et al., 2003). On the basis of the previous derivation, we obtain the Young-Laplace equation as a special case of equation (2.37). We therefore consider the absence of Maxwell stresses and set the fluid velocity $\boldsymbol{u} = 0$. We then find

$$-[\![p]\!] = \gamma_{12}(\boldsymbol{\nabla}_{\mathscr{S}} \cdot \boldsymbol{n}). \tag{2.42}$$

It is worth mentioning that for spatially dependent surface tensions, a static configuration with both fluids at rest cannot be reached, which directly follows from equation (2.38). For reasons to become apparent later, we consider a rotational symmetric interfacial parametrization in cylindrical coordinates of the form $z(r)$. Furthermore, we introduce the mean curvature $\mathscr{H}$ of the fluid interface via $2\mathscr{H} = \boldsymbol{\nabla}_{\mathscr{S}} \cdot \boldsymbol{n}$. Recalling that the gravitational volume force is subdivided into the pressure via equation (2.8), we are led to

$$\Delta p - \Delta\rho\, g z(r) = 2\gamma_{12}\mathscr{H}(r), \tag{2.43}$$

in which $\Delta p = p_1 - p_2$ and $\Delta\rho = \rho_1 - \rho_2$ are the pressure and density differences between phase 1 and phase 2. However, due to the large density differences between liquids and gases, $\Delta\rho$ can often be approximated via $\Delta\rho \approx \rho_1 = \rho$. To gain further insight in the mathematical structure of equation (2.43), we compute the mean curvature for a rotational symmetric interfacial parametrization $z(r)$. The normal vector on the fluid interface is computed following the method presented by Leal (2007). We obtain

$$\boldsymbol{n} = \frac{\boldsymbol{e}_z - \boldsymbol{\nabla} z}{\sqrt{1 + (\boldsymbol{\nabla} z)^2}}, \tag{2.44}$$

from which the mean curvature follows as

$$\mathscr{H}(r) = -\frac{1}{2}\left(\frac{\frac{\mathrm{d}z}{\mathrm{d}r}\left(1+\left(\frac{\mathrm{d}z}{\mathrm{d}r}\right)^2\right)+r\frac{\mathrm{d}^2z}{\mathrm{d}r^2}}{r\left(1+\left(\frac{\mathrm{d}z}{\mathrm{d}r}\right)^2\right)^{\frac{3}{2}}}\right). \tag{2.45}$$

Even for the comparably simple case of a rotational symmetric fluid interface, the Young-Laplace equation is a complex nonlinear differential equation.

In many textbooks, the Young-Laplace equation is derived following the minimization of the potential energy, consisting of gravitational and surface energies under the constraint of volume conservation. In this case, the pressure drop Δp takes the role of a Lagrange multiplier that is introduced to ensure volume conservation throughout the calculation of variations (Myshkis et al., 1987; Langbein, 2002). For convenience, we introduce the short-hand notation $\lambda = -\Delta p$, and treat λ as an unknown constant to be specified during the solution process. Thus, we finally obtain

$$\lambda + \rho g z = \gamma_{12}\left(\frac{\frac{\mathrm{d}z}{\mathrm{d}r}\left(1+\left(\frac{\mathrm{d}z}{\mathrm{d}r}\right)^2\right)+r\frac{\mathrm{d}^2z}{\mathrm{d}r^2}}{r\left(1+\left(\frac{\mathrm{d}z}{\mathrm{d}r}\right)^2\right)^{\frac{3}{2}}}\right). \tag{2.46}$$

In some applications, it is reasonable to rewrite the latter equation in a slightly different form. Especially for large contact angles, the solution of equation (2.46) must often be separated into multiple solution domains, since otherwise the uniqueness of the relation between a certain r-value and the corresponding height of the liquid film cannot be guaranteed (e.g., Wilson and Duffy, 1996). This disadvantage related to large contact angles can be fixed when rewriting the latter equation into three ordinary differential equations in the variables $\{\varphi(s) = \arctan(\mathrm{d}z/\mathrm{d}r), r(s), z(s)\}$ that solely depend on the arc length s of the meniscus (Langbein, 2002). From $\mathrm{d}r = \cos(\varphi(s))\mathrm{d}s$ and $\mathrm{d}z = \sin(\varphi(s))\mathrm{d}s$, we find the following set of ordinary differential equations

$$\gamma_{12}\left(\frac{\mathrm{d}\varphi}{\mathrm{d}s}+\frac{\sin(\varphi)}{r}\right) = \lambda + \rho g z, \tag{2.47}$$

$$\frac{\mathrm{d}r}{\mathrm{d}s} = \cos(\varphi), \tag{2.48}$$

$$\frac{\mathrm{d}z}{\mathrm{d}s} = \sin(\varphi). \tag{2.49}$$

Neglecting the presence of gravity, Myshkis et al. (1987) provided a very insightful derivation of the Young-Laplace equation. In case of a fluid-fluid interface in contact with a solid wall, the authors also considered the first variation of the three-phase contact line displacement (i.e., the line of contact between the fluid-fluid interface and the solid) and obtained Young's law (de Gennes et al., 2003; Tabeling, 2005) that relates the interfacial/surface tensions γ_{12}, $\gamma_{S(1)}$ and $\gamma_{S(2)}$ via

$$\gamma_{12}\cos(\Theta) = \gamma_{S(2)} - \gamma_{S(1)}, \tag{2.50}$$

in which $\gamma_{S(1)}$, $\gamma_{S(2)}$ and Θ are the surface tension between the solid and fluid 1, the surface tension between the solid and fluid 2 and the contact angle between the solid and the fluid. The contact angle is a physical property that depends on the constitution of the substrate and the fluid as well as on other constraints applied to the multiphase configuration, such as temperature (de Gennes et al., 2003). We define solid-fluid configurations with contact angle ranges of $\Theta < 90°$, $90° < \Theta < 150°$ and $150° < \Theta$ as hydrophilic, hydrophobic and superhydrophobic, hereinafter.

2.3 Lamb's general solution of the Stokes equations

Typical flows in microfluidics are characterized by small Reynolds numbers $\mathrm{Re} \ll 1$, leading to the Stokes equations from section 2.1.1. Throughout this section, we consider the motion of a fluid in absence of Maxwell stresses.

The analytical solution of the Stokes equations in spherical coordinates date back to the work of Lamb (1945). The outline of the general strategy of the derivation as well as the application of the analytical solution is the main focus of this section.

When computing the divergence of the linearized momentum equation and making use of the continuity equation (2.2), it follows that the pressure satisfies Laplace's equation

$$\boldsymbol{\nabla}^2 p = 0. \tag{2.51}$$

In general, a solution of the Laplace equation can be written as a sum of solid spherical harmonics, via

$$p = \sum_{n=-\infty}^{\infty} p_n, \tag{2.52}$$

in which p_n is a solid spherical harmonics of order n. A solid spherical harmonic of order n is homogeneous in n (Happel and Brenner, 2012), i.e., $p_n \propto r^n$, in which r is the radial coordinate. It is known from the mathematical theory of Laplace's equation that the angle dependence of the solution can be represented by a set of orthogonal functions defined on a sphere, the so-called surface spherical harmonics (Byerly, 1893; MacRobert, 1947; Jackson, 2007). The solid spherical harmonics p_n are related to the surface spherical harmonics Y_m^k in its most general form as follows

$$p_n = r^n \sum_{m=0}^{k} a_m^k Y_m^k, \tag{2.53}$$

in which a_m^k are constants. Lamb (1945) made use of the mathematical properties of the solid spherical harmonics and derived the following solution for the Stokes equations

$$\begin{aligned} \boldsymbol{u} \;=\; & \sum_{n=-\infty}^{\infty} \Bigg[\boldsymbol{\nabla} \times (\boldsymbol{r}\chi_n) + \boldsymbol{\nabla}\phi_n \\ & + \frac{(n+3)}{2\mu(n+1)(2n+3)} r^2 \boldsymbol{\nabla} p_n - \frac{n}{\mu(n+1)(2n+3)} \boldsymbol{r}\, p_n \Bigg]. \end{aligned} \tag{2.54}$$

The quantities χ_n and ϕ_n are also solid spherical harmonics of order n. The first two terms on the right-hand side of the latter equation correspond to the homogeneous solution of the Stokes equations whereas the terms left-over refer to the particular solution (Lamb, 1945). Effectively, Lamb's general solution transfers the solution of the Stokes equations to the solutions of three Laplace equations that are related through equation (2.54). It should further be noted that the partial sums corresponding to $n < 0$, are sufficient to describe the flow outside a sphere in an unbounded medium, whereas the terms corresponding to $n > 0$ solely determine the flow interior to a sphere. Throughout this work, we are mainly interested in exterior flows and therefore set all solid spherical harmonics of order $n > 0$ to zero. Equations (2.52) & (2.54) can then be transferred into (Happel and Brenner, 2012)

$$p = \sum_{n=1}^{\infty} p_{-(n+1)}, \tag{2.55}$$

$$\begin{aligned} \boldsymbol{u} = \sum_{n=1}^{\infty} \Bigg[& \boldsymbol{\nabla} \times \left(\boldsymbol{r}\, \chi_{-(n+1)} \right) + \boldsymbol{\nabla} \phi_{-(n+1)} \\ & - \frac{(n-2)}{2\mu n(2n-1)} r^2 \boldsymbol{\nabla} p_{-(n+1)} + \frac{(n+1)}{\mu n(2n-1)} \boldsymbol{r}\, p_{-(n+1)} \Bigg]. \end{aligned} \tag{2.56}$$

A complete discussion of the implementation of the boundary conditions into Lamb's general solution is given by Brenner (1964) and Happel and Brenner (2012). In the following, we reiterate their general scheme.

Let $\boldsymbol{u}|_{r=a} = \boldsymbol{V}(\theta, \varphi) = \boldsymbol{V}$ read an arbitrary boundary condition at the surface of the sphere of radius a. Then, the following three quantities have to be expanded in surface spherical harmonics [e.g., following a strategy given by Byerly (1893) and MacRobert (1947)]

$$\frac{\boldsymbol{r}}{r} \cdot \boldsymbol{V} = \sum_{n=1}^{\infty} X_n, \tag{2.57}$$

$$-r \boldsymbol{\nabla} \cdot \boldsymbol{V} = \sum_{n=1}^{\infty} Y_n, \tag{2.58}$$

$$\boldsymbol{r} \cdot \boldsymbol{\nabla} \times \boldsymbol{V} = \sum_{n=1}^{\infty} Z_n, \tag{2.59}$$

in which X_n, Y_n and Z_n are surface spherical harmonics of order n. With the help of equations (2.55) & (2.56) and (2.57) - (2.59), the solid surface harmonics p_n, ϕ_n and χ_n can be expressed through the surface spherical harmonics X_n, Y_n and Z_n via (Happel and Brenner, 2012)

$$p_{-(n+1)} = \frac{\mu(2n-1)}{n+1} \frac{1}{a} \left(\frac{a}{r} \right)^{n+1} [(n+2)X_n + Y_n], \tag{2.60}$$

$$\phi_{-(n+1)} = \frac{1}{2(n+1)} a \left(\frac{a}{r} \right)^{n+1} [nX_n + Y_n], \tag{2.61}$$

$$\chi_{-(n+1)} = \frac{1}{n(n+1)} \left(\frac{a}{r} \right)^{n+1} Z_n. \tag{2.62}$$

Inserting of the latter three equations into equations (2.55) & (2.56) leads to a pressure and velocity field that satisfies Stokes' equations together with the boundary condition $\boldsymbol{V}(\theta,\varphi)$ at the surface of the sphere as well as pressure and velocity fields which decay to zero in the far distance of the particle.

2.4 The domain perturbation method

The domain perturbation method is a common tool in fluid mechanics, where it is mostly employed to compute the interfacial deformation of fluid interfaces, e.g., in form of droplets (Mandal et al., 2015), bubbles (Kang and Leal, 1988; Séro-Guillaume and Er-Riani, 1999) or flat fluid interfaces (Bandopadhyay and Hardt, 2017). Furthermore, the domain perturbation method has been employed to compute the translational and rotational motion of slightly deformed spherical particles in an unbounded fluid (Brenner, 1964). During this work, we make use of the results by Brenner (1964) and introduce the domain perturbation method on the basis of a solid slightly deformed spherical particle.

Slightly deformed spherical particles are typically defined through a surface parametrization $r_{\mathscr{P}}$ that is written in a perturbation series in a small parameter β as follows:

$$r_{\mathscr{P}} = a + \beta a f(\theta,\varphi) + \beta^2 a g(\theta,\varphi) + O(\beta^3). \tag{2.63}$$

a, $f(\theta,\varphi)$ and $g(\theta,\varphi)$ are the radius of an undeformed sphere and two arbitrary functions that describe the exact angle dependence of the shape of the particle. However, to introduce the underlying principle of the domain perturbation method, the first-order expansion in β is sufficient. We therefore limit ourselves to parametrizations up to $O(\beta)$ in this section.

Now, lets consider an arbitrary linear partial differential equation for Γ that has to be solved outside the deformed particle and assume that the boundary condition at the surface of the particle reads

$$\Gamma|_{r_{\mathscr{P}}} = \Gamma_0, \tag{2.64}$$

in which Γ_0 represents a constant. To proceed, we assume that Γ can be written as a perturbation sum in β, such as

$$\Gamma \approx \Gamma^{(0)} + \beta\Gamma^{(1)}, \tag{2.65}$$

where terms of higher order than $O(\beta)$ are neglected. A Taylor expansion of $\Gamma^{(i)}$ around $r = a$ for all orders of the perturbation sum, separately, leads to

$$\Gamma^{(i)} = \Gamma^{(i)}\big|_{r=a} + (r-a)\left.\frac{\partial\Gamma^{(i)}}{\partial r}\right|_{r=a} + O((r-a)^2). \tag{2.66}$$

Evaluating at $r = r_{\mathscr{P}}$ and making use of equation (2.63) leaves us with

$$\Gamma^{(i)}\big|_{r_{\mathscr{P}}} \approx \Gamma^{(i)}\big|_{r=a} + \beta a f(\theta,\varphi)\left.\frac{\partial\Gamma^{(i)}}{\partial r}\right|_{r=a}, \tag{2.67}$$

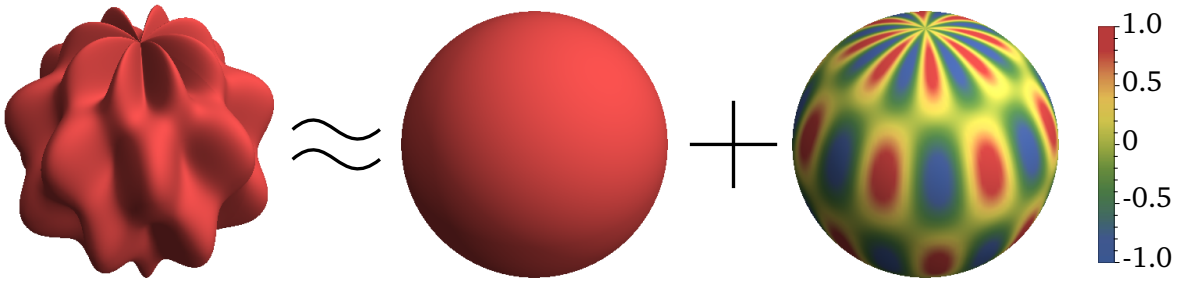

Abbildung 2.2.: Visualization of the domain perturbation method for a surface parametrization that follows equation (2.63) with $a = 1$, $\beta = 0.2$ and $f(\theta, \varphi) = \sin(4\theta)\cos(8\varphi)$. Equation (2.64) with $\Gamma_0 = 1$ is approximated through equations (2.68) & (2.69). For convenience, we set $(\partial\Gamma^{(0)})/(\partial r)\big|_{r=a} = 1$. The color legend corresponds to $\Gamma|_{r=r_\mathscr{P}}$ in the left picture, and $\Gamma^{(i)}\big|_{r=a}$ to both pictures on the right-hand side of the equal sign.

where all terms of higher order than $O(\beta)$ have been omitted. When inserting equation (2.67) into equation (2.65) and subsequently into equation (2.64), we obtain after arranging the results in powers of β

$$\Gamma^{(0)}\big|_{r=a} = \Gamma_0, \tag{2.68}$$

$$\Gamma^{(1)}\big|_{r=a} = -af(\theta,\varphi)\left.\frac{\partial\Gamma^{(0)}}{\partial r}\right|_{r=a}. \tag{2.69}$$

Equation (2.69) reveals that the boundary condition for the first-order solution of the variable $\Gamma^{(1)}$ depends on the zeroth-order solution $\Gamma^{(0)}$, which refers to an undeformed spherical particle. For perturbation orders beyond the linear order, it can be shown that the stepwise dependency of a solution of order n on all order up to order $(n-1)$ remains valid.

Figure 2.2 visualizes the domain perturbation method. The boundary conditions given in equation (2.64) (with $\Gamma_0 = 1$) is approximated with the help of the latter two equations. Effectively, the boundary condition on the bumpy sphere on the left-hand side of the '≈'-sign in figure 2.2 is written into a superposition of two boundary conditions on a sphere. The first picture on the right-hand side of the '≈'-sign in figure 2.2 refers to equation (2.68), whereas the colorful sphere refers to equation (2.69), for a given set of approximations (see caption of figure 2.2). The sum of the solutions of the governing partial differential equations for both perturbation orders in β, referring to the variables $\Gamma^{(i)}$ and satisfying the boundary conditions from equations (2.68) & (2.69) converge to the solution referring to the original problem if β is sufficiently small.

In case of a boundary condition, deviating from that given in equation (2.64), where instead of the variable itself, the normal derivation of the variable has to coincide to a given value, such as

$$\boldsymbol{\nabla}\Gamma\cdot\boldsymbol{n}|_{r_\mathscr{P}} = \Gamma_0', \tag{2.70}$$

the following boundary conditions are obtained

$$\left.\frac{\partial\Gamma^{(0)}}{\partial r}\right|_{r=a} = \Gamma_0', \tag{2.71}$$

$$\left.\frac{\partial \Gamma^{(1)}}{\partial r}\right|_{r=a} = -af(\theta,\varphi)\left.\frac{\partial^2 \Gamma^{(0)}}{\partial r^2}\right|_{r=a} + a\left[\boldsymbol{\nabla}\Gamma^{(0)}\cdot\boldsymbol{\nabla}f(\theta,\varphi)\right]_{r=a}. \tag{2.72}$$

In general, the derivation to obtain the latter two equations is similar to that described above. The only difference is that the normal vector at the surface of the particle has to be similarly expanded in a perturbation sum in β. An extension of the presented approach towards the second-order corrections in β is straightforward.

2.5 Lorentz reciprocal theorem in the extended form

This section introduces the reciprocal theorem that has first been obtained by Lorentz (1896). Hereby, we aim at deriving the extended form following the work by Teubner (1982). The reciprocal theorem, either in its classical or in the extended version, is a common tool in theoretical fluid mechanics. Whenever integral quantities of a flow, such as forces or torques, are of major interest, the reciprocal theorem reveals its maximum strength. Recently, Masoud and Stone (2019) reviewed the historical background and some of the most extensive applications of the reciprocal theorem.

In the following subsection, we present the proof of the reciprocal theorem, following the outline of Teubner (1982), before we go over to compute the force and torque on a spherical particle subjected to an arbitrary velocity field.

2.5.1 Proof of the theorem

We consider an arbitrary shaped particle with a surface $\mathscr{A}_{\mathscr{P}}$ inside a bulk of a fluid volume $\mathscr{V}_{\mathscr{F}}$ and bounded by an outer surface $\mathscr{A}_{\infty}$, located far away from the center of the particle, i.e., $r \to \infty$, with r denoting the distance from the coordinate origin $\mathscr{O}$, as shown in figure 2.3. We assume that $(\bar{\boldsymbol{u}}, \bar{p})$ and $(\boldsymbol{u}, p)$ are solutions of the Stokes equations in the following form

$$0 = -\boldsymbol{\nabla}p + \mu\boldsymbol{\nabla}^2\boldsymbol{u} + \boldsymbol{f}, \qquad \boldsymbol{\nabla}\cdot\boldsymbol{u} = 0, \tag{2.73}$$

$$0 = -\boldsymbol{\nabla}\bar{p} + \mu\boldsymbol{\nabla}^2\bar{\boldsymbol{u}} + \bar{\boldsymbol{f}}, \qquad \boldsymbol{\nabla}\cdot\bar{\boldsymbol{u}} = 0. \tag{2.74}$$

Note that assuming equal viscosities $\mu = \bar{\mu}$ is not necessary as long as both fluids are incompressible and Newtonian. Recalling the definition of the stress tensor via $\bar{\boldsymbol{\sigma}} = -\bar{p}\boldsymbol{I} + \mu(\boldsymbol{\nabla}\bar{\boldsymbol{u}} + (\boldsymbol{\nabla}\bar{\boldsymbol{u}})^{\mathscr{T}})$ and $\bar{\boldsymbol{\sigma}} = \bar{\boldsymbol{\sigma}}^{\mathscr{T}}$, the following identity is verified with the help of index notation

$$\boldsymbol{\nabla}\cdot(\bar{\boldsymbol{u}}\cdot\boldsymbol{\sigma}) = \boldsymbol{\nabla}\bar{\boldsymbol{u}} : \boldsymbol{\sigma} + \bar{\boldsymbol{u}} : (\boldsymbol{\nabla}\cdot\boldsymbol{\sigma}), \tag{2.75}$$

$$= \frac{1}{2}\left(\boldsymbol{\nabla}\bar{\boldsymbol{u}} + (\boldsymbol{\nabla}\bar{\boldsymbol{u}})^{\mathscr{T}}\right) : \boldsymbol{\sigma} - \bar{\boldsymbol{u}}\cdot\boldsymbol{f}. \tag{2.76}$$

: defines the double scalar product (e.g., Altenbach, 2012). Rearranging equation (2.76) and making use of the commutative property of the double scalar product, we eventually obtain

$$\mu(\boldsymbol{\nabla}\cdot(\bar{\boldsymbol{u}}\cdot\boldsymbol{\sigma}) + \bar{\boldsymbol{u}}\cdot\boldsymbol{f}) = \frac{1}{2}(\bar{\boldsymbol{\sigma}} : \boldsymbol{\sigma} + \bar{p}\boldsymbol{I} : \boldsymbol{\sigma}), \tag{2.77}$$

$$= \frac{1}{2}(\bar{\boldsymbol{\sigma}} : \boldsymbol{\sigma} + 3\bar{p}p), \tag{2.78}$$

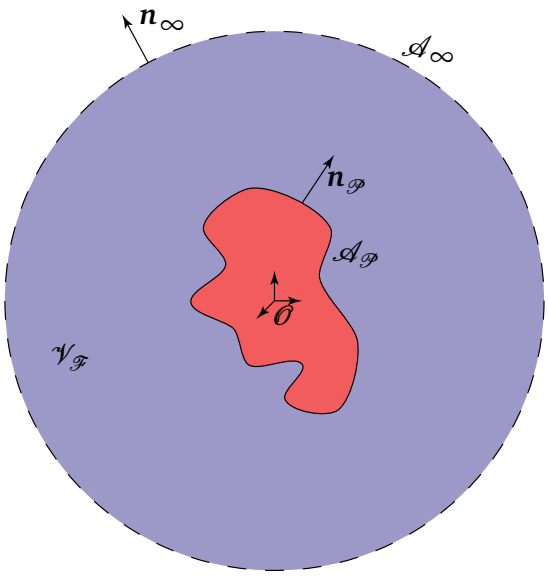

Abbildung 2.3.: Schematic of an arbitrary shaped particle (with surface $\mathscr{A}_\mathscr{P}$ and normal vector $\boldsymbol{n}_\mathscr{P}$ pointing outside the particle) suspended in a bulk of an incompressible Newtonian fluid (volume $\mathscr{V}_\mathscr{F}$). The surface of the far field (denoted with $\mathscr{A}_\infty$ and normal vector $\boldsymbol{n}_\infty$, pointing outside $\mathscr{V}_\mathscr{F}$), corresponds to $r \to \infty$. The origin of the coordinate system is located in the center of the particle.

$$= \mu\left(\boldsymbol{\nabla}\cdot(\boldsymbol{u}\cdot\bar{\boldsymbol{\sigma}}) + \boldsymbol{u}\cdot\bar{\boldsymbol{f}}\right). \tag{2.79}$$

From equation (2.78) to (2.79) we made use of the symmetry of equation (2.78) referring to the overlined and untagged variables. Consequently, both variables are interchangeable. Integrating equation (2.79) over $\mathscr{V}_\mathscr{F}$ and employing the divergence theorem led us to

$$-\int_{\mathscr{A}_\mathscr{P}} (\bar{\boldsymbol{u}}\cdot\boldsymbol{\sigma})\cdot\boldsymbol{n}_\mathscr{P}\,\mathrm{d}\mathscr{A} + \int_{\mathscr{V}_\mathscr{F}} (\bar{\boldsymbol{u}}\cdot\boldsymbol{f})\,\mathrm{d}\mathscr{V} = -\int_{\mathscr{A}_\mathscr{P}} (\boldsymbol{u}\cdot\bar{\boldsymbol{\sigma}})\cdot\boldsymbol{n}_\mathscr{P}\,\mathrm{d}\mathscr{A} + \int_{\mathscr{V}_\mathscr{F}} \left(\boldsymbol{u}\cdot\bar{\boldsymbol{f}}\right)\mathrm{d}\mathscr{V}, \tag{2.80}$$

where we have assumed that the integrands of the surface integrals decay sufficiently fast to zero when approaching $\mathscr{A}_\infty$. The latter equation is the Lorentz reciprocal theorem in the extended form (Teubner, 1982).

2.5.2 Force and torque acting on a spherical particle subjected to an arbitrary flow field

In this subsection we make use of the reciprocal theorem given in equation (2.80) and compute the force and torque acting on a spherical particle of radius a subjected to an arbitrary flow field $\boldsymbol{U}(\boldsymbol{r})$ of a fluid with a viscosity μ in absence of volume forces $\boldsymbol{f} = \bar{\boldsymbol{f}} = 0$. In this context, $(\bar{\boldsymbol{u}}, \bar{p})$ correspond to a hypothetical particle translating with a velocity $\bar{\boldsymbol{u}}|_{r=a} = -\boldsymbol{U}^\infty$, with $\boldsymbol{U}^\infty = \text{const.}$ and $(\boldsymbol{u}, p)$ correspond to a spherical particle with the boundary condition $\boldsymbol{u}|_{r=a} = -\boldsymbol{U}(\boldsymbol{r})$, where $\boldsymbol{U}(\boldsymbol{r})$ is an arbitrary velocity field that satisfies the Stokes equations. Every solution of the (linear) Stokes equations can be written as a sum of many individual solutions (superposition principle). We therefore transferred the far field boundary conditions into boundary conditions on the surface of the sphere. The solution of the Stokes equation for a sphere translating with a constant velocity is readily known (e.g., Guazzelli and Morris, 2011; Happel and Brenner, 2012; Kim and

Karrila, 2013). The surface traction, defining the normal stresses with respect to the surface of the particle, reads in this case $\bar{\boldsymbol{\sigma}} \cdot \boldsymbol{n} = 3\mu/(2a)\boldsymbol{U}^{\infty}$ (Happel and Brenner, 2012). Inserting into equation (2.80) and taking into account that $\boldsymbol{U}^{\infty}$ is a constant vector, the hydrodynamic force $\mathscr{F}$ acting on the sphere subjected to a general flow can be calculated via

$$\mathscr{F} = \int_{\mathscr{A}_{\mathscr{P}}} \boldsymbol{\sigma} \cdot \boldsymbol{n} \mathrm{d}\mathscr{A} = \frac{3\mu}{2a} \int_{\mathscr{A}_{\mathscr{P}}} \boldsymbol{U}(\boldsymbol{r}) \mathrm{d}\mathscr{A}. \tag{2.81}$$

Now, we expand the applied velocity field $\boldsymbol{U}(\boldsymbol{r})$ around the center of the particle, i.e., at $r = 0$, by employing Taylor series and find

$$\boldsymbol{U}(\boldsymbol{r}) = \boldsymbol{U}(\boldsymbol{r})|_{r=0} + \boldsymbol{r} \cdot \boldsymbol{\nabla}\boldsymbol{U}(\boldsymbol{r})|_{r=0} + \frac{\boldsymbol{r}\boldsymbol{r}}{2} : \boldsymbol{\nabla}\boldsymbol{\nabla}\, \boldsymbol{U}(\boldsymbol{r})|_{r=0} + O(r^3). \tag{2.82}$$

In order to evaluate the dyadic surface integral in equation (2.81), we make use of the following integral formula provided by Brenner (1964):

$$\int_{\mathscr{A}_{\mathscr{P}}} \frac{\overbrace{\boldsymbol{r}\boldsymbol{r}\ldots\boldsymbol{r}}^{m-\text{times}}}{r^m} \mathrm{d}\mathscr{A} = \begin{cases} 0 & \text{if } m \text{ is odd,} \\ \frac{4\pi a^2}{(m+1)!} \overbrace{\boldsymbol{\nabla}\boldsymbol{\nabla}\ldots\boldsymbol{\nabla}}^{m-\text{times}} r^m & \text{else,} \end{cases} . \tag{2.83}$$

It immediately follows that all orders of $O(r^m)$, for $m = 1, 3, 5, \ldots$, does not contribute to the force. After a short calculation, we obtain

$$\mathscr{F} = \frac{3\mu}{2a} \left(4\pi a^2\, \boldsymbol{U}(\boldsymbol{r})|_{r=0} + \frac{4\pi a^4}{6} \boldsymbol{\nabla}^2\, \boldsymbol{U}(\boldsymbol{r})|_{r=0} + \frac{\pi a^6}{30} \boldsymbol{\nabla}^2\boldsymbol{\nabla}^2\, \boldsymbol{U}(\boldsymbol{r})|_{r=0} + O(r^6) \right). \tag{2.84}$$

Since $\overbrace{\boldsymbol{\nabla}^2\boldsymbol{\nabla}^2\ldots\boldsymbol{\nabla}^2}^{n-\text{times}} \boldsymbol{U}(\boldsymbol{r}) = 0, \forall n > 1$, due to Stokes' equations (recall that $\boldsymbol{\nabla}^2 p = 0$), the exact solution of the resulting force reads

$$\mathscr{F} = 6\pi\mu a \left(\boldsymbol{U}(\boldsymbol{r})|_{r=0} + \frac{a^2}{6} \boldsymbol{\nabla}^2\, \boldsymbol{U}(\boldsymbol{r})|_{r=0} \right). \tag{2.85}$$

Equation (2.85) is commonly known as Faxén's first law, first derived by Faxén (1922).

The calculation that leads to the torque acting on a spherical particle in an arbitrary applied flow field follows the same train of thought as the computation of the force. Inserting the boundary condition $\bar{\boldsymbol{u}}|_{r=a} = \boldsymbol{\omega} \times \boldsymbol{r}$ and the surface traction $\bar{\boldsymbol{\sigma}} \cdot \boldsymbol{n} = -3\mu\boldsymbol{\omega} \times \boldsymbol{r}/r$ (Happel and Brenner, 2012) into equation (2.80) and making use of the Taylor expansion from equation (2.82), we arrive at

$$\mathscr{T} = 8\pi\mu a^3 \left(\frac{1}{2} \boldsymbol{\nabla} \times \boldsymbol{U}(\boldsymbol{r})|_{r=0} \right). \tag{2.86}$$

The latter equation is known as Faxén's second law (Faxén, 1922).

The computation of the force and torque acting on a spherical particle revealed the maximum strength of the reciprocal theorem which was described by Masoud and Stone (2019) accurately as: 'getting something for nothing'. In this context we obtained the force and torque on a spherical particle subjected to an arbitrary velocity field ('something') without solving the Stokes equations by making use of existing solutions for a constant translating and rotating sphere ('nothing').

For a later reason, we make further use of the results from equations (2.85) & (2.86) for the case of a linearized applied velocity field, which is a reasonable approximation if the spatial changes of the velocity are small compared to the radius of the spherical particle. Then, the velocity field can be written as (Happel and Brenner, 2012)

$$\boldsymbol{U}(\boldsymbol{r}) \approx \boldsymbol{U}^{\infty} + \boldsymbol{\Omega}^{\infty} \times \boldsymbol{r} + \mathfrak{E} \cdot \boldsymbol{r}, \tag{2.87}$$

in which $\boldsymbol{U}^{\infty}$ and $\boldsymbol{\Omega}^{\infty}$ are constant vectors and $\mathfrak{E}$ is a constant, symmetric and traceless dyadic. Making use of elementary vector calculus, we eventually obtain

$$\mathscr{F} = 6\pi\mu a \boldsymbol{U}^{\infty}, \tag{2.88}$$

$$\mathscr{T} = 8\pi\mu a^3 \boldsymbol{\Omega}^{\infty}. \tag{2.89}$$

Consequently, in a linear flow field, the force and torque acting on a spherical particle is solely determined by the translational and rotational components of the applied velocity field, respectively.

2.6 Electric double layers

We consider a spherical particle suspended in the bulk of an electrolyte under stationary conditions. As soon as the particle gets in contact with the electrolyte, it becomes charged. In the literature, many different explanations are given for the origin of the charge, depending, among others, on the material of the suspended particle and on the surrounding fluid (Wall, 2010; Hunter, 2013). Exemplarily, a surface charge can develop due to the ionization of either acid or basic groups at the surface. The acidic or basic strength of the surface groups as well as the pH-value of the electrolyte determines the magnitude of the charge (Masliyah and Bhattacharjee, 2006; Hunter, 2013). Following Coulomb's law [equation (2.12)], charges of opposite sign will attract, whereas charges of equal sign repel. Assuming the particle is negatively charged, cations will be attracted towards the particle whereas anions will be repelled, see figure 2.4. However, at sufficient large distances from the particle, the electrolyte restores electroneutrality. An important length scale, describing the 'thickness' of the electric double layer is the Debye length κ^{-1}. In fact, the thickness of the electric double layer extends beyond κ^{-1} and the surface potential of a particle has dropped by about 66% when reaching a distance of κ^{-1} from the surface of a charged particle (Hunter, 2013). The Debye length solely depends on the physical properties of the electrolyte.

After motivating the existence of an electric double layer, the focus is now on describing the microscopic structure of the double layer in more detail. According to the proposed modeling by Stern (1924), the electric double layer consists of mainly two regions. In the close proximity

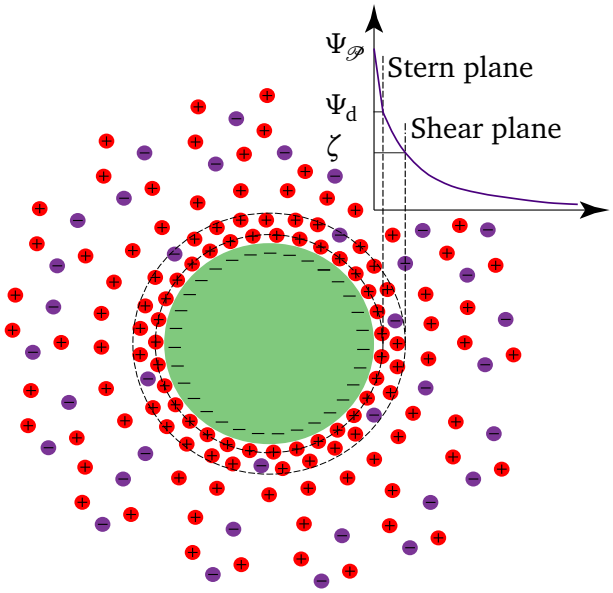

Abbildung 2.4.: Sketch of a charged particle (surface potential $\Psi_{\mathscr{P}}$) suspended in an electrolyte. Due to the negative charge of the particle, cations are attracted to the particle, whereas anions are repelled. At the interface between the particle and the electrolyte, cations stick to the surface (Stern layer) leading to a decrease of the surface charge (Stern potential Ψ_d). About one or two ion radii away from the surface of the particle, the ions are mobile defining the location of the shear plane referring to the ζ-potential.

of the surface of the colloid, the cations stick to the surface and are immobile (Masliyah and Bhattacharjee, 2006; Hunter, 2013). In contrast to an early model by von Helmholtz (1882), in which the ions have effectively been treated as a point (in a mathematical sense), Stern (1924) took the finite size of ions into account. Following the approach by von Helmholtz (1882), the surface charge of the particle could solely be balanced by counterions sticking at the surface of the particle, which contradicts experimental findings, e.g., experimental observations closely related to the DLVO-theory (Masliyah and Bhattacharjee, 2006). Due to the finite size of the ions, the electrostatic potential Ψ drops along the normal direction inside the immobile layer from the surface potential $\Psi_{\mathscr{P}}$ to the finite but (generally) non-zero Stern potential Ψ_d. The imaginary layer referring to the region of immobile ions is referred as Stern layer. Outside the Stern layer in range of one or two ion-radii in normal direction, the ions become mobile, e.g., due to thermal induced motion (Brownian motion). The plane from which ions are mobile is referred as the shear plane. The electrostatic potential located at the shear plane is defined as ζ-potential (Masliyah and Bhattacharjee, 2006; Hunter, 2013). Many interesting physical effects are attributed to the ζ-potential such as stability properties of suspensions (Hunter, 2013).

Assuming that the particle is translating through the electrolyte, the combination of the particle and the ions inside the shear layer form a kinetic unit (Hunter, 2013). From a theoretical point of view, it is therefore reasonable to exclude the whole kinetic unit from the computational domain in a sense that the immobile ions are assumed to correspond to the surface of the particle. Consequently, the hydrodynamic and electrostatic boundary conditions at the surface of the particle are assumed to apply at the shear plane. For the electrostatic boundary conditions it has been experimentally validated that the difference between Ψ_d and ζ are rather small (Masliyah and Bhattacharjee, 2006). Due to the large contrast between the characteristic size of the particle

a and the characteristic size of an ion, it is commonly assumed that the shear plane coincides with the surface of the particle (e.g., Henry, 1931; Overbeek, 1943; Delgado et al., 2007). As already mentioned, ions outside the shear layer are mobile. On the basis of section 2.1.3, the distribution of ions is controlled through convection (transport of ions with the motion of the fluid), diffusion (thermal induced/Brownian motion) and electrostatic migration (due to the charge of the particle and a potentially applied electric field).

3 Electrokinetics of a single interfacial particle

Whenever a charged particle or molecule is dispersed in an electrolyte and subjected to an applied electric field, it starts to move into the direction of the oppositely charged electrode. The motion of the particle relative to the surrounding fluid is known as electrophoresis. The beginning of electrophoresis is often related to the work of Tiselius (1937). The author described an apparatus (known as Tiselius apparatus) that firstly allowed the electrophoretic analysis of colloidal mixtures (Alberty, 1948; Vesterberg, 1989, 1993). Since then, electrophoresis has become one of the most important electrokinetic phenomena, mostly used for the separation of molecules or particles. Exemplarily, electrophoresis is used to analyze DNA (Schwartz and Cantor, 1984; Lagally et al., 2001; Dorfman, 2010), protein and antibody interactions (Ressler, 1960; Laurell, 1966; Gahoual et al., 2016) or to test/modify antibiotics (Flurer, 1999) and vaccines (Nunnally and Yao, 2007). Furthermore, electrophoresis can be used to measure the ζ-potential of particles (Hunter, 2013), molecules (Klodzinska et al., 2010), droplets (Stachurski and Michalek, 1985) or bubbles (Yang et al., 2001) and is probably the most important transport phenomena lab-on-a-chip devices are based on (Harrison et al., 1992; Manz et al., 1992; Mark et al., 2010). However, all applications require a detailed knowledge about the dependence of velocity of the dispersed matter on the material properties (of the particle and the electrolyte) as well as on the applied electric field.

For rigid particles suspended in an electrolyte and subjected to a sufficiently weak applied electric field E_∞, it has been shown that the velocity of the particle U is proportional to the applied electric field, i.e., $U \propto E_\infty$ (Overbeek, 1943; O'Brien and White, 1978). The proportionality constant relating U and E_∞, is the electrophoretic mobility η:

$$U = \eta E_\infty. \tag{3.1}$$

Generally, η depends, among others, on the thickness of the electric double layer around the particle, which develops as a consequence of the charge of the particle, see section 2.6. Pioneering work addressing the calculation of the electrophoretic mobility of a single spherical particle suspended in a bulk electrolyte was carried out by von Smoluchowski (1903), Hückel (1924) and Henry (1931). Von Smoluchowski calculated the electrophoretic mobility of spherical particles in the limit of thin electric double layers (thin Debye length), i.e., $\kappa \to \infty$ (κ is the inverse Debye length, see section 2.6), and obtained the well-known Smoluchowski limit for the electrophoretic mobility $\eta = \epsilon\zeta/\mu$. In many practical applications the thin Debye layer approximation is valid, since the Debye length is often much smaller than the characteristic length of a particle (Fixman, 1980). For particles of arbitrary geometry, the Smoluchowski limit still remains valid (Morrison, 1970; Teubner, 1982). This can be understood as follows: The infinitesimal thin electric double layer can be imagined as a skin that completely encloses the (mathematically smooth) particle. On the length scale of the thickness of the imaginary skin, the exact geometrical shape of the

particle is insignificant, since the surface of the particle converges locally towards a flat surface.

The other asymptotic case, when a large Debye length compared to the size of the spherical particle is considered, a reduction of the electrophoretic mobility $\eta = 2/3\ \epsilon\zeta/\mu$ has been obtained (Hückel, 1924). Under certain assumptions (e.g., rotationally symmetric electric double layers), Henry (1931) generalized the theory for spherical (and cylindrical) particles and obtained the Smoluchowski and Hückel mobility as limiting cases. A theoretical extension of Henry's work was done by Overbeek (1943) and Booth (1950), where the deformation of the electric double layer due to convective processes (so-called relaxation effect), occur for highly charged particles, was taken into account. The high charge of the particle corresponds to a significant flow around the particle, leading to a convective transport of ions behind the particle. The authors found that for moderate values of the Debye length, i.e., $0.2 < \kappa a < 50$ (a is the radius of the spherical particle), the relaxation effect leads to a deceleration of the particle. Later on, Wiersema et al. (1966) extended previous studies in form of numerical simulations and discussed the limit of validity of foregoing work. Wiersema et al. (1966), however, failed to compute convergent solutions for high ζ-potentials of the particle. By employing a different formulation of the governing equations, O'Brien and White (1978) extended the work by Wiersema et al. (1966) and provided a numerical scheme, valid for a broad range of ζ-potentials. More recently, the motion of spherical particles subjected to strong electric fields (compared to the ζ-potential of the particle) have been studied for thin Debye layers (Schnitzer and Yariv, 2012a). By employing the method of matched asymptotic expansions (following the theoretical method introduced by Yariv, 2009), Schnitzer and Yariv (2012a) reobtained the Smoluchowski mobility. Furthermore, if the charge of the particle is asymptotically high, corrections of the Smoluchowski limit have been obtained (Schnitzer and Yariv, 2012b, 2014). It has been found, that the electric double layer consists of a Dukhin-sublayer between the surface of the particle and the diffusive layer (Schnitzer and Yariv, 2012b). Inside the Dukhin-sublayer, tangential ionic fluxes appear effectively as surface currents that modify the electrokinetic transport (Schnitzer and Yariv, 2012b). The effect of the presence of boundaries, such as rigid walls, on the electrophoretic mobility of spherical particles were studied by Keh and Anderson (1985), Keh and Hsieh (2008) and Liu et al. (2014, 2016). The interaction of two charged particles subjected to an external electric field has been studied in the limit of small Debye length (Reed and Morrison, 1976) and large Debye length (Shugai et al., 1997), separately. Apart from rigid particles, the electrophoretic mobility of bubbles (Schnitzer et al., 2014) and droplets (Baygents and Saville, 1991) have also been studied, both in the limit of thin Debye length.

In many practical applications, particles are not suspended in the bulk of a liquid, but are attached to a fluid interface. Examples are particle-laden droplets (often called liquid marbles) (Bormashenko et al., 2012) and Pickering emulsions (Ngai and Bon, 2014). Moreover, it has been shown that the presence of a fluid interface alone can attract particles depending, among others, on the pH-value of the solution (Fan et al., 2004) or on hydrodynamic, diffusiophoretic and wettability forces acting on the particles (Ralston and Dukhin, 1999). Electrophoretic phenomena at fluid interfaces are less investigated than in the bulk, probably due to the complex interplay between hydrodynamics, electrostatics, and the deformation of the interface separating the two fluids. In this context, a huge number of fundamental questions related to fluid interfaces are still open. For example, the charge of a fluid interface is still a matter of controversial discussion (Paluch, 2016). There are experimental indications that the water-air interface carries a negative

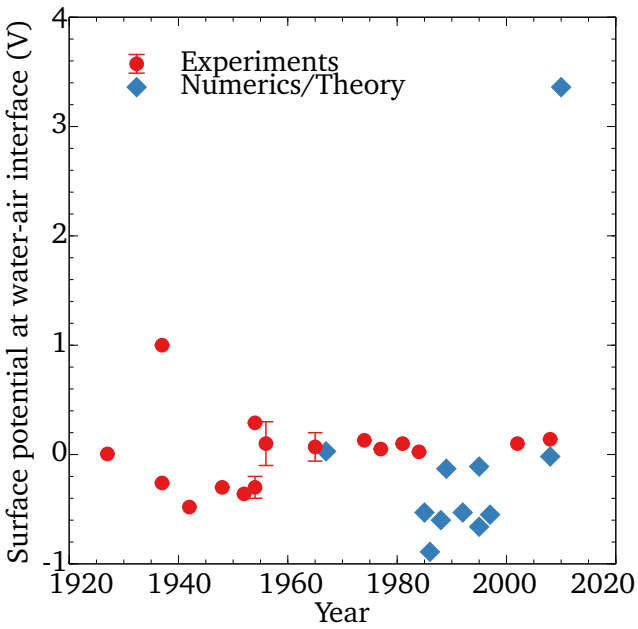

Abbildung 3.1.: A summary of the results obtained for the surface potential of a water-air interface reported by different research groups, employing different methods. The surface potential is plotted over the year of publication. The data was taken from table 1 by Paluch (2016).

charge (Hush, 1948; Frumkin, 1960; Ciunel et al., 2005). Conversely, other experimental papers report a positive charge (Bühl, 1927; Parfenyuk, 2002; Krishtalik, 2008). Theoretical/numerical studies also lead to results varying in magnitude and sign, predicting either a positive (Stillinger and Ben-Naim, 1967; Leung, 2010) or negative (Brodskaya and Zakharov, 1995; Kathmann et al., 2009) charge at the water-air interface. These inconsistencies may be due to the difficulty of a direct measurement (Paluch, 2016) and due to differences in the modeling approaches (Chaplin, 2009). A summary of different values obtained for the charge of a water-air interface is shown in figure 3.1. Some researchers measured the charge of a water-air interface through the electrophoretic mobility of air bubbles dispersed in an aqueous solution and reported that the water-air interface carries a negative charge (except for small pH-values) (Graciaa et al., 1995; Saulnier et al., 1996; Takahashi, 2005; Creux et al., 2009; Flury and Aramrak, 2017). Here, it is mostly claimed that the negative charge arises from an excess of OH^- caused by the orientation of water molecules at the interface (Chaplin, 2009; Paluch, 2016; Flury and Aramrak, 2017). Many authors computed the ζ-potential of the gas bubble with the help of the Smoluchowski mobility, even though the Smoluchowski approximation cannot be employed to determine the ζ-potential of a bubble (Schnitzer et al., 2014; Flury and Aramrak, 2017). For small applied electric fields and small ζ-potentials, Schnitzer et al. (2014) found that the mobility scales $\eta \propto \zeta^3$ in contrast to the linear scaling in the Smoluchowski limit. The reason for this discrepancy is given through the high mobility of charges at the surface of the bubbles. Moreover, it was found experimentally by Takahashi (2005) that the ζ-potential of a micro-bubble is independent of its size, if the effective bubble diameter is between 10 μm and 50 μm in agreement with the theoretical analysis of Schnitzer et al. (2014). Due to the invariance of their measurements on the size of the bubbles, the authors claimed that their results might be extrapolated to flat water-air interfaces.

In many theoretical studies concerning the electrophoretic mobility of particles close to fluid

interfaces, uncharged interfaces are often considered. Tsai et al. (2010) studied the electrophoretic motion of a spherical particle normal to an uncharged, undeformable and flat water-air interface for different Debye thicknesses. The motion parallel to a flat fluid interface was studied by Gao and Li (2008) in the thin Debye layer limit. It is worth mentioning that the presence of a surface charge at the fluid interface, separating a polar and nonpolar medium, leads to the formation of an electric double layer underneath the fluid interface in order to restore electroneutrality in the electrolyte. Depending on the Debye layer thickness of the electric double layer underneath the fluid interface, it might be applicable to consider the fluid interface effectively uncharged on the length scale of the particle, if $\kappa a \to \infty$. Baygents and Saville (1991) calculated the electrophoretic mobility of droplets and bubbles inside an electrolyte assuming chargeless interfaces [in contrast to (Schnitzer et al., 2014)]. The authors claimed that Marangoni stresses and polarization effects at the interface are responsible for the motion of the droplet and bubble subjected to an applied electric field. Besides, Huang et al. (2008) and Schönecker and Hardt (2014) studied the electroosmotic flow over a superhydrophobic surface, assuming charge-free liquid-air interfaces.

In recent years, researchers reported a static interface deformation caused by the charge of a particle attached to a flat fluid interface between an aqueous and nonpolar fluid. This static fluid interface deformation was termed 'electrodipping'. Due to the difference in the dielectric constants of both fluids and an inhomogeneous surface charge of the particle, a force arises that pulls the particle into the fluid with the higher permittivity (Nikolaides et al., 2002). Experimentally, Nikolaides et al. (2002) and Aveyard et al. (2002) obtained a long-range interaction between interfacial particles which gave rise to controversial discussions (Megens and Aizenberg, 2003; Foret and Würger, 2004; Danov et al., 2004; Danov and Kralchevsky, 2006a; Danov et al., 2006; Danov and Kralchevsky, 2006b; Oettel et al., 2006). Danov et al. (2004, 2006) performed experiments for glass particles at oil-water and water-air interfaces and found an interaction of interfacial particles within a shorter range than Nikolaides et al. (2002). Moreover, they found that the electrodipping force in a water-oil system is much higher than in a water-air system. To best of our knowledge, theoretical works so far claim that the force inside the nonpolar fluid acting on the particle is much higher than the force inside the electrolyte (Nikolaides et al., 2002; Foret and Würger, 2004; Danov et al., 2004; Danov and Kralchevsky, 2006a; Danov et al., 2006; Danov and Kralchevsky, 2006b; Oettel et al., 2006), but are all limited to thin Debye layers. Independently from each other, several authors reported an interfacial deformation decaying like $h \propto r^{-4}$, in which h and r denote the deformation of the fluid interface and the distance from the particle, respectively.

As a further extension of previous investigations, we study the motion of a charged particle attached to a fluid interface driven by an external applied electric field. Hereby, we aim at answering the following questions: How is the velocity of an interfacial particle related to the applied electric field? How does the contact angle influence the velocity of the particle? How does the fluid interface deform due to the motion of the particle?

This chapter is organized as follows: Section 3.1 describes theoretical modeling including the underlying assumptions, as well as the simplification and non-dimensionalization of the governing equations and the corresponding boundary conditions. In section 3.2 we analyze the electrokinetics of a nearly arbitrary shaped particle attached to a fluid interface, focusing the electrophoretic mobility at thin Debye layers and on the interfacial deformation caused by the motion of the

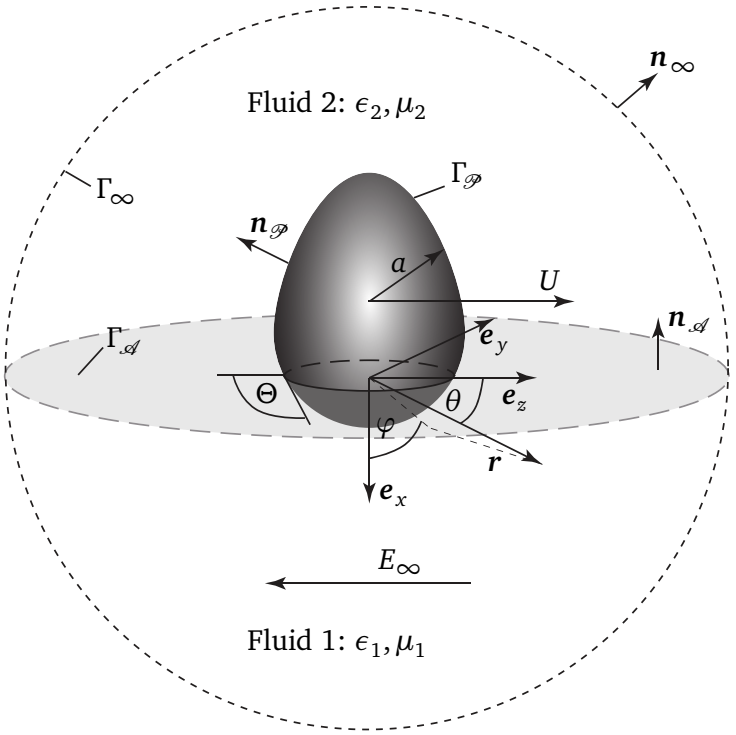

Abbildung 3.2.: Schematic of a particle attached to a fluid interface. Without loss of generality, we assume the negatively charged particle to move with a velocity U in the positive z-direction due to a constant applied electric field E_∞. The contact angle of the fluid interface at the particle surface is denoted by Θ, and a stands for a characteristic length scale. $\Gamma_\mathscr{P}$, $\Gamma_\mathscr{A}$ and Γ_∞ denote the particle, the fluid interface and the far field domain, i.e., a sphere with a radius of $r \to \infty$, respectively. The normal vectors corresponding to the three boundaries of the fluid domain are denoted by $\boldsymbol{n}_\mathscr{A}$, $\boldsymbol{n}_\mathscr{P}$ and $\boldsymbol{n}_\infty$. The origin of the coordinate system lies in the plane of the undeformed fluid interface [reprinted with permission from APS, Phys. Rev. Fluids 3 (2018), Eigenbrod et al. (2018)].

particle. Subsequently, in section 3.3, spherical interfacial particles are considered, for which the electrophoretic mobility, valid for all Debye parameters, as well as the corresponding interfacial deformation, caused by the charge of the particle, is computed. Section 3.4 provides a discussion of the theoretical results including the range of validity, the impact of the interfacial deformation on the electrophoretic mobility as well as a specific application of our theoretical results. A summary of the results and an outlook to further studies is given in section 3.5.

3.1 Model assumptions

We consider the motion of a negatively charged particle with a characteristic size a attached to a fluid interface in an unbounded domain driven by a uniform applied electric field E_∞ tangential to the fluid interface, as sketched in figure 3.2.

In this study we focus on neutrally buoyant particles (e.g., polystyrene particles $\rho_\mathscr{P} \approx 1040\,\mathrm{kg/m^3}$ (Weng et al., 2011) attached to an interface between an aqueous electrolyte and air) translating at small Reynolds numbers $\mathrm{Re} \ll 1$. Both fluid phases are incompressible Newtonian fluids with constant viscosities μ_l and dielectric permittivities ϵ_l, where $l = 1, 2$ denote the two different

phases, respectively. The particle is assumed to be in a stationary-state configuration.

The foregoing assumptions still leave us with a very general problem and do not simplify the governing equations sufficiently to enable an analytical treatment. Therefore, the following assumptions are added and discussed in the subsequent paragraph:

1. The applied electric field E_∞ is uniform and weak;
2. The ζ-potential at the particle surface is small and uniform over each surface portion in contact with a specific fluid;
3. The fluid interface is chargeless $q_{\mathscr{S}} = 0$;
4. The viscosity and permittivity ratios vanish asymptotically, i.e., $\mu_2/\mu_1 \to 0$ and $\epsilon_2/\epsilon_1 \to 0$.

Assumptions 1 & 2 allow us to simplify the governing equations significantly. When assuming that the electrophoretic mobility of interfacial particles is proportional to the ζ-potential of the particle (to be verified a-posteriori), assumptions 1 & 2 are in agreement with the assumption of small Reynolds numbers. Further consequences of the first two assumptions become obvious in the derivation of the governing equations provided in appendix A. Assumption 3 states that the charge at the fluid interface can be neglected throughout this study. Whether or not a Debye layer forms at the fluid interface depends, among others, on the presence of ionic surfactants. Even though, we neglect the presence of surfactants or impurities located at the fluid interface throughout this study, surface charges have been measured for surfactant-free water-air interfaces, see figure 3.1. We do not aim at entering the controversial discussion about the charge of a fluid interface in more detail by assuming that one of the following statements is valid:

- The ζ-potential of the fluid interface is small compared to that of the particle;
- The Debye length is much smaller than the characteristic length of the particle.

Referring the second statement, even in case of a charged interface, a thin Debye layer compared to the characteristic size of the particle ensures that the fluid interface can be regarded as overall electroneutral on the particle scale, as already indicated in the introduction of this chapter. Finally, assumption 4 is reasonably valid, if the two fluids are water and air: $\mu_2/\mu_1 \approx 0.02$ (Petkov et al., 1995) and $\epsilon_2/\epsilon_1 \approx 0.01$ (Mbamala and von Grünberg, 2002).

3.1.1 Governing equations & boundary conditions

The derivation of the simplified governing equations, starting with the most general form given in chapter 2, is provided in appendix A. The simplified equations are

$$\boldsymbol{\nabla}^2\psi_l = \kappa_l^2\psi_l, \tag{3.2}$$

$$p_l^s = \epsilon_l\frac{\kappa_l^2}{2}\psi_l^2, \tag{3.3}$$

$$\boldsymbol{\nabla}\cdot\boldsymbol{u}_l = 0, \tag{3.4}$$

$$-\boldsymbol{\nabla}p_l^d + \mu_l\boldsymbol{\nabla}^2\boldsymbol{u}_l + \epsilon_l\kappa_l^2\psi_l\boldsymbol{\nabla}\phi_l = 0, \tag{3.5}$$

$$\boldsymbol{\nabla}^2\phi_l = 0. \tag{3.6}$$

(p_l^s & ψ_l) and (p_l^d & ϕ_l) are the equilibrium and perturbation pressure & electrostatic potential, in which the former refers to the configuration in absence of an applied electric field and the latter to the perturbation of the equilibrium state, caused by the presence of an external applied electric field, respectively. The subscript $l = 1, 2$ denotes the two phases. Subsequently, suitable boundary conditions at the surface of the particle, in the far field and at the fluid interface are discussed, taking into account the assumptions of the previous subsection.

During the simplification of the governing equations (see appendix A), we introduce the Debye-Hückel approximation, i.e., $\Psi_{\mathscr{P}} \ll k_B T/(\mathfrak{z}e)$. Following the discussion in section 2.6, we employ the approximation $\Psi_{\mathscr{P}} = \zeta$, which is common in electrophoresis (e.g., Wiersema et al., 1966; Shugai et al., 1997; Liu et al., 2014). The ζ-potential depends, among others, on the concentration of ions and the pH-value of the electrolyte (Hunter, 2013) and is therefore not solely determined by the electrostatic charge of the particle. We set

$$\psi_l|_{r_{\mathscr{P}}} = \zeta_l, \tag{3.7}$$

in which ζ_l and $r_{\mathscr{P}}$ denote the ζ-potential corresponding to phase l and the parametrization of the surface of the particle. Further, far away from the particle, the equilibrium potential should decay to zero in both phases, separately. Formally, we have

$$\psi_l|_{r\to\infty} = 0. \tag{3.8}$$

For the derivation of the boundary condition of ϕ at the surface of the particle, we may temporary assume that the permittivity of the particle $\epsilon_{\mathscr{P}}$ is much smaller than the permittivity of the surrounding medium ϵ_l leading to

$$\boldsymbol{\nabla}\, \phi_l \cdot \boldsymbol{n}|_{r_{\mathscr{P}}} = -\frac{\epsilon_{\mathscr{P}}}{\epsilon_l}\, \boldsymbol{\nabla}\phi_{\mathscr{P}} \cdot \boldsymbol{n}|_{r_{\mathscr{P}}} \approx 0, \tag{3.9}$$

in which $\phi_{\mathscr{P}}$ describes the electrostatic potential inside the particle. Even though, the assumption of a small particle permittivity compared to that of the two phases might be a significant restriction, it has been shown, that the electrophoretic mobility of the particle is independent of the boundary condition of ϕ at the surface of the particle, as long as the applied electric field is sufficiently small (O'Brien and White, 1978). Moreover, for aqueous solutions, $\epsilon_1 \gg \epsilon_{\mathscr{P}}$ is usually fairly well satisfied. Whether or not the latter boundary condition holds for phase 2 as well, will shown to be of no importance. Sufficiently far away from the particle, the negative gradient of the electrostatic potential has to coincide with the applied electric field in both phases, separately. Without loss of generality, we assume the applied electric field aligned in negative z-direction, having an absolute value of E_∞, as sketched in figure 3.2:

$$\phi_l|_{r\to\infty} = E_\infty r\cos(\theta). \tag{3.10}$$

Due to assumption 3, we limit ourselves to effectively uncharged fluid interfaces. Following equation (2.40), we then find

$$\boldsymbol{\nabla}\psi_1 \cdot \boldsymbol{n}|_{\mathscr{A}} = \frac{\epsilon_2}{\epsilon_1}\,\boldsymbol{\nabla}\psi_2 \cdot \boldsymbol{n}|_{\mathscr{A}} \approx 0, \tag{3.11}$$

$$\boldsymbol{\nabla}\phi_1 \cdot \boldsymbol{n}|_{\mathscr{A}} = \frac{\epsilon_2}{\epsilon_1}\,\boldsymbol{\nabla}\phi_2 \cdot \boldsymbol{n}|_{\mathscr{A}} \approx 0. \tag{3.12}$$

For the last equality in both equations, we have employed assumption 4. Equation (3.11) can also be obtained on the basis of equation (2.41) after employing the perturbation series described in appendix A.

Assuming a constant externally applied electric field as well as a constant ζ-potential in both phases, the motion of the particle is primarily translational. Taking the direction of the applied electric field into account, we set

$$\boldsymbol{u}_l|_{r_{\mathscr{P}}} = U\boldsymbol{e}_z, \tag{3.13}$$

with U being the magnitude of the particle velocity directed in positive z-direction. It is further assumed that both fluids are at rest far away from the particle

$$\boldsymbol{u}_l|_{r\to\infty} = 0, \tag{3.14}$$

which motivates us to set the pressure in the far field to zero:

$$p_l^s\big|_{r\to\infty} = p_l^d\big|_{r\to\infty} = 0. \tag{3.15}$$

Before we analyze the evolution equation of the fluid interface [see equation (2.36)], we rewrite the set of governing equations in dimensionless form and introduce the following set of non-dimensional quantities

$$\tilde{\boldsymbol{\nabla}} = a\boldsymbol{\nabla},\quad \tilde{\boldsymbol{u}}_l = \boldsymbol{u}_l/U,\quad \tilde{\psi}_l = \psi_l/\zeta_1,\quad \tilde{\phi}_l = \phi_l/(E_\infty a),\quad \tilde{p}_l^s = \frac{a^2}{\epsilon_1\zeta_1^2}p_l^s,\quad \tilde{p}_l^d = \frac{a}{\mu_1 U}p_l^d. \tag{3.16}$$

According to the Smoluchowski mobility, the non-dimensional electrophoretic mobility is introduced as follows

$$\frac{U}{E_\infty} = \eta = \frac{\epsilon_1\zeta_1}{\mu_1}\tilde{\eta}. \tag{3.17}$$

When inserting the aforementioned quantities into equation (3.2) - (3.6), the following non-dimensional governing equations are obtained

$$\tilde{\boldsymbol{\nabla}}^2\tilde{\psi}_l = (\kappa_l a)^2\tilde{\psi}_l, \tag{3.18}$$

$$\tilde{p}_l^s = \frac{\epsilon_l}{\epsilon_1}\frac{(\kappa_l a)^2}{2}\tilde{\psi}_l^2, \tag{3.19}$$

$$\tilde{\boldsymbol{\nabla}}\cdot\tilde{\boldsymbol{u}}_l = 0, \tag{3.20}$$

$$-\tilde{\boldsymbol{\nabla}}\tilde{p}_l^d + \frac{\mu_l}{\mu_1}\tilde{\boldsymbol{\nabla}}^2\tilde{\boldsymbol{u}}_l + \frac{\epsilon_l}{\epsilon_1}\frac{1}{\tilde{\eta}}\tilde{\boldsymbol{\nabla}}^2\tilde{\psi}_l\tilde{\boldsymbol{\nabla}}\tilde{\phi}_l = 0, \tag{3.21}$$

$$\tilde{\boldsymbol{\nabla}}^2\tilde{\phi}_l = 0. \tag{3.22}$$

When employing assumption 4 in equation (3.19) and (3.21), it follows that $\tilde{p}_2^s = \tilde{p}_2^d = 0$ [see equation (3.15)]. As one important consequence, phase 2 does not contribute to the electrophoretic mobility of the particle. It should be noticed further that the osmotic pressure $\tilde{p}_1^s$ has no contribution to the electrophoretic mobility of the particle, since it leads to a symmetric pressure with respect to the direction of motion. The boundary conditions of the fluid interface related to the governing equations of the velocity field read in dimensionless form (see equation (2.31) & (2.36) for comparison)

$$\tilde{\boldsymbol{u}}_1 = \tilde{\boldsymbol{u}}_2, \tag{3.23}$$

$$\mathrm{Ce}\left[(\tilde{p}_1^s - \tilde{p}_2^s)\boldsymbol{I} + \frac{\epsilon_2}{\epsilon_1}\tilde{\boldsymbol{\sigma}}_{M_2}^s - \tilde{\boldsymbol{\sigma}}_{M_1}^s\right]\cdot\boldsymbol{n}^s = \boldsymbol{n}^s\left(\tilde{\boldsymbol{\nabla}}\cdot\boldsymbol{n}^s\right), \tag{3.24}$$

$$\mathrm{Ca}\left[(\tilde{p}_1^d - \tilde{p}_2^d)\boldsymbol{I} + \frac{\mu_2}{\mu_1}\tilde{\boldsymbol{T}}_2 - \tilde{\boldsymbol{T}}_1 + \frac{1}{\tilde{\eta}}\left(\frac{\epsilon_2}{\epsilon_1}\tilde{\boldsymbol{\sigma}}_{M_2}^d - \tilde{\boldsymbol{\sigma}}_{M_1}^d\right)\right]\cdot\boldsymbol{n}^d = \boldsymbol{n}^d\left(\tilde{\boldsymbol{\nabla}}\cdot\boldsymbol{n}^d\right), \tag{3.25}$$

$$\text{with} \quad \mathrm{Ca} = \frac{\mu_1 U}{\gamma_{12}} \quad \text{and} \quad \mathrm{Ce} = \frac{\epsilon_1\zeta_1^2}{a\gamma_{12}}. \tag{3.26}$$

We have used the short hand notation $\tilde{\boldsymbol{T}}_j = \tilde{\boldsymbol{\nabla}}\tilde{\boldsymbol{u}}_j + (\tilde{\boldsymbol{\nabla}}\tilde{\boldsymbol{u}}_j)^{\mathscr{T}}$ and the Maxwell stress $\boldsymbol{\sigma}_M$ defined in equations (A.31) & (A.32). γ_{12} is the surface tension between phase 1 and phase 2. Moreover, we have introduced the capillary and electric capillary number, denoted as Ca and Ce, respectively. Ca represents the relative strength of the viscous forces compared to the capillary forces, whereas Ce is the relative strength of the electrostatic forces compared to capillary forces. The reader should note that due to equation (3.24) an interfacial deformation might occur, even in absence of an applied electric field. Assumption 4 applied to equation (3.24) and (3.25) reveals that the interfacial deformation is independent of phase 2. Therefore, we neglect phase 2 in the subsequent sections and omit the index labeling of the phases from now on, with the convention that all quantities refer to phase 1.

When discussing the physical relevance of the Péclet number on the ionic concentration (in appendix A) we have already made use of the measured velocities reported by Lee and Li (2006) and Zhang et al. (2018). Recalling that the experimentally obtained velocities are superposed with a convective velocity due to electro-osmotic flow, they can still be employed to approximate orders of magnitude of Ca and Ce. The capillary and electric capillary number evaluated for the case of a dilute 1 mM NaCl-water solution lead to $\mathrm{Ca} = O(10^{-6})$ and $\mathrm{Ce} = O(10^{-7})$. Given that example, we expect both dimensionless numbers small in magnitude and expand all physical quantities of equation (3.24) and (3.25) in a perturbation series in Ca and Ce up to the first order, respectively. Exemplarily, this is done in the following way:

$$\boldsymbol{n}^s = \boldsymbol{n}_{(0)}^s + \mathrm{Ce}\,\boldsymbol{n}_{(1)}^s + O(\mathrm{Ce}^2), \tag{3.27}$$

$$\boldsymbol{n}^d = \boldsymbol{n}_{(0)}^d + \mathrm{Ca}\,\boldsymbol{n}_{(1)}^d + O(\mathrm{Ca}^2). \tag{3.28}$$

After inserting the perturbation expansions into equations (3.24) and (3.25) and grouping in terms of equal orders in Ce or Ca, respectively, we find

$$0 = \boldsymbol{n}_{(0)}\left(\tilde{\boldsymbol{\nabla}}\cdot\boldsymbol{n}_{(0)}\right), \quad \text{for } O(1), \tag{3.29}$$

$$\left[\tilde{p}^{s}_{(0)}\boldsymbol{I}-\tilde{\boldsymbol{\sigma}}^{s}_{M_{(0)}}\right]\cdot\boldsymbol{n}_{(0)} = \boldsymbol{n}_{(0)}\left(\tilde{\boldsymbol{\nabla}}\cdot\boldsymbol{n}^{s}_{(1)}\right), \quad \text{for } O(\mathrm{Ce}), \tag{3.30}$$

$$\left[\tilde{p}^{d}_{(0)}\boldsymbol{I}-\tilde{\boldsymbol{T}}_{(0)}-\frac{1}{\tilde{\eta}}\tilde{\boldsymbol{\sigma}}^{d}_{M_{(0)}}\right]\cdot\boldsymbol{n}_{(0)} = \boldsymbol{n}_{(0)}\left(\tilde{\boldsymbol{\nabla}}\cdot\boldsymbol{n}^{d}_{(1)}\right), \quad \text{for } O(\mathrm{Ca}). \tag{3.31}$$

In the latter equations we have used that the zeroth-order normal vector $\boldsymbol{n}_{(0)}$ corresponds to an 'equilibrium' fluid interface, and therefore coincides for both perturbations in Ca and Ce, independently. We define the term 'equilibrium' interface as the interface corresponding to an uncharged but geometrically equivalent and stationary interfacial particle. Equation (3.30) describes the interfacial deformation caused by the charge of the interfacial particle in absence of an applied electric field. On the other hand, equation (3.31) covers the interfacial deformation caused by the motion of the particle along the fluid interface. It is worth mentioning that the contributions to the interfacial deformation proportional to Ce and Ca are solely determined by physical quantities corresponding to the equilibrium interface. In theoretical papers dealing with particle-interface interaction, the deformation is typically computed on the basis of solutions corresponding to an undeformed interface. Therefore, interfacial deformations computed with this approach are a first order solution in the corresponding dimensionless number. We follow the same train of thought hereinafter.

For convenience, we may subdivide the latter equations into normal and tangential parts similar to section 2.2 and find after scalar multiplying with $\boldsymbol{n}_{(0)}$ or $\boldsymbol{t}_{i,(0)}$ $(i=1,2)$ from the left side, respectively:

$$0 = \tilde{\boldsymbol{\nabla}}\cdot\boldsymbol{n}_{(0)}, \quad \text{for } O(1), \tag{3.32}$$

$$\tilde{p}^{s}_{(0)}-\boldsymbol{n}_{(0)}\cdot\tilde{\boldsymbol{\sigma}}^{s}_{M_{(0)}}\cdot\boldsymbol{n}_{(0)} = \tilde{\boldsymbol{\nabla}}\cdot\boldsymbol{n}^{s}_{(1)}, \quad \text{for } O(\mathrm{Ce}), \tag{3.33}$$

$$\boldsymbol{t}_{i,(0)}\cdot\tilde{\boldsymbol{\sigma}}^{s}_{M_{(0)}}\cdot\boldsymbol{n}_{(0)} = 0, \quad \text{for } O(\mathrm{Ce}), \tag{3.34}$$

$$\tilde{p}^{d}_{(0)}-\boldsymbol{n}_{(0)}\cdot\tilde{\boldsymbol{T}}_{(0)}\cdot\boldsymbol{n}_{(0)}-\frac{1}{\tilde{\eta}}\boldsymbol{n}_{(0)}\cdot\tilde{\boldsymbol{\sigma}}^{d}_{M_{(0)}}\cdot\boldsymbol{n}_{(0)} = \tilde{\boldsymbol{\nabla}}\cdot\boldsymbol{n}^{d}_{(1)}, \quad \text{for } O(\mathrm{Ca}), \tag{3.35}$$

$$\boldsymbol{t}_{i,(0)}\cdot\tilde{\boldsymbol{T}}_{(0)}\cdot\boldsymbol{n}_{(0)}-\frac{1}{\tilde{\eta}}\boldsymbol{t}_{i,(0)}\cdot\tilde{\boldsymbol{\sigma}}^{d}_{M_{(0)}}\cdot\boldsymbol{n}_{(0)} = 0, \quad \text{for } O(\mathrm{Ca}). \tag{3.36}$$

Equation (3.34) is automatically satisfied, which follows when inserting equation (A.31) and taking into account the boundary condition at the free interface, i.e., equation (3.11). Following the same train of thought, equation (3.36) simplifies to

$$\boldsymbol{t}_{i,(0)}\cdot\tilde{\boldsymbol{T}}_{(0)}\cdot\boldsymbol{n}_{(0)} = 0, \quad \text{for } O(\mathrm{Ca}). \tag{3.37}$$

In summary, the evolution equations for the fluid interface are given in equations (3.32), (3.33) and (3.35).

After we have derived the governing equations, the corresponding boundary conditions as well as the evolution equations of the fluid interface on the basis of the underlying assumptions, we

are now in the position to study the electrokinetics of interfacial particles, starting with a particle of arbitrary shape.

3.2 Electrokinetics of an arbitrarily shaped interfacial particle

We consider a single, arbitrarily shaped particle characterized by a length scale a, attached to a fluid interface and translating with a velocity U due to an uniform applied electric field E_∞, as shown in figure 3.2.

Without loss of generality, we assume a negatively charged particle with a translational motion in z-direction. The equilibrium deformation of the fluid interface, given in equation (3.32), refers to an uncharged and stationary particle. For now, we may consider a three-phase contact line (separating the surface of the particle, phase 1 and phase 2) coplanar with the (y,z)-plane. Additionally, we assume that the fluid interface is unaffected by the presence of the particle at large distances. Both boundary conditions together with equation (3.32) lead to

$$\boldsymbol{n}_{(0)} = -\boldsymbol{e}_x. \tag{3.38}$$

Consequently, the equilibrium interface corresponds to a flat interface.

3.2.1 Electrophoretic mobility of an interfacial particle attached to a flat interface in the thin Debye-layer limit

We first concentrate on the electrophoretic mobility of an arbitrary particle attached to a flat fluid interface in the thin Debye-layer limit, i.e., $\kappa a \to \infty$. Typically, the electrophoretic mobility of a particle is calculated through a force balance at the particle, accounting for electrostatic and hydrodynamic forces. However, in this paragraph we go along a different route by making use of symmetry arguments.

As already mentioned, the upper fluid does not contribute to the electrophoretic mobility in the asymptotic limit of vanishing viscosity and permittivity ratios. Furthermore, based on the boundary conditions, the flat fluid interface represents a symmetry boundary, leading to an equivalent problem formulation in which the part of the particle immersed in fluid 1 is mirror reflected at the flat interface (see figure 3.3). This results in two fused particle components in an unbounded medium. In previous work, it was already shown that the Smoluchowski limit for the electrophoretic mobility holds no matter what the geometrically shape of the particle is (Morrison, 1970; Teubner, 1982). The electrophoretic mobility for such a particle then reads

$$\tilde{\eta} = 1, \qquad \text{for } \kappa a \to \infty. \tag{3.39}$$

The latter equation is a generalization of the Smoluchowski mobility for particles attached to flat fluid interfaces. This result is of general validity as long as the (zeroth-order) interfacial deformation is rather small and the Debye layer is asymptotically thin compared to the characteristic size of the particle. The most important consequence of the generalized extension of Smoluchowski's mobility towards interfacial particles is that it applies to spherical interfacial

particles independently of the contact angle between the particle surface and the fluid interface, determining its degree of immersion in fluid 1.

3.2.2 Dynamical interfacial deformation for arbitrary Debye-layer thicknesses

The evolution equations for the fluid interface are equations (3.33) & (3.35), revealing that two different contributions superpose to the total interfacial deformation, i.e., the charge of the particle in absence of an applied electric field (proportional to Ce) and the motion of the particle due to the presence of an applied electric field (proportional to Ca). In this paragraph, we concentrate on the interfacial deformation caused by the motion of the particle. It has been reported that spherical particles driven by an external force (acting in the center of mass of the particle) translate along the fluid interface in a tilted position (Dörr and Hardt, 2015). The goal of this paragraph is to determine whether a tilting also occurs if the external force is created through an applied electric field. In contrast to the previous subsection, we may relax the assumption of a thin Debye layer around the particle.

To start with, we integrate equation (3.21) (for $l = 1$) over the volume of fluid 1 and apply the divergence theorem leading to a force balance over the three bounding surfaces ($\Gamma_{\mathscr{P}}$, $\Gamma_{\mathscr{A}}$, Γ_∞), see figure 3.2. The forces acting on the far field boundary vanish, which follows as a consequence of the boundary conditions at the far field. Since the net force at the particle (sum of hydrodynamic and electrostatic forces) is identically zero, as it is used to calculate the electrophoretic mobility of the particle, the force acting on the fluid interface has to vanish, leading to

$$\mathscr{F}_{\mathscr{S}} = \int\limits_{\Gamma_{\mathscr{A}}} \left(\tilde{\boldsymbol{\sigma}}^d \cdot \boldsymbol{n} + \frac{1}{\bar{\eta}} \tilde{\boldsymbol{\sigma}}_M^d \cdot \boldsymbol{n} \right) \mathrm{d}\mathscr{A} = 0. \tag{3.40}$$

Assuming a mirror-symmetric particle shape with respect to the plane perpendicular to the direction of motion [(x, y)-plane], as sketched in figure 3.2, it is also reasonable to assume that the integrand in the previous equation is odd with respect to the z-coordinate. For a single spherical particle attached to a fluid interface and translating with a velocity U along the interface, an odd interfacial deformation with respect to z has been obtained by Dörr and Hardt (2015). The tilting angle of the particle was computed through a torque balance. We may therefore take the overall torque balance into account. The torque on the far field vanishes, again due to the boundary conditions. Therefore, the torque acting on the sphere has to be balanced by the torque acting on the fluid interface. The torque acting on the flat fluid interface can be written as

$$\mathscr{T}_{\mathscr{S}} = \int\limits_0^{2\pi} \int\limits_{\tilde{r}_{\mathscr{P}}(\vartheta)}^{\infty} \tilde{r}^2 \boldsymbol{e}_r \times \left(\tilde{\boldsymbol{\sigma}}^d \cdot \boldsymbol{n} + \frac{1}{\bar{\eta}} \tilde{\boldsymbol{\sigma}}_M^d \cdot \boldsymbol{n} \right) \Big|_{\varphi = \frac{\pi}{2}, \frac{3\pi}{2}} \mathrm{d}\tilde{r}\ \mathrm{d}\vartheta, \text{ with } \boldsymbol{n} = \pm \boldsymbol{e}_\varphi, \tag{3.41}$$

where we have used spherical coordinates, defined in figure 3.2 and $\vartheta = \theta + \frac{\pi}{2}$. We define the abbreviation $\boldsymbol{I}(\tilde{r}, \theta) = \tilde{\boldsymbol{\sigma}}^d \cdot \boldsymbol{n} + \frac{1}{\tilde{\eta}} \tilde{\boldsymbol{\sigma}}_M^d \cdot \boldsymbol{n}$ and expand equation (3.41) into

$$\mathcal{T}_{\mathscr{S}} = \int_0^{\pi} \int_{\tilde{r}_{\mathscr{P}}(\vartheta)}^{\infty} \tilde{r}^2 \boldsymbol{e}_r \times \boldsymbol{I}(\tilde{r}, \vartheta)|_{\varphi=\frac{\pi}{2}, \frac{3\pi}{2}} \, \mathrm{d}\tilde{r} \, \mathrm{d}\vartheta + \int_{\pi}^{2\pi} \int_{\tilde{r}_{\mathscr{P}}(\vartheta)}^{\infty} \tilde{r}^2 \boldsymbol{e}_r \times \boldsymbol{I}(\tilde{r}, \vartheta)|_{\varphi=\frac{\pi}{2}, \frac{3\pi}{2}} \, \mathrm{d}\tilde{r} \, \mathrm{d}\vartheta. \tag{3.42}$$

The latter integral can further be transferred into

$$\int_{\pi}^{2\pi} \int_{\tilde{r}_{\mathscr{P}}(\vartheta)}^{\infty} \tilde{r}^2 \boldsymbol{e}_r \times \boldsymbol{I}(\tilde{r}, \vartheta)|_{\varphi=\frac{\pi}{2}, \frac{3\pi}{2}} \, \mathrm{d}\tilde{r} \, \mathrm{d}\vartheta = -\int_0^{-\pi} \int_{\tilde{r}_{\mathscr{P}}(\vartheta)}^{\infty} \tilde{r}^2 \boldsymbol{e}_r \times \boldsymbol{I}(\tilde{r}, \vartheta)|_{\varphi=\frac{\pi}{2}, \frac{3\pi}{2}} \, \mathrm{d}\tilde{r} \, \mathrm{d}\vartheta, \tag{3.43}$$

$$= \int_0^{-\pi} \int_{\tilde{r}_{\mathscr{P}}(\vartheta)}^{\infty} \tilde{r}^2 \boldsymbol{e}_r \times \boldsymbol{I}(\tilde{r}, -\vartheta)|_{\varphi=\frac{\pi}{2}, \frac{3\pi}{2}} \, \mathrm{d}\tilde{r} \, \mathrm{d}\vartheta, \tag{3.44}$$

where we have used $\boldsymbol{I}(\tilde{r}, \vartheta) = -\boldsymbol{I}(\tilde{r}, -\vartheta)$ due to the assumption of an odd force distribution around the particle. However, when employing the substitution $\chi = -\vartheta$, we find

$$\int_0^{-\pi} \int_{\tilde{r}_{\mathscr{P}}(\vartheta)}^{\infty} \tilde{r}^2 \boldsymbol{e}_r \times \boldsymbol{I}(\tilde{r}, -\vartheta)|_{\varphi=\frac{\pi}{2}, \frac{3\pi}{2}} \, \mathrm{d}\tilde{r} \, \mathrm{d}\vartheta = -\int_0^{\pi} \int_{\tilde{r}_{\mathscr{P}}(-\chi)}^{\infty} \tilde{r}^2 \boldsymbol{e}_r \times \boldsymbol{I}(\tilde{r}, \chi)|_{\varphi=\frac{\pi}{2}, \frac{3\pi}{2}} \, \mathrm{d}\tilde{r} \, \mathrm{d}\chi. \tag{3.45}$$

Recalling the assumption of a mirror-symmetric particle shape with respect to the (x, y)-plane, it follows that $\tilde{r}_{\mathscr{P}}(-\vartheta) = \tilde{r}_{\mathscr{P}}(\vartheta)$ and therefore equation (3.41) is identically zero. Consequently, there is no net torque acting on the particle and no tilting. In other words, the sum of the hydrodynamic and electrostatic torque acting on the surface of the particle perfectly balance. Therefore, to the first order in Ca, the electrophoretic motion of the particle itself does not cause a deformation of the fluid interface, independent of the thickness of the Debye layer. The electrostatic interfacial deformation, on the other hand, cannot be quantified without any further specification of the particle shape. Hence, in the following we will concentrate on spherical particles attached to fluid interfaces, which is the case of highest practical relevance.

3.3 Electrokinetics of a spherical interfacial particle

We now consider a spherical particle of radius a attached to a fluid interface with a contact angle Θ between the surface of the colloid and the fluid interface. A sphere clearly fulfills all symmetry constraints described in section 3.2. Thus, the electrophoretic mobility in the thin Debye layer limit is given by equation (3.39) and consequently independent of the contact angle. Moreover, the motion of the particle does not cause a deformation of the fluid interface up to the first order in Ca. Therefore, the remaining task is to compute the electrophoretic mobility of a spherical interfacial particle for arbitrary Debye lengths and the interfacial deformation caused by the charge of the particle, known as electrodipping. To lowest order, the interface is flat, so

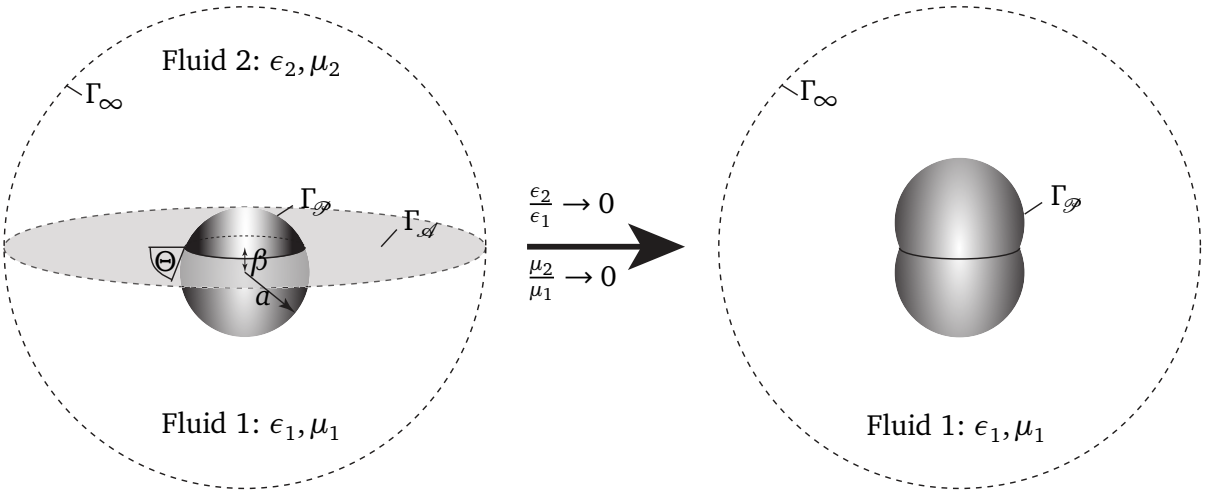

Abbildung 3.3.: Schematic of the two equivalent systems considered when computing the electrophoretic mobility of a sphere attached to a flat fluid interface. The electrophoretic mobility of a sphere attached to a flat fluid interface is equal to the mobility of two spherical caps fused at the three-phase contact line. The perturbation parameter β represents the shift of the center of the sphere along the x-direction relative to the fluid interface (see figure 3.2). a denotes the radius of the sphere [reprinted with permission from APS, Phys. Rev. Fluids 3 (2018), Eigenbrod et al. (2018)].

the configuration is equivalent to a system of two spherical caps fused at the three-phase contact line and suspended in an unbounded medium (phase 1), as sketched in figure 3.3.

3.3.1 Electrophoretic mobility for a flat interface

In order to keep the computational effort manageable, we restrict our analysis to small contact angle perturbations around 90°. Based on that, by defining $\beta = \cos(\Theta)$, it follows that $\beta \ll 1$. Consequently, β takes a role of a perturbation parameter (Dörr and Hardt, 2015; Dörr et al., 2016). In dimensionless form, β is directly linked to the vertical shift of the particle center relative to the flat interface in x-direction. The parametrization of the fused spherical caps can be obtained with the help of elementary geometrical calculations

$$\tilde{r}_\mathscr{P} = \beta \sin(\theta)|\cos(\varphi)| + \sqrt{1-\beta^2\left[1-\sin^2(\theta)\cos^2(\varphi)\right]} \tag{3.46}$$

$$= 1 + \beta f(\theta,\varphi) + \beta^2 g(\theta,\varphi) + O(\beta^3), \tag{3.47}$$

with

$$f(\theta,\varphi) = \sin(\theta)|\cos(\varphi)| \quad \text{and} \quad g(\theta,\varphi) = \frac{\sin^2(\theta)\cos^2(\varphi)-1}{2}. \tag{3.48}$$

In this section, we omit all terms higher than the linear order in β. Equation (3.47) is a parametrization of a slightly deformed sphere. This type of geometry has been studied in Stokes flow without source terms (Brenner, 1964), and in context with electrophoretic (Kim and Yoon, 2002), thermophoretic (Senchenko and Keh, 2007) as well as diffusiophoretic (Khair, 2013) motion. To solve the governing equations for a slightly deformed sphere, a domain perturbation method (discussed in section 2.4) is employed requiring an expansion of all physical quantities in

a perturbation series in β up to the first order. It should be noted that in the present context, the zeroth-order quantities refer to an interfacial particle having a contact angle of $\Theta = 90°$, whereas the first-order quantities describe the influence of slight variations of the contact angle around 90°. Following the scheme outlined in section 2.4, the following boundary conditions have to be satisfied at the surface of a spherical particle (the subscript denotes the order of perturbation in β)

$$\tilde{\psi}_{(0)}\big|_{\tilde{r}=1} = 1, \tag{3.49}$$

$$\tilde{\psi}_{(1)}\big|_{\tilde{r}=1} = -f(\theta,\varphi)\left.\frac{\partial\tilde{\psi}_{(0)}}{\partial\tilde{r}}\right|_{\tilde{r}=1}, \tag{3.50}$$

$$\left.\frac{\partial\tilde{\phi}_{(0)}}{\partial\tilde{r}}\right|_{\tilde{r}=1} = 0, \tag{3.51}$$

$$\left.\frac{\partial\tilde{\phi}_{(1)}}{\partial\tilde{r}}\right|_{\tilde{r}=1} = -f(\theta,\varphi)\left.\frac{\partial^2\tilde{\phi}_{(0)}}{\partial\tilde{r}^2}\right|_{\tilde{r}=1} + \tilde{\boldsymbol{\nabla}}\,\tilde{\phi}_{(0)}\big|_{\tilde{r}=1}\cdot\tilde{\boldsymbol{\nabla}}f(\theta,\varphi), \tag{3.52}$$

$$\tilde{\boldsymbol{u}}_{(0)}\big|_{\tilde{r}=1} = \boldsymbol{e}_z, \tag{3.53}$$

$$\tilde{\boldsymbol{u}}_{(0)}\big|_{\tilde{r}=1} = -f(\theta,\varphi)\left.\frac{\partial\tilde{\boldsymbol{u}}_{(1)}}{\partial\tilde{r}}\right|_{\tilde{r}=1}. \tag{3.54}$$

The far field boundary conditions read

$$\tilde{\phi}_{(0)}\big|_{\tilde{r}\to\infty} = \tilde{r}\cos(\theta), \tag{3.55}$$

$$\tilde{\phi}_{(1)}\big|_{\tilde{r}\to\infty} = \tilde{\psi}_{(0)}\big|_{\tilde{r}\to\infty} = \tilde{\psi}_{(1)}\big|_{\tilde{r}\to\infty} = \tilde{\boldsymbol{u}}_{(0)}\big|_{\tilde{r}\to\infty} = \tilde{\boldsymbol{u}}_{(1)}\big|_{\tilde{r}\to\infty} = 0. \tag{3.56}$$

In agreement with physical intuition, a perturbation of the shape of the spherical particle does therefore not affect the far field behavior of the electrostatic potentials, as well as the velocity field. We are now in the position to solve the governing equations up to the first order in β. To be explained subsequently, the reciprocal theorem [see section 2.5] will prove useful in the present context.

Application of the reciprocal theorem

As already pointed out, the electrophoretic mobility is typically archived through a force balance at the surface of the particle. Among others, the governing equations of the fluid flow, i.e., equation (3.20) and (3.21) ($l = 1$), have to be solved for the given set of boundary conditions. Traditionally, researches spend most effort on computing analytical solutions of the Stokes equations in absence of source terms [e.g., Lamb's general solution (Lamb, 1945; Happel and Brenner, 2012; Kim and Karrila, 2013)]. It is therefore desirable to describe the hydrodynamic force acting on an electrophoretic driven particle on the basis of the hydrodynamic force acting on a particle moving with the same velocity, but in absence of an external electric field. We may now prove that the reciprocal theorem takes the role of such a valuable tool. The subsequent deduction is based on the general outline from section 2.5.

We introduce a set of two solutions consisting of a solution of the classical Stokes equations

($\boldsymbol{f} = 0$; subscript c) $(\tilde{\boldsymbol{\sigma}}_c, \tilde{\boldsymbol{u}}_c)$ and a solution of the Stokes equations including a body force [such as equation (3.21)] with $(\tilde{\boldsymbol{\sigma}}, \tilde{\boldsymbol{u}}, \tilde{\boldsymbol{f}})$. Employing the extended Lorentz reciprocal theorem from equation (2.80), we have

$$-\int_{\mathscr{A}_\mathscr{P}} (\tilde{\boldsymbol{u}}_c \cdot \tilde{\boldsymbol{\sigma}}) \cdot \boldsymbol{n} \mathrm{d}\mathscr{A} + \int_{\mathscr{V}_\mathscr{F}} \left(\tilde{\boldsymbol{u}}_c \cdot \tilde{\boldsymbol{f}}\right) \mathrm{d}\mathscr{V} = -\int_{\mathscr{A}_\mathscr{P}} (\tilde{\boldsymbol{u}} \cdot \tilde{\boldsymbol{\sigma}}_c) \cdot \boldsymbol{n} \mathrm{d}\mathscr{A}. \tag{3.57}$$

We assume that the particle translates with the same (constant) velocity, irrespective of whether an applied electric field is present or not: $\tilde{\boldsymbol{u}} = \tilde{\boldsymbol{u}}_c = \boldsymbol{e}_z$ on $\mathscr{A}_\mathscr{P}$. Further, the electrostatic body force reads [equation (3.21)]: $\tilde{\boldsymbol{f}} = (1/\tilde{\eta})\tilde{\boldsymbol{\nabla}}^2\tilde{\psi}\tilde{\boldsymbol{\nabla}}\tilde{\phi}$. Then

$$\int_{\mathscr{A}_\mathscr{P}} (\boldsymbol{e}_z \cdot \tilde{\boldsymbol{\sigma}}) \cdot \boldsymbol{n} \mathrm{d}\mathscr{A} = \int_{\mathscr{A}_\mathscr{P}} (\boldsymbol{e}_z \cdot \tilde{\boldsymbol{\sigma}}_c) \cdot \boldsymbol{n} \mathrm{d}\mathscr{A} + \frac{1}{\tilde{\eta}} \int_{\mathscr{V}_\mathscr{F}} \left(\tilde{\boldsymbol{\nabla}}^2\tilde{\psi}\tilde{\boldsymbol{\nabla}}\tilde{\phi} \cdot \tilde{\boldsymbol{u}}_c\right) \mathrm{d}\mathscr{V}. \tag{3.58}$$

The left-hand side of the latter equation is the hydrodynamic force (in z-direction) acting on a electrophoretically driven particle. Interestingly, this force is a superposition of the hydrodynamic force on a translating particle in absence of any source terms (first term on the right-hand side) and a correction term due to the presence of the applied electric field and the electric double layer around the particle. The latter one of the two forces can be computed on the basis of the velocity field corresponding to an translating particle in absence of electric field and the solutions of the electrostatic equations. However, applying a force balance at the surface of the particle in z-direction we find

$$\int_{\mathscr{A}_\mathscr{P}} (\boldsymbol{e}_z \cdot \tilde{\boldsymbol{\sigma}}) \cdot \boldsymbol{n} \mathrm{d}\mathscr{A} = \frac{1}{\tilde{\eta}} \int_{\mathscr{V}_\mathscr{F}} \left(\tilde{\boldsymbol{\nabla}}^2\tilde{\psi}\tilde{\boldsymbol{\nabla}}\tilde{\phi} \cdot \boldsymbol{e}_z\right) \mathrm{d}\mathscr{V}. \tag{3.59}$$

Replacing the hydrodynamic force acting on an electrophoretically driven particle from equation (3.58) through equation (3.59) and solving for $\tilde{\eta}$ we finally obtain (note the change of the sign due to the assumption: $\zeta < 0$)

$$\tilde{\eta} = \frac{\int_{\mathscr{V}_\mathscr{F}} \left[\tilde{\boldsymbol{\nabla}}^2\tilde{\psi}\tilde{\boldsymbol{\nabla}}\tilde{\phi} \cdot (\boldsymbol{u}_c - \boldsymbol{e}_z)\right] \mathrm{d}\mathscr{V}}{\int_{\mathscr{A}_\mathscr{P}} (\boldsymbol{e}_z \cdot \tilde{\boldsymbol{\sigma}}_c) \cdot \boldsymbol{n} \mathrm{d}\mathscr{A}}. \tag{3.60}$$

Equation (3.60) allows the computation of the electrophoretic mobility on the basis of solutions of the Stokes equations in absence of source terms, reflecting the presence of an external electric field. Teubner (1982) first employed a slightly different notation of equation (3.60) and reproduced the results from Henry (1931). It should be noted that it took Henry (1931) about 24 pages of cumbersome mathematics to obtain the electrophoretic mobility of a weakly charged spherical particle subjected to an applied electric field. Teubner (1982), however, obtained the same result with a significant shorter calculation by employing the reciprocal theorem. We therefore make use of the reciprocal theorem, i.e., equation (3.60) for the computation of the electrophoretic mobility of interfacial particles, hereinafter.

Zeroth-order solution; $\Theta = 90°$

The zeroth-order solution corresponds to an undeformed sphere in an unbounded fluid. Under the assumptions made, this problem is equivalent to the problem studied by Henry (1931). The solutions of the Stokes equations in absence of source terms, of the Poisson-Boltzmann equation, as well as of the Laplace equation satisfying the corresponding boundary conditions are readily known (Teubner, 1982; Masliyah and Bhattacharjee, 2006)

$$\tilde{\boldsymbol{u}}_{\mathrm{c}}^{(0)} = -\frac{1}{2}\cos(\theta)\left(\tilde{r}^{-3} - 3\tilde{r}^{-1}\right)\boldsymbol{e}_r - \frac{1}{4}\sin(\theta)\left(\tilde{r}^{-3} + 3\tilde{r}^{-1}\right)\boldsymbol{e}_\theta, \tag{3.61}$$

$$\tilde{p}_{\mathrm{c}}^{(0)} = \frac{3}{2}\cos(\theta)\tilde{r}^{-2}, \tag{3.62}$$

$$\tilde{\psi}^{(0)} = \exp[-\kappa a(\tilde{r}-1)]\tilde{r}^{-1}, \tag{3.63}$$

$$\tilde{\phi}^{(0)} = \cos(\theta)\left(\tilde{r} + \frac{1}{2}\tilde{r}^{-2}\right). \tag{3.64}$$

After inserting equations (3.61) - (3.64) into equation (3.60) and evaluating the integrals, the zeroth-order electrophoretic mobility is obtained

$$\tilde{\eta}^{(0)} = \frac{1}{144}\left(96 + (\kappa a)^2(3+\kappa a)(2+(\kappa a-4)\kappa a) + \exp(\kappa a)(\kappa a)^4((\kappa a)^2-12)\mathrm{Ei}(-\kappa a)\right), \tag{3.65}$$

in which $\mathrm{Ei}(x)$ denote the exponential integral function, defined by

$$\mathrm{Ei}(x) = -\int_{-x}^{\infty} \frac{\exp(-t)}{t}\,\mathrm{d}t. \tag{3.66}$$

As expected, the Smoluchowski ($\kappa a \to \infty$) and Hückel ($\kappa a \to 0$) mobilities can formally be obtained through equation (3.65).

First-order solution; $\Theta \neq 90°$

The solution of the Stokes equations (without source terms) satisfying the boundary conditions (3.54) and $\tilde{\boldsymbol{u}}|_{\tilde{r}\to\infty} = 0$ is available (Brenner, 1964). More detailed information on the solution procedure for a translating slightly deformed spherical particle is given by Brenner (1964) or in a slightly different context in chapter 4. Here, we focus on the solution of the governing equations of the electrostatic problem in more detail. With the help of equations (3.63) and (3.64), the boundary conditions (3.50) and (3.52) can be further simplified. After a short deduction, we obtain

$$\tilde{\psi}^{(1)}\Big|_1 = (1+\kappa a) f(\theta,\varphi), \tag{3.67}$$

$$\left.\frac{\partial\tilde{\phi}^{(1)}}{\partial\tilde{r}}\right|_1 = -\frac{9}{2}\cos(\theta) f(\theta,\varphi). \tag{3.68}$$

l	$f(\vartheta,\varphi)$	$\vartheta f(\vartheta,\varphi)$
0	$\frac{1}{2}$	0
1	0	$\frac{3\vartheta}{8}$
2	$-\frac{5}{32}[-1+3\vartheta^2+3(\vartheta^2-1)\cos(2\varphi)]$	0

Tabelle 3.1.: Expansion of $f(\theta,\varphi)$ and $\cos(\theta)f(\theta,\varphi)$, with $f(\theta,\varphi)=|\cos(\varphi)|\sin(\theta)$ into surface spherical harmonics following equations (3.69) - (3.72). Note: $\vartheta=\cos(\theta)$.

Following the general method from section 2.3, the right-hand side of equations (3.67) and (3.68) have to be expanded in a sum of surface spherical harmonics which are a complete and orthogonal set of functions defined on a sphere (Byerly, 1893; MacRobert, 1947). We introduce a notation that represents an expansion of a function $\chi(\theta,\varphi)$ into surface spherical harmonics such that $\chi_l(\theta,\varphi)$ represents the l-th partial sum of the expansion of $\chi(\theta,\varphi)=\sum_{l=0}^{\infty}\chi_l(\theta,\varphi)$. Following Byerly (1893), a function $\chi(\theta,\varphi)$ can be expressed through surface spherical harmonics via [for short-hand notation, we define $\vartheta=\cos(\theta)$]

$$A_{0,l} = \frac{2l+1}{4\pi}\int_0^{2\pi}\int_{-1}^{1}\chi(\vartheta,\varphi)P_l(\vartheta)\,\mathrm{d}\vartheta\,\mathrm{d}\varphi, \tag{3.69}$$

$$A_{m,l} = \frac{2l+1}{2\pi}\frac{(l-m)!}{(l+m)!}\int_0^{2\pi}\int_{-1}^{1}\chi(\vartheta,\varphi)\cos(m\varphi)P_l^m(\vartheta)\,\mathrm{d}\vartheta\,\mathrm{d}\varphi, \tag{3.70}$$

$$B_{m,l} = \frac{2l+1}{2\pi}\frac{(l-m)!}{(l+m)!}\int_0^{2\pi}\int_{-1}^{1}\chi(\vartheta,\varphi)\sin(m\varphi)P_l^m(\vartheta)\,\mathrm{d}\vartheta\,\mathrm{d}\varphi, \tag{3.71}$$

$$\chi_l(\vartheta,\varphi) = A_{0,l}P_l(\vartheta)+\sum_{m=1}^{l}\left(A_{m,l}\cos(m\varphi)+B_{m,l}\sin(m\varphi)\right)P_l^m(\vartheta), \tag{3.72}$$

in which $P_l^m(x)$ are the associated Legendre polynomials. Exemplarily, we have listed the first three surface spherical harmonic expansions of $f(\vartheta,\varphi)=\sqrt{1-\vartheta^2}|\cos(\varphi)|$ and $\vartheta f(\vartheta,\varphi)=\vartheta\sqrt{1-\vartheta^2}|\cos(\varphi)|$ in table 3.1. Note that all $f_j(\theta,\varphi)$, with $j=2l-1$ vanish, since $f(\theta,\varphi)$ is even with respect to $\cos(\theta)$. Consequently, $\cos(\theta)f(\theta,\varphi)$ is odd with respect to $\cos(\theta)$ implying that all even expansion orders, i.e., $j=2l$, vanish.

Coming back to the solution of the governing equations for both electrostatic potentials. In agreement to the expansion of the boundary conditions at the surface of the particle, we assume the solution of the electrostatic potentials of the following form

$$\tilde{\psi}^{(1)}=\sum_{l=0}^{\infty}\tilde{\psi}_l^{(1)},\quad \tilde{\phi}^{(1)}=\sum_{l=0}^{\infty}\tilde{\phi}_l^{(1)}. \tag{3.73}$$

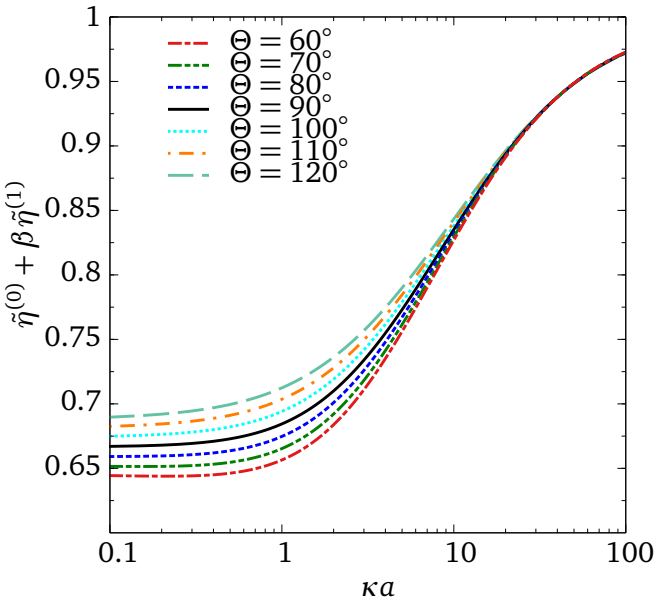

Abbildung 3.4.: Electrophoretic mobility of a spherical particle attached to a flat fluid interface as a function of the Debye parameter for different contact angles $\beta = \cos(\Theta)$. The analytical expressions for $\tilde{\eta}^{(0)}$ and $\tilde{\eta}^{(1)}$ are taken from equation (3.65) and (3.77), respectively [reprinted with permission from APS, Phys. Rev. Fluids 3 (2018), Eigenbrod et al. (2018)].

The solutions of the Poisson-Boltzmann and Laplace equation are available in multipole notation (Kim and Yoon, 2002). Translated to our notation they read

$$\tilde{\phi}_l^{(1)} = \frac{9}{2}\frac{\tilde{r}^{-(l+1)}}{l+1}[\cos(\theta)f(\theta,\varphi)]_l\,, \tag{3.74}$$

$$\tilde{\psi}_l^{(1)} = (1+\kappa a)\tilde{r}^{-(l+1)}\exp(-\kappa a(\tilde{r}-1))\frac{\mathrm{K}_l(\kappa a\,\tilde{r})}{\mathrm{K}_l(\kappa a)}f_l(\theta,\varphi), \tag{3.75}$$

$$\mathrm{K}_l(x) = \sum_{s=0}^{l}\frac{2^s l!(2l-s)!}{s!(2l)!(l-s)!}x^s. \tag{3.76}$$

We have employed the notation $[.]_l$ denoting the l-th partial sum of the surface spherical harmonic expansion of the term in brackets. Now, we directly go over to compute the electrophoretic mobility on the basis of the reciprocal theorem following equation (3.60). Solely the terms corresponding to $l = 0, 1, 2$ contribute to the electrophoretic mobility (Kim and Yoon, 2002). We obtain

$$\begin{aligned}\tilde{\eta}^{(1)} = {} & \frac{1}{1536(3+\kappa a\{3+\kappa a\})}(-192+\kappa a\{-384+\kappa a(24+\kappa a\{-304\\ & +\kappa a(-726+\kappa a\{-352+\kappa a(27+\kappa a\{46+5\kappa a\})\})\})\}+\exp(\kappa a)(\kappa a)^4(-840\\ & +\kappa a\{-1032+\kappa a(-356+\kappa a\{68+\kappa a(51+5\kappa a)\})\})\mathrm{Ei}(-\kappa a))\,.\end{aligned} \tag{3.77}$$

Figure 3.4 shows the electrophoretic mobility of a spherical particle attached to a flat fluid interface as a function of the contact angle and the Debye parameter. The independence of the electrophoretic mobility on the contact angle for thin Debye layers is reobtained. More specifically,

the electrophoretic mobility is nearly independent of the contact angle if the Debye parameter is above 30. It can further be observed that hydrophobic particles have a higher mobility than hydrophilic particles. In this case, the electrostatic forces dominate over the hydrodynamic drag forces. In the Hückel limit, if the radius of the spherical particle is small compared to the thickness of the electric double layer, one obtains

$$\lim_{\kappa a \to 0} (\tilde{\eta}^{(0)} + \cos(\Theta)\tilde{\eta}^{(1)}) = \frac{2}{3} - \frac{\cos(\Theta)}{24}. \tag{3.78}$$

3.3.2 Interfacial deformation

As already discussed in section 3.2.2, the translational motion of the particle does not lead to a deformation of the fluid interface in the first order of the capillary number Ca. The only remaining contribution is called electrodipping (Danov et al., 2004). Essentially, the sum of the Maxwell stresses and the osmotic pressure inside the electric double layer is balanced by the capillary pressure induced through a deformation of the fluid interface. In contrast to all published works concerning the electrodipping effect, we do not limit our analysis to the case of a thin Debye layer. However, in this work the static interfacial deformation is independent of the nonpolar fluid, as a consequence of assumption 4, as opposed to the works by Foret and Würger (2004), Danov et al. (2004), Danov and Kralchevsky (2006a) and Danov et al. (2006). In the present context, we are therefore focusing on the interfacial deformation caused by the electric double layer developing at the surface of the particle immersed in the fluid of higher viscosity and permittivity in absence of an applied electric field.

The computation of the interfacial deformation is straightforward, since we already provided the solution of the electrostatic potential $\tilde{\psi}$ up to the first order in β [see equations (3.63) and (3.75)] as well as the static (osmotic) pressure (see equation (3.19) with $l = 1$.). The evolution equation accounting for the electrodipping effect is equation (3.33). Clearly, all quantities on the left-hand side of equation (3.33) have to be evaluated at the interface, i.e., $\varphi = \frac{\pi}{2}, \frac{3\pi}{2}$. In the static state, the electrostatic potential $\tilde{\psi}$ and the osmotic pressure $\tilde{p}^s$ are axisymmetric around the particle, consequently the interfacial deformation as well. For the computation of the interfacial deformation, we introduce cylindrical coordinates $(\tilde{\varrho}, \vartheta, \tilde{x})$, as defined by Dörr and Hardt (2015)

$$\tilde{\varrho} = \sqrt{\tilde{y}^2 + \tilde{z}^2}, \tag{3.79}$$

$$\vartheta = \theta + \frac{\pi}{2}. \tag{3.80}$$

The fluid interface follows the parametrization:

$$\tilde{x} = \tilde{h}(\tilde{\varrho}). \tag{3.81}$$

In agreement to our foregoing analysis, we expand $\tilde{h}(\tilde{\varrho})$ up to the linear order in Ce, leading to $\tilde{h}(\tilde{\varrho}) \approx \mathrm{Ce}\,\tilde{\mathfrak{h}}(\tilde{\varrho})$. The normal vector corresponding to the perturbation expansion in Ce (pointing outwards of phase 1) has the following first-order contribution

$$\boldsymbol{n}^{s}_{(1)} = \frac{\mathrm{d}\tilde{\mathfrak{h}}(\tilde{\varrho})}{\mathrm{d}\tilde{\varrho}}\boldsymbol{e}_{\tilde{\varrho}}. \tag{3.82}$$

Computing the divergence of the normal vector $\boldsymbol{n}^{s}_{(1)}$ evolves equation (3.33) into

$$\tilde{p}^{s}|_{\varphi=\frac{\pi}{2},\frac{3\pi}{2}} - \tilde{\sigma}^{s,\varphi\varphi}_{M}\big|_{\varphi=\frac{\pi}{2},\frac{3\pi}{2}} = \frac{1}{\tilde{\varrho}}\frac{\mathrm{d}}{\mathrm{d}\tilde{\varrho}}\left(\tilde{\varrho}\frac{\mathrm{d}\tilde{\mathfrak{h}}}{\mathrm{d}\tilde{\varrho}}\right), \tag{3.83}$$

in which $\tilde{\sigma}^{s,\varphi\varphi}_{M}$ denotes the $\varphi\varphi$-component of the Maxwell stress tensor defined in equation (A.31). Up to the first order in β, we find for the left-hand side of the latter equation

$$\tilde{\sigma}^{s,\varphi\varphi}_{M} = -\frac{1}{2}\left(\frac{\partial\tilde{\psi}_{(0)}}{\partial\tilde{r}}\right)^{2} - \beta\frac{\partial\tilde{\psi}_{(0)}}{\partial\tilde{r}}\frac{\partial\tilde{\psi}_{(1)}}{\partial\tilde{r}} + O(\beta^{2}), \tag{3.84}$$

$$\tilde{p}^{s} = \frac{(\kappa a)^{2}}{2}(\tilde{\psi}_{(0)})^{2} + \beta(\kappa a)^{2}\tilde{\psi}_{(0)}\tilde{\psi}_{(1)} + O(\beta^{2}). \tag{3.85}$$

Interfacial deformation for $\Theta = 90^{\circ}$

For $\beta = 0$, corresponding to a particle having a contact angle of $\Theta = 90^{\circ}$ the evolution equation reads

$$\frac{1}{2}\left[(\kappa a)^{2}(\tilde{\psi}_{(0)})^{2} + \left(\frac{\partial\tilde{\psi}_{(0)}}{\partial\tilde{\varrho}}\right)^{2}\right]\Bigg|_{\varphi=\frac{\pi}{2},\frac{3\pi}{2}} = \frac{1}{\tilde{\varrho}}\frac{\mathrm{d}}{\mathrm{d}\tilde{\varrho}}\left(\tilde{\varrho}\frac{\mathrm{d}\tilde{\mathfrak{h}}_{(0)}}{\mathrm{d}\tilde{\varrho}}\right). \tag{3.86}$$

The left-hand side of this equation is a function of $\tilde{\varrho}$ alone, say $k(\tilde{\varrho})$. Given that $\lim_{\tilde{\varrho}\to\infty} k(\tilde{\varrho}) = 0$, $\lim_{\tilde{\varrho}\to\infty} \tilde{\mathfrak{h}}(\tilde{\varrho}) = 0$ and $\lim_{\tilde{\varrho}\to\infty} \tilde{\mathfrak{h}}'(\tilde{\varrho}) = 0$, the solution of equation (3.86) can be written as

$$\tilde{\mathfrak{h}}(\tilde{\varrho}) = \int_{\tilde{\varrho}}^{\infty} \ln\left(\frac{\rho}{\tilde{\varrho}}\right)\rho k(\rho)\,\mathrm{d}\rho. \tag{3.87}$$

A formal proof of the latter transformation can be found in appendix D by Eigenbrod et al. (2018). When inserting the solution for the electrostatic potential $\tilde{\psi}$ and evaluating the integral one obtains

$$\tilde{\mathfrak{h}}_{(0)}(\tilde{\varrho}) = \frac{\exp[-2\kappa a(\tilde{\varrho}-1)]}{8\tilde{\varrho}^{2}}\left[1 + 2\kappa a\tilde{\varrho} + 4\exp(2\kappa a\tilde{\varrho})(\kappa a)^{2}\tilde{\varrho}^{2}\mathrm{Ei}(-2\kappa a\tilde{\varrho})\right]. \tag{3.88}$$

Interfacial deformation for $\Theta \neq 90°$

The evolution equation for the first-order correction of the interfacial deformation caused by the charge of a spherical interfacial particle having a contact angle slightly deviating from $\Theta = 90°$ reads

$$\left[(\kappa a)^2 \tilde{\psi}_{(0)} \tilde{\psi}_{(1)} + \frac{\partial \tilde{\psi}_{(0)}}{\partial \tilde{\varrho}} \frac{\partial \tilde{\psi}_{(1)}}{\partial \tilde{\varrho}}\right]\Bigg|_{\varphi=\frac{\pi}{2},\frac{3\pi}{2}} = \frac{1}{\tilde{\varrho}} \frac{\mathrm{d}}{\mathrm{d}\tilde{\varrho}} \left(\tilde{\varrho} \frac{\mathrm{d}\tilde{\mathfrak{h}}_{(1)}}{\mathrm{d}\tilde{\varrho}}\right), \tag{3.89}$$

that leads, when making use of equation (3.87), to

$$\tilde{\mathfrak{h}}_{(1)} = \int_{\tilde{\varrho}}^{\infty} \ln\left(\frac{\rho}{\tilde{\varrho}}\right) \rho \left[(\kappa a)^2 \tilde{\psi}_{(0)} \tilde{\psi}_{(1)} + \frac{\partial \tilde{\psi}_{(0)}}{\partial \rho} \frac{\partial \tilde{\psi}_{(1)}}{\partial \rho}\right]\Bigg|_{\varphi=\frac{\pi}{2},\frac{3\pi}{2}} \mathrm{d}\rho. \tag{3.90}$$

By employing the product rule, it can be shown that

$$(\kappa a)^2 \tilde{\psi}_{(0)} \tilde{\psi}_{(1)} + \frac{\partial \tilde{\psi}_{(0)}}{\partial \rho} \frac{\partial \tilde{\psi}_{(1)}}{\partial \rho} = \left[(\kappa a)^2 \tilde{\psi}_{(0)} - \frac{\partial^2 \tilde{\psi}_{(0)}}{\partial \rho^2}\right] \tilde{\psi}_{(1)} + \frac{\partial}{\partial \rho} \left(\frac{\partial \tilde{\psi}_{(0)}}{\partial \rho} \tilde{\psi}_{(1)}\right). \tag{3.91}$$

Further, $\tilde{\psi}_{(0)}$ has to satisfy the linearized Poisson-Boltzmann equation. Substituting $(\kappa a)^2 \tilde{\psi}_{(0)}$ for the Laplacian of the potential $\tilde{\psi}_{(0)}$ in spherical coordinates we get

$$\tilde{\mathfrak{h}}_{(1)} = \int_{\tilde{\varrho}}^{\infty} \ln\left(\frac{\rho}{\tilde{\varrho}}\right) \rho \left[\frac{2}{\rho} \frac{\partial \tilde{\psi}_{(0)}}{\partial \rho} \tilde{\psi}_{(1)} + \frac{\partial}{\partial \rho} \left(\frac{\partial \tilde{\psi}_{(0)}}{\partial \rho} \tilde{\psi}_{(1)}\right)\right]\Bigg|_{\varphi=\frac{\pi}{2},\frac{3\pi}{2}} \mathrm{d}\rho. \tag{3.92}$$

Then, after partial integration of the second term in brackets, using the boundary conditions for equilibrium potential, we obtain

$$\tilde{\mathfrak{h}}_{(1)} = \int_{\tilde{\varrho}}^{\infty} \left[\ln\left(\frac{\rho}{\tilde{\varrho}}\right) - 1\right] \frac{\partial}{\partial \rho} \left(\frac{\partial \tilde{\psi}_{(0)}}{\partial \rho} \tilde{\psi}_{(1)}\right)\Bigg|_{\varphi=\frac{\pi}{2},\frac{3\pi}{2}} \mathrm{d}\rho. \tag{3.93}$$

It is known that elliptic partial differential equations take their extremal values at the boundary of the domain (so-called maximum principle) (Lee, 2014; Gilberg and Trudinger, 2015). The boundaries of the first-order contribution of the electrostatic potential $\tilde{\psi}_{(1)}$ are $\tilde{\varrho} = 1$ and $\tilde{\varrho} \to \infty$. Since the potential decays to zero far away from the particle we are left with the boundary condition at $\tilde{\varrho} = 1$ that reads in the present context [see equation (3.67)]

$$\left[\tilde{\psi}_{(1)}\big|_{\tilde{\varrho}=1}\right]\Big|_{\varphi=\frac{\pi}{2},\frac{3\pi}{2}} = (1+\kappa a) \left(\sum_{l=0}^{\infty} f_l(\theta,\varphi)\right)\Bigg|_{\varphi=\frac{\pi}{2},\frac{3\pi}{2}}, \tag{3.94}$$

$$= (1+\kappa a)\, f(\theta,\varphi)\big|_{\varphi=\frac{\pi}{2},\frac{3\pi}{2}}. \tag{3.95}$$

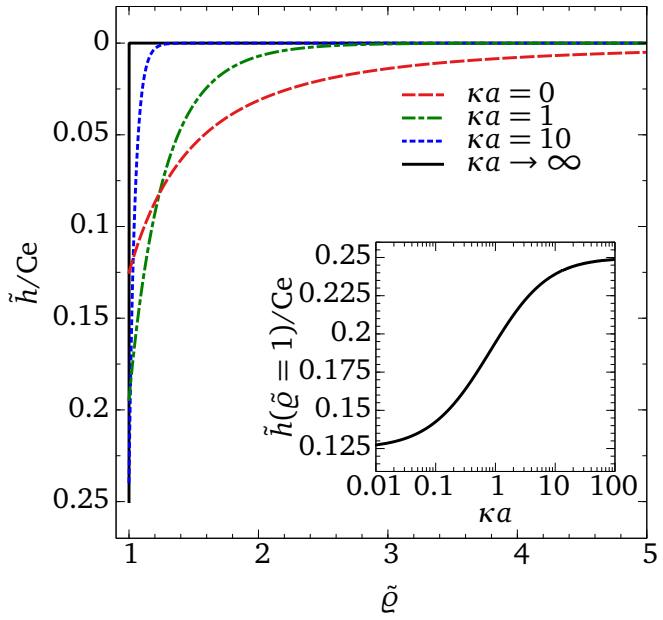

Abbildung 3.5.: Plot of the first-order interfacial deformation $\frac{\tilde{h}}{\mathrm{Ce}} = \tilde{\mathfrak{h}}$ (in Ce) over the dimensionless distance $\tilde{\varrho}$ for different values of the dimensionless Debye length [see equation (3.88)]. Inset: Dipping depth [see equation (3.97)] of the particle as a function of the Debye length [reprinted with permission from APS, Phys. Rev. Fluids 3 (2018), Eigenbrod et al. (2018)].

Since $f(\theta, \pi/2) = f(\theta, 3\pi/2) = 0$, $\tilde{\psi}_{(1)}$ is identically zero at the boundaries and therefore zero everywhere at the undeformed fluid interface. Consequently, the $O(\beta)$-correction of the interfacial deformation vanishes

$$\tilde{\mathfrak{h}}_{(1)} = 0. \tag{3.96}$$

The interfacial deformation up to $O(\beta)$ for different values of the Debye length is shown in figure 3.5 [see equation (3.88) with $\tilde{h} = \mathrm{Ce}\,\tilde{\mathfrak{h}} + O(\mathrm{Ca}^2, \mathrm{Ce}^2, \beta^2)$]. In agreement with physical intuition, the deformation of the fluid interface strongly depends on the Debye length. In the Smoluchowski limit ($\kappa a \to \infty$), the interfacial deformation occurs on a very short length scale, as already suggested by Foret and Würger (2004) and Danov et al. (2004). For fluids with a permittivity ratio which is no longer small and for $\kappa a \to \infty$, this contribution only affects the interfacial deformation in close proximity of the particle, whereas the long-range deformation is dominated by the force arising inside the non-polar fluid. The interfacial deformation due to the charges at the particle-non-polar fluid boundary is shown to scale like $\tilde{h} \propto \tilde{\varrho}^{-4}$ (see Megens and Aizenberg, 2003; Foret and Würger, 2004; Danov and Kralchevsky, 2006a; Oettel et al., 2006) which is clearly a longer-range deformation as obtained previously in the thin Debye length limit. But in case of $\kappa a \to 0$, we obtain from equation (3.88): $\tilde{h} = \mathrm{Ce}/(8\tilde{\varrho}^2)$, which is a longer-range deformation than in the opposite case for $\kappa a \to \infty$. Even more, for $\kappa a \to 0$ the interfacial deformation induced by the electric double layer is of longer range than the interfacial deformation induced by the non-polar fluid. As the results by Foret and Würger (2004) are valid at large distances, a superposition of both expressions could be suitable to take both the short-range and long-range interfacial deformations into account.

The gradient of the equilibrium potential $\tilde{\psi}$ is linked to the force acting on the particle. It is

therefore evident that the dipping depth decreases with an increasing Debye length. The dipping depth of the particle can be found according to:

$$\tilde{h}(\tilde{\varrho}=1)=\frac{\mathrm{Ce}}{8}\left(1+2\kappa a+4\exp(2\kappa a)\kappa a^2\mathrm{Ei}(-2\kappa a)\right)+O(\mathrm{Ca}^2,\mathrm{Ce}^2,\beta^2). \tag{3.97}$$

The curve corresponding to equation (3.97) is shown in the inset of figure 3.5. The two limiting values can be found via

$$\lim_{\kappa a\to 0}\tilde{h}(\tilde{\varrho}=1)=\frac{\mathrm{Ce}}{8}+O(\mathrm{Ca}^2,\mathrm{Ce}^2,\beta^2),\ \lim_{\kappa a\to\infty}\tilde{h}(\tilde{\varrho}=1)=\frac{\mathrm{Ce}}{4}+O(\mathrm{Ca}^2,\mathrm{Ce}^2,\beta^2). \tag{3.98}$$

3.4 Discussion

3.4.1 Validity range of the theory for the electrophoretic mobility

The validity range of our theory for the electrophoretic mobility of interfacial particles is discussed for three different impact parameters. First, the effect of higher applied electric field is reviewed on the basis of experimental observation for bulk particles. The effect of large ζ-potentials on the electrophoretic mobility of interfacial particles is discussed subsequently. Finally, the errors introduced by limiting the description to a first-order perturbation around a contact angle of 90° are estimated.

We considered a weak applied electric field which allowed us to derive the present set of governing equations based on a perturbation approach around the equilibrium state (see appendix A). Consequently, we obtained a linear relationship between the particle velocity and the electric field, see equation (3.1). Whenever the applied electric field is sufficiently strong, a second cloud of counterions (outside the EDL) is induced because of concentration polarization (Barany, 2009). In other words, the stronger applied electric field induces a variation of the electrolyte concentration outside the Debye layer leading to a third-order correction to the electrophoretic velocity (Shilov et al., 2003; Barany, 2009), i.e.,

$$U=\eta^{(1)}E_\infty+\eta^{(3)}E_\infty^3+O(E_\infty^5). \tag{3.99}$$

Barany (2009) has presented experimental results to identify the range of validity of the weak-field approximation. Among others, graphite and γ-Al_2O_3 particles in high electric fields were studied and the weak-field approximation was found to be valid up to 50 V/cm and 200 V/cm, respectively, for thin Debye layers. Zhang et al. (2018) measured the electrokinetic velocity of polystyrene particles attached to a 1 mM NaCl-air interface employing external electric field strength up to 10 V/cm and observed a linear relation between the velocity and the electric field strength. The applied electric field is an input parameter during experimental verifications or ζ-potential measurements of interfacial particles. Accordingly, assuming a small applied electric field does not strongly limit the practical use of the theory.

Assumption 2, i.e., a small ζ-potential, has been widely discussed in the literature already shortly after the first theoretical works on electrophoretic transport of bulk particles have been published, especially after the publication by Henry (1931). Large ζ-potentials cause a reduction of the

velocity of a particle for moderate Debye parameters $0.2 < \kappa a < 50$ (Overbeek, 1943). In the numerical work of Wiersema et al. (1966), the authors found the highest discrepancy between the linear theory of Henry (1931) and their results to occur at $\kappa a \approx 5$. At this value of the Debye parameter, they showed that the linear theory is valid up to $\tilde{\zeta} := \frac{e\zeta}{k_B T} \approx 1.5$ or $\zeta \approx \pm 37$ mV at room temperature. For different values of κa the range of validity increases. $\zeta \approx \pm 37$ mV, however, includes the range of ζ-potentials of many materials (see e.g., Kirby and Hasselbrink, 2004). It should be noted that in case of a thin Debye layer $\kappa a \to \infty$, for asymptotically high charges of the particle, the shape independence of the electrophoretic mobility obtained by Morrison (1970) is no longer valid (Schnitzer and Yariv, 2012b). However, the commercial ζ-potential measurement apparatus *Zetasizer Nano* by Malvern Instruments Ltd. (2013) makes use of the electrophoretic mobility obtained by Henry (1931) to relate the measured particle velocities to the ζ-potential.

We expect that the previous discussion on the validity of the weak-field approximation and the assumption of small ζ-potentials can be largely transferred to the case of interfacial particles, since the scenario of electrophoretic transport of a spherical particle in the bulk is contained in our analysis as the special case of a flat fluid interface and a contact angle of 90°.

We calculated the electrophoretic mobility of spherical interfacial particles up to the first order in the deviation of the contact angle from 90°. The range of contact angles that is fairly well approximated by our theory is a priori unknown. To check the validity of the first-order approximation, we used the commercial finite-element solver COMSOL Multiphysics® (version 5.3 a; `https://www.comsol.com`) to solve the set of governing equations. The detailed description of the numerical procedure can be found in appendix G by Eigenbrod et al. (2018). The comparison between the theoretical model and the numerical simulations is shown in figure 3.6. In figure 3.6 a), the electrophoretic mobility is plotted against the Debye parameter for different contact angles around 90°. The model clearly predicts the electrophoretic mobility of hydrophilic particles better than that of hydrophobic ones. Over the whole range of contact angles considered, the maximum discrepancy between the numerical results and our model is found to be within 4%. In order to capture the dependency of the mobility on the contact angle over a broader range, simulations for two specific values of the Debye parameter were performed. The plot in figure 3.6 b) supports the insights from figure 3.6 a). In general, the theory is found to be more accurate for small Debye lengths. Interestingly, the theory is still accurate even for very small contact angles. The deviation between the theoretical and the simulation results is found to be smaller than 4% even for $\Theta = 5°$, while the deviations between theory and simulations become larger for hydrophobic particles. However, when defining the range of validity of the theory by demanding deviations of less than 5% from the simulation results, our theory is valid up to $\Theta = 130°$. This includes all conventional hydrophobic surfaces, but excludes superhydrophobic materials. We are therefore left with the conclusion that in terms of the contact angle the theory provides a good approximation to the electrophoretic mobility of almost all interfacial particles.

However, some additional effects might limit the application of our theory in the Hückel limit ($\kappa a \to 0$). In this case, the particle can be very small (recall: $\kappa^{-1} \approx O(10^{-8})$ m in case of 1 mM NaCl-water solution), making the effects of Brownian motion more prominent. While the same is true for particles in the bulk, the presence of the fluid interface introduces additional effects, i.e., the Brownian motion of the particle gives rise to capillary waves (e.g., Boniello et al., 2015). Moreover, the relative surface roughness (compared to the size of the particle) of a small particle

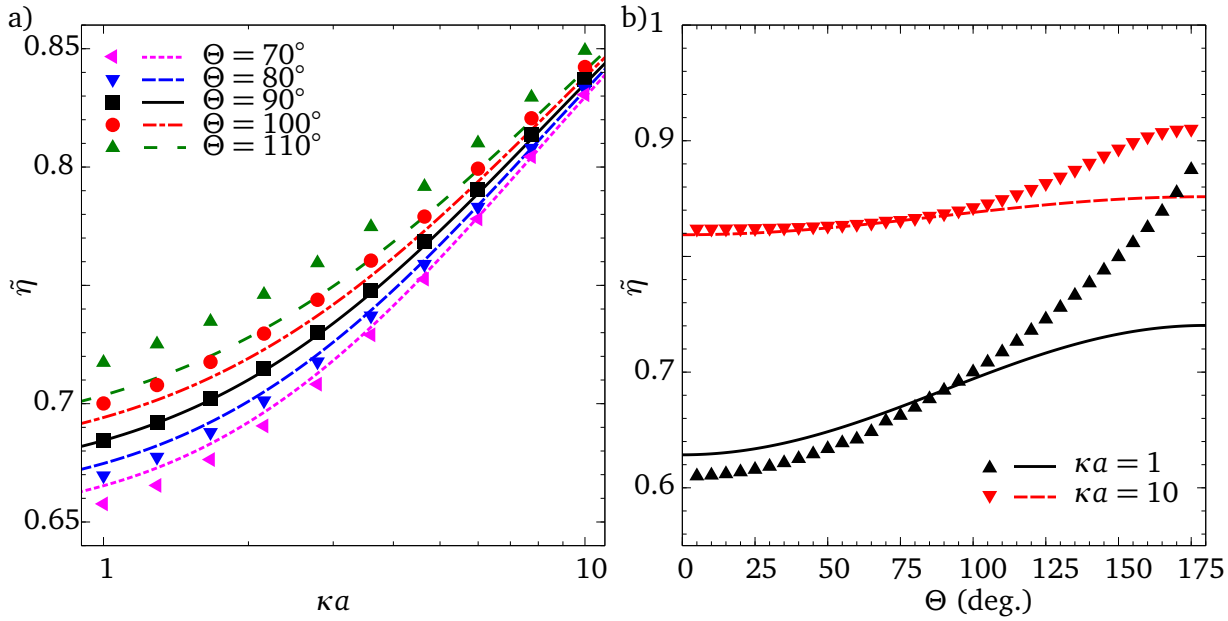

Abbildung 3.6.: Comparison between the numerical results and the predictions of the theory. a) Electrophoretic mobility as a function of the Debye parameter obtained with equation (3.65) and (3.77) for different contact angles compared to numerical simulations. The lines indicate the analytical, the symbols the numerical results. b) Electrophoretic mobility as a function of the contact angle for two different values of the Debye parameter. The lines indicate the analytical, the symbols the numerical results [reprinted with permission from APS, Phys. Rev. Fluids 3 (2018), Eigenbrod et al. (2018)].

can be very significant, leading to a non-circular three-phase contact line at the particle surface. In this case, the zeroth-order solution does not yield a fluid-interface profile as considered in our model.

3.4.2 Impact of the static interfacial deformation on the electrophoretic mobility

We calculated the electrophoretic mobility of interfacial particles on the basis of a flat interface, which effectively is the leading order approximation in both dimensionless numbers related to the interfacial deformation, i.e., Ca and Ce. We have not, however, made any predictions about the impact of the static interfacial deformation on the electrophoretic mobility. In this section, our discussion is limited to thin Debye layers that corresponds to $\kappa a \to \infty$.

As can be shown from figure 3.5, the interfacial deformation caused by the charge of the particle is limited to a region very close to the surface of the particle in case of thin Debye layers. In this case, the interfacial deformation can be approximated through

$$\tilde{h}(\tilde{\varrho}) = \begin{cases} \dfrac{\mathrm{Ce}}{4}, & \text{for } \tilde{\varrho} = 1 \\ 0, & \text{for } \tilde{\varrho} > 1 \end{cases}, \tag{3.100}$$

which is supposed to be valid up to the first order in β, Ca and Ce. In the last equation, the interfacial deformation is limited to the immediate neighborhood of the three-phase contact line and can therefore effectively be seen as a variation of the contact angle at the particle surface,

while the fluid interface remains flat. It is known from literature that the presence of a Debye layer modifies the apparent contact angle (Chou, 2001; Dörr and Hardt, 2014). The variation of the contact angle Θ_{app} can be found through geometrical considerations, leading to

$$\Theta_{\text{app}} = \Theta - \frac{\text{Ce}}{4} + O(\beta^2, \text{Ce}^2). \tag{3.101}$$

Equation (3.101) is valid up to first order in β, since higher order effects in β have not been explored in this work and might lead to correction in the interfacial deformation. In the thin Debye layer limit, the contact angle at the surface of a charged particle decreases with increasing electric capillary number Ce. For example, for $\text{Ce} = 0.1$ and $\Theta = 90°$, the effective contact angle reaches $\Theta_{\text{app}} \approx 88.57°$. Based on this scenario where only the contact angle gets modified but the interface remains flat, the Smoluchowski limit [see equation (3.39)] remains valid. Even at higher orders in Ce the interface deformation should only occur in the upmost vicinity of the particle surface if the thin Debye layer limit applies. Consequently, the Smoluchowski mobility should remain (approximately) valid as long as assumption 4 is reasonably well satisfied.

3.4.3 Application: Separation of Janus particles

It has been reported in the literature that the presence of a fluid interface might cause a migration of particles towards the interface (Ralston and Dukhin, 1999; Fan et al., 2004). Our theory might therefore be relevant for a broad range of electrokinetic processes in which fluid interfaces are present. In this subsection, we focus on the transport of so-called Janus particles, i.e., spherical particles composed of two different hemispheres carrying different material properties.

Janus particles have been intensely studied in recent years due to their various applications, e.g., in e-paper display technologies (Yin et al., 2011) or drug delivery (Yang et al., 2012). In this subsection, we discuss the differences in electrophoretic transport of Janus particles suspended in a bulk liquid and Janus particles attached to a fluid interface. Due to the different wetting properties of the two materials the particle consists of, an interfacial Janus particle will usually align itself at the interface in such a way that only one hemisphere is immersed in the electrolyte solution (e.g., Park et al., 2011; Gao et al., 2014). In this case, the electrophoretic mobility of the particle is equal to that of a homogeneous particle having the same ζ-potential and contact angle as the immersed part of the Janus particle. However, Janus particles suspended in the bulk of a liquid behave differently. The theoretical framework of the electrophoretic motion of bulk-suspended Janus particles is included in the work of Kim and Yoon (2002). Subsequently, we briefly discuss the electrophoretic mobility and the particle alignment in the bulk, to point out the differences to a Janus particle attached to a fluid interface.

We consider a ζ-potential distribution around the particle according to

$$\zeta(\theta) = \begin{cases} \zeta_0, \text{ for } 0 < \theta \leq \frac{\pi}{2}, \\ \alpha\, \zeta_0, \text{ for } \frac{\pi}{2} < \theta \leq \pi, \end{cases} \text{, with } -1 \leq \alpha \leq 1. \tag{3.102}$$

Following Kim and Yoon (2002), the ζ-potential distribution has to be expanded in terms of the first three ($l = 0, 1, 2$) spherical harmonics, according to equations (3.69) - (3.72), since higher-order terms do not contribute to the electrophoretic mobility. Further, the terms with

$l = 0$ and $l = 2$ solely contribute to the translational mobility, whereas $l = 1$ influences the rotation of the particle, i.e., the alignment with the electric field. After some calculation, the translational electrophoretic mobility is found

$$\tilde{\eta}_{\text{Janus}} = \frac{1+\alpha}{2}\tilde{\eta}_0, \tag{3.103}$$

with $\tilde{\eta}_0$ from equation (3.65). In other words, the electrophoretic mobility is identical to that of a homogeneous particle with the average value of the ζ-potential, clearly in agreement with physical intuition. For $\alpha = -1$, the mobility vanishes. In this case, the particle will not exhibit any steady-state translation but align itself in the electric field through rotation. By contrast, if the particle gets attached to a fluid interface, its electrophoretic mobility is given by equations (3.65) and (3.77), where the ζ-potential of the hemisphere immersed in the electrolyte solution is of decisive interest. This means that in contrast to the case of a fully immersed particle, an interfacial particle translates along the interface if $\zeta_0 \neq 0$. More generally, electrophoresis of particles attached to a fluid interface enables separation processes that are not possible in the bulk of a liquid. In the bulk, a Janus particle translates with a velocity corresponding to its average ζ-potential, which makes the separation of different particles with the same average ζ-potential impossible. Electrophoretic transport along a fluid interface, however, enables the separation of different Janus particles if only the ζ-potentials of the hemispheres immersed in the electrolyte are different.

3.5 Summary & Outlook

In this chapter, we have studied the electrophoretic motion of a single neutrally buoyant particle attached to a fluid interface in case of vanishing viscosity and permittivity ratios. Along with that, the deformation of the fluid interface due to the Debye layer around the particle was analyzed. The analysis is based on combined perturbation expansions in the capillary number, the electric capillary number, and the deviation of the contact angle at the particle surface from 90°. In the leading order perturbation, corresponding to a flat fluid interface, we found a generalization of the Smoluchowski mobility for particles of arbitrary shape. As a consequence, the Smoluchowski limit holds for spherical particles independently of the contact angle at the particle surface. The overall interfacial deformation is a superposition of a dynamic (due to hydrodynamic stress) and a static (due to electrostatic stress) deformation. Assuming a mirror-symmetric shape of the particle with respect to the plane perpendicular to the direction of motion, we found that the motion of the particle (controlled by the capillary number Ca) does not contribute to the interfacial deformation, no matter what the Debye layer thickness is. In order to compute the electrophoretic mobility for arbitrary values of the Debye layer thickness, we considered a spherical particle with a contact angle in the vicinity of 90°. Hydrophobic particles have a higher electrophoretic mobility than hydrophilic ones. Further, the static interfacial deformation was computed. From the evolution of the shape of the fluid interface the dipping depth of the particle can be calculated, taking values of $a\text{Ce}/4$ and $a\text{Ce}/8$ for thin and thick Debye layers, respectively, in which a denotes the radius of the spherical particle and Ce the electric capillary number. Our results further indicate that even when gravity is neglected, a long-range capillary interaction between two particles [as observed from the experimental results in Nikolaides et al. (2002) and

Aveyard et al. (2002)] is still possible if the Debye length is large compared to the particle radius. Moreover, we discussed the influence of the electrodipping effect on the electrophoretic mobility. In the case of a small Debye length we found that the Smoluchowski limit should remain valid even for a deformed fluid interface, since the interface deformation is equivalent to a change in the contact angle at the particle surface. We also examined the validity limits of our model. We especially considered the influence of strong applied fields, large ζ-potentials and contact angle deviations from 90°. The influence of the contact angle was studied by comparing the analytical results to the results of numerical simulations for Debye parameters κa taking values between 1 and 10. For contact angles on the particle smaller than 130°, the maximum deviation between the analytical and the numerical results are limited to 5%, which leaves us with the conclusion that our theory is sufficiently accurate for almost all practically relevant contact angles.

The results may find applications in different contexts. First, they could help understanding the response of soft matter systems with interfacial particles such as Pickering emulsions or liquid marbles to electric fields. An overview of the response of particle-laden drops under electric fields was given by Dommersnes and Fossum (2016). For example, our analysis could be relevant for the electric-field induced coalescence of particle-covered water drops, as reported in Chen et al. (2013). Second, we provided the theoretical background that enables the separation of Janus particles, with two hemispheres carrying the same ζ-potential in magnitude but of opposite sign.

In further studies, the electrophoretic motion of interfacial particles should be studied experimentally. It is worth mentioning that a few scientists have measured the electrokinetic velocities of interfacial particles (Lee and Li, 2006; Zhang et al., 2018), without focusing on the electrophoretic mobility of the particles. Instead, the electrophoretic velocity of the particle superposed with the electro-osmotic velocity of the electrolyte has been measured. Due to a different setup, the experimental results are not consistent: While Lee and Li (2006) obtained a smaller electrokinetic velocity of interfacial particles compared to bulk particles in an open channel, Zhang et al. (2018) obtained the opposite behavior in a closed channel. The inconsistencies are due to the difference in the induced electro-osmotic flow of the electrolyte. Furthermore, Zhang et al. (2018) studied the influence of the size of the particles on the electrokinetic velocity and obtained that bigger particles ($2a = 10\ \mu$m) are less mobile than smaller particles ($2a = 3\ \mu$m). The authors claimed that the dependency of the electrokinetic velocity on the size of the particle is a consequence of a higher Stokes drag in the liquid phase, which is not in agreement with our theory, since the size of the particle increases both the hydrodynamic drag and the electrostatic driving force equally (if $\kappa a \to \infty$). It is worth mentioning that the same size dependency of the electrophoretic mobility has been measured at water-dodecane interfaces. In contrast, in the numerical work by Wang et al. (2018), the authors obtained that larger interfacial particles have a higher electrokinetic mobility than smaller particles attached to water-oil interfaces. Most surprisingly, the work by Zhang et al. (2018) and Wang et al. (2018) was published by the same corresponding author, without mentioning the respective other work. The physical explanation of the size dependency of the electrophoretic mobility in both papers is a clear contradiction to the explanation in the respective work. Referring both experimental papers by Zhang et al. (2018) and Lee and Li (2006), the authors did not mention the presence of a gel bridge, commonly used to shield the electrodes from the region of interest and avoid the production of bubbles through electrolysis (Takamura et al., 2003) and a spatial change in the pH-value inside the electrolyte (Persat et al., 2009a,b), that occurs even in case of relatively small applied electric fields. Given

the previous discussion, there is still a lack of reliable experiments focusing on the measurement of the electrophoretic mobility of interfacial particles.

4 Effective interfacial viscosities of a particle-laden interface in the dilute limit

In the last chapter, we have studied the effect of a fluid interface on the motion of a single charged particle driven by an applied electric field. In this chapter we go along a different route and assume the presence of a large number of particles attached to a fluid interface of a moving two-fluid system. Hereby, we do not specify the reasons of fluid motion but focus on the effect of the presence of particles on the flow properties of the multiphase system. We aim to answer the following questions: Does the presence of interfacial particles affect the flow of a multiphase system? How big is the effect of the wetting properties of the particles on the global properties of the flow?

In many engineering applications flows consist of more than a single phase. The presence of particles, droplets or bubbles dispersed in the bulk of a moving fluid makes the physical description of the system considerably more difficult, compared to the flow of a single-phase system. Neglecting the dispersion of bubbles, three other scenarios are typically distinguished in the literature as summarized in figure 4.1 (Guazzelli and Morris, 2011). A dispersion consisting of solid particles distributed in an outer liquid is called suspension [see figure 4.1 a)]. Common examples of suspensions are landslides, mudflows, magma flows (Mueller et al., 2010), paint flows (Lim and Ahn, 2013) and blood flows (Viallat and Abkarian, 2020), where blood is a typical example to emphasize the complexity of suspensions. On top of the deformability, the complex shape and the high concentration of non-rigid red blood cells, that are suspended in a carrier liquid, the vessels are also deformable. Emulsions, i.e., the dispersion of droplets in a different liquid carrying deviating material properties [see figure 4.1 b)], often occur naturally in food industry, such as in milk (oil in water) or in butter (water in oil) (Shah et al., 2008), but also provide a huge range of applications in biochemistry based delivery processes (Ge et al., 2007; Theberge et al., 2010) and oil or water recovery (Huang and Varadaraj, 1996; Zhang et al., 2013). Aerosols, on the other hand, are dispersions of solid particles or liquid droplets in a gas flow [see figure 4.1 c)]. Familiar examples of aerosols are dust, sprays or exhaust fumes.

Einstein (1906) first concerned with dilute suspensions of spherical particles. As part of his Ph.D. thesis, Einstein (1906) computed the effective (shear) viscosity of a dilute suspension of rigid spherical particles suspended in a Newtonian fluid. More specifically, the presence of particles in a fluid flow was shown to increase the overall energy dissipation in the bulk caused by an additional deformation of the fluid elements in the vicinity of the rigid particles. The additional energy dissipation was attributed to an effective increase in the viscosity. Einstein (1906) computed the rate of viscous dissipation in a large control volume concentric with a single particle and obtained the so-called Einstein viscosity (to be discussed in more detail at the end of this paragraph). It should be noted that the Einstein viscosity allows the computation of the flow of a dilute suspension on a macroscopic level without resolving the dispersed particles inside the liquid, which reduces the analytical/computational effort significantly. Another very large contribution in suspension rheology was made by Batchelor (1970). By averaging the stresses

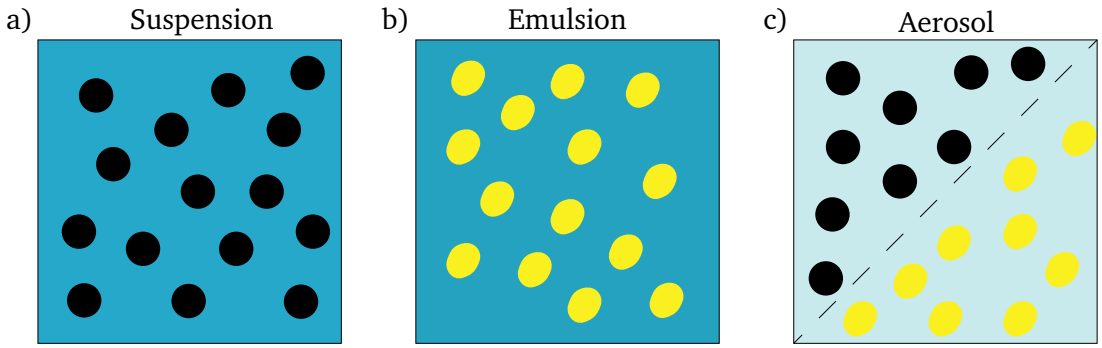

Abbildung 4.1.: Classification of dispersions. a) Suspension: Solid particles are suspended in a surrounding liquid. b) Emulsion: Droplets are dispersed in a different liquid carrying deviating material properties. c) Aerosol: Solid particles or liquid droplets are distributed in a gas.

over the total volume of the suspension, he found an elegant way to determine the effective suspension properties, which is generally valid for arbitrary particle concentrations and shapes. His analytical solutions, however, are limited to dilute suspensions where only a single particle or the interaction of two particles are taken into account. Batchelor and Green (1972) have managed to go beyond that limit and computed the viscosity of suspensions up to the second order in the volume concentration $\phi_\mathcal{V}$. For non-dilute volume concentrations up to $\phi_\mathcal{V} \lesssim 0.25$, the suspension still behaves effectively like a Newtonian fluid (Mueller et al., 2010). In a more concentrated regime, characterized by a rapid growth of the apparent viscosity, an effectively shear-thinning behavior has been reported (Stickel and Powell, 2005; Mueller et al., 2010). Due to the hydrodynamic interactions of sufficiently small particles at higher concentrations, Brownian motion has to be taken into account that can be represented as a stochastic force (Batchelor, 1976, 1977). However, Brownian motion does not affect the apparent viscosity of a bulk suspension consisting of rigid spherical particles in the dilute limit, as shown independently by Hinch and Leal (1972) and Batchelor (1977). Because of the enormous difficulties associated with larger particle concentrations, numerical simulations are often employed (Foss and Brady, 2000; Sierou and Brady, 2001). More recent work dealing with the rheology of bulk suspensions focus on different surface properties of the particles, such as Janus particles with no-slip/slip surfaces (Ramachandran and Khair, 2009) or colloidal particles having a hairy and/or rough surface (Schroyen et al., 2019), as well as active/self propelled particles (Burkholder and Brady, 2020).

Beside transport processes of interfacial particles, such as curvature induced motion (Léandri and Würger, 2013; Galatola and Fournier, 2014), which has been studied quite intensively in recent years, researchers studied static particle-interface interactions, such as particle-laden droplets. These composite structures are often referred to as liquid marbles (Aussillous and Quéré, 2001). It has been observed that interfacial particles mechanically stabilize droplets (e.g., Binks, 2002; Aveyard et al., 2003; Dickinson, 2010; Wu and Ma, 2016; De Corato and Garbin, 2018). The evaporation rate of liquid marbles on surfaces is lower than that of bare droplets, since no liquid is in direct contact with the substrate (McHale and Newton, 2011). Liquid marbles enable the creation of hollow granules (Eshtiaghi et al., 2010) and are usually more mobile on surfaces than bare droplets and can be positioned and transported via gravity (more precisely than a bare droplet since contact angle hysteresis is negligible) (Aussillous and

Quéré, 2001), applied magnetic (Bormashenko et al., 2008) or electric fields (Newton et al., 2007). Due to these unique properties, potential applications are abundant. Liquid marbles are used in pharmaceutical, medical, chemical, and cosmetic industries (Avrămescu et al., 2018). Apart from that, particles attached to fluid interfaces play a role in creating nanostructured materials based on the Langmuir and Langmuir-Blodgett techniques (Park and Advincula, 2011) or in the stabilization of emulsions (Wu and Ma, 2016; Mei et al., 2016).

Probably inspired by the manifold applications of interfacial particles, Lishchuk and Halliday (2009) were the first to calculate the effective dilatational and shear viscosity of a particle-laden interface in the dilute limit (small surface concentration $\phi_L \ll 1$) for particles having a contact angle of $\Theta = 90°$. They used a method similar to that of Einstein (1906). They further verified their results with Lattice-Boltzmann simulations and demonstrated good agreement if $\phi_L \leq 0.15$. Later on, Lishchuk (2014) modeled the effective dilatational viscosity of an interface densely decorated with particles, where Brownian motion was neglected and the contact angle was fixed to $\Theta = 90°$. By employing a toroidal coordinate system, Lishchuk (2016) calculated the effective dilatational surface viscosity in the dilute limit as a function of the contact angle Θ, valid if both phases have a large viscosity contrast. The resulting integral had to be solved numerically.

In order to consider the effective interfacial viscosities, closed-form analytical expressions have to be derived. The case of a particle-laden interface separating two fluids with a large viscosity contrast, valid for a broad range of contact angles Θ, is the subject of the current chapter.

This chapter is subdivided as follows: Before introducing the underlying model assumptions and discussing the governing equations as well as the corresponding boundary conditions in section 4.1, the stresslet is introduced as part of the computation of the Einstein viscosity, revealing its significance in suspension rheology. In section 4.2, a method for the computation of effective interfacial viscosities is presented, on which the asymptotic calculation (section 4.3) is based on. The discussion of potential applications in numerical simulations, the effect of interfacial particles on the stability of a free liquid jet as well as an excursion towards the computation of the trajectories of slightly deformed particles is given in section 4.4. The results are summarized in section 4.5.

Definition of the stresslet and its significance in suspension rheology; Einstein viscosity

The aim of this paragraph is the definition of the so-called stresslet and the computation of the Einstein viscosity. In contrast to the original derivation by Einstein (1906), we follow the more advanced procedure due to Batchelor (1970) in which the stresslet is naturally defined, since it appears during the derivation. In the context of this chapter, we should be content with this less formal definition of the stresslet. The following deduction is part of several textbooks dealing, among others, with suspension rheology (e.g., Guazzelli and Morris, 2011; Kim and Karrila, 2013).

The underlying hypothesis is closely related to that of a continuum (Altenbach, 2012). It is assumed that a particle-laden fluid can macroscopically be represented by an effective fluid (meta fluid) reflecting the averaged hydrodynamic behavior of the suspension. Therefore, a representative volume element is cut out of the suspension [such as sketched in figure 4.1 a)], large enough to contain a statistically significant number of particles but small enough to exclude

the scale of variations of interest from a macroscopic point-of-view (Kim and Karrila, 2013). In this spirit, the volume average of the stress tensor $\langle\boldsymbol{\sigma}\rangle_{\mathscr{V}}$ is defined as

$$\mathscr{V}\langle\boldsymbol{\sigma}\rangle_{\mathscr{V}} = \int\limits_{\mathscr{V}} \boldsymbol{\sigma}\,\mathrm{d}\mathscr{V} = \int\limits_{\mathscr{V}_{\mathscr{F}}} \boldsymbol{\sigma}\,\mathrm{d}\mathscr{V} + \int\limits_{\sum_{i=1}^{N}\mathscr{V}_{\mathscr{P}}^{(i)}} \boldsymbol{\sigma}\,\mathrm{d}\mathscr{V}, \tag{4.1}$$

where we decomposed the total volume $\mathscr{V}$ into the volume of the fluid $\mathscr{V}_{\mathscr{F}}$ and the sum of all particle volumes $\sum_{i=1}^{N}\mathscr{V}_{\mathscr{P}}^{(i)}$. N denotes the total number of particles. Inside the fluid, the stress tensor is related to the deformation of the fluid elements through equation (2.5). Obviously, equation (4.1) can then be written as

$$\mathscr{V}\langle\boldsymbol{\sigma}\rangle_{\mathscr{V}} = -\mathscr{V}\langle p\rangle_{\mathscr{V}}\boldsymbol{I} + 2\mu\mathscr{V}\langle\boldsymbol{\mathfrak{E}}\rangle_{\mathscr{V}} + \int\limits_{\sum_{i=1}^{N}\mathscr{V}_{\mathscr{P}}^{(i)}} \boldsymbol{\sigma} + p\boldsymbol{I} - 2\mu\boldsymbol{\mathfrak{E}}\;\mathrm{d}\mathscr{V}, \tag{4.2}$$

in which we used the abbreviation $\boldsymbol{\mathfrak{E}} = 1/2(\boldsymbol{\nabla u} + (\boldsymbol{\nabla u})^{\mathscr{T}})$, i.e., the symmetric part of the velocity gradient (known as the rate of strain tensor). For an incompressible fluid, the pressure can be expressed as the average of normal stress components of the stress tensor $p = -(1/3)\mathrm{Tr}(\boldsymbol{\sigma})$ (e.g., Brenner, 1991; Guazzelli and Morris, 2011), in which the operator Tr defines the trace, i.e., the sum of all diagonal elements of a matrix. In absence of volume forces [that cannot be subsumed into the thermodynamic pressure, see equation (2.8)], the Stokes equations read $\boldsymbol{\nabla}\cdot\boldsymbol{\sigma} = 0$ [see equation (2.3)]. The momentum balance inside the particles also read $\boldsymbol{\nabla}\cdot\boldsymbol{\sigma} = 0$, as long as volume forces can be neglected (Batchelor, 1970). The following two identities are valid in the fluid and in the particles and are readily shown (Guazzelli and Morris, 2011; Kim and Karrila, 2013)

$$\mathrm{Tr}(\boldsymbol{\sigma}) = \boldsymbol{\nabla}\cdot(\boldsymbol{\sigma}\cdot\boldsymbol{r}), \qquad \boldsymbol{\sigma} = \boldsymbol{\nabla}\cdot(\boldsymbol{\sigma}\boldsymbol{r}). \tag{4.3}$$

Making use of the these identities, equation (4.2) can be transformed into a sum of integrals evaluated over all particle surfaces:

$$\langle\boldsymbol{\sigma}\rangle_{\mathscr{V}} = -\langle p\rangle_{\mathscr{V}}\boldsymbol{I} + 2\mu\langle\boldsymbol{\mathfrak{E}}\rangle_{\mathscr{V}} + \frac{1}{\mathscr{V}}\boldsymbol{\Sigma}_{\mathscr{B}}^{\mathscr{P}} \tag{4.4}$$

$$\boldsymbol{\Sigma}_{\mathscr{B}}^{\mathscr{P}} = \int\limits_{\sum_{i=1}^{N}\mathscr{A}_{\mathscr{P}}^{(i)}} \boldsymbol{n}\cdot(\boldsymbol{\sigma}\boldsymbol{r}) - \frac{1}{3}(\boldsymbol{n}\cdot\boldsymbol{\sigma}\cdot\boldsymbol{r})\boldsymbol{I} - \mu(\boldsymbol{n}\boldsymbol{u} + \boldsymbol{u}\boldsymbol{n})\;\mathrm{d}\mathscr{A}. \tag{4.5}$$

$\boldsymbol{\Sigma}_{\mathscr{B}}^{\mathscr{P}}$ and $\mathscr{A}_{\mathscr{P}}^{(i)}$ is the excess particle stress in the bulk and the surface of particle i. It is worth mentioning that $\boldsymbol{\Sigma}_{\mathscr{B}}^{\mathscr{P}}$ (effectively) reflects the presence of particles in the fluid, whereas the first two terms in equation (4.4) maintain the same mathematical structure even in absence of particles. In this case, of course, the volume averaging would be performed exclusively over the volume of the fluid. Following Batchelor (1970), the antisymmetric part of equation (4.5) is

closely related to the torque acting on the suspended particles which is neglected throughout this derivation (more details are given in section 4.1). To be more precise, the antisymmetric part of the volume averaged stresses are equal to the antisymmetric part of the integral in equation (4.5) that is equal to the volume averaged torque acting on the particles. The symmetric part, evaluated for a single particle, defines the stresslet:

$$\mathscr{S} = \int\limits_{\mathscr{A}_{\mathscr{P}}^{(i)}} \frac{1}{2}(\boldsymbol{n}\cdot(\boldsymbol{r}\boldsymbol{\sigma})+(\boldsymbol{r}\boldsymbol{\sigma})\cdot\boldsymbol{n}) - \frac{1}{3}(\boldsymbol{r}\cdot\boldsymbol{\sigma}\cdot\boldsymbol{n})\boldsymbol{I} - \mu(\boldsymbol{n}\boldsymbol{u}+\boldsymbol{u}\boldsymbol{n})\ \mathrm{d}\mathscr{A}. \tag{4.6}$$

When assuming that the stresslet of every particle is in the same mathematical form, which is approximately valid whenever the volume concentration of the particles inside the fluid is small enough, the symmetric portion of the surface integral from equation (4.5) equals N-times the stresslet of a single particle. With the help of the volume concentration $\phi_{\mathscr{V}} = N\mathscr{V}_{\mathscr{P}}^{(i)}/\mathscr{V}$ we obtain

$$\langle\boldsymbol{\sigma}\rangle_{\mathscr{V}} = -\langle p\rangle_{\mathscr{V}}\boldsymbol{I} + 2\mu\langle\boldsymbol{\mathfrak{E}}\rangle_{\mathscr{V}} + \frac{3}{4\pi a^3}\phi_{\mathscr{V}}\mathscr{S}. \tag{4.7}$$

The stresslet is closely related to an additional energy dissipation caused by the presence of particles in a bulk (Batchelor, 1970) and reads for a spherical particle of radius a in linear shear flow $\mathscr{S} = (20/3)\pi\mu a^3\langle\boldsymbol{\mathfrak{E}}\rangle_{\mathscr{V}}$ (Batchelor, 1970; Guazzelli and Morris, 2011; Kim and Karrila, 2013). Finally, the effective viscosity of a dilute bulk suspension of spherical particles can be computed leading to the Einstein viscosity μ_E

$$\langle\boldsymbol{\sigma}\rangle_{\mathscr{V}} = -\langle p\rangle_{\mathscr{V}}\boldsymbol{I} + 2\mu_E\langle\boldsymbol{\mathfrak{E}}\rangle_{\mathscr{V}}, \qquad \mu_E = \mu\left(1+\frac{5}{2}\phi_{\mathscr{V}}\right). \tag{4.8}$$

The stresslet also takes a major role in the computation of the effective interfacial viscosities of particle-laden interfaces, as shown later in this chapter.

4.1 Model assumptions

We consider a particle-laden, infinitesimally thin fluid interface [so-called dividing surface or Gibbs interface (Slattery et al., 2007)], having N identical colloids (radius a) with a contact angle Θ attached to it. We assume an 'ideal' [massless/incompressible with vanishing surface stresses (Wang and Oberlack, 2011)] fluid interface, which is commonly assumed in the absence of surfactants or impurities (e.g., Brenner, 1991). We aim at computing the interfacial viscosities arising through the presence of the interfacial particles as a function of the contact angle Θ with the help of a homogenization method, where the particle-laden interface is represented by a homogeneous and compressible Newtonian interface [so-called Boussinesq-Scriven interface (Boussinesq, 1913; Scriven, 1960)] having effective viscosities (figure 4.2, top left and top right), analogously to the derivation of the Einstein viscosity.

In general, hydrodynamic interparticle interactions (at high particle concentrations), Brownian translational (Toro-Mendoza et al., 2017) and rotational motion (Stocco et al., 2019) as well

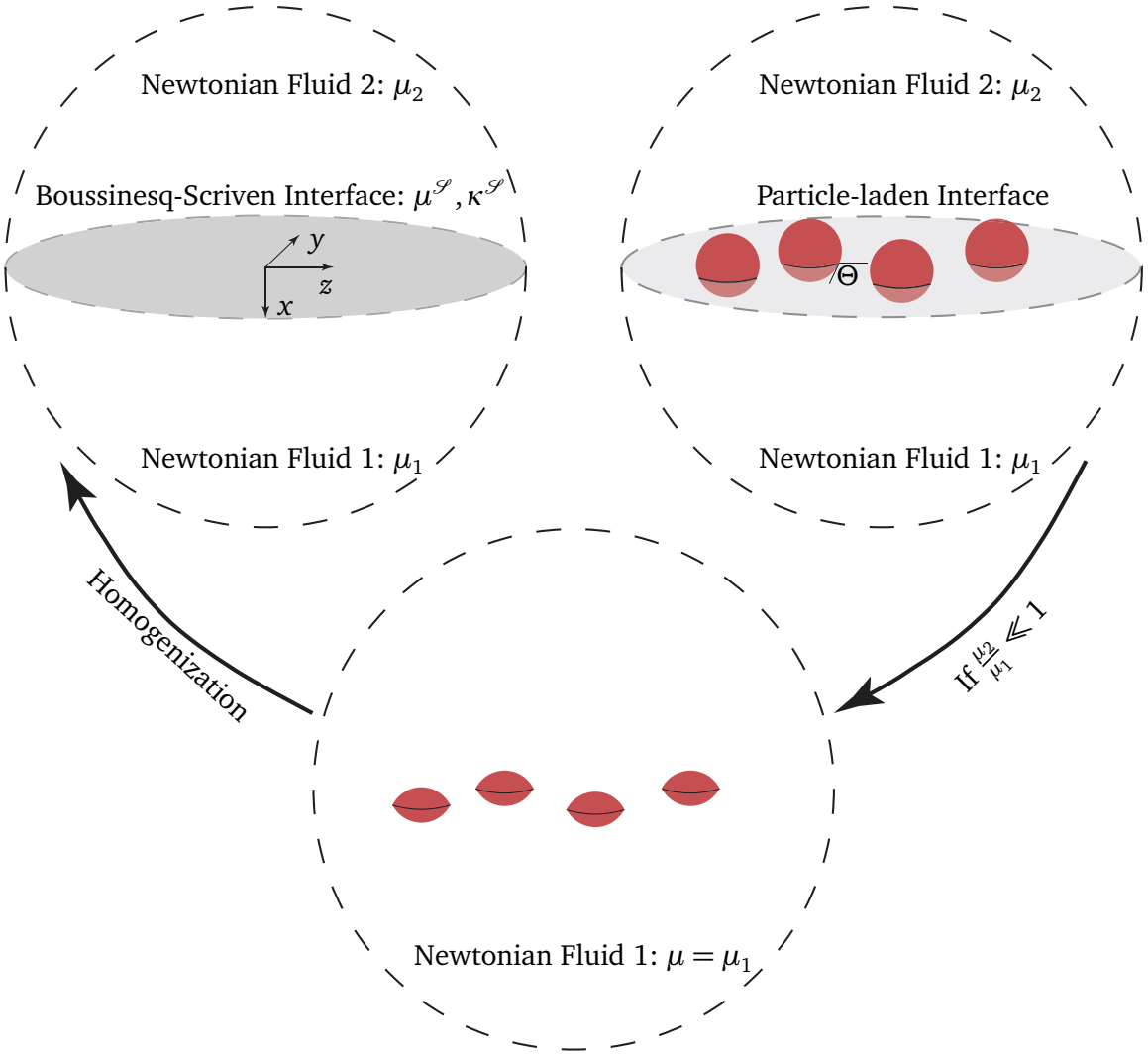

Abbildung 4.2.: Visualization of the similarities used for the computation of the effective surface viscosities represented by a Boussinesq-Scriven constitutive law (top left), see equation (4.42). The basis of the calculation are spherical particles attached to an ideal interface (massless and vanishing stresses) which is equivalent to mirror-fused particles suspended in an infinite bulk fluid if the viscosity ratio μ_2/μ_1 vanishes asymptotically.

as long-range capillary interactions [due to a deformation of the fluid interface through gravity (e.g., Boneva et al., 2007) and/or curvature driven motion (Léandri and Würger, 2013; Galatola and Fournier, 2014)] bring along many complications that leave us with a very complex problem that is usually inaccessible to analytical methods. To keep the problem tractable, the following assumptions are introduced, to be discussed in more detail subsequently:

1. Both fluid phases are Newtonian and incompressible;
2. The Reynolds number in phase 1 is small, i.e., $\mathrm{Re}_1 \ll 1$;
3. The radius of curvature of the fluid interface separating both phases is much larger than the characteristic size a of the particles and the capillary number Ca is sufficiently small;
4. The viscosity ratio between both phases vanishes asymptotically, i.e., $\mu_2/\mu_1 \to 0$;
5. The interfacial particles are neutrally buoyant, rigid, of spherical shape with radius a, while the fluid interface assumes a contact angle of Θ on the particle surface;

6. The interfacial suspension is dilute;
7. Brownian motion is negligible;
8. No external force or torque is applied to the particles and the Stokes numbers reflecting the relaxation time scales for the linear and angular momentum of the particles are sufficiently small.

Even though assumption 1 is a very common assumption in fluid mechanics, it can be violated if particles are suspended in the bulk phase. A sufficiently high concentration of particles is needed to lead to an effectively non-Newtonian rheological behavior (Stickel and Powell, 2005), while even a low concentration of rigid particles in a bulk can lead to an apparent volume viscosity, reflecting compressible behavior in both phases (Brady et al., 2006). The results by Brady et al. (2006) might go against the intuition in which incompressible particles suspended in an incompressible fluid should effectively not provide a compressible rheological behavior. However, their theoretical analysis reveals the counter-intuitive result. Thus, it is assumed that no particles are suspended in the bulk of the fluids. Assumption 2 simplifies the momentum balance by neglecting any transient and convective terms as discussed in section 2.1.1. For small capillary numbers Ca, the stress balance at the interface can be expanded into a perturbation series in Ca, as shown in section 3.1.1. As long as the radius of curvature of the interface is much larger than the characteristic size of a particle (assumption 3), the curvature of the interface can asymptotically be neglected in the zeroth order of Ca. Assumption 4 is a reasonable approximation for any liquid-gas system, given the discussion in the previous chapter. When assuming that the spherical particles are neutrally buoyant and rigid, the fluid interface remains flat even if particles are attached to it (assumption 5). Generally, fluid interfaces are free of shear stresses (if no Marangoni stresses are present) and together with assumption 3, the interface therefore has all properties of a symmetry plane (a further discussion is given in chapter 3). Consequently, the velocity and pressure field around the particles can be calculated by replacing the interfacial particles with particles consisting of two fused mirror-reflected spherical caps in an unbounded fluid, as shown in figure 4.2 (top right and bottom). This kind of symmetry argument has already been applied in chapter 3, and, among others, in the numerical calculation of the effective dilatational viscosity of particle-laden interfaces (Lishchuk, 2016). Consequently, the upper phase (phase 2) does not affect the motion of the interfacial particles. The effective interfacial properties are therefore solely determined by the stresses in fluid phase 1. From now on, all material properties appearing in the equations correspond to phase 1 and we suppress the subscripts.

As already discussed, interfacial particles may interact through different mechanisms, e.g., through hydrodynamic interactions due to the mean relative velocity of the particles or through velocity fluctuations due to Brownian motion (Batchelor and Green, 1972; Batchelor, 1976, 1977). Furthermore, it has been shown that interfacial particles can execute an oscillating translational (Toro-Mendoza et al., 2017) and rotational (Stocco et al., 2019) motion normal to the interface from which the resulting capillary waves induce an interaction. A particle-particle interaction is also induced by the dynamic interfacial deformation of particles moving along a fluid interface with a constant velocity (Dörr and Hardt, 2015). Even in static cases, a charged particle leads to a deformation of the fluid interface as shown in section 3.3.2 that implies a capillary interaction between neighboring particles. Naturally, all of these interactions decay with the interparticle distance. In a similar way as in the computation of the Einstein viscosity of a bulk

suspension we assume that the interparticle distance is large enough to render these interactions negligible (assumption 6). Therefore, the perturbation velocity field due to the presence of a particle does not influence neighboring particles. It should be noted that Hinch and Leal (1972) and Batchelor (1977) have shown that the dilute-limit solution by Einstein (1906) holds even in the presence of Brownian motion. However, this general statement cannot be made in case of interfacial particles, due to the capillary waves mentioned above. Even in absence of interparticle interactions, capillary waves influence the flow around the particles significantly and probably disables an analytical treatment. Brownian motion is therefore neglected (assumption 7). When no external force or torque is applied to the particles (e.g., through an external electric field as discussed in the previous chapter) and inertial effects (in both, the fluid and the particle motion) are neglected, the particles follow the flow in such a way that the sum of the force/torque due to the translation/rotation of a particle and the force/torque induced by translational/rotational velocity of the surrounding fluid are identically zero (assumption 8). As a prominent example, for a single spherical particle suspended in an unbounded Newtonian fluid and subjected to an arbitrary flow field, it is known that the translational and rotational velocity of the particle coincides with that of the applied velocity field (Happel and Brenner, 2012; Kim and Karrila, 2013).

Before proceeding, we comment on the surface concentration defined by Lishchuk and Halliday (2009), i.e.,

$$\phi_L = \frac{N\pi a^2}{A}. \tag{4.9}$$

A is the total area of the fluid interface, N the number of particles attached to the interface and a the radius of the particles. The authors kept the definition from equation (4.9) when computing the dilatational viscosity as a function of the contact angle (Lishchuk, 2016). However, for contact angles deviating from $\Theta = 90°$, the area fraction of the fluid interface cutting through the particle is smaller than that and given by

$$\phi = \frac{N\pi a^2[1-\cos^2(\Theta)]}{A}. \tag{4.10}$$

We later compare the semi-analytical results by Lishchuk (2016) to our theoretical results and therefore have to keep both definitions in mind. Apart from that, we do not use the definition from equation (4.9).

4.1.1 Governing equations and boundary conditions

As already pointed out when discussing the underlying assumptions, particles at ideal interfaces can be represented by mirror-fused particles in a bulk fluid, see figure 4.2 (top right and bottom). We therefore describe the governing equations and the corresponding boundary conditions referring to mirror-fused particles as shown at the bottom of figure 4.2.

The governing equations are the Stokes equations (see section 2.1.1), reading

$$\boldsymbol{\nabla} p_{\mathrm{tot}} = \mu \boldsymbol{\nabla}^2 \boldsymbol{u}_{\mathrm{tot}}, \qquad \boldsymbol{\nabla} \cdot \boldsymbol{u}_{\mathrm{tot}} = 0, \tag{4.11}$$

in which p_{tot} is the total thermodynamic pressure, $\boldsymbol{u}_{\text{tot}}$ the total velocity field, and μ the viscosity (referring to phase 1). Here, $\boldsymbol{u}_{\text{tot}} = \boldsymbol{u}^{\infty} + \boldsymbol{u}$ is the superposition of an applied velocity field $\boldsymbol{u}^{\infty}$ and a disturbance velocity field $\boldsymbol{u}$ occurring through the presence of particles. The same superposition is employed for the pressure. The applied velocity field also satisfies Stokes' equations and is therefore (mathematically) smooth and a Taylor series can be employed around the origin of the coordinate system (shown in figure 4.2, top left), leading up to the first order to (Happel and Brenner, 2012)

$$\boldsymbol{u}^{\infty}(\boldsymbol{r}) \approx \boldsymbol{U}^{\infty} + \boldsymbol{\Omega}^{\infty} \times \boldsymbol{r} + \mathfrak{E} \cdot \boldsymbol{r}, \tag{4.12}$$

in which $\boldsymbol{r}$ is the position vector and $|\boldsymbol{r}| = r$ its length (see section 2.5.2 for more details). As a consequence of the applied velocity field $\boldsymbol{u}^{\infty}(\boldsymbol{r})$, a particle suspended in the bulk might execute a translation and rotation. Additionally, if the suspension is not dilute, perturbations of the velocity field originating from nearby particles might also affect the motion of a dispersed particle. Taking assumption 6 into account and neglecting interparticle effects, the far field boundary condition for every particle is of the same mathematical form. In the following, we represent all non-interacting particles by a single (representative) particle, located at the center of the coordinate system. The Stokes equations are linear and consequently, the boundary conditions at the surface of the representative particle as well as far away from the particle can be written as the difference between the translational and rotational velocity of the particle and the unperturbed, applied and linearized velocity field, leading to

$$\boldsymbol{u}|_{r_{\mathscr{P}}} = \boldsymbol{U}^{\text{eff}} + \boldsymbol{\omega}^{\text{eff}} \times \frac{\boldsymbol{r}}{r} r_{\mathscr{P}} - \mathfrak{E} \cdot \frac{\boldsymbol{r}}{r} r_{\mathscr{P}}, \text{ and } \lim_{r \to \infty} \boldsymbol{u} = 0, \tag{4.13}$$

in which $\boldsymbol{U}^{\text{eff}} = \boldsymbol{U} - \boldsymbol{U}^{\infty}$ and $\boldsymbol{\omega}^{\text{eff}} = \boldsymbol{\omega} - \boldsymbol{\Omega}^{\infty}$ are the effective translational velocity, defined as the difference between the velocity of each particle and the applied translational velocity, and the effective angular (or rotational) velocity, respectively. $r_{\mathscr{P}}$ is the parametrization of the surface of the particle. The effective translational/rotational velocity of the particle is typically obtained through a force/torque balance, as already applied in the context of the previous chapter 3 in order to compute the electrophoretic mobility of a single interfacial particle. It should be noted that the computation of the effective velocities of a non-spherical particle is non-trivial and can often lead to very tedious computations even in case of relatively simple geometries, such as spheroids (Jeffery, 1922). For spheres ($r_{\mathscr{P}} = a$) in an unbounded medium, it is known (Happel and Brenner, 2012; Kim and Karrila, 2013) in the absence of external forces or torques (assumption 8) that $\boldsymbol{U}^{\text{eff}} = 0$ and $\boldsymbol{\omega}^{\text{eff}} = 0$, leading to the boundary condition $\boldsymbol{u}|_a = -\mathfrak{E} \cdot \frac{r}{r} a$ at the surface of the spherical particle. The vanishing of both effective velocities can be shown with the help of equations (2.88) & (2.89), when replacing $\boldsymbol{U}^{\infty}$ and $\boldsymbol{\Omega}^{\infty}$ with $\boldsymbol{U}^{\text{eff}}$ and $\boldsymbol{\omega}^{\text{eff}}$, respectively, and further setting $\mathscr{F} = \mathscr{T} = 0$. Translated to interfacial particles, this corresponds to a sphere having a contact angle of $\Theta = 90°$. For non-spherical particles symmetries break down and an effective translation and rotation could exist, which affects the boundary conditions at the surface of the representative particle and consequently the effective viscosities. We may show in the subsequent paragraph that the effective translational and rotational velocities do not need to be considered in the present study. Consequently, the boundary conditions at the surface of the particle correspond to a pure straining flow field.

Due to assumption 1 and the absence of Marangoni stresses, the rate of strain tensor $\mathfrak{E}$ has to be restricted to ensure a shear-free fluid interface, whereas the restrictions of $\boldsymbol{U}^{\infty}$ and $\boldsymbol{\Omega}^{\infty}$ are of minor interest, since they do not need to be considered in the present context as shown in the subsequent paragraph. The rate of strain tensor then reads

$$\mathfrak{E} = \begin{bmatrix} -\boldsymbol{\nabla}^{\mathscr{S}} \cdot \boldsymbol{u}^{\mathscr{S}} & 0 & 0 \\ 0 & \mathfrak{E}^{\mathscr{S}}_{yy} & \mathfrak{E}^{\mathscr{S}}_{yz} \\ 0 & \mathfrak{E}^{\mathscr{S}}_{yz} & \mathfrak{E}^{\mathscr{S}}_{zz} \end{bmatrix}, \qquad \mathfrak{E}^{\mathscr{S}} = \begin{bmatrix} \mathfrak{E}^{\mathscr{S}}_{yy} & \mathfrak{E}^{\mathscr{S}}_{yz} \\ \mathfrak{E}^{\mathscr{S}}_{yz} & \mathfrak{E}^{\mathscr{S}}_{zz} \end{bmatrix}, \tag{4.14}$$

with $\boldsymbol{\nabla}^{\mathscr{S}} \cdot \boldsymbol{u}^{\mathscr{S}} = \mathfrak{E}^{\mathscr{S}}_{yy} + \mathfrak{E}^{\mathscr{S}}_{zz}$. The boundary conditions for a mirror-fused bulk particle can therefore be written as

$$\boldsymbol{u}|_{r_{\mathscr{P}}} = -\mathfrak{E} \cdot \frac{\boldsymbol{r}}{r} r_{\mathscr{P}}, \text{ and } \lim_{r\to\infty} \boldsymbol{u} = \boldsymbol{0}. \tag{4.15}$$

In summary, equation (4.11) & (4.15) provide a closed equation system to compute the flow around a mirror-fused particle in an unbounded fluid.

Effective translational and rotational motion of a slightly deformed sphere in linear flow and the consequences on the stresslet

As already indicated in the introducing example when computing the Einstein viscosity, the stresslet will be shown to take a major role in the computation of the effective surface viscosities of a particle-laden interface. We may therefore discuss the impact of the effective translational and rotational motion of a slightly deformed sphere on the stresslet of the particle. We assume a parametrization of the surface of the particle up to the second order in a perturbation parameter $\beta \ll 1$ as given in equation (2.63) and let $f(\theta,\varphi)$ and $g(\theta,\varphi)$ take the role of two arbitrary shape functions. The boundary condition at the surface of the particle is given through equation (4.13). The formal procedure for the computation of the boundary conditions using a domain perturbation method up to the first order in β has already been described in section 2.4. The same strategy holds for arbitrary perturbation orders and lead for the given boundary condition to

$$\boldsymbol{u}^{(0)}\big|_{r=a} = -\mathfrak{E} \cdot \frac{\boldsymbol{r}}{r} a, \tag{4.16}$$

$$\boldsymbol{u}^{(1)}\big|_{r=a} = \left(\boldsymbol{U}^{\mathrm{eff},(1)} + \boldsymbol{\omega}^{\mathrm{eff},(1)} \times \frac{\boldsymbol{r}}{r} a\right) - a f(\theta,\varphi)\left(\mathfrak{E} \cdot \frac{\boldsymbol{r}}{r} + \frac{\partial \boldsymbol{u}^{(0)}}{\partial r}\bigg|_{r=a}\right), \tag{4.17}$$

$$\begin{aligned} \boldsymbol{u}^{(2)}\big|_{r=a} &= \left(\boldsymbol{U}^{\mathrm{eff},(2)} + \boldsymbol{\omega}^{\mathrm{eff},(2)} \times \frac{\boldsymbol{r}}{r} a\right) - a f(\theta,\varphi) \frac{\partial \boldsymbol{u}^{(1),\mathrm{T}}}{\partial r}\bigg|_{r=a} \\ &+ a f(\theta,\varphi)\left(\boldsymbol{\omega}^{\mathrm{eff},(1)} \times \frac{\boldsymbol{r}}{r} - \frac{\partial \boldsymbol{u}^{(1),\mathrm{R}}}{\partial r}\bigg|_{r=a}\right) - a f(\theta,\varphi) \frac{\partial \boldsymbol{u}^{(1),\mathrm{S}}}{\partial r}\bigg|_{r=a} \\ &- a g(\theta,\varphi)\left(\mathfrak{E} \cdot \frac{\boldsymbol{r}}{r} + \frac{\partial \boldsymbol{u}^{(0)}}{\partial r}\bigg|_{r=a}\right) - \frac{a^2}{2} f(\theta,\varphi)^2 \frac{\partial^2 \boldsymbol{u}^{(0)}}{\partial r^2}\bigg|_{r=a}. \end{aligned} \tag{4.18}$$

In the latter equations we have used the expansions $\boldsymbol{U}^{\mathrm{eff}} = \beta \boldsymbol{U}^{\mathrm{eff},(1)} + \beta^2 \boldsymbol{U}^{\mathrm{eff},(2)}$, $\boldsymbol{\omega}^{\mathrm{eff}} = \beta \boldsymbol{\omega}^{\mathrm{eff},(1)} + \beta^2 \boldsymbol{\omega}^{\mathrm{eff},(2)}$, as well as $\boldsymbol{u}^{(1)} = \boldsymbol{u}^{(1),\mathrm{T}} + \boldsymbol{u}^{(1),\mathrm{R}} + \boldsymbol{u}^{(1),\mathrm{S}}$, i.e., the decomposition of the first-order velocity

field in translational, rotational and pure straining contributions. Both zeroth-order contributions in the effective translational and rotational velocity correspond to a sphere and are therefore identically zero. It should further be noted that equations (4.16) - (4.18) correspond to the zeroth, first and second order expansion of the velocity (in β), respectively.

The boundary condition from equation (4.16) clearly corresponds to a spherical particle in pure straining flow. Equation (4.17) on the other hand, is a superposition of an undeformed sphere translating and rotating with $\boldsymbol{U}^{\mathrm{eff},(1)}$ and $\boldsymbol{\omega}^{\mathrm{eff},(1)}$, respectively, and a first-order correction term corresponding to a slightly deformed sphere in pure straining flow. However, since a translational and rotational motion of a sphere does not contribute to the stresslet of a sphere it is sufficient to consider the pure straining boundary condition in the first order of our analysis. Analogously, in the second order in β, the first term in round brackets on the right-hand side of equation (4.18) does not need to be considered, since it refers to an undeformed sphere in a constant translational and rotational velocity field. The following two terms, that correspond to the first-order correction of a slightly deformed sphere in pure translational and rotational flow, respectively [for comparison, see equations (3.9) and (4.3) by Brenner (1964)], might possibly contribute to the stresslet. The remaining terms correspond to the a second-order slightly deformed sphere in pure straining flow. Whether the motion of the slightly deformed spherical particle contributes to the effective rheological properties of a suspension in the second order of β, strongly depends on the actual shape of the slightly deformed sphere. In the following, we calculate the first-order effective velocities ($\boldsymbol{U}^{\mathrm{eff},(1)}$, $\boldsymbol{\omega}^{\mathrm{eff},(1)}$) on the basis of a force and torque balance for the most general parametrization of a slightly deformed sphere.

To start with, we may expand the force $\mathscr{F}$ and torque $\mathscr{T}$ acting on the particle in a perturbation sum in β up to the first order leading to

$$\mathscr{F} \approx \mathscr{F}^{(0)} + \beta \mathscr{F}^{(1)}, \tag{4.19}$$

$$\mathscr{T} \approx \mathscr{T}^{(0)} + \beta \mathscr{T}^{(1)}. \tag{4.20}$$

The zeroth-order force and torque acting on a spherical particle translating with a velocity $\boldsymbol{U}$ and rotating with an angular velocity $\boldsymbol{\Omega}$ is readily known from equations (2.88) & (2.89) when replacing $\boldsymbol{U}^{\infty}$ and $\boldsymbol{\Omega}^{\infty}$ with $-\boldsymbol{U}$ and $-\boldsymbol{\Omega}$, respectively:

$$\mathscr{F}^{(0)} = -6\pi\mu a \boldsymbol{U}, \tag{4.21}$$

$$\mathscr{T}^{(0)} = -8\pi\mu a^3 \boldsymbol{\Omega}. \tag{4.22}$$

The first-order contribution of the force and torque can be decomposed in a translational, rotational and straining contribution. The force and torque can be calculated using the following relations, derived on the basis of Lamb's general solution (Brenner, 1964; Kim and Karrila, 2013)

$$\mathscr{F} = -4\pi \boldsymbol{\nabla}(r^3 p_{-2}), \tag{4.23}$$

$$\mathscr{T} = -8\pi\mu \boldsymbol{\nabla}(r^3 \chi_{-2}), \tag{4.24}$$

in which p_{-2} and χ_{-2} are solid spherical harmonics of order -2 as part of Lamb's general solution (see section 2.3). We use the solution of the Stokes equations for pure straining flow, derived in appendix B, and find the following first-order corrections of the force and torque after a rather long calculation

$$\mathscr{F}^{(1)} = \mathscr{F}^{(1),\mathrm{T}} + \mathscr{F}^{(1),\mathrm{R}} + \mathscr{F}^{(1),\mathrm{S}}, \tag{4.25}$$
$$\mathscr{T}^{(1)} = \mathscr{T}^{(1),\mathrm{T}} + \mathscr{T}^{(1),\mathrm{R}} + \mathscr{T}^{(1),\mathrm{S}}, \tag{4.26}$$

with

$$\mathscr{F}^{(1),\mathrm{T}} = -6\pi\mu a\left(\boldsymbol{U} f_0 - \frac{1}{10}\boldsymbol{U}\cdot\boldsymbol{\nabla}\boldsymbol{\nabla}\left(r^2 f_2\right)\right), \tag{4.27}$$
$$\mathscr{F}^{(1),\mathrm{R}} = -6\pi\mu a^2\boldsymbol{\Omega}\times\boldsymbol{\nabla}\left(r^2 f_2\right), \tag{4.28}$$
$$\mathscr{F}^{(1),\mathrm{S}} = -4\pi\mu a^2\left(\frac{1}{14}\boldsymbol{\mathfrak{E}} : \boldsymbol{\nabla}\boldsymbol{\nabla}\boldsymbol{\nabla}\left(r^3 f_3\right) - \frac{3}{2}\boldsymbol{\mathfrak{E}}\cdot\boldsymbol{\nabla}\left(r f_1\right)\right), \tag{4.29}$$

and

$$\mathscr{T}^{(1),\mathrm{T}} = 6\pi\mu a^2\boldsymbol{U}\times\boldsymbol{\nabla}\left(r f_1\right), \tag{4.30}$$
$$\mathscr{T}^{(1),\mathrm{R}} = -24\pi\mu a^3\left(\boldsymbol{\Omega} f_0 - \frac{1}{10}\boldsymbol{\Omega}\cdot\boldsymbol{\nabla}\boldsymbol{\nabla}\left(r^2 f_2\right)\right), \tag{4.31}$$
$$\mathscr{T}^{(1),\mathrm{S}} = 4\pi\mu a^3\boldsymbol{\nabla}\times\left(\boldsymbol{\mathfrak{E}}\cdot\boldsymbol{\nabla}\left(r^2 f_2\right)\right), \tag{4.32}$$

in which f_k [$f_k = f_k(\theta,\varphi)$] is the k-th partial sum of the spherical harmonic expansion of the shape function $f(\theta,\varphi)$. Employing a force and torque balance in the first order and setting $\boldsymbol{U} = \beta\boldsymbol{U}^{\mathrm{eff},(1)}$ and $\boldsymbol{\Omega} = \beta\boldsymbol{\omega}^{\mathrm{eff},(1)}$, respectively, we find

$$\boldsymbol{U}^{\mathrm{eff},(1)} = a\left(\boldsymbol{\mathfrak{E}}\cdot\boldsymbol{\nabla}\left(r f_1\right) - \frac{1}{21}\boldsymbol{\mathfrak{E}} : \boldsymbol{\nabla}\boldsymbol{\nabla}\boldsymbol{\nabla}\left(r^3 f_3\right)\right), \tag{4.33}$$
$$\boldsymbol{\omega}^{\mathrm{eff},(1)} = \frac{1}{2}\boldsymbol{\nabla}\times\left(\boldsymbol{\mathfrak{E}}\cdot\boldsymbol{\nabla}\left(r^2 f_2\right)\right). \tag{4.34}$$

It should be noted that these results are valid for an arbitrarily shaped slightly deformed sphere subjected to a linear flow field in the first order of β.

At this point, we are in the position to compute the effective translational and rotational velocity of a mirror-fused particle in the first order of β. The expansion of the function $f(\theta,\varphi) = \sin(\theta)\,|\cos(\varphi)|$ into surface spherical harmonics is given in table 3.1. Since $f_k = 0$, if $k = 2l-1$, the effective translational velocity is identically zero in the first order of β. When inserting $f_2 = -(5/32)[\cos^2(\theta) - 1 + 3(\cos^2(\theta) - 1)\cos(2\varphi)]$ and equation (4.14) into equation (4.34), it also follows that $\boldsymbol{\omega}^{\mathrm{eff},(1)} = 0$. Therefore, up to the second order in β, the effective translational and rotational velocity does not need to be considered during the computation of the effective interfacial viscosities for a particle shape given through $f(\theta,\varphi) = \sin(\theta)\,|\cos(\varphi)|$. It is therefore sufficient to consider pure straining flow [see equation (4.15)].

The results given in equations (4.33) & (4.34) can be used in a different context, i.e., the computation of the trajectory of a slightly deformed spherical particle. An excursion dealing with

the computation of the trajectory of a slightly deformed spherical particle is provided in section 4.4.3.

4.2 Underlying method for the computation of the effective interfacial viscosities

The aim of this section is the introduction of the general train of thought underlying the computation of the effective interfacial viscosities, which is closely related to the work by Batchelor (1970). We refer to figure 4.2 (top left & bottom) and relate the suspension stresses inside the bulk (subscript $\mathscr{B}$) to effective interfacial properties (subscript $\mathscr{S}$).

To start with, we compute the volume averaged stresses $\langle \boldsymbol{\sigma}_i \rangle_{\mathscr{V}}$ referring to the bulk containing mirror-fused particles ($i = \mathscr{B}$, see bottom of figure 4.2) and the configuration reflecting effective interfacial suspension properties ($i = \mathscr{S}$, see top left of figure 4.2). The latter contains a compressible Newtonian interface that is characterized by non-vanishing surface stresses. This leads to

$$\langle \boldsymbol{\sigma}_{\mathscr{B}} \rangle_{\mathscr{V}} = \frac{1}{\mathscr{V}_{\mathscr{B}}} \int_{\mathscr{V}_{\mathscr{B}}} \boldsymbol{\sigma} \, \mathrm{d}\mathscr{V}, \tag{4.35}$$

$$\langle \boldsymbol{\sigma}_{\mathscr{S}} \rangle_{\mathscr{V}} = \frac{1}{\mathscr{V}_{\mathscr{S}}} \left[\int_{\mathscr{V}_{\mathscr{S}}} \boldsymbol{\sigma} \, \mathrm{d}\mathscr{V} + \int_{\mathscr{A}} \boldsymbol{\sigma}_{\mathscr{D}}^{\mathscr{S}} \, \mathrm{d}\mathscr{A} \right], \tag{4.36}$$

in which $\mathscr{V}_i$, $\mathscr{A}$, $\boldsymbol{\sigma}$ and $\boldsymbol{\sigma}_{\mathscr{D}}^{\mathscr{S}}$ are the total volume ($i = \mathscr{B}, \mathscr{S}$), the area of the Boussinesq-Scriven interface, the total bulk stress and the deviatoric interfacial stress, respectively. In view of figure 4.2, it follows that $\mathscr{V}_{\mathscr{B}} = 2\,\mathscr{V}_{\mathscr{S}}$. Batchelor (1970) has shown that the right-hand side of equation (4.35) can be rewritten into a superposition of terms due to the applied velocity field and an additional term reflecting the stresses due the presence of particles $\boldsymbol{\Sigma}_{\mathscr{B}}^{\mathscr{P}}$ [see equation (4.4)]:

$$\langle \boldsymbol{\sigma}_{\mathscr{B}} \rangle_{\mathscr{V}} = -\langle p \rangle_{\mathscr{V}} \boldsymbol{I} + 2\mu \langle \boldsymbol{\mathfrak{E}} \rangle_{\mathscr{V}} + \frac{1}{\mathscr{V}_{\mathscr{B}}} \boldsymbol{\Sigma}_{\mathscr{B}}^{\mathscr{P}}, \tag{4.37}$$

where $\boldsymbol{\mathfrak{E}}$ is the rate of strain tensor [see equation (4.12)] and p the pressure field corresponding to the applied velocity field. The same rationale can be applied to the formulation relying on the Boussinesq-Scriven interface, assuming that the presence of particles solely affects the effective rheological properties of the fluid interface. We have

$$\langle \boldsymbol{\sigma}_{\mathscr{S}} \rangle_{\mathscr{V}} = -\langle p \rangle_{\mathscr{V}} \boldsymbol{I} + 2\mu \langle \boldsymbol{\mathfrak{E}} \rangle_{\mathscr{V}} + \frac{1}{\mathscr{V}_{\mathscr{S}}} \int_{\mathscr{A}} \boldsymbol{\sigma}_{\mathscr{D}}^{\mathscr{S}} \, \mathrm{d}\mathscr{A}. \tag{4.38}$$

To relate the surface stress to the corresponding volumetric quantities, we utilize the two different expressions for the volume averaged stress to compute the total energy dissipation. More precisely, the total energy dissipation due to the Boussinesq-Scriven interface coincides with the energy dissipation due to mirror-fused particles suspended in a bulk. Recalling that $\boldsymbol{\mathfrak{E}}$ and $\boldsymbol{\mathfrak{E}}^{\mathscr{S}}$ are constant tensors, the energy dissipation of the Boussinesq-Scriven interface is the

double contraction (denoted by :) of the last term on the right-hand side of equation (4.38) with $\mathfrak{E}^{\mathscr{S}}$, while the last term on the right-hand side of equation (4.37) double contracted with $\mathfrak{E}$ leads to the volumetric equivalence. We find, after computing the area average of the interfacial energy dissipation

$$\langle \boldsymbol{\sigma}^{\mathscr{S}}_{\mathscr{D}} \rangle : \mathfrak{E}^{\mathscr{S}} = \frac{1}{2A} \boldsymbol{\Sigma}^{\mathscr{P}}_{\mathscr{B}} : \mathfrak{E}. \tag{4.39}$$

Making further use of the results obtained by Batchelor (1970) on the relation between the particle stresses $\boldsymbol{\Sigma}^{\mathscr{P}}_{\mathscr{B}}$ and the stresslet [see equation (4.6)], we obtain

$$\langle \boldsymbol{\sigma}^{\mathscr{S}}_{\mathscr{D}} \rangle : \mathfrak{E}^{\mathscr{S}} = \frac{N}{2A} \mathscr{S} : \mathfrak{E}. \tag{4.40}$$

Since $N/A = \phi / \left(\pi a^2 \left[1 - \cos^2(\Theta) \right] \right)$ [see equation (4.10)], we finally get

$$\langle \boldsymbol{\sigma}^{\mathscr{S}}_{\mathscr{D}} \rangle : \mathfrak{E}^{\mathscr{S}} = \frac{\phi}{2\pi a^2 [1 - \cos^2(\Theta)]} \mathscr{S} : \mathfrak{E}, \tag{4.41}$$

which enables us to calculate the effective interfacial viscosities of a particle-laden interface on the basis of mirror-fused particles in a bulk fluid. The stresslet plays an important role for the computation of the effective surface viscosities, similar to the computation of the effective viscosities in volume suspensions [see equation (4.7)].

The foregoing derivation is still very general, since we have not specified a constitutive equation for the interfacial stresses. As already indicated, we consider a compressible Newtonian interface, which is described by a Boussinesq-Scriven law (Boussinesq, 1913; Scriven, 1960):

$$\boldsymbol{\sigma}^{\mathscr{S}}_{\mathscr{D}} = (\kappa^{\mathscr{S}} - \mu^{\mathscr{S}}) \left(\boldsymbol{\nabla}^{\mathscr{S}} \cdot \boldsymbol{u}^{\mathscr{S}} \right) \boldsymbol{I}^{\mathscr{S}} + 2\mu^{\mathscr{S}} \mathfrak{E}^{\mathscr{S}}. \tag{4.42}$$

$\kappa^{\mathscr{S}}$, $\mu^{\mathscr{S}}$ and $\boldsymbol{I}^{\mathscr{S}}$ are the surface dilatational viscosity, the surface shear viscosity and the surface identity tensor, respectively. As for the constitutive law of a Newtonian fluid in the bulk, it can be shown with the help of the second law of thermodynamics that $\kappa^{\mathscr{S}} \geq 0$ and $\mu^{\mathscr{S}} \geq 0$ (Gatignol and Prud'homme, 2001). Usually $\kappa^{\mathscr{S}} > \mu^{\mathscr{S}}$ in the case of particle-free interfaces, as estimated experimentally (e.g., Fox and Rock, 1946; Maru and Wasan, 1979). Based on the Boussinesq-Scriven law, we write

$$\langle \boldsymbol{\sigma}^{\mathscr{S}}_{\mathscr{D}} \rangle : \mathfrak{E}^{\mathscr{S}} = (\kappa^{\mathscr{S}} - \mu^{\mathscr{S}}) \left(\langle \boldsymbol{\nabla}^{\mathscr{S}} \cdot \boldsymbol{u}^{\mathscr{S}} \rangle \right)^2 + 2\mu^{\mathscr{S}} \left(\langle \mathfrak{E}^{\mathscr{S}} \rangle \right)^2, \tag{4.43}$$

where we have used the short-hand notation $\left(\langle \mathfrak{E}^{\mathscr{S}} \rangle \right)^2 = \langle \mathfrak{E}^{\mathscr{S}} \rangle : \langle \mathfrak{E}^{\mathscr{S}} \rangle$.

4.3 Calculation of the effective surface viscosities

We are now in the position to calculate the effective surface viscosities based on the method described in the previous section. Our general solution strategy is based on the domain perturbation method. To keep the calculation manageable, we limit ourselves to the second-order perturbation

in a small parameter β.

The parametrization of a slightly deformed sphere is given in equation (3.47). With equation (3.47) and (4.15), the boundary condition can be transferred onto an undeformed sphere, following the general outline given in section 2.4. After expanding the velocity and pressure field into a perturbation series in β, we expand all quantities of each order in β in r around $(r-a)$ in a Taylor series. After some rearrangement, the following boundary conditions are obtained:

$$\boldsymbol{u}^{(0)}\big|_{r=a} = -\boldsymbol{\mathfrak{E}}\cdot\frac{\boldsymbol{r}}{r}a, \tag{4.44}$$

$$\boldsymbol{u}^{(1)}\big|_{r=a} = -af(\theta,\varphi)\left(\boldsymbol{\mathfrak{E}}\cdot\frac{\boldsymbol{r}}{r}+\frac{\partial\boldsymbol{u}^{(0)}}{\partial r}\bigg|_{r=a}\right), \tag{4.45}$$

$$\begin{aligned}\boldsymbol{u}^{(2)}\big|_{r=a} = {} & -af(\theta,\varphi)\,\frac{\partial\boldsymbol{u}^{(1)}}{\partial r}\bigg|_{r=a} - ag(\theta,\varphi)\left(\boldsymbol{\mathfrak{E}}\cdot\frac{\boldsymbol{r}}{r}+\frac{\partial\boldsymbol{u}^{(0)}}{\partial r}\bigg|_{r=a}\right)\\ & -\frac{a^2}{2}f(\theta,\varphi)^2\,\frac{\partial^2\boldsymbol{u}^{(0)}}{\partial r^2}\bigg|_{r=a}.\end{aligned} \tag{4.46}$$

Here, the superscript corresponds to the approximation order in β. Clearly, the solution of the Stokes equations satisfying boundary condition (4.44) corresponds to an undeformed sphere in pure straining and is readily known. To proceed, both functions $f(\theta,\varphi)$ and $g(\theta,\varphi)$ [defined in equation (3.48)] are expanded in surface spherical harmonics (f_k and g_k, in which k is the summation index), following equations (3.69) - (3.72). We obtain an infinite sum with $f_{2m-1}(\theta,\varphi)=0, \forall m=1,2,\ldots$ and $f_{2m}(\theta,\varphi)\neq 0, \forall m=0,1,\ldots$. Even though the first-order stresslet can be calculated exactly, as shown in appendix B for an arbitrary slightly deformed sphere, the boundary condition for the second-order solution has to be approximated due to the presence of the term proportional to the normal gradient of $\boldsymbol{u}^{(1)}$ in equation (4.46). We discuss this problem in more detail in section 4.3.3.

For convenience, we may also expand the stresslet into a perturbation series:

$$\mathscr{S} \approx \mathscr{S}^{(0)} + \beta\mathscr{S}^{(1)} + \beta^2\mathscr{S}^{(2)}. \tag{4.47}$$

With the help of equation (4.41) we obtain up to second order in $\beta=\cos(\Theta)$

$$\langle\boldsymbol{\sigma}^{\mathscr{S}}_{\mathscr{D}}\rangle : \boldsymbol{\mathfrak{E}}^{\mathscr{S}} = \frac{\phi}{2\pi a^2}\left[\mathscr{S}^{(0)} + \beta\mathscr{S}^{(1)} + \beta^2\left(\mathscr{S}^{(0)}+\mathscr{S}^{(2)}\right)\right] : \boldsymbol{\mathfrak{E}}, \tag{4.48}$$

if the surface concentration is defined as in equation (4.10). In contrast, by employing the surface concentration defined by Lishchuk and Halliday (2009), we find up to the second order

$$\langle\boldsymbol{\sigma}^{\mathscr{S}}_{\mathscr{D}}\rangle : \boldsymbol{\mathfrak{E}}^{\mathscr{S}} = \frac{\phi_L}{2\pi a^2}\left(\mathscr{S}^{(0)} + \beta\mathscr{S}^{(1)} + \beta^2\mathscr{S}^{(2)}\right) : \boldsymbol{\mathfrak{E}}. \tag{4.49}$$

Again, equation (4.49) is used for verification purposes only, since we prefer using ϕ for the surface concentration. The double contraction product of the stresslet and the rate of strain

tensor is proportional to the square of the surface divergence of the surface velocity as well as to the double contraction of the surface rate of strain tensor. We may write

$$\mathscr{S}^{(0)} : \mathfrak{E} = \pi a^3 \mu \Big[C_1^{(0)} \big(\langle \nabla^{\mathscr{S}} \cdot \boldsymbol{u}^{\mathscr{S}} \rangle \big)^2 + C_2^{(0)} \big(\langle \mathfrak{E}^{\mathscr{S}} \rangle \big)^2 \Big], \tag{4.50}$$

$$\mathscr{S}^{(1)} : \mathfrak{E} = \pi a^3 \mu \Big[C_1^{(1)} \big(\langle \nabla^{\mathscr{S}} \cdot \boldsymbol{u}^{\mathscr{S}} \rangle \big)^2 + C_2^{(1)} \big(\langle \mathfrak{E}^{\mathscr{S}} \rangle \big)^2 \Big], \tag{4.51}$$

$$\big(\mathscr{S}^{(0)} + \mathscr{S}^{(2)} \big) : \mathfrak{E} = \pi a^3 \mu \Big[C_1^{(2)} \big(\langle \nabla^{\mathscr{S}} \cdot \boldsymbol{u}^{\mathscr{S}} \rangle \big)^2 + C_2^{(2)} \big(\langle \mathfrak{E}^{\mathscr{S}} \rangle \big)^2 \Big], \tag{4.52}$$

from which the constants $C_1^{(i)}$ and $C_2^{(i)}$, with $i = 0, 1, 2$, are calculated in the subsequent sections. Using equation (4.43), we may expand $\mu^{\mathscr{S}}$ and $\kappa^{\mathscr{S}}$ as

$$\mu^{\mathscr{S}} \approx \mu^{\mathscr{S}(0)} + \beta \mu^{\mathscr{S}(1)} + \beta^2 \mu^{\mathscr{S}(2)}, \tag{4.53}$$

$$\kappa^{\mathscr{S}} \approx \kappa^{\mathscr{S}(0)} + \beta \kappa^{\mathscr{S}(1)} + \beta^2 \kappa^{\mathscr{S}(2)}. \tag{4.54}$$

By comparing coefficients in equations (4.50) - (4.52), we find the following relations:

$$\mu^{\mathscr{S}} = \frac{\phi \mu a}{4} \Big[C_2^{(0)} + \beta C_2^{(1)} + \beta^2 C_2^{(2)} \Big], \tag{4.55}$$

$$\kappa^{\mathscr{S}} = \frac{\phi \mu a}{2} \left[C_1^{(0)} + \frac{1}{2} C_2^{(0)} + \beta \left(C_1^{(1)} + \frac{1}{2} C_2^{(1)} \right) + \beta^2 \left(C_1^{(2)} + \frac{1}{2} C_2^{(2)} \right) \right]. \tag{4.56}$$

4.3.1 Zeroth-order solution

In this subsection we compute the effective surface viscosities for $\Theta = 90°$. This special case has already been studied by Lishchuk and Halliday (2009) and can therefore be considered as a benchmark for our approach. The stresslet of a spherical particle in a pure straining flow is readily known (e.g., Kim and Karrila, 2013) and therefore the double contraction with the rate of strain tensor from equation (4.14) can be evaluated, leading to

$$\mathscr{S}^{(0)} : \mathfrak{E} = \frac{20\pi}{3} \mu a^3 \Big[\big(\langle \nabla^{\mathscr{S}} \cdot \boldsymbol{u}^{\mathscr{S}} \rangle \big)^2 + \big(\langle \mathfrak{E}^{\mathscr{S}} \rangle \big)^2 \Big], \tag{4.57}$$

from which the constants in equation (4.50) can be read off:

$$C_1^{(0)} = C_2^{(0)} = \frac{20}{3}. \tag{4.58}$$

The zeroth-order interfacial viscosities follow from equations (4.55) & (4.56)

$$\mu^{\mathscr{S}(0)} = \frac{5}{3} \phi \mu a, \tag{4.59}$$

$$\kappa^{\mathscr{S}(0)} = 5 \phi \mu a. \tag{4.60}$$

The zeroth-order solutions are identical to the results reported in Lishchuk and Halliday (2009) and therefore provide verification for the method presented in section 4.2.

Before we proceed to calculate the first-order corrections of the interfacial viscosities, we introduce the Lorentz reciprocal theorem (Lorentz, 1896) as a useful tool for the following analysis.

Application of the Lorentz reciprocal theorem

Following section 2.5, the Lorentz reciprocal theorem reads in absence of any source terms (Lorentz, 1896; Brenner, 1991; Kim and Karrila, 2013)

$$\int\limits_{\mathscr{A}_\mathscr{P}} \boldsymbol{u}\cdot\bar{\boldsymbol{\sigma}}\cdot\boldsymbol{n}\,\mathrm{d}\mathscr{A} = \int\limits_{\mathscr{A}_\mathscr{P}} \bar{\boldsymbol{u}}\cdot\boldsymbol{\sigma}\cdot\boldsymbol{n}\,\mathrm{d}\mathscr{A}, \tag{4.61}$$

in which $(\boldsymbol{u}, \boldsymbol{\sigma})$ and $(\bar{\boldsymbol{u}}, \bar{\boldsymbol{\sigma}})$ satisfy the Stokes equations for the same flow geometry but with different boundary conditions. In this context, $(\bar{\boldsymbol{u}}, \bar{\boldsymbol{\sigma}})$ correspond to a spherical particle with the boundary condition (4.44) and a vanishing velocity field at $r \to \infty$. The surface stress for this case reads $\bar{\boldsymbol{\sigma}}\cdot\boldsymbol{n} = 3\mu a\boldsymbol{\mathfrak{E}}\cdot\frac{\boldsymbol{r}}{r}$ (Happel and Brenner, 2012). Inserting the expression for the surface stress as well as equation (4.44) (here: $\bar{\boldsymbol{u}} = -\boldsymbol{\mathfrak{E}}\cdot\boldsymbol{r}a/r$) into equation (4.61), we get

$$\left(3\mu\int\limits_{\mathscr{A}_\mathscr{P}} \boldsymbol{u}\boldsymbol{n}\,\mathrm{d}\mathscr{A}\right) : \boldsymbol{\mathfrak{E}} = \left(-\int\limits_{\mathscr{A}_\mathscr{P}} \boldsymbol{r}\boldsymbol{\sigma}\cdot\boldsymbol{n}\,\mathrm{d}\mathscr{A}\right) : \boldsymbol{\mathfrak{E}}. \tag{4.62}$$

Since $\boldsymbol{\mathfrak{E}}$ is an arbitrary (but symmetric) tensor, the (symmetric part of the) two terms inside the brackets need to be identical. When calculating the symmetric and traceless part of the terms inside the brackets, we find

$$\begin{aligned}\int\limits_{\mathscr{A}_\mathscr{P}} \frac{3\mu}{2}(\boldsymbol{u}\boldsymbol{n}+\boldsymbol{n}\boldsymbol{u}) - \mu(\boldsymbol{u}\cdot\boldsymbol{n})\boldsymbol{I}\,\mathrm{d}\mathscr{A} \;&=\; -\int\limits_{\mathscr{A}_\mathscr{P}} \frac{1}{2}(\boldsymbol{r}\boldsymbol{\sigma}+\boldsymbol{\sigma}\boldsymbol{r})\cdot\boldsymbol{n} \\ &\quad -\frac{1}{3}(\boldsymbol{r}\cdot\boldsymbol{\sigma}\cdot\boldsymbol{n})\,\boldsymbol{I}\,\mathrm{d}\mathscr{A}.\end{aligned} \tag{4.63}$$

For a rigid particle we have $\boldsymbol{u}\cdot\boldsymbol{n} = 0$. When adding $\int_{\mathscr{A}_\mathscr{P}} \mu(\boldsymbol{u}\boldsymbol{n}+\boldsymbol{n}\boldsymbol{u})\mathrm{d}\mathscr{A}$ to both sides of the last equation, the right-hand side corresponds to the negative stresslet. Therefore, we finally find

$$\mathscr{S} = -\frac{5\mu}{2}\int\limits_{\mathscr{A}_\mathscr{P}} (\boldsymbol{u}\boldsymbol{n}+\boldsymbol{n}\boldsymbol{u})\,\mathrm{d}\mathscr{A}. \tag{4.64}$$

In contrast to equation (4.6), in which the calculation of the stresslet requires detailed information on the velocity and pressure fields around the particle, equation (4.64) only involves an integration of the boundary conditions over the particle surface. It should be noted that the validity of equation (4.64) can be verified with the help of Lamb's general solution (Happel and Brenner, 2012; Kim and Karrila, 2013). After a lengthy calculation the expression of equation (B.35) is recovered.

4.3.2 First-order solution

Equations (4.44) - (4.46) display the successive solution process for slightly deformed spheres, i.e., the n-th order boundary condition is solely determined by the solutions up to $(n-1)$-th order. Therefore, the first-order correction of the stresslet acting on a slightly deformed sphere can be calculated by inserting equation (4.45) in equation (4.64). Alternatively, the stresslet can be calculated according to equation (B.35), but requires the solution of the Stokes equations to first order in β. In appendix B we derive the first-order solution for a slightly deformed sphere in pure straining and provide an expression for the stresslet [see equation (B.37)]. By using these results, we find after a short deduction

$$\mathscr{S}^{(1)} : \mathfrak{E} = 20\pi\mu a^3 \left[\frac{35}{48} \left(\langle \boldsymbol{\nabla}^{\mathscr{S}} \cdot \boldsymbol{u}^{\mathscr{S}} \rangle \right)^2 + \frac{5}{12} \left(\langle \mathfrak{E}^{\mathscr{S}} \rangle \right)^2 \right], \tag{4.65}$$

from which the following coefficients can be read off

$$C_1^{(1)} = \frac{175}{12}, \qquad C_2^{(1)} = \frac{25}{3}. \tag{4.66}$$

The first-order effective surface viscosities then read

$$\mu^{\mathscr{S}(1)} = \frac{25}{12}\phi\mu a, \tag{4.67}$$

$$\kappa^{\mathscr{S}(1)} = \frac{75}{8}\phi\mu a. \tag{4.68}$$

It should be noted that, up to first order in β, both definitions of the surface concentration [equation (4.9) and (4.10)] lead to the same effective viscosities.

4.3.3 Second-order solution

To obtain the second-order solution for the stresslet, we make use of the Lorentz reciprocal theorem from section 4.3.1. The second-order boundary condition at the surface of an undeformed sphere is given in equation (4.46). For reasons that will become clear later, we decompose equation (4.46) into two contributions, a first one proportional to the normal gradient of $\boldsymbol{u}^{(1)}$, and a second one containing all other terms. When employing the reciprocal theorem [equation (4.64)], we start by evaluating the integral over all contributions that are not proportional to the normal gradient of $\boldsymbol{u}^{(1)}$ and find

$$\begin{aligned} \mathscr{S}^{(2)} : \mathfrak{E} &= -\frac{20\pi}{7}\mu a^3 \left[4 \left(\langle \boldsymbol{\nabla}^{\mathscr{S}} \cdot \boldsymbol{u}^{\mathscr{S}} \rangle \right)^2 + 5 \left(\langle \mathfrak{E}^{\mathscr{S}} \rangle \right)^2 \right] \\ &\quad + \frac{5}{2}\mu a \left[\int_{A_{\mathscr{P}}} f(\theta,\varphi) \left[\left. \frac{\partial \boldsymbol{u}^{(1)}}{\partial r} \right|_{r=a} \frac{\boldsymbol{r}}{r} + \frac{\boldsymbol{r}}{r} \left. \frac{\partial \boldsymbol{u}^{(1)}}{\partial r} \right|_{r=a} \right] \mathrm{d}\mathscr{A} \right] : \mathfrak{E}. \end{aligned} \tag{4.69}$$

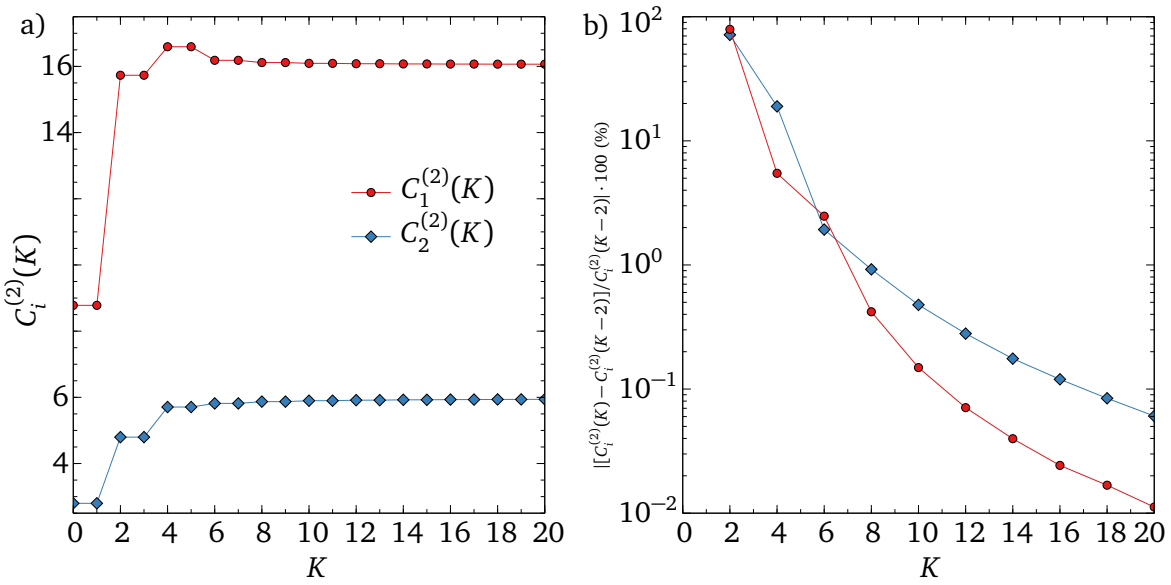

Abbildung 4.3.: Convergence plot showing the dependency of the coefficients $C_i^{(2)}(\ i = 1,2)$ referring to the second-order calculation of the stresslet of a slightly deformed sphere, on the summation limit K. a) Absolute value of $C_i^{(2)}(\ i = 1,2)$ versus summation limit K. b) Relative change of $C_i^{(2)}(\ i = 1,2)$ between $K+2$ and K in percent.

$\boldsymbol{u}^{(1)}$ is written as an expansion in spherical harmonics [see equation (B.34)], reflecting the angular dependence of $f(\theta,\varphi)$. We truncate the infinite sum by setting

$$\boldsymbol{u}^{(1)} \approx \sum_{k=0}^{K} \boldsymbol{u}_k^{(1)}. \tag{4.70}$$

Inserting equation (4.70) into equation (4.69), and evaluating the remaining integral in equation (4.69) for $K = 20$, we find

$$\begin{aligned} \mathscr{S}^{(2)} : \mathfrak{E} \quad \approx \quad & \pi\mu a^3 \Bigg[\frac{1555263045342049}{165476499980288} \left(\langle \boldsymbol{\nabla}^{\mathscr{S}} \cdot \boldsymbol{u}^{\mathscr{S}} \rangle \right)^2 \\ & - \frac{60053874226845}{82738249990144} \left(\langle \mathfrak{E}^{\mathscr{S}} \rangle \right)^2 \Bigg]. \end{aligned} \tag{4.71}$$

With the help of equations (4.50) & (4.52), the second-order coefficients are obtained as

$$C_1^{(2)} \approx \frac{7975319135631907}{496429499940864} \approx 16.065, \quad C_2^{(2)} \approx \frac{1474603377122345}{248214749970432} \approx 5.941. \tag{4.72}$$

To show that the 20 partial sums are sufficient to approximate the velocity field around the particle reasonably well, we plot the constants $C_1^{(2)}$ and $C_2^{(2)}$ as a function of K in figure 4.3. Figure 4.3 a) shows both coefficients as a function of K. The relative error of both coefficients, defined as a relative change in %, decreases with increasing K and falls below 0.1% for $K = 20$, as shown in figure 4.3 b). All calculated coefficients are collected in table 4.1. The second-order

n	$C_1^{(n)}$	$C_2^{(n)}$
0	20/3	20/3
1	175/12	25/3
2	$\frac{7975319135631907}{496429499940864}$	$\frac{1474603377122345}{248214749970432}$

Tabelle 4.1.: Coefficients related to equations (4.50) - (4.52)

correction of the surface viscosities are computed for two different definitions of the surface concentration, i.e., equations (4.9) and (4.10), as follows

$$\mu^{\mathscr{S}(2)} \approx 1.4853\phi\mu a, \quad \text{or} \quad \mu^{\mathscr{S}(2)} \approx -0.1815\phi_L\mu a \tag{4.73}$$

$$\kappa^{\mathscr{S}(2)} \approx 9.5178\phi\mu a, \quad \text{or} \quad \kappa^{\mathscr{S}(2)} \approx 4.5179\phi_L\mu a. \tag{4.74}$$

4.4 Discussion and application

The aim of this section is the discussion of the results obtained for the effective surface viscosities. Furthermore, we compare our theoretical result for the effective surface dilatational viscosity to the semi-analytical solution obtained in a previous work by Lishchuk (2016). After that, we briefly discuss the application of our theory in the context of numerical simulations. Finally, after using our results to study the influence of interfacial particles on the stability of a liquid jet, we briefly discuss the computation of trajectories of a slightly deformed particle subjected to a linear flow field.

With the help of equations (4.53), (4.54) as well as (4.59), (4.60), (4.67), (4.68), (4.73) and (4.74), we may summarize our results for the effective surface viscosities as follows

$$\mu^{\mathscr{S}} \approx \frac{5}{3}\mu a\phi\left(1+\frac{5}{4}\cos(\Theta)+0.8912\cos^2(\Theta)\right), \tag{4.75}$$

$$\kappa^{\mathscr{S}} \approx 5\mu a\phi\left(1+\frac{15}{8}\cos(\Theta)+1.9036\cos^2(\Theta)\right), \tag{4.76}$$

or when using the surface concentration as defined in Lishchuk and Halliday (2009), i.e., equation (4.9),

$$\mu^{\mathscr{S}} \approx \frac{5}{3}\mu a\phi_L\left(1+\frac{5}{4}\cos(\Theta)-0.1089\cos^2(\Theta)\right), \tag{4.77}$$

$$\kappa^{\mathscr{S}} \approx 5\mu a\phi_L\left(1+\frac{15}{8}\cos(\Theta)+0.9036\cos^2(\Theta)\right). \tag{4.78}$$

In figure 4.4 a), a comparison between equation (4.78) and the semi-analytical solution from Lishchuk (2016) is shown. For a broad range of contact angles $\Theta \in [40°; 105°]$ the deviation between the theoretical and the semi-analytical results is less than 5% (dark gray region in figure 4.4 a). The lighter gray areas correspond to a deviation of less than 10%. Similar as in previous studies (Dörr and Hardt, 2015; Dörr et al., 2016), as well as the results from chapter 3, the

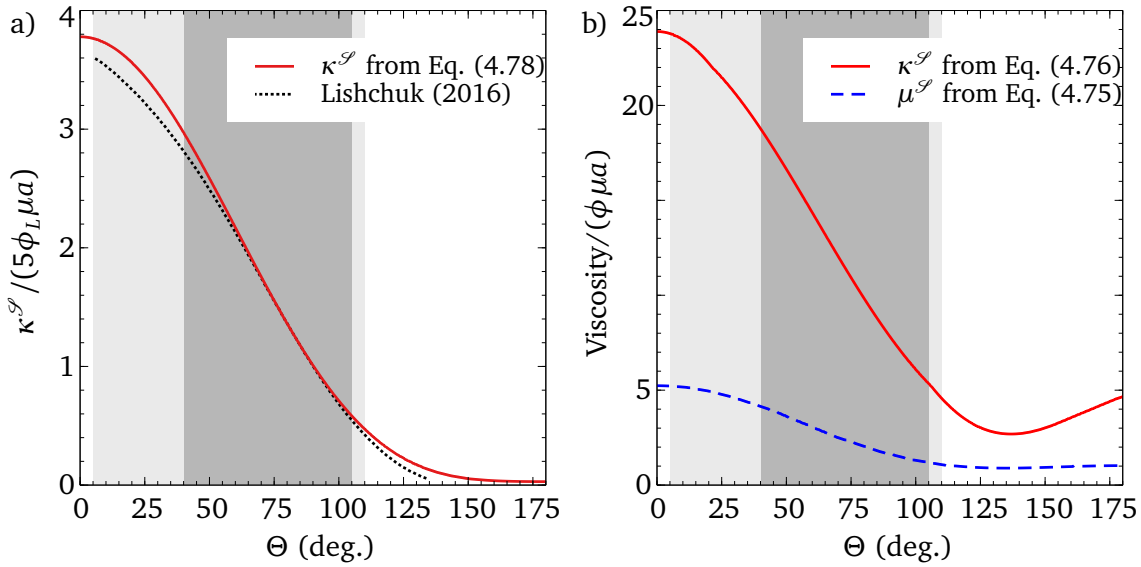

Abbildung 4.4.: a) Comparison between the prediction of equation (4.78) and the semi-analytical solution obtained in Lishchuk (2016). The scaled dimensionless dilatational viscosity is shown as a function of the contact angle Θ, where the definition of surface concentration from equation (4.9) is used. In the dark gray region the deviation between both solutions is smaller than 5%, whereas the light gray region corresponds to deviations smaller than 10%. b) Dimensionless effective dilatational and shear viscosity as a function of the contact angle. In contrast to part a), the physically correct surface concentration as defined in equation (4.10) is used. For the gray regions the same convention as in part a) applies.

domain perturbation method leads to a better agreement with the semi-analytical results for hydrophilic particles than for hydrophobic ones.

In figure 4.4 b), we plot the results of equations (4.75) and (4.76) over the contact angle Θ of the particles. Again, the shaded areas refer to deviations of 5% and 10% between the analytical and the semi-analytical results for the dilatational viscosity. The dilatational viscosity shows a stronger dependence on the contact angle than the shear viscosity and also has a larger magnitude for all contact angles. Clearly, outside the shaded area towards superhydrophobic contact angles, both viscosities behave differently than expected ($\kappa^{\mathcal{S}}, \mu^{\mathcal{S}} \neq 0$, for $\Theta \to 180°$).

Our theoretical model is limited to dilute suspensions in which $\phi \ll 1$. By employing Lattice-Boltzmann simulations, Lishchuk and Halliday (2009) showed that the effective dilatational viscosity for interfacial particles having a contact angle of $\Theta = 90°$ is valid up to surface concentrations of $\phi_L \approx 0.15$. We view this as a rough guideline for the range of validity of our theory for all contact angles. Compared to volumetric suspensions, in which the classic expression by Einstein (1906) is typically valid up to volume concentrations of 0.05 (Guazzelli and Morris, 2011; Mewis and Wagner, 2012), higher-order corrections in the particle concentration appear less important. However, for fluid interfaces densely packed with particles the interfacial viscosities should show the same divergent behavior as known for volumetric suspensions. The dilatational viscosity of a particle-laden interface where the particles have a contact angle of $\Theta = 90°$ was studied by Lishchuk (2014). A divergent behavior similar to that of volumetric suspensions was obtained. We therefore hypothesize that our theoretical results for the dilute

limit provide a lower bound to the effective viscosities and significantly underestimate these, especially for higher surface concentrations. In other words, our results always represent the minimum influence of interfacial particles, a statement of relevance in different applications, to be further discussed in section 4.4.2.

Apart from the dimensionless surface viscosities discussed in figure 4.4 b), two additional dimensionless groups were shown to have an important influence on the evolution of a fluid interface, i.e., the dilatational and shear Boussinesq numbers (Brenner, 1991)

$$B_{\mu^{\mathscr{S}}} = \frac{\mu^{\mathscr{S}}}{\mu L} = \phi\left(\frac{5}{3}+\frac{25}{12}\cos(\Theta)+1.4853\cos^2(\Theta)\right)\frac{a}{L}, \tag{4.79}$$

$$B_{\kappa^{\mathscr{S}}} = \frac{\kappa^{\mathscr{S}}}{\mu L} = \phi\left(5+\frac{75}{8}\cos(\Theta)+9.5178\cos^2(\Theta)\right)\frac{a}{L}, \tag{4.80}$$

in which L is a characteristic dimension of the flow domain. Further, it might be required to evaluate the ratio of both Boussinesq numbers. Up to $O(\cos^2(\Theta))$, we find

$$\frac{B_{\kappa^{\mathscr{S}}}}{B_{\mu^{\mathscr{S}}}} = \frac{\kappa^{\mathscr{S}}}{\mu^{\mathscr{S}}} = 3+\frac{15}{8}\cos(\Theta)+0.6936\cos^2(\Theta). \tag{4.81}$$

Equation (4.81) reveals that the ratio of the surface viscosities varies between 5 and 2.5 in the dark shaded region of figure 4.4, reflecting the range of validity of our theory.

4.4.1 Towards numerical simulations of particle-laden interfaces

To make full use of our theoretical results in numerical simulations involving particle-laden interfaces, the isotropic part of the interfacial stress tensor [i.e., the effective interfacial tension (Brenner, 1991)] has to be considered as well. We follow the general idea described by Bormashenko et al. (2013), in which the effective interfacial tension is defined as the ratio of the total interfacial free energy and the total surface area. We have

$$\mathscr{E}_{\mathrm{sf}} = \gamma_{12}A_{12}+N\left(\gamma_{\mathscr{P}(1)}A_{\mathscr{P}(1)}+\gamma_{\mathscr{P}(2)}A_{\mathscr{P}(2)}\right), \tag{4.82}$$

$$= \gamma_{12}A_{12}+N\left(-\gamma_{12}\cos(\Theta)A_{\mathscr{P}(1)}+4\pi a^2\gamma_{\mathscr{P}(2)}\right), \tag{4.83}$$

in which γ_{12}, A_{12}, $\gamma_{\mathscr{P}(i)}$, $A_{\mathscr{P}(i)}$ and N is the interfacial tension between the two fluids, the area of the interface between the two fluids, the interfacial tension between a particle and phase i, the area between a particle and phase i and the number of interfacial particles, respectively. We further made use of the relation $4\pi a^2 = A_{\mathscr{P}(1)}+A_{\mathscr{P}(2)}$, and Young's law [see equation (2.50)]. The total area of the interface is $A = A_{12}+N\pi a^2(1-\cos^2(\Theta))$, or, when using equation (4.10)

$$A_{12} = A(1-\phi). \tag{4.84}$$

The solid-fluid interfacial area of the portion of the particle immersed in fluid 1 reads

$$A_{\mathscr{P}(1)} = 2\pi a^2(1+\cos(\Theta)). \tag{4.85}$$

After inserting equations (4.84) and (4.85) into (4.83) and making use of equation (4.10), we find:

$$\mathscr{E}_{\mathrm{sf}} = \left[\gamma_{12}(1-\phi) + \phi\left\{-\gamma_{12}\frac{2\cos(\Theta)(1+\cos(\Theta))}{1-\cos^2(\Theta)} + \gamma_{\mathscr{P}(2)}\frac{4}{1-\cos^2(\Theta)}\right\}\right]A. \tag{4.86}$$

The term in square brackets represent the effective surface tension $\gamma^{\mathscr{S}}$. To be consistent to our foregoing modeling, we employ a Taylor series up to the second order in $\cos(\Theta)$ and obtain the following expression

$$\gamma^{\mathscr{S}} \;=\; \gamma_{12} - \left[(1+2\cos(\Theta)\{1+\cos(\Theta)\})\gamma_{12} + 4(1+\cos^2(\Theta))\gamma_{\mathscr{P}(2)}\right]\phi. \tag{4.87}$$

The total surface stress tensor $\boldsymbol{\sigma}^{\mathscr{S}}$, reflecting the presence of a particle-laden fluid interface, can therefore be written as

$$\boldsymbol{\sigma}^{\mathscr{S}} = \gamma^{\mathscr{S}}\boldsymbol{I}^{\mathscr{S}} + (\kappa^{\mathscr{S}} - \mu^{\mathscr{S}})\left(\boldsymbol{\nabla}^{\mathscr{S}}\cdot\boldsymbol{u}^{\mathscr{S}}\right)\boldsymbol{I}^{\mathscr{S}} + 2\mu^{\mathscr{S}}\boldsymbol{\mathfrak{E}}^{\mathscr{S}}. \tag{4.88}$$

The coefficients $\gamma^{\mathscr{S}}$, $\mu^{\mathscr{S}}$ and $\kappa^{\mathscr{S}}$ can be taken from equations (4.87), (4.75) and (4.76), respectively.

In a numerical simulation, the transport equations for the fluid interface have to be solved in addition to the transport equations in the bulk. A derivation and discussion of the transport equations in interfacial flows can be found in Wang and Oberlack (2011), for example. In cases where the evolution of the concentration field of interfacial particles needs to be taken into account, an additional transport equation has be solved, including all relevant forces acting on the particles, such as the drag force (Dörr et al., 2016) or the force due to the curvature of the interface (Léandri and Würger, 2013; Galatola and Fournier, 2014).

4.4.2 Stability of a free liquid jet with a particle-laden interface

In this subsection, we discuss a potential application of our theoretical analysis in terms of the Rayleigh-Plateau instability of a liquid cylinder having particles attached to its surface. The basis of this example is the analysis by Martínez-Calvo and Sevilla (2018), who studied the temporal axisymmetric instability of a free liquid cylinder coated with insoluble surfactant, including surface elasticity as well as Marangoni effects. We may simplify their dispersion relation [equation (3.26) in Martínez-Calvo and Sevilla (2018)] by neglecting the parameter β accounting for the Gibbs elasticity. In addition to our assumptions listed in section 4.1, it is assumed that the curvature-driven motion of the particles attached to the fluid interface (see Léandri and Würger, 2013; Galatola and Fournier, 2014) is much slower than the decay of the liquid cylinder. Correspondingly, we can assume a homogeneous particle distribution at the interface and therefore exclude Marangoni effects. This might be in agreement with the underlying linear stability analysis, since small deviations from a perfectly cylindrical surface are

considered. By employing a slightly different notation and neglecting the surface elasticity, we rewrite the dispersion relation into (Martínez-Calvo and Sevilla, 2018)

$$\begin{aligned}&\frac{\mathrm{Re}}{\mathrm{Ca}}\omega^2 F(k) - k^2(1-k^2) + k^4\frac{\mathrm{Ca}}{\mathrm{Re}}\left[4 + 6B_{\mu^{\mathscr{S}}} + \frac{1-k^2}{\omega}\left(B_{\mu^{\mathscr{S}}} + B_{\kappa^{\mathscr{S}}}\right) - 2B_{\kappa^{\mathscr{S}}}(1+2B_{\mu^{\mathscr{S}}})\right]\\ &(F(k) - F(\tilde{k})) + \omega k^2\left[2(B_{\mu^{\mathscr{S}}} - B_{\kappa^{\mathscr{S}}})F(k) + (B_{\mu^{\mathscr{S}}} + B_{\kappa^{\mathscr{S}}})(F(k)F(\tilde{k}) + 1)\right.\\ &\left. + 2(2F(k) - 1)\right] = 0,\end{aligned} \tag{4.89}$$

with

$$\tilde{k} = \sqrt{k^2 + \frac{\mathrm{Re}}{\mathrm{Ca}}\omega} \quad \text{and} \quad F(x) = x\frac{I_0(x)}{I_1(x)}, \tag{4.90}$$

in which $\mathrm{Re} = \rho UR/\mu$, $\mathrm{Ca} = \mu U/\gamma^{\mathscr{S}}$, k, ω, R and $I_n(x)$ are the Reynolds number, the capillary number, the wavenumber, the temporal growth-rate, the radius of the unperturbed liquid jet and the n-th order modified Bessel function of the first kind (Martínez-Calvo and Sevilla, 2018), respectively. It should be noted that the capillary number depends on the contact angle through the effective surface tension $\gamma^{\mathscr{S}}$, derived in the previous subsection. Consequently, changing the wettability of the interfacial particles under constant flow conditions changes the ratio of Reynolds and capillary number. We make use of the Boussinesq numbers from equations (4.79) and (4.80) with length scale $L = R$, which reveals that the influences of the effective surface viscosities can only be considered asymptotically, since ϕ and a/R are both small parameters. Note that the latter ratio needs to be a small to satisfy assumption 3. In what follows we set $\phi = 0.15$ and $a/R = 0.1$. The combination of a highly viscous liquid and sufficiently small characteristic velocities U should result in $\mathrm{Re} \ll 1$ and $\mathrm{Ca} \ll 1$, in line with the assumptions made to compute the effective viscosities. We therefore consider a silicone oil thread (100 cSt, $\rho = 0.96$ g/ml, $\gamma_{12} = 20$ mN/m; the values are taken from the data sheet of CAS Number 63148-62-9 by Sigma-Aldrich) with a radius $R = 1$ mm. Based on these values and for $U = 10$ mm/s, we find $\mathrm{Re} = O(10^{-1})$. Assuming a small particle concentration, the effective surface tension is comparable to the surface tension of the bare silicone oil. The capillary number is then $\mathrm{Ca} = O(10^{-2})$. Equation (4.87) requires knowledge about the interfacial tensions between the particles and the surrounding media. We consider polystyrene particles for which $\gamma_{\mathscr{P}(\mathrm{air})} = 35$ mN/m (Shimizu and Demarquette, 2000). When we vary the contact angle, we keep $\gamma_{\mathscr{P}(\mathrm{air})}$ fixed to that value. After inserting the Boussinesq numbers and the capillary number into equations (4.89) and (4.90), we employ a Taylor series up to the second order in $\cos(\Theta)$ and up to the first order in ϕ, to be consistent with our previous derivation. Subsequently, we solve equation (4.89) numerically, using Newton's method implemented in MATHEMATICA®. The results are shown in figure 4.5.

The influence of surface particles on the dispersion relation is such that the growth rate of perturbations reduces when particles are present. This qualitative observation agrees with various experiments performed in different contexts (e.g., Binks, 2002; Aveyard et al., 2003; Dickinson, 2010; Wu and Ma, 2016; De Corato and Garbin, 2018). A surface concentration of $\phi = 0.15$ yields a growth rate reduced by about 20% compared to a particle-free surface. In this particular example, interfacial particles with a contact angle deviating from $\Theta = 90°$ slow down the growth

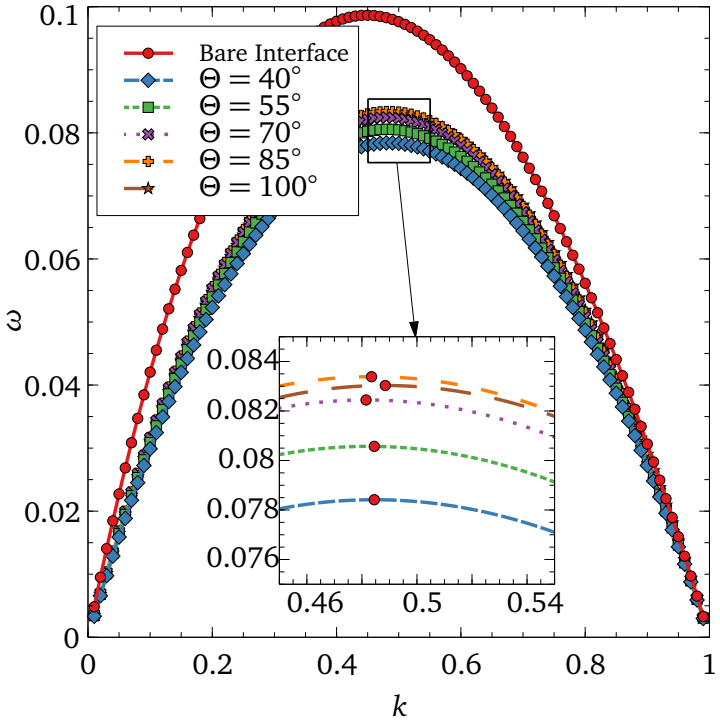

Abbildung 4.5.: Plot of temporal growth rate ω over the wave number k of a particle-laden liquid jet for different contact angles Θ, obtained from the dispersion relation from equation (4.89) (Martínez-Calvo and Sevilla, 2018). For comparison, a particle-free bare interface is added to the plot. The red dots in the inset refer to the maximum of the curves.

of modes more significantly than particles with a contact angle close to 90°. Owing to the presence of particles, the critical wave number increases by about 7% for all contact angles considered. It could be tempting to use the computed surface viscosity values for cases with higher surface concentrations. As explained above, we expect that our theory underestimates the influence of interfacial particles for larger values of ϕ. In other words, in these cases the presence of interfacial particles is expected to influence the dispersion relation even more significantly than visible in figure 4.5. However, we have assumed a uniform concentration of interfacial particles. Although the exclusion of curvature driven motion might be asymptotically satisfied, since the force acting on interfacial particles scales with (the gradient of) the second-order Gaussian and mean curvature (Foret and Würger, 2004; Galatola and Fournier, 2014), a local change of the surface area (in the pinching region) induces a local change in the surface concentration which generates a Marangoni flow that has been neglected. Nevertheless, the example provided in this subsection mainly serves as a proof-of-concept and paves the way for a more advanced modeling.

In the following subsection, we slightly deviate from the actual topic and focus on the computation of trajectories of a slightly deformed spherical particle suspended in the bulk of a fluid, since we have already provided a theoretical basis with equations (4.33) & (4.34). After that, we summarize the results of this chapter.

4.4.3 Excursion: The trajectory of a slightly deformed sphere suspended in a bulk and subjected to a linear flow field

In this subsection, we make use of results that have (so far) received little attention during the previous derivations and apply them in a slightly different context. We have already indicated that equations (4.33) & (4.34) allow us to compute the trajectory of a slightly deformed sphere suspended in a Newtonian fluid and subjected to a linear flow field. The aim of this excursion is to draw a general outline for the computation of the effective particle motion, the validation of equations (4.33) & (4.34) by comparing our results to the rotational motion of spheroids subjected to a shear flow, leading to the well known Jeffery orbits (Jeffery, 1922), and the computation of the orientation of spheroids subjected to a pure straining flow.

To begin with, we introduce a non-inertial coordinate system, i.e., a reference frame fixed in the center of a translating/rotating particle. Through elementary vector calculus, the inertial and particle-fixed reference frames can be related. It is known that additional terms arise on the left-hand side of the Navier-Stokes equations if the coordinate system is fixed to the center of the moving particle (White and Corfield, 2006; Böhme, 2013). However, under Stokes flow conditions, both coordinate systems lead to the same governing equation (Jeffery, 1922; Guazzelli and Morris, 2011). We may therefore assume that the effective translational and rotational velocity given in equations (4.33) & (4.34) refer to the particle fixed reference frame denoted by (x', y', z'). It is useful, to introduce Euler angles relating the rotation of the particle-fixed frame to the stationary reference frame (x, y, z) (e.g., Hinch and Leal, 1979). We define the Euler angles in agreement with the work by Hinch and Leal (1979) as follows: $\alpha_1 \in (0, 2\pi)$ refers to the rotation around the z-coordinate, leading to the coordinates (x_1, y_1, z). $\alpha_2 \in (0, \pi)$ describes the rotation around the x_1-axis leading to (x_1, y_2, z_2). Finally, $\alpha_3 \in (0, 2\pi)$ denotes the angle corresponding to the rotation around the z_2-axis leading to the rotational contribution of the particle fixed coordinates (x', y', z'). The rotation matrix $\boldsymbol{R}$ relating the coordinate systems is given by Hinch and Leal (1979) [the authors defined the rotation matrix with $\boldsymbol{A}$ and the relation between the angles is $(\alpha_1, \alpha_2, \alpha_3) = (\phi, \theta, \psi)$]. Making use of elementary vector calculus, the rotational velocity in the particle-fixed reference frame (ω_i') is related to the time derivative of the Euler angles $(\dot{\alpha}_i)$ as follows

$$\begin{bmatrix} \dot{\alpha}_1 \\ \dot{\alpha}_2 \\ \dot{\alpha}_3 \end{bmatrix} = \begin{bmatrix} \sin(\alpha_3)/\sin(\alpha_2) & \cos(\alpha_3)/\sin(\alpha_2) & 0 \\ \cos(\alpha_3) & -\sin(\alpha_3) & 0 \\ -\sin(\alpha_3)/\tan(\alpha_2) & -\cos(\alpha_3)/\tan(\alpha_2) & 1 \end{bmatrix} \begin{bmatrix} \omega_1' \\ \omega_2' \\ \omega_3' \end{bmatrix}, \tag{4.91}$$

in which the vector $\boldsymbol{\omega}'$ is given through equation (4.34), transferred into Cartesian coordinates. The translational velocity, on the other hand, is related to the time derivative of the particle fixed coordinate system through

$$\dot{\boldsymbol{r}}' = \boldsymbol{u}', \tag{4.92}$$

in which $\boldsymbol{u}'$ is given through equation (4.33) in Cartesian coordinates and $\boldsymbol{r}'$ is the position vector of the particle-fixed reference frame. Any applied velocity field can be rewritten in the particle fixed coordinates and the corresponding vector basis with the help of the rotation matrix $\boldsymbol{R}$. We are then left with a system of 6 nonlinear, coupled ordinary differential equations in time

that, in general, requires numerical methods to obtain solutions. Since we have neglected the time dependency during the derivation of equations (4.33) & (4.34), the translation and rotation of the particle is effectively quasi-static. Less formal, one could think of a trapped particle, which is released at a certain time in arbitrary orientation and follows the flow without temporal discrepancy (see assumption 8).

For simplicity, we limit ourselves to spheroids, prescribed through the following parametrization

$$\frac{x^2+y^2}{a^2}+\frac{z^2}{a^2(1-\beta)^2} = 1, \tag{4.93}$$

$$r_{\mathscr{P}} \approx a(1-\beta\cos^2(\theta)). \tag{4.94}$$

For $\beta > 0$, the spheroid is oblate, whereas $\beta < 0$ characterizes a prolate spheroid (Brenner, 1964). Following equations (3.69) - (3.72), we expand $f(\theta) = -\cos^2(\theta)$ in a sum of surface spherical harmonics and find

$$f(\theta) = f_0 + f_2(\theta), \tag{4.95}$$

$$f_0 = -\frac{1}{3}, \quad \text{and} \quad f_2(\theta) = \frac{1}{3} - \cos^2(\theta). \tag{4.96}$$

Consequently, the effective translational velocity of the spheroid subjected to an arbitrary linear flow field is identically zero which follows immediately from equation (4.33).

A spheroid subjected to an applied shear flow: Jeffery orbits

We assume an externally applied shear flow (shear rate $\dot{\gamma}$) given in the inertial coordinate system such as

$$\boldsymbol{U}(\boldsymbol{r}) = \dot{\gamma} y \boldsymbol{e}_x. \tag{4.97}$$

The latter equation can now be transferred into the particle fixed coordinate system and the corresponding translational and rotational velocities following equations (4.91) & (4.92) can be computed. A general strategy of such calculations is given by Jeffery (1922) or Hinch and Leal (1979). We eventually obtain the following set of ordinary differential equations

$$\dot{\alpha}_1 = \frac{\dot{\gamma}}{2}(-1+\beta\cos(2\alpha_1)), \tag{4.98}$$

$$\dot{\alpha}_2 = \frac{\beta\,\dot{\gamma}}{4}\sin(2\alpha_2)\sin(2\alpha_1), \tag{4.99}$$

$$\dot{\alpha}_3 = -\frac{\beta\,\dot{\gamma}}{2}\cos(\alpha_2)\cos(2\alpha_1). \tag{4.100}$$

The latter three equations are equal to the first-order expansions of the equations obtained by Hinch and Leal (1979), apart from a sign error in the equation for $\dot{\phi}$ ($\dot{\alpha}_1$ in our notation) on page 596 in their work. The authors introduced a variable r that reads (translated to our notation) $1-\beta$, and is therefore a measure of ellipticity. At this point we do not aim at solving the set of

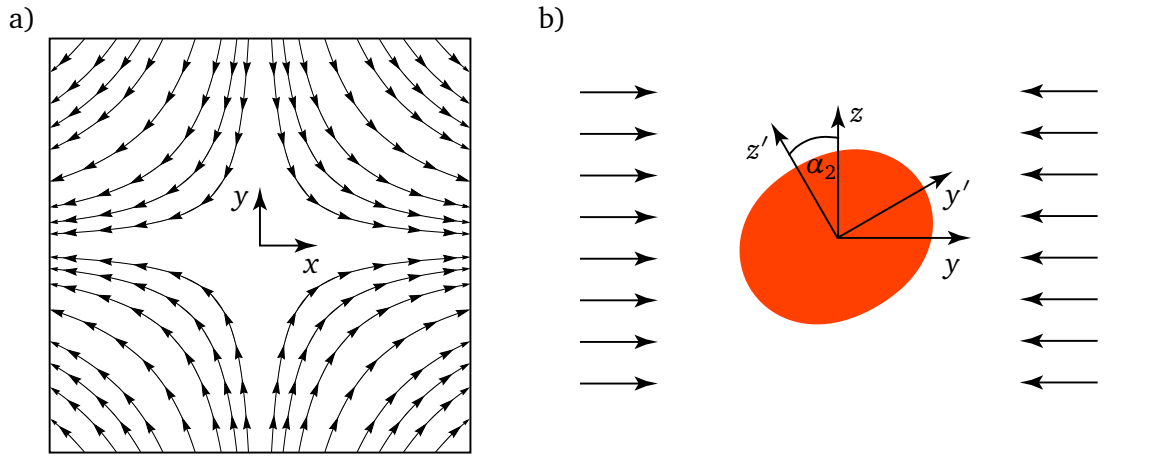

Abbildung 4.6.: A spheroid subjected to a 2D pure straining flow. a) Streamlines corresponding to equation (4.101) with $\dot{\epsilon} = 1$. b) The parametrization of the surface of the spheroid is given through equation (4.94), with $\beta = 0.2$ (oblate spheroid). Initially, the spheroid is orientated such that the particle fixed coordinate x' coincides with the inertial coordinate x, where both coordinate origins are located at the center of the particle.

ordinary equations and reiterate a complete discussion of the properties of Jeffery orbits, since complete discussions can be found in literature (Jeffery, 1922; Hinch and Leal, 1979; Duprat and Stone, 2015). An insightful graphical explanation of the Jefferey orbits is provided in figures 2.12 & 2.13 by Duprat and Stone (2015).

A spheroid subjected to a pure, 2D straining flow

Here, we consider an applied velocity field given in the inertial coordinate system as follows

$$\boldsymbol{U}(\boldsymbol{r}) = \dot{\epsilon} x \boldsymbol{e}_x - \dot{\epsilon} y \boldsymbol{e}_y, \tag{4.101}$$

in which $\dot{\epsilon}$ represents a constant strain rate. The latter equation represents a 2D straining flow, as sketched in figure 4.6 a). After transferring equation (4.101) into the particle fixed coordinates system and evaluating equation (4.34), we eventually obtain the following set of ordinary differential equations

$$\dot{\alpha}_1 = -\beta \dot{\epsilon} \sin(2\alpha_1), \tag{4.102}$$

$$\dot{\alpha}_2 = \frac{\beta\ \dot{\epsilon}}{2} \cos(2\alpha_1)\sin(2\alpha_2), \tag{4.103}$$

$$\dot{\alpha}_3 = \beta \dot{\epsilon} \sin(2\alpha_1)\cos(\alpha_2). \tag{4.104}$$

Assuming an initial orientation given by $\alpha_i(0) = \alpha_i^0$, for $i = 1, 2, 3$, the solution of the previous set of equations read

$$\cot(\alpha_1) = \exp(\beta \dot{\epsilon} t)\cot(\alpha_1^0), \tag{4.105}$$

$$\cot(\alpha_2) = \frac{\exp(2\beta\dot{\epsilon}t)}{\sqrt{\exp(2\beta\dot{\epsilon}t)\cos^2(\alpha_1^0)+\sin^2(\alpha_1^0)}(\tan^4(\alpha_2^0))^{1/4}}, \tag{4.106}$$

$$\alpha_3 - \alpha_3^0 = \int_0^t \frac{\beta\dot{\epsilon}\sin(2\ \mathrm{arccot}[\exp(2\beta\dot{\epsilon}\tau)\cot(\alpha_1^0)])}{\sqrt{1+\exp(-2\beta\dot{\epsilon}\tau)\left(\exp(4\beta\dot{\epsilon}\tau)\cos^2(\alpha_1^0)+\sin^2(\alpha_1^0)\right)\tan^2(\alpha_2^0)}}\mathrm{d}\tau, \tag{4.107}$$

In its most general form, the integral in equation (4.107) cannot be solved analytically. However, when considering an oblate spheroid ($\beta > 0$) with an initial orientation where the x-axis of the particle fixed reference frame coincides to the inertial frame, both located at the center of the particle as sketched in figure 4.6 b), we simplified the problem to a 1D rotation around the x-axis given through α_2 and set $\alpha_1^0 = \alpha_3^0 = 0$. We then find

$$\alpha_1 = 0, \tag{4.108}$$

$$\alpha_2 = \arctan[\exp(\beta\dot{\epsilon}t)\tan(\alpha_2^0)], \tag{4.109}$$

$$\alpha_3 = 0. \tag{4.110}$$

Equation (4.109) reveals, that for an initial orientation $\alpha_2^0 \neq 0$, the oblate spheroid always reaches a value of $\alpha_2 = 90°$ after a sufficiently long time. Furthermore, the larger the shape deviation from a perfect sphere (controlled through β) and the larger the strain rate $\dot{\epsilon}$, the faster the particle aligns in the flow. For $\alpha_2^0 = 0$ on the other hand, the particle does not align itself in the flow. This configuration is clearly not stable and therefore should not be observable through experiments since any small deviation from that initial orientation, e.g., though a perturbation of the flow field or due to Brownian motion, will cause to particle to align itself with an angle of $\alpha_2 = 90°$. When solving the integral from equation (4.107) numerically, it can be observed that any initial orientation will lead to such an orientation. The orientation of a prolate spheroid ($\beta < 0$) is equivalent to that of an oblate spheroid, i.e., the long semi-axis aligns with the x-axis after a sufficiently long time. The alignment of spheroidal particles in pure straining flow is in agreement with physical intuition.

4.5 Summary & Outlook

In summary, we have studied the dissipation effects due to spherical particles adsorbed at the interface between two fluids with large viscosity contrast and computed the effective interfacial dilatational and shear viscosity. We limited our study to flat interfaces and small Reynolds numbers. Furthermore, a dilute interfacial suspension was considered, that allows the negligence of the hydrodynamic, capillary and Brownian interactions between particles. We took advantage of symmetry arguments stating that the physical situation of a particle attached to a flat interface between fluids of very different viscosity is equivalent to that of a mirror-fused particle in the bulk of the fluid with higher viscosity. We applied the stress-averaging method by Batchelor (1970) to interfacial suspensions and found that the effective surface viscosities are solely determined by the stresslet acting on the mirror-fused particle.

The shape of the mirror-fused particle was modeled based on a domain perturbation method, where the contact angle Θ of the more viscous fluid on the particle surface defines the particle

shape. By applying the Lorentz reciprocal theorem (Lorentz, 1896) and solving the Stokes equations for the mirror-fused particle in a pure straining flow up to first order in the perturbation parameter $\beta = \cos(\Theta)$, we computed both interfacial viscosities of a Boussinesq-Scriven interface up to the second order in β. We found that the dilatational viscosity is more sensitive to the contact angle than the shear viscosity. Further, the magnitude of the dilatational viscosity was shown to be larger than the magnitude of the shear viscosity, which is in agreement with experimental results obtained for particle-free fluid interfaces (Fox and Rock, 1946; Maru and Wasan, 1979). Usually, in the corresponding articles clean interfaces are considered, but recent results indicate that in practice, surface contaminations are very difficult to avoid (Peaudecerf et al., 2017). By comparing our results with the semi-analytical results of Lishchuk (2016), we found that our perturbation approach agrees well with the semi-analytical data (deviation less than 5%) in a contact angle range between 40° and 105°. To provide a complete picture of the interfacial stresses, we presented an expression for the effective interfacial tension as a function of the contact angle.

An application of our theory was discussed in terms of the decay of a liquid cylinder whose surface is decorated with particles. Based on the theory by Martínez-Calvo and Sevilla (2018) and considering a particle surface concentration of 15%, we found that interfacial particles slow down the decay by about 20% compared to a bare interface.

The main results may prove useful in different contexts. First, they could help understanding low-concentration particle-laden interfacial flows, especially the role of the contact angle in these flows. Second, in a similar way as with theories for the effective viscosity of a bulk suspension, our findings could pave the way to follow-up studies considering higher particle concentrations. This could enable understanding the hydrodynamics of systems as complex as Pickering emulsions and liquid marbles.

We further sketched the outline of the computation of the trajectories of a slightly deformed sphere suspended in a bulk liquid and subjected to a linear velocity field. Throughout this excursion, we limited ourselves to spheroidal particles and reobtained the ordinary differential equations leading to the well-known Jeffery orbits (Jeffery, 1922). Furthermore, we studied the orientation of an oblate spheroid in pure 2D straining flow. Our theory allows the computation of the trajectory of an arbitrary slightly deformed sphere in an arbitrary linear flow field leading to a set of six coupled, nonlinear ordinary differential equations that, in general, has to be solved numerically. These results might help to understand a flow controlled orientation of particles which could be important in the application-oriented process of multi-composite materials, such as wood-plastic composites (Ashori, 2008), where a defined alignment of non-spherical composites optimize the mechanical properties of the material (Suarez et al., 1986). We further believe these results leave a broad range for further research, including the computation of time depending trajectories of bulk particles and the corresponding effective bulk suspension viscosities.

5 Hydrodynamic shielding of an object of arbitrary shape in a Hele-Shaw cell through EOF

Microfluidic devices are significantly influenced by the constitution and presence of boundaries due to the small volume-to-surface ratio typically occurring in microscale flows. Exemplarily, a circular channel characterized by a small radius $R \ll 1$ and a length L has a volume-to-surface ratio of $R/2 \ll 1$. Therefore, the flow near a boundary, influenced by its physical constitution, has considerable effect on the global parameters of the device, such as the volumetric flow rate. An electrolyte bounded by charged walls can be accelerated in close proximity to the wall if an external electric field is applied to the system. This effect is known as electro-osmosis (e.g., Masliyah and Bhattacharjee, 2006). Assuming that a wall is charged in a spatially controlled region [e.g., through deposition of a polyelectrolyte (Paratore et al., 2019b) or through a gate electrode (Paratore et al., 2019a)], an applied electric field induces an electro-osmotic flow restricted to a domain where a charge is induced at the boundary. The aim of this chapter is to answer the following question: Is it possible to induce an electro-osmotic flow around an obstacle such that the obstacle is hydrodynamically shielded against an external flow in a narrow channel?

The reduction of drag is a very common technical and engineering problem, often related to the motion of vehicles, such as cars (Hassan et al., 2014) or ships (Ahmadzadehtalatapeh and Mousavi, 2015), or in many different sports, such as cycling (Crouch et al., 2017), aiming to increase efficiency. The previous examples have in common that the Reynolds numbers Re are high, at least compared to flows in microchannels or other microfluidic devices under typical conditions. However, the drag reduction of flows at comparably small Reynolds numbers has also been studied, e.g., for superhydrophobic surfaces (Truesdell et al., 2006). If the contact area between a liquid and a solid surface is minimized, e.g., through the interplay of a rough microstructure of the solid surface and the presence of air pockets between the solid and the liquid, the no-slip boundary condition is no longer valid as the liquid effectively 'slips' along the surface (Schönecker et al., 2014) and reduces the force acting on the solid surface.

Recently, Park et al. (2019) studied cloaking of a cylindrical obstacle in a narrow channel (so-called Hele-Shaw channel). The authors introduced a second-order spatially dependent viscosity tensor in order to manipulate the flow around the obstacle and found that in the inner region, where the viscosity provides the strongest spatial dependency, flow can nearly be suppressed. In theory, the drag force on the obstacle is identically zero. However, numerically the authors obtained a remarkable drag reduction of about six times compared to an cylindrical obstacle in absence of the cloak. Park et al. (2019) explained the discrepancy between theory and their numerical simulations through 'mathematical iterations', without going into further detail. Since the numerical software employed by the authors (COMSOL Multiphysics®) does not include the feature of a spatial dependent second-order viscosity tensor, the equations had to be implemented

manually. The term 'mathematical iterations' therefore probably corresponds to their custom-made pressure correction. Otherwise, since the authors employed 3D simulations, whereas their theoretical work is limited to 2D, the finite height of the channel (third dimension) might also explain the differences observed. In order to realize a spatially dependent viscosity experimentally, the authors designed ten rows of a microstructured array surrounding the cylindrical obstacle that effectively increases the viscosity depending on the shape and distance of the array. This idea is closely related to the general idea of the computation of effective viscosities in suspensions, in which the presence of particles lead to an effective increase of the viscosity. However, in view of figure 3 (e) by Park et al. (2019) the distance between the microstructured array decreases in direction towards the obstacle and the positions of the approximately rectangular pillars indicate that no streamline can reach the obstacle without being redirected through the pillars leading to a significantly lower drag force on the obstacle. Finally, the authors self-critically admitted that the practical use of their work is limited, since the spatially dependent viscosity has to be increased significantly, leading to a large number of microstructured pillars around the obstacle. Furthermore, the fabrication of a porous mircostructure surrounding an obstacle is challenging.

In this chapter, we describe a novel method to reduce the drag on an obstacle fixed inside a Hele-Shaw channel with the help of an electro-osmotic flow induced by the interplay of an applied electric field and a ζ-potential located at a spatially controllable region of the upper and lower wall of the channel. The theoretical paper by Boyko et al. (2015), dealing with spatially controlled electro-osmotic flow in a Hele-Shaw channel in absence of an obstacle, is the basis of the subsequent analysis. The authors are our cooperation partners of the work presented in this chapter. The following sections mainly exclude their contributions, as far it is possible in a cooperation project.

This chapter is arranged as follows: In section 5.1, we introduce the configuration, the underlying methods as well as the assumptions, our theoretical modeling is based on. Then, after introducing the governing equations and the corresponding boundary conditions, we go over to discuss the most general case of the shielding of an arbitrarily shaped obstacle in a Hele-Shaw channel in section 5.2. After that, a slightly deformed cylindrical obstacle is considered, for which the specific shape of the spatially controllable ζ-potential annulus is obtained that allows the isolation of the obstacle from an outer pressure driven flow (section 5.3). The numerical method introduced in section 5.4 is used for the validation of the theoretical modeling in section 5.5. The chapter is concluded in section 5.6.

5.1 Model assumptions

We consider an arbitrarily shaped obstacle of characteristic size a fixed in the center of a rectangular channel having a height H and a length L in both directions tangential to the lower wall [see figure 5.1 a)]. A Newtonian electrolyte is pumped through the channel (with velocity U_{ext}) and subjected to an applied electric field E_∞ (both in x-direction). Furthermore, a spatially controlled region of characteristic length r_a carrying a ζ-potential enclosing the obstacle at the upper and lower wall is considered [see figure 5.1 b) & c)]. The following assumptions are employed throughout this study, to be explained in more detail subsequently:

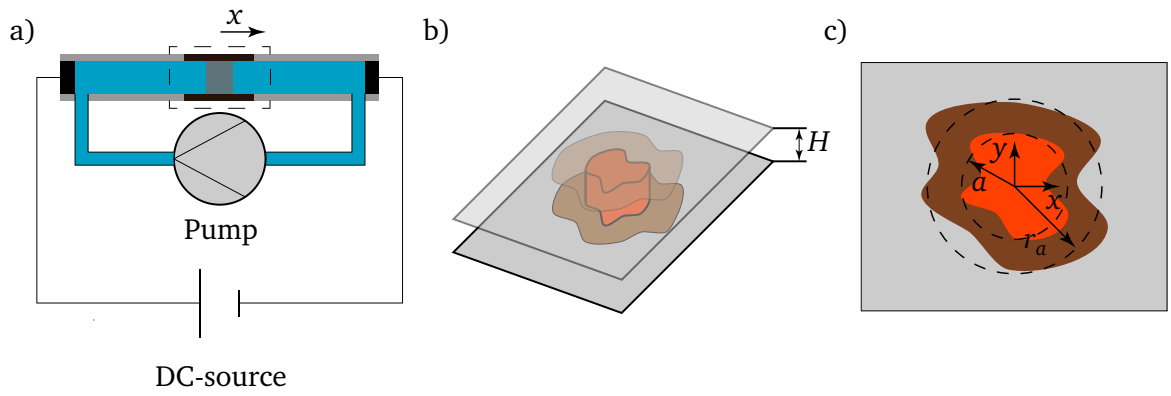

Abbildung 5.1.: Schematic of the configuration. a) A pump creates a flow of an electrolyte through the channel in x-direction. Additionally, an electric field is applied in the direction of flow. Far away from the flow inlet and outlet, an obstacle is positioned in the center of the channel surrounded by a spatially defined region carrying a ζ-potential (so-called ζ-potential annulus). b) Detail view of the channel in the vicinity to the obstacle. H defines the height of the channel. The orange region refers to the obstacle whereas the brown region sketches the ζ-potential annulus. c) Top view of b). The coordinate system (x, y) tangential to the lower and upper wall of the channel is located in the center of the obstacle. The vertical coordinate z points from the lower wall towards the upper wall. a and r_a are the characteristic length of the obstacle and the characteristic length of the ζ-potential annulus, respectively.

1. The length of the rectangular channel in in-plane direction L is large compared to the characteristic size of the obstacle a and even larger than the height of the channel H, such that: $H \ll a \ll L$;
2. The ζ-potential annuli at the lower wall $z = 0$ and at the upper wall $z = H$ have the same geometrical shape and carry the same ζ-potential: ζ_0;
3. The ζ-potential of the obstacle is ζ_0;
4. The Debye layer thickness is small compared to all length scales, i.e., especially $\kappa H \to \infty$.

Assumption 1 is commonly employed in the theoretical description of flows in Hele-Shaw channels. Assuming $H \ll L$, simplifies the problem and enables us to neglect the effect of side-walls on the flow inside the Hele-Shaw cell. For a unidirectional flow through a rectangular channel it has been shown that side wall effects can be neglected if $H/L < 0.1$ (Tabeling, 2005). However, the range of validity is by no means clear for all possible configurations and depends, among others, on the boundary conditions. Gat et al. (2009) managed to go beyond the leading-order Hele-Shaw approximation and studied the influence of the no-slip boundary conditions at the side walls on the flow inside a straight and curved narrow channel through matched asymptotic expansions in absence of electro-osmotic flow. However, for sufficiently narrow channels it is reasonable to assume that the height of the channel is also small compared to the characteristic length of the obstacle, i.e., $H \ll a$. Actually, assumption 1 has already been applied in the case of an electro-osmotic flow in a Hele-Shaw channel in absence of an obstacle (Boyko et al., 2015). The theoretical analysis by Boyko et al. (2015) has been tested in experiments (Paratore et al., 2019b), confirming that assumption 1 is reasonably well satisfied. Assumption 2 is not very restrictive and depends on the applied method to create a local ζ-potential at the upper and lower walls of the channel (Paratore et al., 2019a,b). We further assume that the

ζ-potential at the obstacle coincides with that of the annulus [assumption 3]. Even though, the practical use of the 'polyelectrolyte deposition'-method employed by Paratore et al. (2019b) is mainly restricted by the limited number of polyeletrolytes available, the practical use of a gate electrode provides a great degree of freedom controlling the range of ζ-potentials (Schasfoort et al., 1999; Paratore et al., 2019a). Therefore, for a given ζ-potential of the obstacle, the applied voltage of the gate electrode could be chosen such that assumption 3 is sufficiently well satisfied. Assumption 4 simplifies the problem further, since it allows neglecting the electrostatic effects in the momentum balance. Hereby, the electrostatic effects are fully governed in the electro-osmotic slip condition (Yariv, 2009). The characteristic thickness of the electric double layer (Debye length) is typically of order $O(10^{-8} - 10^{-7})$ m and therefore small compared to the height of a narrow channel. The electro-osmotic slip condition is usually obtained through the method of matched asymptotic expansions, where the domain is separated into an outer and inner domain. The inner domain has a characteristic length of the Debye layer and captures all electro-hydrodynamic effects (Yariv, 2009). The analytical solutions of the governing equations inside the inner domain lead to effective boundary conditions for the velocity field outside the double layer. The electro-osmotic slip condition applied in the present context (to be explained in more detail in the subsequent section) is limited to 'moderately' charged surfaces. The assumption of moderately charged surfaces go beyond the Debye-Hückel approximation, implying a broader range of validity, i.e., for higher surface charges (see figure 1 by Schnitzer and Yariv, 2012b). As already discussed in the introduction of chapter 3, high surface charges induce a significant ion-flux in tangential direction to the surface of the particle, which requires a more advanced modeling (Schnitzer and Yariv, 2012b). At the line of contact between the obstacle and the annulus ($r = r_{\emptyset}$ and $z = 0, z = L$), a rapid geometrical change appears that affects the validity of the electro-osmotic slip boundary conditions as shown by Craven et al. (2008) through numerical simulations. Indeed, the theoretical calculation by Yariv (2009) applies to surfaces whose geometrical changes are small compared to the characteristic thickness of the electric double layer. However, this effect has exceeded the range of discussion in the present context.

5.1.1 Governing equations & boundary conditions

The complete derivation of the governing equations for the flow in a Hele-Shaw channel is provided in appendix C, starting with the classical equations of fluid motion, i.e., equation (2.2) & (2.6). The key part of the derivation is carried out under the approximation $H/a = \varepsilon \ll 1$ and focused on the terms of leading order. The following non-dimensional set of simplified equations has been obtained:

$$\tilde{\boldsymbol{\nabla}}_{\parallel} \cdot \langle \tilde{\boldsymbol{u}}_{\parallel} \rangle_H = \tilde{w}|_{\tilde{z}=0} - \tilde{w}|_{\tilde{z}=1}\,, \tag{5.1}$$

$$\langle \tilde{\boldsymbol{u}}_{\parallel} \rangle_H = -\frac{1}{12}\tilde{\boldsymbol{\nabla}}_{\parallel}\tilde{p} + \frac{1}{2}\left(\tilde{\boldsymbol{u}}_{\parallel}\big|_{\tilde{z}=0} + \tilde{\boldsymbol{u}}_{\parallel}\big|_{\tilde{z}=1}\right). \tag{5.2}$$

$\langle \tilde{\boldsymbol{u}}_{\parallel} \rangle_H$, $\tilde{\boldsymbol{\nabla}}_{\parallel}$ and $\tilde{w}$ denote the depth-averaged velocity vector in in-plane direction with respect to the upper and lower wall, the Nabla-operator in in-plane direction and the velocity component in z-direction, respectively. From now on we suppress to carry the subscript H for the height-averaged velocity. The non-dimensional quantities are defined in equation (C.1). The characteristic velocity $U_{\parallel}$, used for the non-dimensionalization of the tangential velocities $\langle \tilde{\boldsymbol{u}}_{\parallel} \rangle$ is set via $U_{\parallel} = U_{\text{ext}}$, i.e., the inlet velocity of the fluid. It is worth recalling that the electro-osmotic

flow induced by the interplay of the applied electric field and the ζ-potential inside the annulus is taken into account through the boundary conditions at the upper and lower wall. In contrast to section 3, the electric double layer is not explicitly resolved. The governing equation for the electrostatic potential is the two-dimensional Laplace equation, since outside the electric double layer the electrolyte restores electroneutrality

$$\tilde{\boldsymbol{\nabla}}_{\parallel}^{2}\tilde{\phi} = 0. \tag{5.3}$$

For the non-dimensionalization of the electrostatic potential we have used $E_{\infty}a$. We are now in the position to discuss appropriate boundary conditions. To start with, we introduce two parametrizations accounting for the shape of the obstacle ($\mathscr{O}$) as well as the ζ-potential annulus ($\mathscr{A}$) via $\tilde{r}_{\mathscr{O}}$ and $\tilde{r}_{\mathscr{A}}$. Both parametrizations are non-dimensionalized through the characteristic length of the obstacle a and refer to the center of the obstacle given in polar coordinates $(\tilde{\varrho}, \varphi) = (\sqrt{\tilde{x}^2 + \tilde{y}^2}, \arctan(y/x))$.

The boundary conditions for the electrostatic potential $\tilde{\phi}$ have already been provided in section 3.1.1 when computing the electrophoretic mobility of interfacial particles, see equations (3.9) and (3.10). Translated to the present notation, they read

$$\tilde{\boldsymbol{\nabla}}_{\parallel}\tilde{\phi}\big|_{\tilde{\varrho}=\tilde{r}_{\mathscr{O}}} \cdot \boldsymbol{n}_{\mathscr{O}} = 0, \qquad \tilde{\phi}\big|_{\tilde{\varrho}\to\infty} = -\tilde{\varrho}\cos(\varphi). \tag{5.4}$$

$\boldsymbol{n}_{\mathscr{O}}$ is the normal vector pointing outwards from the obstacle.

We consider an idealized pumping of the electrolyte inside the channel and therefore assume that the depth-averaged velocity reaches a constant value U_{ext} sufficiently far away from the obstacle

$$\langle \tilde{\boldsymbol{u}}_{\parallel} \rangle\big|_{\tilde{\varrho}\to\infty} = \cos(\varphi)\, \boldsymbol{e}_{\varrho} - \sin(\varphi)\, \boldsymbol{e}_{\varphi}. \tag{5.5}$$

The boundary conditions at the surface of the obstacle can be subdivided into boundary conditions for the velocity in normal and tangential direction with respect to the obstacle. It is assumed that the obstacle is a rigid, non-porous body. Consequently, no liquid can penetrate into the obstacle

$$\langle \tilde{\boldsymbol{u}}_{\parallel} \rangle\big|_{\tilde{\varrho}=\tilde{r}_{\mathscr{O}}} \cdot \boldsymbol{n}_{\mathscr{O}} = 0. \tag{5.6}$$

The same rationale applies to the upper and lower wall leading to

$$\tilde{w}|_{\tilde{z}=0} = \tilde{w}|_{\tilde{z}=1} = 0. \tag{5.7}$$

In view of the setup, it is reasonable to discuss the boundary conditions for the fluid motion tangentially to the channel walls for the two regions $\tilde{r}_{\mathscr{O}} < \tilde{\varrho} \leq \tilde{r}_{\mathscr{A}}$ and $\tilde{r}_{\mathscr{A}} < \tilde{\varrho}$, separately. We may designate the region corresponding to $\tilde{r}_{\mathscr{O}} < \tilde{\varrho} \leq \tilde{r}_{\mathscr{A}}$ and $\tilde{r}_{\mathscr{A}} < \tilde{\varrho}$ the inner and outer region, respectively. The walls in the outer region do not carry a ζ-potential and consequently the velocity has to satisfy the no-slip boundary condition at the upper and lower wall, i.e.,

$$\tilde{\boldsymbol{u}}_{\parallel}\big|_{\tilde{z}=0} = \tilde{\boldsymbol{u}}_{\parallel}\big|_{\tilde{z}=1} = 0, \qquad \text{for } \tilde{r}_{\mathscr{A}} < \tilde{\varrho}. \tag{5.8}$$

The electro-osmotic slip velocity, often called Helmholtz-Smoluchowski velocity, is related to the tangential velocity at a charged surface with the tangential gradient of the electrostatic potential (e.g., Morrison, 1970). In non-dimensional form, we have

$$\tilde{\boldsymbol{u}}_{\parallel}\big|_{\tilde{z}=0} = \tilde{\boldsymbol{u}}_{\parallel}\big|_{\tilde{z}=1} = \Lambda\tilde{\boldsymbol{\nabla}}_{\parallel}\tilde{\phi}, \qquad \text{for } \tilde{r}_{\mathscr{O}} < \tilde{\varrho} \leq \tilde{r}_{\mathscr{A}}, \tag{5.9}$$

$$\Lambda = \frac{\epsilon\zeta_0 E_\infty}{\mu U_{\text{ext}}}. \tag{5.10}$$

Λ takes the role of a dimensionless quantity relating the externally induced pressure driven flow with the electro-osmotic flow induced in the inner region.

Coming back to the boundary conditions at the obstacle in tangential direction. It is known that the leading-order Hele-Shaw approximation generally does not provide sufficient degrees of freedom to satisfy all boundary conditions at the surface of an obstacle (Riegels, 1938; Thompson, 1968; Lee and Fung, 1969). Lee and Fung (1969) studied the flow around a cylindrical post in a Hele-Shaw channel theoretically and found that corrections to the leading order approximation are needed to satisfy the no-slip condition at the post. Rapid changes in the tangential velocity in normal direction to the post were observed, strongly depending on H/a. As shown in figure 5 in the work by Lee and Fung (1969), the drag coefficient increases rapidly for decreasing H/a. The drag force on the obstacle is closely related to the spatial changes of the velocity components in normal direction to the post. The larger the corrections of the velocity field required to satisfy the boundary condition at the obstacle, the larger the gradient of the velocity field in normal direction to the obstacle and consequently the higher the resulting drag force on the post. Therefore it might be desirable to find a suitable ζ-potential annulus parametrization that leads to a tangential velocity field that matches the electro-osmotic slip velocity as close as possible in the leading-order approximation.

The electro-osmotic boundary condition for the tangential velocity at the surface of the obstacle reads

$$\langle\tilde{\boldsymbol{u}}_{\parallel}\rangle\big|_{\tilde{\varrho}=\tilde{r}_{\mathscr{O}}} \cdot \boldsymbol{t}_{\mathscr{O}} = \Lambda\,\tilde{\boldsymbol{\nabla}}_{\parallel}\tilde{\phi}\big|_{\tilde{\varrho}=\tilde{r}_{\mathscr{O}}} \cdot \boldsymbol{t}_{\mathscr{O}}, \tag{5.11}$$

in which $\boldsymbol{t}_{\mathscr{O}}$ is the tangential vector at the surface of the obstacle. Making use of equations (5.7) - (5.9), the governing equations of fluid motion read for the inner and outer region, separately:

$$\tilde{\boldsymbol{\nabla}}_{\parallel} \cdot \langle\tilde{\boldsymbol{u}}_{\parallel}\rangle_i = 0; \qquad i = \text{in}, \text{out}, \tag{5.12}$$

$$\langle\tilde{\boldsymbol{u}}_{\parallel}\rangle_{\text{in}} = -\frac{1}{12}\tilde{\boldsymbol{\nabla}}_{\parallel}\tilde{p}_{\text{in}} + \Lambda\tilde{\boldsymbol{\nabla}}_{\parallel}\tilde{\phi}, \tag{5.13}$$

$$\langle\tilde{\boldsymbol{u}}_{\parallel}\rangle_{\text{out}} = -\frac{1}{12}\tilde{\boldsymbol{\nabla}}_{\parallel}\tilde{p}_{\text{out}}. \tag{5.14}$$

Following the equation of continuity, the normal component of the inner velocity field has to coincide with the normal velocity component in the outer region at $\tilde{\varrho} = \tilde{r}_{\mathscr{A}}$. Furthermore, the pressure is assumed to be continuous over the interface between the inner and outer region. Mathematically, the matching conditions read

$$\langle\tilde{\boldsymbol{u}}_{\parallel}\rangle_{\text{in}}\big|_{\tilde{\varrho}=\tilde{r}_{\mathscr{A}}} \cdot \boldsymbol{n}_{\mathscr{A}} = \langle\tilde{\boldsymbol{u}}_{\parallel}\rangle_{\text{out}}\big|_{\tilde{\varrho}=\tilde{r}_{\mathscr{A}}} \cdot \boldsymbol{n}_{\mathscr{A}}, \tag{5.15}$$

$$\tilde{p}_{\text{in}}|_{\tilde{\varrho}=\tilde{r}_{\mathscr{A}}} = \tilde{p}_{\text{out}}|_{\tilde{\varrho}=\tilde{r}_{\mathscr{A}}}. \tag{5.16}$$

In summary, equations (5.3) - (5.6) and (5.12) - (5.16) are the full set of governing equations and corresponding boundary conditions that describe the superposition of a pressure induced flow and a spatially controlled electro-osmotic flow around an obstacle in a narrow channel at the leading order.

5.2 Arbitrarily shaped obstacle

The aim of this section is to provide general results valid for arbitrarily shaped obstacles in a Hele-Shaw cell on the basis of the governing equations derived in the previous subsection.

The no-penetration boundary condition at the obstacle [equation (5.6)] can be rewritten into a boundary condition for the inner pressure with the help of equation (5.13) leading to

$$\tilde{\boldsymbol{\nabla}}_{\parallel}\tilde{p}_{\text{in}}\big|_{\tilde{\varrho}=\tilde{r}_{\mathscr{O}}} \cdot \boldsymbol{n}_{\mathscr{O}} = 12\Lambda\, \tilde{\boldsymbol{\nabla}}_{\parallel}\tilde{\phi}\big|_{\tilde{\varrho}=\tilde{r}_{\mathscr{O}}} \cdot \boldsymbol{n}_{\mathscr{O}} = 0, \tag{5.17}$$

where equation (5.4) has been used. Now it is assumed that a parametrization of the ζ-potential annulus is given such that the electro-osmotic slip boundary condition from equation (5.11) is satisfied at the surface of the obstacle. Such a parametrization is desirable, as discussed in the previous subsection, even though a general existence is by no means guaranteed. For the case of a slightly deformed circular obstacle, a suitable ζ-potential annulus parametrization can be obtained (as shown in the subsequent section) that might motivate us to generalize these findings for obstacles of arbitrary shape. In the view of the following equations, it becomes obvious that the pressure in the inner region is a constant (say 0) if the electro-osmotic slip condition is fulfilled. Inserting equation (5.13) into equation (5.11) and recalling that the pressure gradient normal to the surface of the obstacle vanishes [see equation (5.17)], leaves us with the proof

$$\langle \tilde{\boldsymbol{u}}_{\parallel}\rangle_{\text{in}}\big|_{\tilde{\varrho}=\tilde{r}_{\mathscr{O}}} \cdot \boldsymbol{t}_{\mathscr{O}} = -\frac{1}{12}\tilde{\boldsymbol{\nabla}}_{\parallel}\, \tilde{p}_{\text{in}}|_{\tilde{\varrho}=\tilde{r}_{\mathscr{O}}} \cdot \boldsymbol{t}_{\mathscr{O}} + \Lambda\, \tilde{\boldsymbol{\nabla}}_{\parallel}\tilde{\phi}\big|_{\tilde{\varrho}=\tilde{r}_{\mathscr{O}}} \cdot \boldsymbol{t}_{\mathscr{O}}, \tag{5.18}$$

$$\tilde{\boldsymbol{\nabla}}_{\parallel}\, \tilde{p}_{\text{in}}|_{\tilde{\varrho}=\tilde{r}_{\mathscr{O}}} \cdot \boldsymbol{t}_{\mathscr{O}} = 0, \tag{5.19}$$

$$\Rightarrow \tilde{p}_{\text{in}} = 0. \tag{5.20}$$

Consequently, the pressure drag force, resulting from the integration of the pressure over the surface of the obstacle, is identically zero. Remarkably, the pressure force vanishes independently of the shape of the obstacle in the leading-order Hele-Shaw approximation as long as the electro-osmotic slip velocity is satisfied at the surface of the obstacle. Due to the vanishing pressure in the inner region, the inner velocity field is solely determined through the electrostatic potential, via

$$\langle \tilde{\boldsymbol{u}}_{\parallel}\rangle_{\text{in}} = \Lambda\tilde{\boldsymbol{\nabla}}_{\parallel}\tilde{\phi}. \tag{5.21}$$

Furthermore, the matching conditions at $\tilde{\varrho} = \tilde{r}_{\mathscr{A}}$ simplify to

$$\tilde{\boldsymbol{\nabla}}_{\parallel}\tilde{p}_{\text{out}}\big|_{\tilde{\varrho}=\tilde{r}_{\mathscr{A}}} \cdot \boldsymbol{n}_{\mathscr{A}} = -12\Lambda\, \tilde{\boldsymbol{\nabla}}_{\parallel}\tilde{\phi}\big|_{\tilde{\varrho}=\tilde{r}_{\mathscr{A}}} \cdot \boldsymbol{n}_{\mathscr{A}}, \tag{5.22}$$

$$\tilde{p}_{\text{out}}|_{\tilde{\varrho}=\tilde{r}_{\mathscr{A}}} = 0. \tag{5.23}$$

It is worth mentioning that the foregoing results can be used in numerical simulations. When computing the divergence of equation (5.14), the continuity equation helps to receive the Laplace equation for the outer pressure field. Assuming a given shape of the obstacle, both Laplace equations for the outer pressure and the electrostatic potential can be solved and lead, together with equation (5.5) and (5.23), to a suitable parametrization of the ζ-potential annulus $\tilde{r}_{\mathscr{A}}$. However, the numerical treatment is not straightforward, since it leads to an optimization problem, in which the annulus is successively changed until the electro-osmotic boundary condition is satisfied at the surface of the obstacle. The expected computational effort and the corresponding order of convergence of such an optimization cannot be easily estimated and goes beyond the scope of this work. It should be noted that this method can also be applied in opposite direction. For a given parametrization of $\tilde{r}_{\mathscr{A}}$, the shape of the obstacle can be computed that satisfies the electro-osmotic slip velocity at its surface. This direction might be useful, if a controlled shaping of deformable objects is desired.

Before we go over to compute the exact shape of the ζ-potential annulus that leads to a vanishing pressure drag force on a slightly deformed obstacle, we discuss some general properties of the flow field.

The stream function ψ, whose contour lines represent streamlines, can be defined for a two dimensional flow via (e.g., Leal, 2007)

$$\boldsymbol{u} = \boldsymbol{\nabla} \times \boldsymbol{\psi}, \tag{5.24}$$

in which $\boldsymbol{\psi} = (0, 0, \psi)^T$ and $\boldsymbol{u} = (u_1, u_2, 0)^T$ is the vector of the stream function ψ and an arbitrary two dimensional velocity field. The latter equation clearly holds independently of the coordinate system. However, the inner velocity field $\langle \tilde{\boldsymbol{u}}_{\parallel} \rangle_{\text{in}}$ is proportional to the gradient of the electrostatic potential as shown in equation (5.21). We may introduce the dimensionless stream function as $\tilde{\psi} = \psi/(U_{\text{ext}} a)$. In absence of an inner pressure field, the streamlines inside the annulus are orthogonal to the electric field lines. The proof is rather simple but worth to be mentioned. We have

$$\tilde{\boldsymbol{\nabla}} \tilde{\psi}_{\text{in}} \cdot \tilde{\boldsymbol{\nabla}} \tilde{\phi} = (-\tilde{u}_{\varphi,\text{in}} \boldsymbol{e}_{\varrho} + \tilde{u}_{\varrho,\text{in}} \boldsymbol{e}_{\varphi}) \cdot \tilde{\boldsymbol{\nabla}} \tilde{\phi} = \Lambda \left((-\tilde{\boldsymbol{\nabla}} \tilde{\phi} \cdot \boldsymbol{e}_{\varphi}) \boldsymbol{e}_{\varrho} + (\tilde{\boldsymbol{\nabla}} \tilde{\phi} \cdot \boldsymbol{e}_{\varrho}) \boldsymbol{e}_{\varphi} \right) \cdot \tilde{\boldsymbol{\nabla}} \tilde{\phi} = 0. \tag{5.25}$$

Furthermore, following the same strategy we find that the streamlines corresponding to the outer velocity field are perpendicular to the pressure contour lines. The importance of the streamlines for the experimental validation of our theoretical results is discussed in the conclusion of this chapter.

5.3 Slightly deformed circular obstacle

The results of the previous section are of general validity but are based on the assumption that a parametrization of the ζ-potential annulus exists such that the electro-osmotic slip boundary condition at the surface of the obstacle is satisfied in the leading order. In this section we search for the exact shape of ζ-potential annulus that satisfies all restrictions in order to shield a slightly deformed circular obstacle from an outer flow field.

To start with, we assume the following parametrizations

$$\tilde{r}_{\mathscr{O}} = 1+\beta f(\varphi), \tag{5.26}$$
$$\tilde{r}_{\mathscr{A}} = \tilde{r}_a+\beta \tilde{r}_a g(\varphi), \tag{5.27}$$

in which $f(\varphi)$ and $g(\varphi)$ are two arbitrary functions and $\tilde{r}_a$ is a dimensionless characteristic radius of the annulus, as shown in figure 5.1 c). In agreement with the previous chapters, β takes the role of a perturbation parameter. The normal and tangential vector corresponding to the latter parametrizations are found [up to $O(\beta)$]:

$$\boldsymbol{n}_{\mathscr{O}} = \boldsymbol{e}_{\varrho}-\beta\tilde{\boldsymbol{\nabla}}_{\parallel} f(\varphi), \qquad \boldsymbol{t}_{\mathscr{O}} = \beta\left(\tilde{\boldsymbol{\nabla}}_{\parallel} f(\varphi)\cdot\boldsymbol{e}_{\varphi}\right)\boldsymbol{e}_{\varrho}+\boldsymbol{e}_{\varphi}, \tag{5.28}$$
$$\boldsymbol{n}_{\mathscr{A}} = \boldsymbol{e}_{\varrho}-\beta\tilde{r}_a\tilde{\boldsymbol{\nabla}}_{\parallel} g(\varphi), \qquad \boldsymbol{t}_{\mathscr{A}} = \beta\tilde{r}_a\left(\tilde{\boldsymbol{\nabla}}_{\parallel} g(\varphi)\cdot\boldsymbol{e}_{\varphi}\right)\boldsymbol{e}_{\varrho}+\boldsymbol{e}_{\varphi}. \tag{5.29}$$

We expand all physical quantities in a perturbation sum in β up to the first order following the same train of thought as in section 2.4. Subsequently, we derive the solutions of the governing equations starting with the electrostatic potential.

5.3.1 Electrostatic potential

We have already discussed the significance of the electrostatic potential in the hydrodynamic shielding of an obstacle. The inner velocity field is solely determined through the electrostatic potential. The governing equation for the electrostatic potential is the 2D Laplace equation. The boundary conditions are given in equation (5.4). Following section 2.4, we find the following boundary conditions mapped on the surface of an undeformed cylindrical obstacle

$$\left.\frac{\partial\tilde{\phi}^{(0)}}{\partial\tilde{\varrho}}\right|_{\tilde{\varrho}=1} = 0, \tag{5.30}$$
$$\left.\frac{\partial\tilde{\phi}^{(1)}}{\partial\tilde{\varrho}}\right|_{\tilde{\varrho}=1} = \left.\tilde{\boldsymbol{\nabla}}_{\parallel}\tilde{\phi}^{(0)}\right|_{\tilde{\varrho}=1}\cdot\left.\tilde{\boldsymbol{\nabla}}_{\parallel} f(\varphi)\right|_{\tilde{\varrho}=1} - f(\varphi)\left.\frac{\partial^2\tilde{\phi}^{(0)}}{\partial\tilde{\varrho}^2}\right|_{\tilde{\varrho}=1}. \tag{5.31}$$

For the far-field boundary, we have

$$\left.\tilde{\phi}^{(0)}\right|_{\tilde{\varrho}\to\infty} = -\tilde{\varrho}\cos(\varphi), \qquad \left.\tilde{\phi}^{(1)}\right|_{\tilde{\varrho}\to\infty} = 0. \tag{5.32}$$

The zeroth-order solution, satisfying the corresponding boundary conditions, is readily obtained by separation of variables as

$$\tilde{\phi}^{(0)} = -\tilde{\varrho}\left(1+\frac{1}{\tilde{\varrho}^2}\right)\cos(\varphi). \tag{5.33}$$

Obviously, the zeroth-order solution corresponds to a cylindrical obstacle subjected to an applied electric field.

An arbitrary function depending on the polar angle φ, can be expressed as an infinite sum with the help of Fourier series (e.g., Byerly, 1893) via

$$f(\varphi) = \frac{a_0}{2} + \sum_{k=1}^{\infty} \left(a_k \cos(k\varphi) + b_k \sin(k\varphi)\right), \tag{5.34}$$

$$a_k = \frac{1}{\pi} \int_0^{2\pi} f(\varphi) \cos(k\varphi)\, \mathrm{d}\varphi, \tag{5.35}$$

$$b_k = \frac{1}{\pi} \int_0^{2\pi} f(\varphi) \sin(k\varphi)\, \mathrm{d}\varphi. \tag{5.36}$$

The mathematical properties of Fourier series are comparable to that of surface spherical harmonics. Most important, the Fourier series is a complete and orthogonal set of functions (e.g., Byerly, 1893). Separating the variables and taking into account that the first-order correction of the electrostatic potential has to vanish sufficiently far away from the obstacle, the following solution is postulated

$$\tilde{\phi}^{(1)} = \sum_{m=1}^{\infty} \tilde{\varrho}^{-m} \left(C_m^{\mathrm{I}} \cos(m\varphi) + C_m^{\mathrm{II}} \sin(m\varphi)\right), \tag{5.37}$$

whereas C_m^{I} and C_m^{II} are constants to be determined through equation (5.31). Inserting leads to the following condition

$$\begin{aligned} &\sum_{m=1}^{\infty} \left(-m \left(C_m^{\mathrm{I}} \cos(m\varphi) + C_m^{\mathrm{II}} \sin(m\varphi)\right)\right) = \\ &2 \sum_{k=1}^{\infty} \left[\{-k \sin(k\varphi)\sin(\varphi) + \cos(k\varphi)\cos(\varphi)\}\, a_k \right. \\ &\left. + \{k \cos(k\varphi)\sin(\varphi) + \sin(k\varphi)\cos(\varphi)\}\, b_k\right]. \end{aligned} \tag{5.38}$$

Multiplying both sides of the latter equation with $(1/\pi)\cos(m\varphi)$ and integrating over $\varphi \in [-\pi, \pi]$ enables us to make use of the orthogonality relations. The following results are obtained:

$$C_m^{\mathrm{I}} = a_{m+1} - a_{m-1}, \qquad C_m^{\mathrm{II}} = b_{m+1} - b_{m-1}, \qquad \text{for } m > 0. \tag{5.39}$$

Equations (5.33), (5.37) & (5.39) provide the set of solutions for the electrostatic potential for a slightly deformed cylindrical obstacle up to the first order in the perturbation parameter β.

5.3.2 Pressure field outside the annulus

The governing equation for the outer pressure can be derived when inserting equation (5.14) into (5.12) and result in the 2D Laplace equation. Far away from the obstacle, the outer pressure is fixed so the depth-averaged velocity field parallel to the upper and lower wall leads to a constant, i.e., $\langle \tilde{\boldsymbol{u}}_{\parallel} \rangle = \boldsymbol{e}_x$ for $\tilde{\varrho} \to \infty$. In addition, we make use of the boundary condition given

in equation (5.23), i.e., the pressure decays to zero at the transition between the annulus and outer region. After expanding the outer pressure in a perturbation sum up to the first order in β, we obtain the following boundary conditions mapped onto a circular ζ-potential annulus of radius $\tilde{r}_a$, as well as for the far field

$$\tilde{p}^{(0)}_{\text{out}}\big|_{\tilde{\varrho}=\tilde{r}_a} = 0, \tag{5.40}$$

$$\tilde{p}^{(1)}_{\text{out}}\big|_{\tilde{\varrho}=\tilde{r}_a} = -\tilde{r}_a g(\varphi)\left.\frac{\partial \tilde{p}^{(0)}_{\text{out}}}{\partial \tilde{\varrho}}\right|_{\tilde{\varrho}=\tilde{r}_a}, \tag{5.41}$$

$$\tilde{p}^{(0)}_{\text{out}}\big|_{\tilde{\varrho}\to\infty} = -12\tilde{\varrho}\cos(\varphi) \quad , \qquad \tilde{p}^{(1)}_{\text{out}}\big|_{\tilde{\varrho}\to\infty} = 0. \tag{5.42}$$

We also expand $g(\varphi)$ in a Fourier series following equations (5.34) - (5.36) with corresponding coefficients d_m and h_m referring to a_m and b_m, respectively. More precisely, the constants d_m and h_m are proportional to the $\cos(m\varphi)$ and $\sin(m\varphi)$ terms in the Fourier series, respectively. Apart from that, the solution strategy is similar to that of the previous subsection and therefore not repeated in more detail. The solution of the zeroth- and first-order outer pressure yields

$$\tilde{p}^{(0)}_{\text{out}} = 12\tilde{\varrho}\left(\frac{\tilde{r}_a^2}{\tilde{\varrho}^2} - 1\right)\cos(\varphi), \tag{5.43}$$

$$\tilde{p}^{(1)}_{\text{out}} = \sum_{m=1}^{\infty} \tilde{\varrho}^{-m}\left\{K^{\text{I}}_m \cos(m\varphi) + K^{\text{II}}_m \sin(m\varphi)\right\}. \tag{5.44}$$

The constants K^{I}_m and K^{II}_m are determined along the line presented in the previous subsection. We find after a short calculation

$$K^{\text{I}}_m = 12\tilde{r}_a^{m+1}(d_{m+1} + d_{m-1}), \qquad K^{\text{II}}_m = 12\tilde{r}_a^{m+1}(h_{m+1} + h_{m-1}), \text{ for } m > 0. \tag{5.45}$$

5.3.3 Determination of the shape of the ζ-potential annulus

After we have determined the electrostatic potential and the outer pressure field in the previous subsections, we are now in the position to compute the exact shape of the ζ-potential annulus by making use of the matching condition given in equation (5.22). More precisely, we may obtain a suitable value for Λ that relates the strength of the electro-osmotic flow with the applied velocity field and further observe unique conditions that relate the shape constants corresponding to the annulus, i.e., d_m and h_m, with the shape constants of the obstacle, i.e., a_m and b_m, respectively. Up to the first order in β, equation (5.22) can be rewritten as follows

$$\left.\frac{\partial \tilde{p}^{(0)}_{\text{out}}}{\partial \tilde{\varrho}}\right|_{\tilde{\varrho}=\tilde{r}_a} = -12\Lambda \left.\frac{\partial \tilde{\phi}^{(0)}}{\partial \tilde{\varrho}}\right|_{\tilde{\varrho}=\tilde{r}_a}, \tag{5.46}$$

$$-\frac{1}{\tilde{r}_a}\left.\frac{\partial \tilde{p}^{(0)}_{\text{out}}}{\partial \varphi}\right|_{\tilde{\varrho}=\tilde{r}_a}\frac{\mathrm{d}g(\varphi)}{\mathrm{d}\varphi} + \left.\frac{\partial \tilde{p}^{(1)}_{\text{out}}}{\partial \tilde{\varrho}}\right|_{\tilde{\varrho}=\tilde{r}_a} + \tilde{r}_a g(\varphi)\left.\frac{\partial^2 \tilde{p}^{(0)}_{\text{out}}}{\partial \tilde{\varrho}^2}\right|_{\tilde{\varrho}=\tilde{r}_a} =$$

$$-12\Lambda\left(-\frac{1}{\tilde{r}_a}\left.\frac{\partial\tilde{\phi}^{(0)}}{\partial\varphi}\right|_{\tilde{\varrho}=\tilde{r}_a}\frac{\mathrm{d}g(\varphi)}{\mathrm{d}\varphi}+\left.\frac{\partial\tilde{\phi}^{(1)}}{\partial\tilde{\varrho}}\right|_{\tilde{\varrho}=\tilde{r}_a}+\tilde{r}_a g(\varphi)\left.\frac{\partial^2\tilde{\phi}^{(0)}}{\partial\tilde{\varrho}^2}\right|_{\tilde{\varrho}=\tilde{r}_a}\right). \tag{5.47}$$

Inserting the zeroth-order solutions for the electrostatic potential [see equation (5.33)] and the outer pressure field [see equation (5.43)] into equation (5.46), we find after a short calculation that the matching condition is satisfied, if (and only if)

$$\Lambda=-\frac{2\tilde{r}_a^2}{\tilde{r}_a^2-1} \tag{5.48}$$

Consequently, a circular obstacle can be shielded from an applied velocity field U_{ext}, for a given applied electric field E_∞ and a ζ-potential ζ_0, if the radius of the circular annulus is $\tilde{r}_a=(\Lambda/(2+\Lambda))^{0.5}$. We may exemplarily consider a setup in which the electrolyte has an electro-osmotic mobility of $(-\epsilon\zeta_0/\mu)=O(10^{-8})$ m^2/(s V), such as recently studied by Paratore et al. (2019b). The authors employed an applied electric field of order $E_\infty=O(10^3)$ V/m (Paratore et al., 2019b). For an inflow velocity of $U_{\mathrm{ext}}=O(10^{-6})$ m/s, we find that the radius of the circular annulus is in the same order as the radius of the obstacle: $\tilde{r}_a=O(1)$. Under realistic experimental conditions, the size of the ζ-potential annulus is therefore not extended over a large domain in order to shield an object from an applied velocity field. Clearly, equation (5.48) should preferably be used to determine the required electro-osmotic flow that shields the obstacle in contrast to the example given previously. However, the latter example shows that, under real experimental conditions, our modeling provides a realizable size of the ζ-potential annulus that is in agreement with the underlying assumptions.

But how does a slight variation in the shape of the obstacle affect the shape of the annulus? It might be intuitive to assume that a linearly scaled parametrization of the obstacle employed for the ζ-potential annulus, such as sketched in figure 5.1 c) can satisfy the matching condition. However, we will show subsequently that the exact shape deviates from a simple linear extension of the shape of the obstacle.

When inserting the solutions (up to the first order in β) into equation (5.47) and again making use of orthogonality relations we obtain after a short calculation the following relations

$$\tilde{r}_a a_{m-1}-\tilde{r}_a a_{m+1}+\tilde{r}_a^m\left(\tilde{r}_a^2 d_{m+1}-d_{m-1}\right) = 0, \tag{5.49}$$
$$\tilde{r}_a b_{m-1}-\tilde{r}_a b_{m+1}+\tilde{r}_a^m\left(\tilde{r}_a^2 h_{m+1}-h_{m-1}\right) = 0. \tag{5.50}$$

On the first look, the latter equations might provide a certain degree of freedom in the choice of the constants. However, we have shown that a circular obstacle can be shielded with the help of a circular ζ-potential annulus. For $m=1$ [in equation (5.49)] the a_0 and d_0 term therefore have to balance, leading to a unique condition for a_2 and d_2. Without limitation of generality, we further assume that the centroids of both parametrizations coincide. After a short calculation it can be shown that the centroids of both parametrizations are proportional to a_1, b_1 (in x-direction and y-direction) and d_1, h_1, respectively. The constants are therefore uniquely related through the following remarkably simple relationships:

$$d_m=\tilde{r}_a^{-m}a_m, \qquad h_m=\tilde{r}_a^{-m}b_m. \tag{5.51}$$

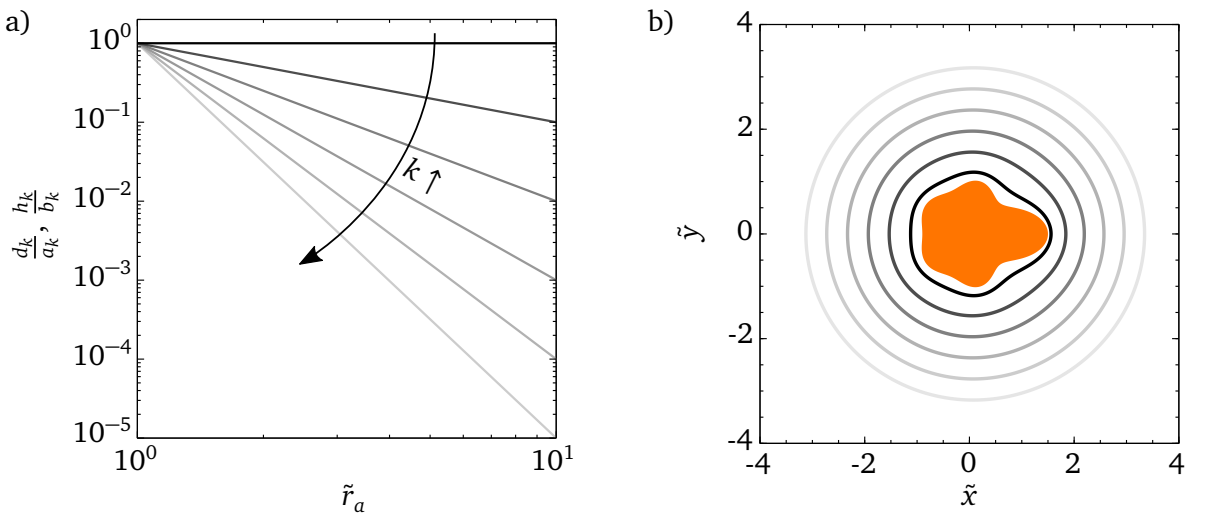

Abbildung 5.2.: a) Plot of the shape constants related to the ζ-potential annulus [see equation (5.51)] over the characteristic radius $\tilde{r}_a$ for varying values of k ranging from $k = 0$ (black) to $k = 5$ (light gray). b) Plot of the shape of the ζ-potential annulus corresponding to an obstacle parametrization of $f(\varphi) = \sum_{k=1}^{5} a_k \cos(k\varphi)$, with $a_k = 1$, for $k = 1$ to $k = 5$ and $\beta = 0.1$. The parametrization of the annulus is given in equation (5.51) and the values of $\tilde{r}_a$ range from 1.2 (black) to 3.2 (light gray) with a step-width of 0.4.

As an important consequence, an obstacle having a shape perturbation related to the Fourier coefficients up to order m can be isolated against an applied flow with the help of a ζ-potential annulus having the same frequency of shape perturbation but with a different amplitude. The results of this section might indicate that higher-order shape perturbations of the obstacle and the annulus (in β) lead to an unique relation between the Fourier constants in every order of β, separately. As an important consequence, a ζ-potential annulus region that implies the fulfillment of the electro-osmotic slip condition at the surface of the obstacle could exist, independently of the geometrical shape.

Exemplarily, figure 5.2 a) shows the evolution of the constants d_k and h_k over the characteristic radius of the annulus region in a double logarithmic plot for $k = 0, \ldots, 5$. Clearly, the constants corresponding to high frequency shape deviations from a cylindrical obstacle (higher k) decrease faster for increasing $\tilde{r}_a$. The annulus region corresponding to an obstacle parametrization of $f(\varphi) = \sum_{k=1}^{5} a_k \cos(k\varphi)$, with $a_k = 1$ for $k = 1, \ldots, 5$, as a function of $\tilde{r}_a$ is shown in figure 5.2 b) for $\beta = 0.1$. Even for comparably small values of $\tilde{r}_a$, locally large curvatures, corresponding to high frequencies, decrease fast. Low frequency perturbations remain present up to a characteristic annulus radius of about $\tilde{r}_a \approx 2.8$.

5.4 Numerical Simulations using COMSOL Multiphysics®

The aim of this section is the introduction of the numerical simulation employed to determine the range of validity of our theoretical work focusing on the dependency of our solution on β. The range of validity with respect to the Hele-Shaw approximation is not part of this work and requires full 3D simulations that will be carried out by our cooperation partners. The introduction to the numerical method employed in this section is by far not complete, readers are referred to

the numerous literature for more details (e.g., Schäfer, 2013; Schwarz, 2013).

The numerical simulations were carried out with COMSOL Multiphysics® (version 5.5; `https://www.comsol.com`), a commercial software base on finite-element method (FEM). Among pre-defined solvers for common physical problems, COMSOL Multiphysics® provides a MATHEMATICS-module consisting of a WEAK FORM PDE sub-module in which users can implement arbitrary partial differential equations with arbitrary boundary conditions, both, of course, in the weak form. During the numerical simulations, we do not make use of the results from section 3.2 and also consider the potential existence of an inner pressure field. Clearly, if the parametrization of the ζ-potential annulus is not chosen appropriately, an inner pressure builds up leading to an effective pressure force acting on the obstacle. Consequently, the governing equations for the electrostatic potential $\tilde{\phi}$, the inner pressure $\tilde{p}_{\text{in}}$ and the outer pressure $\tilde{p}_{\text{out}}$ are 2D Laplace equations. The boundary conditions corresponding to the different variables either fix the value of the variable at a certain boundary (so-called Dirichlet boundary conditions) or fix the slope of the variable in normal direction to a certain boundary (so-called Neumann boundary condition). We may therefore outline the scheme of employing the boundary conditions into COMSOL Multiphysics® starting with the weak form, subsequently.

Without limitation of generality, we consider a 2D domain $\mathscr{A}$ bounded by two curves, the inner and outer boundary, i.e., $\mathscr{C}_{\text{in}}$ and $\mathscr{C}_{\text{out}}$, respectively. The weak formulation of the Laplace equation for a variable Φ in a domain $\mathscr{A}$ is derived, assuming that the boundary condition at $\mathscr{C}_{\text{in}}$ is of Neumann-type, whereas the boundary condition at $\mathscr{C}_{\text{out}}$ is a Dirichlet boundary condition. To start with, the Laplace equation is multiplied by a test function λ_1 and integrated over the domain $\mathscr{A}$. After employing the two-dimensional product rule and employing the Gauss-integral theorem, we obtain

$$\int_{\mathscr{A}} \boldsymbol{\nabla}\Phi\cdot\boldsymbol{\nabla}\lambda_1 \mathrm{d}\mathscr{A} = \oint_{\mathscr{C}_{\text{in}}} (\boldsymbol{n}\cdot\boldsymbol{\nabla}\Phi)\lambda_1 \mathrm{d}\mathscr{C} + \oint_{\mathscr{C}_{\text{out}}} (\boldsymbol{n}\cdot\boldsymbol{\nabla}\Phi)\lambda_1 \mathrm{d}\mathscr{C}. \tag{5.52}$$

The contour integrals on the right-hand side of the latter equation refer to Neumann boundary conditions at the inner and outer boundary, respectively. We assume that the normal gradient on $\mathscr{C}_{\text{in}}$ should read $\dot{\Phi}_n$, whereas the Φ should become Φ_0 on the outer boundary. The Neumann boundary condition on the outer contour $\mathscr{C}_{\text{out}}$ can be rewritten such that the Dirichlet boundary condition is satisfied. Equation (5.52) then turns into

$$\int_{\mathscr{A}} \boldsymbol{\nabla}\Phi\cdot\boldsymbol{\nabla}\lambda_1 \mathrm{d}\mathscr{A} = \oint_{\mathscr{C}_{\text{in}}} \dot{\Phi}_n\lambda_1 \mathrm{d}\mathscr{C} + \oint_{\mathscr{C}_{\text{out}}} \left[\dot{\Psi}_n\lambda_1 + (\Phi-\Phi_0)\lambda_2\right] \mathrm{d}\mathscr{C}. \tag{5.53}$$

Here, λ_2 is the test function corresponding to the artificially introduced normal flux $\dot{\Psi}_n$. The contour integrals on the right-hand side of the latter equation are implemented in COMSOL Multiphysics® in the pre-defined boundary condition: WEAK CONTRIBUTION. A strong coupling between the variables at the boundaries is done automatically throughout the solution procedure. A sketch of the computational domain is given in figure 5.3 and the corresponding boundary conditions can be found in table 5.1. In contrast to our arguments from section 5.2, we solve the pressure inside the annulus. We therefore probably violate the electro-osmotic slip condition

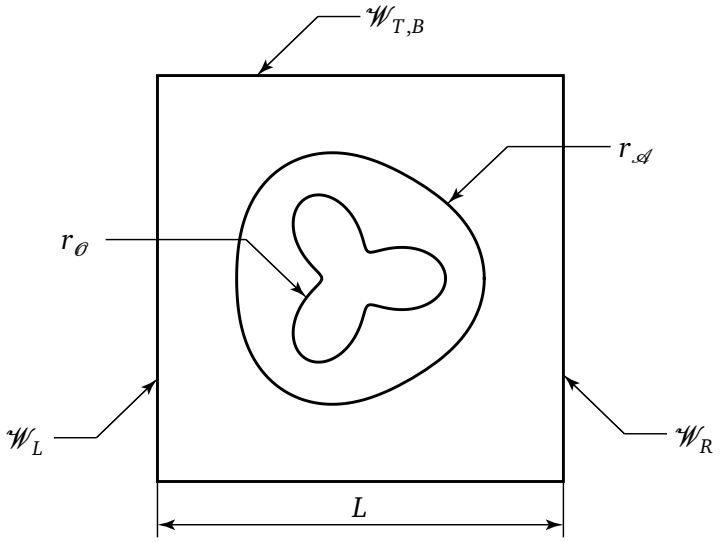

Abbildung 5.3.: Sketch of the quadratic computational domain employed throughout the COMSOL Multiphysics® simulations. L is the length of the each side of the square. $\mathscr{W}_{\mathrm{T,B}}$ refer to the top and bottom boundary of the domain. The shape of the obstacle is given through equation (5.26). The ζ-potential annulus follows equation (5.27), whereas we have employed the Fourier constants according to equation (5.51).

Boundary ↓ | Variables →	$\tilde{\phi}$	$\tilde{p}_{\mathrm{in}}$	$\tilde{p}_{\mathrm{out}}$
$r_{\mathscr{O}}$	$\boldsymbol{n}\cdot\boldsymbol{\nabla}\tilde{\phi}=0$	$\boldsymbol{n}\cdot\boldsymbol{\nabla}\tilde{p}_{\mathrm{in}}=0$	-
$r_{\mathscr{A}}$	-	$\tilde{p}_{\mathrm{in}}=\tilde{p}_{\mathrm{out}}$	$\boldsymbol{n}\cdot\boldsymbol{\nabla}\tilde{p}_{\mathrm{out}}=\boldsymbol{n}\cdot\boldsymbol{\nabla}\tilde{p}_{\mathrm{in}}-12\Lambda\boldsymbol{n}\cdot\boldsymbol{\nabla}\tilde{\phi}$
$\mathscr{W}_L$	$\tilde{\phi}=L/2$	-	$\tilde{p}_{\mathrm{out}}=12L/2$
$\mathscr{W}_R$	$\tilde{\phi}=-L/2$	-	$\tilde{p}_{\mathrm{out}}=-12L/2$
$\mathscr{W}_{T,B}$	$\boldsymbol{n}\cdot\boldsymbol{\nabla}\tilde{\phi}=0$	-	$\boldsymbol{n}\cdot\boldsymbol{\nabla}\tilde{p}_{\mathrm{out}}=0$

Tabelle 5.1.: Boundary conditions employed in the COMSOL Multiphysics® simulation, see figure 5.3. Λ is taken from equation (5.48).

at the surface of the obstacle and consequently obtain a non-vanishing pressure force at $\tilde{r}_{\mathscr{O}}$. In the close proximity of the obstacle and at the transition between the inner and outer region, we generate a very fine mesh, since we expect the highest gradients here. Everywhere else, we employed a coarser mesh. Further, second-order Lagrangian shape functions have been used to discretize all variables. COMSOL Multiphysics® is based on the Galerkin method, i.e., the test functions are chosen analogously to the shape functions (Schwarz, 2013). The resulting system of algebraic equations is then solved using the direct solver PARDISO. We have further set $L = 500a$ throughout all simulations in order to minimize the effect of the boundaries. The degrees of freedom are about 600 000 in every simulation leading to an average computation time for a single simulation of about 4 seconds on a typical office computer.

5.5 Comparison between theory and COMSOL Multiphysics® simulations

Our theory provides an analytical solution for the hydrodynamic shielding of arbitrary shaped obstacles (as long as the shape perturbation compared to a cylinder is small enough). It is,

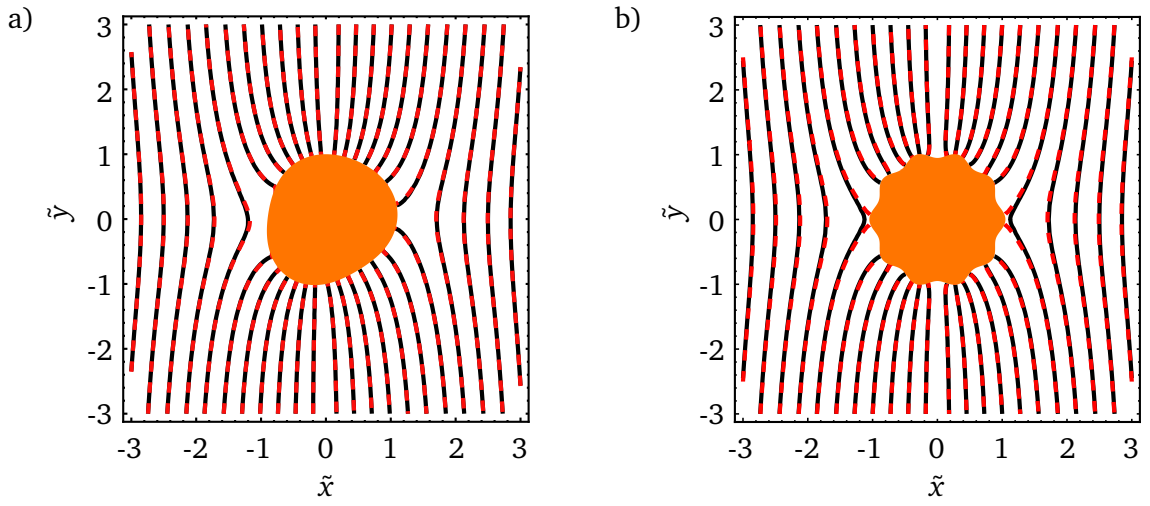

Abbildung 5.4.: Comparison between the electrostatic contour lines ($\tilde{\phi} = \text{const.}$) obtained analytically (black line) and numerically (red dashed line) for $\beta = 0.05$ and $L = 200a$. The parametrization of the obstacle follows a) equation (5.54) and b) equation (5.55).

however, impossible to make general statements about the validity of our theoretical results concerning the value of the parameter β. Theoretical investigations on the range of validity of a general slightly deformed obstacle is far beyond the scope of this work. We may therefore choose a small number of different parametrizations throughout this subsection.

To start with, we compare the contour lines of the electrostatic potential $\tilde{\phi}$ given by equations (5.33), (5.37) and (5.39) with simulated results, since they are closely related to the flow field inside the ζ-potential annulus. We hereby focus on two different parametrizations of the obstacles, given through

$$\tilde{r}_{\mathcal{O}} = 1 + \beta\left(\cos(\varphi) + \sin(2\varphi) + \cos(3\varphi)\right), \tag{5.54}$$

$$\tilde{r}_{\mathcal{O}} = 1 + \beta\cos(10\varphi), \tag{5.55}$$

with $\beta = 0.05$ fixed. The parametrization given in equation (5.54) refers to a deformed cylindrical obstacle with a shape deviation mainly controlled through low frequency perturbations, whereas equation (5.55) refers to a high frequency shape perturbation. Figure 5.4 shows a comparison between the analytical and numerical solutions. In general, good agreement is quite obvious, except that in the close vicinity of the obstacle referring the shape according to equation (5.55) showing a stronger deviation between theory and numerics [figure 5.4 b)]. Low frequency perturbations, on the other hand, provide a better agreement [figure 5.4 a)]. However, a more direct comparison between theory and numerics can be obtained when comparing the flow fields.

Here, we consider an obstacle shape defined through the following parametrization reflecting a medium shape perturbation frequency compared to equations (5.54) & (5.55):

$$\tilde{r}_{\mathcal{O}} = 1 + \beta\cos(5\varphi). \tag{5.56}$$

Besides the influence of increasing values of β, we further investigate the influence of the parameter $\tilde{r}_a$ on the comparison between the two different approaches. $\tilde{r}_a$ might play an important role on the validity of the results, since small $\tilde{r}_a$ come along with rapid changes of the velocity in the proximity of the obstacle. However, the following comparison is limited to certain values of β and $\tilde{r}_a$ and to the parametrization given in the latter equation and should therefore not be considered as a complete study of validity even though the results might indicate a broad range for which our results are applicable.

We may start with the effect of the parameter $\tilde{r}_a$. Figure 5.5 shows a comparison between the analytical (a & c) and numerical solution (b & d) for $\tilde{r}_a = 1.25$ and $\tilde{r}_a = 2$ and $\beta = 0.05$. Both, the pressure contours (black lines) and the streamlines (white lines) agree pretty well for different values of $\tilde{r}_a$. It should be noted that for the numerical solution (b & d) a single pressure contour line penetrates into the annulus region, revealing that the inner pressure is not identically zero as theoretically predicted. However, the small error is most likely caused by the meshing of the finite numerical domain. The non-zero (but indeed small) pressure variation around the obstacle, induces a pressure force on the obstacle, to be discussed later in this chapter in more detail. Furthermore, figure 5.5 shows that the ζ-potential annulus is nearly circular if $\tilde{r}_a = 2$. In agreement with our observations, the pressure contour lines outside the annulus are perpendicular to the streamlines.

The effect of the value of the perturbation parameter β on the validity of our theory is shown in figure 5.6 for $\beta = 0.1$ and $\beta = 0.2$ with a fixed annulus radius of $\tilde{r}_a = 2$ (a & c: theory, b & d numerics). While the analytical solution referring to $\beta = 0.1$ still provides a pretty good agreement to the numerical solution, larger deviations are observed for $\beta = 0.2$. In fact, two streamlines point towards the obstacle, implying a penetrating flow into the surface of the obstacle. Although our analytical solution satisfies the no penetration boundary condition at the surface of the obstacle, larger values of β imply nonlinear effects that are excluded in our theoretical framework. It is noteworthy to recall that the obtained range of validity for β is, strictly speaking, just valid for an obstacle given in equation (5.56). Nevertheless, we do not a expect a completely deviating range of validity for other shapes of the obstacle.

The numerical simulations presented in this work are not sufficient to validate our theoretical work in real systems implying finite values of $\varepsilon = H/L$. Full 3D simulations as well as an experimental validation are not part of my contribution to the project and therefore, as already mentioned in the introduction of this chapter, exceed the range of this work.

In the following subsection, we compute the pressure force acting on a slightly deformed cylindrical obstacle in absence of an electro-osmotic flow. Here, to be consistent with the foregoing analysis, we focus on the leading-order Hele-Shaw approximation which implies that the no-slip boundary condition on the obstacle is violated. However, the computed force in the subsequent section provides a minimum of the force acting on the obstacle due to our discussion from section 5.1.1 and the results obtained by Lee and Fung (1969).

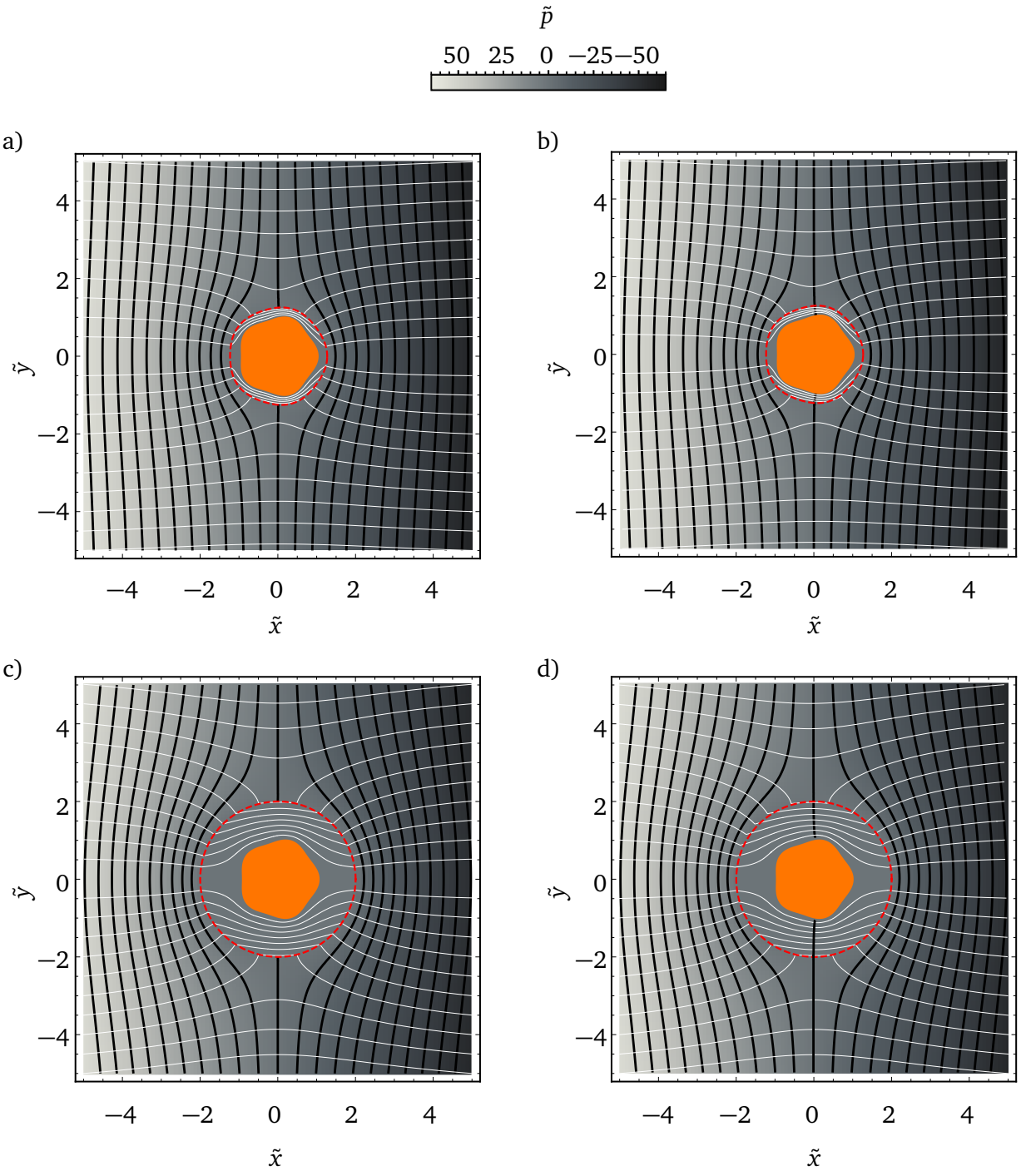

Abbildung 5.5.: Comparison between the flow field obtained with the analytical solution (a and c) and the numerical solution (b and d) for $L = 200r_a$ and $\beta = 0.05$ for different values of r_a. The white lines are the streamlines, the black lines are the pressure contours and the color shading refers to the pressure $\tilde{p}$. The shape of the obstacle is given by $\tilde{r}_\partial = 1 + \beta\cos(5\varphi)$. The Fourier constants of the ζ-potential annulus parametrization are given in equation (5.51). a) & b) $\tilde{r}_a = 1.25$. c) & d) $\tilde{r}_a = 2$.

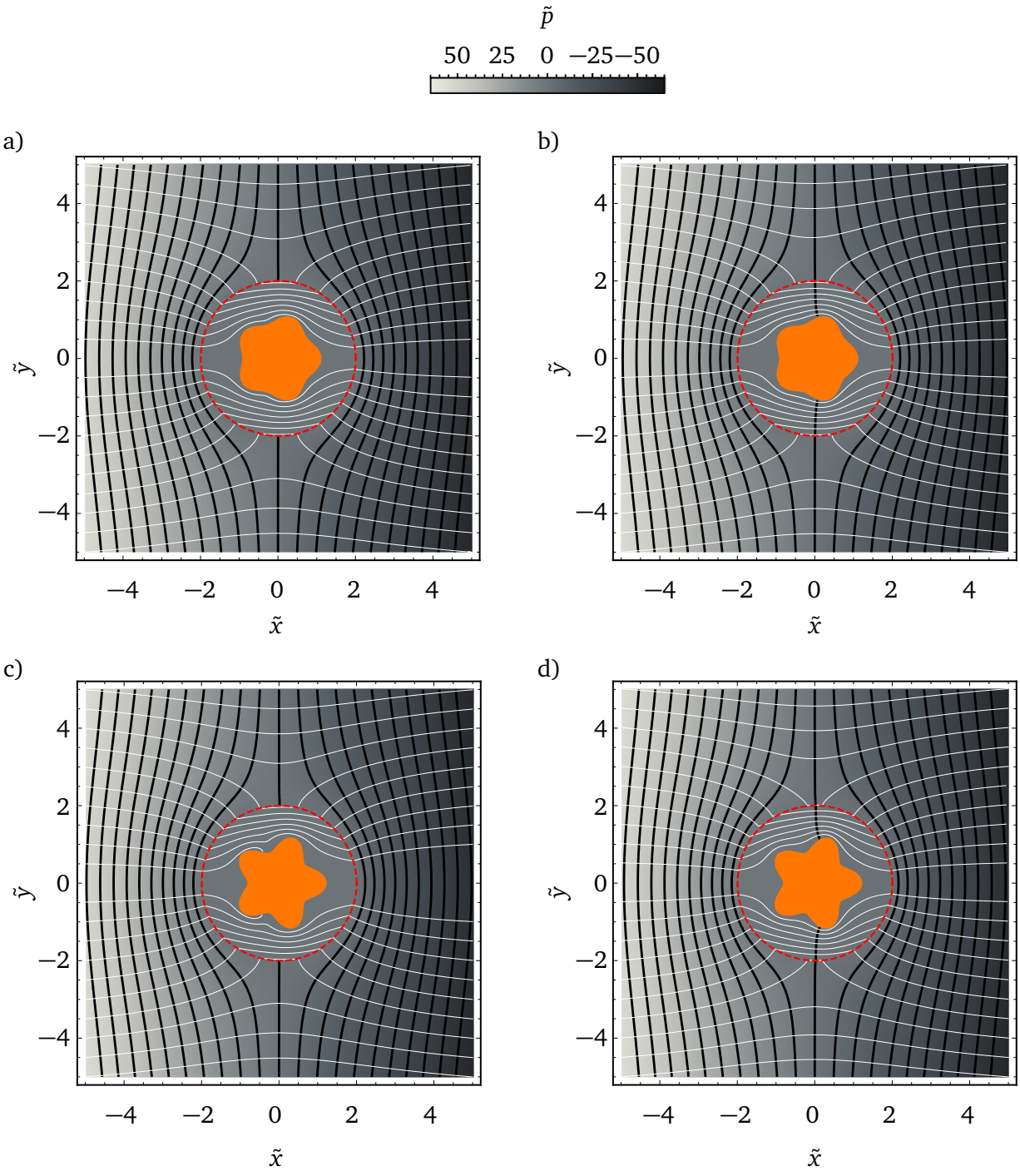

Abbildung 5.6.: Comparison between the flow field obtained with the analytical solution (a and c) and the numerical solution (b and d) for $L = 500a$ and $\tilde{r}_a = 2$ for different values of β. The white lines are the streamlines, the black lines are the pressure contours and the color shading refers to the pressure $\tilde{p}$. The shape of the obstacle is given by $\tilde{r}_{\mathcal{O}} = 1 + \beta \cos(5\varphi)$. The Fourier constants of the ζ-potential annulus parametrization are given in equation (5.51). a) & b) $\beta = 0.1$. c) & d) $\beta = 0.2$.

5.5.1 Pressure force in absence of EOF

The pressure in absence of an induced electro-osmotic flow $\tilde{\mathfrak{p}}$ is also computed through a 2D Laplace equation. The obstacle is impenetrable and the constant inflow velocity is directed along the x-coordinate. The zeroth- and first-order solution for the pressure is closely related to that of the electrostatic potential $\tilde{\phi}$ (see section 5.3.1). We therefore suppress a more detailed description of the solution process. We obtain the following expressions, for the zeroth and first order, respectively:

$$\tilde{\mathfrak{p}}^{(0)} = -12\left(\tilde{\varrho} + \frac{1}{\tilde{\varrho}}\right)\cos(\varphi), \tag{5.57}$$

$$\tilde{\mathfrak{p}}^{(1)} = 12\sum_{k=1}^{\infty}\tilde{\varrho}^{-k}\left[(a_{k+1}-a_{k-1})\cos(k\varphi)+(b_{k+1}-b_{k-1})\sin(k\varphi)\right]. \tag{5.58}$$

The 2D pressure drag force, i.e., the pressure force averaged over the height of the channel, is generally computed via

$$\tilde{\mathscr{F}}_{\mathfrak{p}} = -\int_{\tilde{r}_{\mathscr{O}}} \tilde{\mathfrak{p}}\boldsymbol{n}\,\mathrm{d}\mathscr{C}. \tag{5.59}$$

The integration of the pressure field along the contour of the obstacle therefore leads to the height-averaged force. For slightly deformed obstacles, the pressure force can be obtained through an integration of slightly more complex terms over the contour of a circular obstacle, in agreement with the procedures discussed in chapters 3 & 4. After a short deduction, the following expressions are obtained

$$\tilde{\mathscr{F}}_{\mathfrak{p}}^{(0)} = -\int_0^{2\pi} \tilde{\mathfrak{p}}^{(0)}\big|_{\tilde{\varrho}=1}\,\boldsymbol{e}_{\varrho}\,\mathrm{d}\varphi, \tag{5.60}$$

$$\begin{aligned}\tilde{\mathscr{F}}_{\mathfrak{p}}^{(1)} = -\int_0^{2\pi}\Bigg[&\left\{f(\varphi)\left.\frac{\partial\tilde{\mathfrak{p}}^{(0)}}{\partial\tilde{\varrho}}\right|_{\tilde{\varrho}=1} + \tilde{\mathfrak{p}}^{(1)}\big|_{\tilde{\varrho}=1} + f'(\varphi)\,\tilde{\mathfrak{p}}^{(0)}\big|_{\tilde{\varrho}=1}\right\}\boldsymbol{e}_{\varrho}\\ &-\frac{\mathrm{d}f(\varphi)}{\mathrm{d}\varphi}\,\tilde{\mathfrak{p}}^{(0)}\big|_{\tilde{\varrho}=1}\,\boldsymbol{e}_{\varphi}\Bigg]\mathrm{d}\varphi.\end{aligned} \tag{5.61}$$

Clearly, the zeroth-order force contribution corresponds to an undeformed cylindrical obstacle. Evaluating the integrals leads us to the following solution

$$\tilde{\mathscr{F}}_{\mathfrak{p}} \approx \tilde{\mathscr{F}}_{\mathfrak{p}}^{(0)} + \beta\tilde{\mathscr{F}}_{\mathfrak{p}}^{(1)} = (24\pi[1-\beta(a_2-a_0)])\boldsymbol{e}_x - (24\pi\beta b_2)\boldsymbol{e}_y. \tag{5.62}$$

In agreement with the drag force on a slightly deformed sphere [see equation (4.27)] solely the a_0, a_2 and b_2 constants lead to a force contribution in the first order of β. Therefore, obstacle shapes as shown in figure 5.4 b) (or figures 5.5 & 5.6) experience the same pressure drag as an undeformed cylindrical obstacle. Furthermore, for a non-zero constant b_2, an obstacle also experiences a pressure force in y-direction.

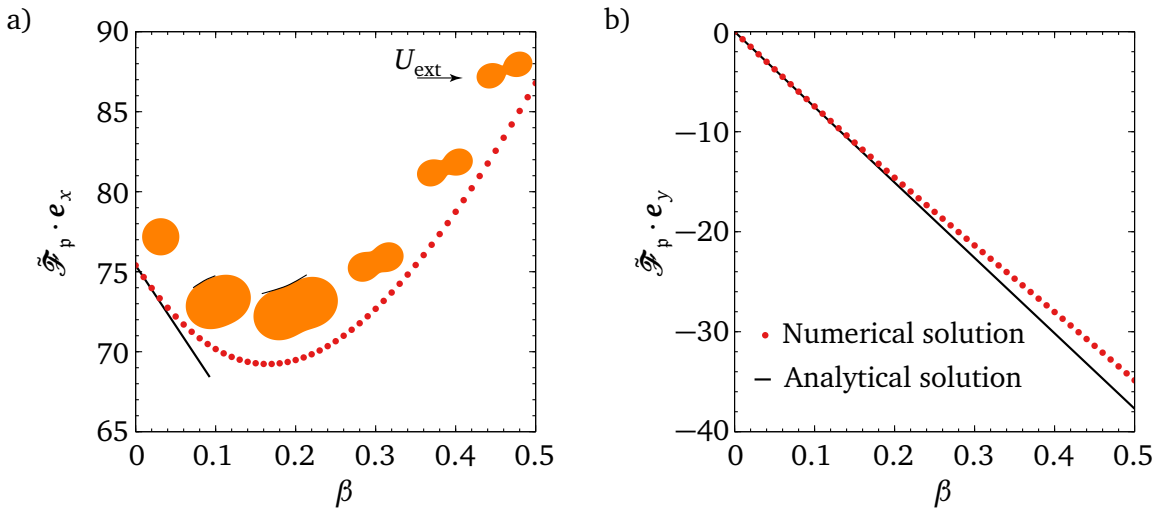

Abbildung 5.7.: Comparison between equation (5.62) (black lines) and the pressure induced force obtained numerically with COMSOL Multiphysics® (red dots) in absence of electro-osmotic flow plotted over the perturbation parameter β. The side length of the domain is $\tilde{L} = 500a$. The parametrization of the body is given through $\tilde{r}_\partial = 1 + \beta(\cos(2\varphi) + \sin(2\varphi))$ ($a_2 = b_2 = 1$). a) Force in x-direction. The insets show the shape evolution depending on β. b) Force in y-direction.

Method	β	No EOF	EOF	Drag Reduction in %
Theory	0 0.05 0.1 0.2	≈ 75.398	0	100
COMSOL Multiphysics®	0	75.396	0.002	≈ 99.997
	0.05	76.233	0.28	≈ 99.633
	0.1	78.622	1.2	≈ 98.474
	0.2	86.881	4.4	≈ 94.936

Tabelle 5.2.: Dimensionless pressure forces in the direction of the applied velocity field for an obstacle shape given in equation (5.56) and $\tilde{r}_a = 2$.

Figure 5.7 shows a comparison between the numerically and theoretically obtained force in x- and y-direction, plotted over the perturbation parameter β. The parametrization of the obstacle is given by $\tilde{r}_\partial = 1 + \beta(\cos(2\varphi) + \sin(2\varphi))$. Whereas the force in y-direction shows good agreement over the full range of β, the force in x-direction reveals a change of sign in the slope for increasing β which is clearly not covered in our linear theory. In the inset of figure 5.7 a) the shape evolution of the obstacle depending on the perturbation parameter β is shown. Between $\beta = 0.1$ and $\beta = 0.2$, the curvature of the obstacle at the small semi-axis changes its sign (see the black lines drawn at the surface of the obstacle). The change of sign of the curvature at the obstacle might cause the sign-changing in the slope of the force in x-direction as well.

As already mentioned, the numerically obtained pressure force in case of an applied electric-osmotic flow deviates from zero (even for very small values of β) probably due to the finite computational domain as well as the accuracy of the numerical procedure. However, table 5.2 contains a list of numerically obtained pressure forces in x-direction with and without the

presence of an applied electric field corresponding to an obstacle shape given in equation (5.56). The strength of the induced electro-osmotic flow has been computed on the basis of equation (5.48) and the shape constants of the ζ-potential annulus follow equation (5.51). Even though, the pressure force acting on the obstacle increases with increasing β, the pressure force reduction is within 96% even for $\beta = 0.2$.

5.6 Summary & Outlook

In summary, we have presented a novel method for the pressure force reduction of an obstacle in a Hele-Shaw channel subjected to an unidirectional flow field. Whenever a charged obstacle (with a ζ-potential of ζ_0) is surrounded by a ζ-potential annulus (carrying the same ζ-potential as the obstacle) located at the upper and lower wall of the channel and subjected to an applied electric field, an electro-osmotic flow is induced that has the ability to shield the obstacle from the outer flow field. More precisely, if the electro-osmotic slip boundary condition is satisfied at the surface of the obstacle in the leading order ($H/a \to 0$), the pressure force is identically zero. Further, we have argued that a certain parametrization of the annulus region can be found that automatically satisfies the electro-osmotic slip condition. Exemplarily, we have applied these results to slightly deformed cylindrical obstacles and computed the required shape of the annulus as well as the value of the electro-osmotic velocity in order to shield the obstacle. Even for a moderate characteristic length of the annulus region, the exact geometrical shape converges fast towards a circle. We have verified our theoretical prediction with COMSOL Multiphysics® simulations that were also carried out in the Hele-Shaw approximation. Here, we found that the flow field shows good agreement up to a perturbation parameter of $\beta = 0.1$.

We believe that our method is an improvement compared to the strategy reported by Park et al. (2019), since we do not require the presence of a porous layer around the obstacle. With the methods employed by Paratore et al. (2019a,b), the creation of a spatially controlled ζ-potential annulus should be realizable. Even though an exact shaping of deformable objects is generally possible, it has to be emphasized that the experimental realization might be challenging, since the shape deviation of a circle is not very significant.

In further work, full 3D simulations should be employed to reveal the range of validity of the leading-order Hele-Shaw approximation. Furthermore, an experimental validation is desirable, but the direct measurement of the pressure drag force on the obstacle in a Hele-Shaw channel is very challenging, if not impossible. It is therefore more reasonable, to compare experimentally obtained streamlines with theoretically/numerically obtained streamlines for the purpose of validation. The present work could be extended towards higher order Hele-Shaw approximations of the governing equations. The presence of walls, sufficiently far away from a slightly deformed obstacle could also be taken into account following the method of reflections (Brenner and Cox, 1963; Cox and Brenner, 1967).

6 Stability and collapse of a single defect in a bounded liquid layer

The previous chapters dealt with the hydrodynamic interaction between particles or obstacles and complex boundaries, such as fluid interfaces or narrow and partially charged channel walls. In contrast, this chapter focuses on the stability and collapse of defects (holes) in a bounded liquid film in absence of another suspended medium. Nevertheless, we are again focusing on the influence of the boundaries, either at the three-phase contact line of the defect or at the bounding wall. We attempt to answer the following questions: Under which conditions is a defect stable? How does the wetting property of the liquid influence the stability and collapse of a defect? How big is the influence of the contact angle between the liquid film and substrate below? Does the lateral extension of the liquid film influence the stability and the collapse of a single circular hole in a liquid layer?

Surface tension enables liquids to minimize their surface area, and to form various morphologies under external forces or geometrical constraints, such as puddles (de Gennes et al., 2003), thin/thick films (Debregéas et al., 1998; Craster and Matar, 2009), liquid rings (Texier et al., 2013), liquid layers with holes (Taylor and Michael, 1973; Moriarty and Schwartz, 1993; López et al., 2001; Bankoff et al., 2003; Dijksman et al., 2015; Bostwick et al., 2017; Zheng et al., 2018a,b) or fingers (Craster and Matar, 2009). A fundamental understanding of the statics and dynamics of thin liquid films is of crucial importance since the aim of many engineering processes is to produce a uniform liquid film on a solid. The most prominent example are coating processes, in which one or several liquid layers are deposited on a substrate and dried or cured to form a solid layer that carries specific physical properties, in order to improve physico-chemical (e.g., corrosion protection), mechanical (e.g., hardness of the solid surface), optical (e.g., anti-reflection), electrical or magnetic (e.g., insulating the solid) (Montemor, 2014) or wetting properties [e.g., through liquid infused surfaces (Eifert et al., 2014) or sol-gel coating (Kaneko et al., 2019)]. The film is typically deposited on the solid substrate through different methods such as dip or roll coating (Coyle et al., 1990) that typically leads to an nonuniform film thickness. Depending on various parameters and constraints, the film might level itself leading to a uniform film height, or dewet the substrate. Other possible reasons for dewetting are high substrate temperatures (Bäumchen and Jacobs, 2009) or the impact of objects on a thin liquid film. The characterization of the important parameters that determine the stability of defects in liquid films are, among others, the subject of this chapter. It is worth mentioning that after the solidification of the liquid, many other interesting phenomena influence the quality of the coating, such as curling of the solid substrate (in case of soft substrates) or cracking of the dried coating (in case of rigid substrates), due to the stress that builds up during solidification. The former example is known from painting with water colors on a paper. A summary of different phenomena influencing the quality of coatings is given in figure 6.1 by Kistler and Schweizer (1997). However, throughout this chapter, we exclude the solidification process and focus on the physical state of a liquid film that has, for whatever reason, a defect.

The growth and collapse of a dry spot in a thin liquid film is a classical problem in the field of fluid mechanics. Equilibrium solutions for the profiles of axisymmetric systems date back to the early comprehensive works of Lamb (1916) and Padday (1971). Padday (1971) performed one of the first experimental studies of the process of formation and rupture of a thin liquid film on a hydrophobic surface (wax or polytetrafluoroethylene), in which it was found that the liquid film ruptures when its thickness is smaller than a critical value. This critical thickness was found to increase with increasing contact angles between the film and the substrate. A pioneering work carried out by Taylor and Michael (1973), utilizing air jets to study hole formation in water films, indicates the existence of a critical hole diameter representing the stability limit of an infinitely extended film with arbitrary thickness and arbitrary contact angle on the substrate. Furthermore, the authors studied the stability of a two liquid layer configuration, i.e., a water film on a mercury film, where the hole has been created using exchangeable cylindrical probes located at the center of the container. After the probes have been removed, the stability and the collapse of the hole was recorded. However, through energetic arguments, the authors obtained a critical height h_∞, valid for infinitely extended liquid films, as follows

$$h_\infty = 2l_c \sin\left(\frac{\Theta}{2}\right), \tag{6.1}$$

in which $l_c = \sqrt{\gamma_{12}/(\rho g)}$ and Θ are the capillary length relating the importance of gravity relative to surface tension (de Gennes et al., 2003) and the contact angle between the liquid and the solid substrate. For water at room temperature, the capillary length is $l_c \approx 2.73$ mm. Furthermore, equation (6.1) also refers to the maximum height of an infinitely extended liquid puddle (de Gennes et al., 2003). Following Taylor and Michael (1973), holes in liquid films with a height $h < h_\infty$ will enlarge, while for $h > h_\infty$ they close, regardless of their initial diameter d. Experiments by the same authors on holes in a water layer on paraffin wax surfaces did not give an unambiguous picture of hole stability, but demonstrated a wide range of possibilities under which a hole can remain stationary, mainly resulting from contact line friction. Contact line friction is often related to the so-called contact angle hysteresis, i.e., the difference between the contact angle of an advancing liquid puddle (so-called advancing contact angle Θ_a) and the contact angle of a receding liquid puddle (so-called receding contact angle Θ_r) (de Gennes et al., 2003). Moreover, Taylor and Michael (1973) only considered hydrophobic surfaces in their experiments.

Probably inspired by these seminal works, numerous studies have been devoted to the stability of a hole in a liquid layer. Using energy criteria, Sharma and Ruckenstein (1990) theoretically showed that for a given contact angle in a finite domain, a single, circular hole can remain stable. The practically most relevant scenario involves liquid films whose thickness is dictated by a balance between gravitational and surface tension forces that leads, for infinitely extended liquid films, to the height given in equation (6.1). It is known that holes in such capillary-stabilized liquid films are sensitive to the lateral extension of the film. Lubrication theory is commonly employed to compute the hole closure dynamics for finite liquid domains. Moriarty and Schwartz (1993) employed the lubrication theory and studied the stability and evolution of an axisymmetric dry spot in a thin liquid film bounded by rigid vertical walls, showing that the holes either close to form a uniform liquid film or enlarge until a stable equilibrium position is reached. Moreover, the contact line motion at the edge of the dry spot was taken into account by constraining the

radial flow near the contact line (to zero) until the advancing contact angle is reached leading to an artificially adjusted contact line motion. The authors found that external vibrations could give rise to a closure of a hole that is statically stable. When the radius of the hole is small, axisymmetric equilibrium holes in thin liquid layers in an unbounded domain under the influence of surface tension and gravity have been studied by Wilson and Duffy (1996) using matched asymptotic expansions. Their theoretical analysis is valid for a contact angle of $\Theta = 180^\circ$. By employing linear stability theory, López et al. (2001) found that for a substrate of a fixed diameter the axisymmetric equilibrium solutions with dry spots are always unstable to asymmetric perturbations. Furthermore, the stability against axisymmetric disturbances increases, as the size of the dry spot increases. Employing lubrication approximation, Zheng et al. (2018a,b) studied the surface-tension-driven leveling dynamics of a thin viscous film after the closure of an initial 'hole', and they obtained a self-similar solution describing the dynamics of the film profile. However, these results are based on the existence of a precursor film (Bonn et al., 2009; Popescu et al., 2012), i.e., a thin film connecting the flanks of the hole, and consequently, the hole closure dynamics obtained in their study are mainly valid for small contact angles. Very recently, Lu and Corvalan (2019) employed numerical simulations on the dynamics of the collapse of a small circular hole. The authors employed a mirror reflected hole geometry (with respect to the substrate) and therefore limited their simulation to contact angles of 90°. The dewetting and surface deformation of a fluid film, caused by an external air jet, has been studied by Ojiako et al. (2020), employing thin film modeling, numerical simulations as well as experimental methods.

The hole collapse in liquid layers has also been studied experimentally. In the work of Diez et al. (1992), a closing dry spot in an axisymmetric flow of a very viscous fluid toward a central outlet was studied. The experiments were done in a region where there was a balance between gravity and viscous forces, whereas surface tension effects were assumed to be small. A self-similar solution was constructed and shown to compare well with the experimental results after the radius of the dry spot is sufficiently small compared to its initial radius. By employing external forcing such as blowing, Bankoff et al. (2003) studied the diameter, front velocity, dynamic contact angle and interface shape related to a dry spot moving in a thin viscous film and their dependence on the film thickness. Their results show that the final size of the hole increases as the initial fluid depth decreases. Utilizing the centrifugal force by rotating an axisymmetric fluid reservoir, Dijksman et al. (2015) studied the hole collapse in a liquid film, ranging from the limit of pure gravitational driving to entirely surface-tension-driven flows. More recently, Bostwick et al. (2017) studied the collapse dynamics of an axisymmetric thin film that completely wets the bottom of a rotating container with vertical side walls. The effects of capillary, gravitational and centrifugal forces on this converging flow was analyzed using lubrication theory. The motion of the three-phase contact line was modeled with the help of a slip boundary condition, in contrast to the precursor film approach by Zheng et al. (2018a). Under certain circumstances, both modeling approaches (precursor film and slip boundary condition) have shown to lead to comparable results (Savva and Kalliadasis, 2011). Bostwick et al. (2017) report power-law forms for the collapse time when gravitational or surface tension forces dominate the dynamics. By a combination of theory and experimental work, Zheng et al. (2018a) showed the existence of a self-similar solution for the profile and front location in the inward spreading process of a thin viscous liquid film filling a hole.

In spite of all these efforts, the dependence of the critical diameter and the collapse of a hole on

the contact angle and the size of the liquid film has remained largely obscure, probably because studying large contact angles goes beyond the commonly employed lubrication theory. To gain further insight into the stability behavior, an experimental setup has been established which covers a broad range of parameters, such as the contact angle and the extension of the liquid film.

The time evolution of the hole collapse is found to follow a power law. The driving forces (e.g., capillary forces and gravity) and the different resistive forces (inertial forces and viscosity), as well as the geometry of the system and other constraints, strongly influence the exponent in the power law. Redon et al. (1991) found that the expansion rate of the diameter d of a dry patch obeys $d \propto t$, governed by the competition between capillary and viscous forces. The radial component of the velocity is independent of d and the film thickness, but inversely proportional to the viscosity and very sensitive to the contact angle [$u_r \propto \Theta^3$ for small contact angles in agreement with the Cox-Voinov law (Voinov, 1976; Cox, 1986; Bonn et al., 2009)]. In the experiments by Diez et al. (1992), a highly viscous liquid was filled into a circular basin (diameter 40 cm) limited by a concentric circular dam (diameter 10 cm). When the dam is quickly lifted, the liquid surrounding the circular basin flows toward the center. The diameter d of the dry spot was found to scale $d \propto t^{0.762}$, independent of different inertial film heights. In the experiments by Dijksman et al. (2015), a hole was created through rotation of the circular container. After stopping the rotation, a scaling law $d \propto t^{0.55\pm0.05}$ of the collapsing hole was found. The authors explained that the difference between their results and the results obtained by Diez et al. (1992) is due to a larger influence of surface tension compared to gravity. Recently, Bostwick et al. (2017) theoretically studied the evolution of a collapsing hole in the lubrication approximation. For small Bond numbers (capillary dominated flow), they obtained $d \propto t^{0.55}$, whereas $d \propto t^{0.762}$ is the limiting behavior for large Bond numbers, indicating a larger influence of gravity compared to surface tension. The authors obtained good agreement with the experiments by Dijksman et al. (2015) when fitting the relation between contact angle and velocity of the contact line to the experimental data. Very recently, Zheng et al. (2018a) studied the healing of a perfectly wetting fluid film in a circular container. They found a $d \propto t^{0.49}$ scaling and demonstrated agreement between theory and experiments.

This chapter is organized as follows: In section 6.1, the focus lies on the determination of a stability criterion for a single circular hole in a bounded liquid layer. By employing different modeling and simulation methods, the critical diameter of the hole is experimentally, numerically and theoretically obtained. Section 6.2 describes the dynamics of hole collapse. A simple theoretical model is employed that catches the underlying physics of hole collapse. Furthermore, the pinch-off dynamics of the enclosed air bubble is studied and the corresponding scaling laws are determined. A summary of this chapter is given in section 6.3.

6.1 Stability of a hole

The main subject of this section is the determination of stability criterion of a circular hole in a bounded liquid layer. To start with, the experimental setup is presented and experimental results are shown, before we go over to introduce the theoretical/numerical modeling. After that, the theoretical/numerical results are compared to the experimental results.

6.1.1 Experimental analysis

Experimental setup & sample preparation

The experimental setup consists of a linear three-axis translation stage fixed on an optical table, exchangeable flat substrates partially fixed in Plexiglas boxes of different sizes, a high-speed camera (Photron Fastcam SA1.1 Model 675K-M1), an illumination source (LED) and a syringe pump (KD Scientific KDS 210 CE). The high-speed camera was fixed in a specially fabricated device, allowing to translate the camera in three dimensions. Furthermore, the camera can be rotated, allowing the recording of the hole collapse in top view. We employed Plexiglas boxes with a square cross-section in order to minimize the effect of light refraction when recording the time evolution of the holes in side view. The illumination source was placed behind the boxes during the experiments in side view leading to a sharp contrast at the flanks of the hole. This method is known as shadowgraphy (Tropea, 2011). A sketch of the setup is given in figure 6.1 a).

The experiments were performed with four different substrates that were partially fixed at the bottom of the Plexiglas boxes in order to enable a wide range of different contact angles. Among Teflon surfaces and silicone wafers, that were previously cleaned with ethanol and water, we employed superhydrophobic aluminum substrates and liquid infused glass surfaces. All substrates were precisely cut to fit into the container.

The superhydrophobic aluminum substrates (Al) were fabricated following a method closely related to that described by Song et al. (2012). Al plates of a thickness of 2 mm were cleaned by detergent to remove dirt an oil from it. By polishing the surfaces of the Al plates with sandpaper (granulation 500), the oxidation layer was removed. After cleaning the substrates with acetone and water, the samples were immersed into a 4 mol/l aqueous hydrochloric acid solution for $8-12$ minutes. Consequently, the surface roughness of the samples increased. After that, the samples were put into an ultrasonic cleaner in order to remove residual imperfections. After preparing a 1 wt% FAS-ethanol solution (FAS: fluoroalkylsilane) and mixing it for about 2 hours, the specimen were immersed in the FAS solution for about 40 minutes. Care must be taken here, as the specimen has to be completely dry before immersing it into the FAS-ethanol solution. Finally, the specimen was kept in an oven at 100 °C for about 1 hour.

The hydrophobic liquid-infused glass surfaces were prepared following the procedure described by Eifert et al. (2014). After the glass substrates were cleaned with acetone and water, they were immersed in a container filled with silicon oil ($\mu = 5$ cSt) and put inside an oven. Subsequently, the temperature was increased to 300 °C and maintained at this temperature for 3 minutes. After cooling down, the substrates were cleaned using ethanol. Following Eifert et al. (2014), a silicone layer of a thickness of 2.3 nm remains on the glass substrate. Next, the samples were rinsed in fresh silicon oil ($\mu = 5$ cSt) and kept in a vertical position for about 1 hour in order to minimize the oil film thickness.

Wettability characterization

In all experiments, Milli-Q water was used, either as a pure liquid or mixed with glycerol. It is known that when adding glycerol to water the contact angle for many different substrates

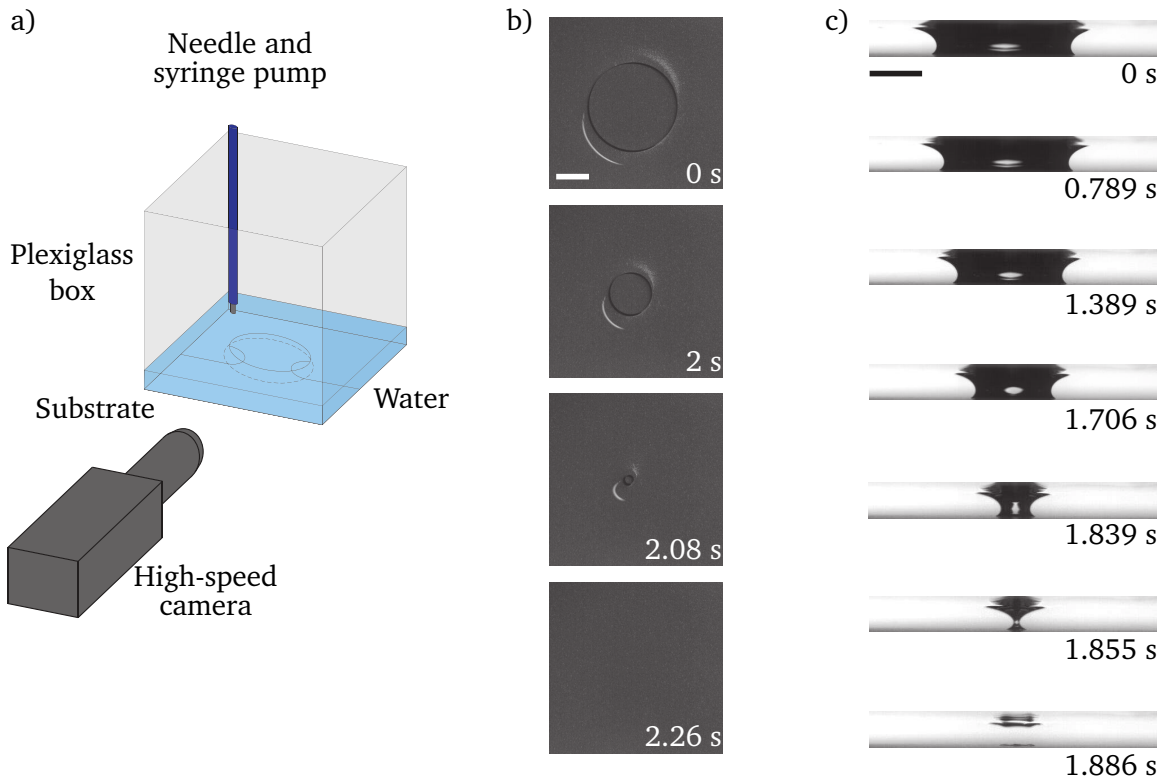

Abbildung 6.1.: a) Schematic illustration of the experimental setup with a needle connected to a syringe pump controlling the flow rate. Time lapse images of the collapse of a hole at the center of a liquid layer on a bounded superhydrophobic Al plate are shown in top b) and side c) view, respectively, which are results from two different experiments. The top view indicates that the hole collapses with a circular shape. The side view (the dark regions are air and the light regions are water) suggests that the thickness of the liquid layer does not change appreciably relative to the situation before the collapse of the hole. The scale bars represent 10 mm [reprinted with permission from Cambridge University Press, J. Fluid Mech. 855 (2018), Lv et al. (2018)].

remain constant, even for concentrations up to 70 wt% glycerol (Sharp, 2012). The wettability characterization was therefore only carried out for water.

By employing a commercial contact angle measurement apparatus (Krüss DSA 100; Krüss Company, Ltd. Germany), the contact angle Θ, the advancing contact angle Θ_a and the receding contact angle Θ_r were measured. The contact angle hysteresis is defined as $\Delta\Theta = \Theta_a - \Theta_r$. We created 5 μl droplets of pure Milli-Q water and carefully placed them on the substrates. For the Al and glass substrates the 5 μl droplet was produced and translated along the surface of each substrate. The angle in front of the droplet, with respect to the translation direction, represents the advancing contact angle, whereas the angle behind the droplet is the receding contact angle. For Teflon, the silicon wafer and the Plexiglas boxes, the advancing and receding contact angles were measured by smoothly increasing and decreasing the volume of the droplet. Each value listed in table 6.1 is the average of ten measurements with standard deviations.

Substrate	Θ (deg.)	Θ_a (deg.)	Θ_r (deg.)	$\Delta\Theta$ (deg.)
Aluminum (Song et al., 2012)	166.3 ± 1.4	167.5 ± 0.7	164.1 ± 1.1	3.5 ± 0.9
Teflon	119.1 ± 2.6	125.6 ± 0.7	93.6 ± 2.3	31.9 ± 1.5
Glass (Eifert et al., 2014)	92.5 ± 4.3	97.6 ± 2.3	93.0 ± 1.7	4.6 ± 2.0
Silicon wafer	50.7 ± 3.9	55.9 ± 1.8	39.1 ± 0.9	16.8 ± 1.4
Plexiglas	90.6 ± 1.6	113.4 ± 1.8	73.8 ± 1.6	39.6 ± 2.8

Tabelle 6.1.: Wettability properties of the substrates, obtained for Milli-Q water.

Experimental procedure

Given the wettability properties of the substrates summarized in table 6.1, the experiments were first carried out with Al, since it provides the lowest contact angle hysteresis. After fixing the substrate inside the box, a thin layer of either water or water-glycerol mixture was added into the Plexiglas container. The height of the liquid film was about $\approx h_\infty/2$ [see equation (6.1)]. Then, using a jet of clean compressed air, a comparatively large hole was created in the center of the container. The nozzle through which the air flows had a diameter of about ≈ 3 mm and the distance towards the substrate was about ≈ 2 cm. Before the hole reaches a stationary and nearly perfect circular shape, strong surface waves were observed caused by the air flow in combination with the comparably low viscosity of the liquid. Then, with the help of the syringe pump the liquid layer was continuously fed with additional liquid at a flow rate of $\mathfrak{Q} = 0.1$ ml/min without any appreciable perturbation of the liquid layer. Six different square boxes have been used with a side length ranging from $L = 7.5$ cm to $L = 19.5$ cm. It is worth mentioning that even in the smallest box the height of the liquid layer only increases by $\mathfrak{Q}/L^2 \approx 0.3$ μm/s. Therefore, the liquid layer is quite close to a static configuration while liquid is supplied and the influence of the liquid inflow is small. As shown in figure 6.1 b) [$t = 0$ refers to the moment when the recording starts] in top view, the hole maintains a circular shape during the collapse. The data of the experiments has been extracted from the side view [see figure 6.1 c)]. In doing so, a custom-made MATLAB® code has been developed that automatically measures the minimum hole diameter by computing the gradient of the grayscale in every image of the sequence. Following figure 6.1 c), the spatial position in which the gradient reaches its maximum corresponds to the flanks of the hole. To guarantee a sufficient long time recording, imaging was performed at 500 frames per second (fps). In order to capture the dynamics of the collapse more precisely, the number of frames per second was increased up to 100 000, but with a smaller field of view (fov).

Experimental results

In agreement to previous theoretical studies, the hole remains open and static as long as the diameter of the hole is larger than a critical value, i.e., d_c. After this diameter has been reached, a highly dynamical process sets in and the hole suddenly collapses (see supplementary movie 1 by Lv et al. (2018) available at `https://doi.org/10.1017/jfm.2018.680`). This behavior was not observed during the studies of Taylor and Michael (1973) or Bankoff et al. (2003), since the authors first produced a liquid layer with a specific thickness, and then created a hole by removing an object which was placed in advance at the center of the liquid layer or by blowing

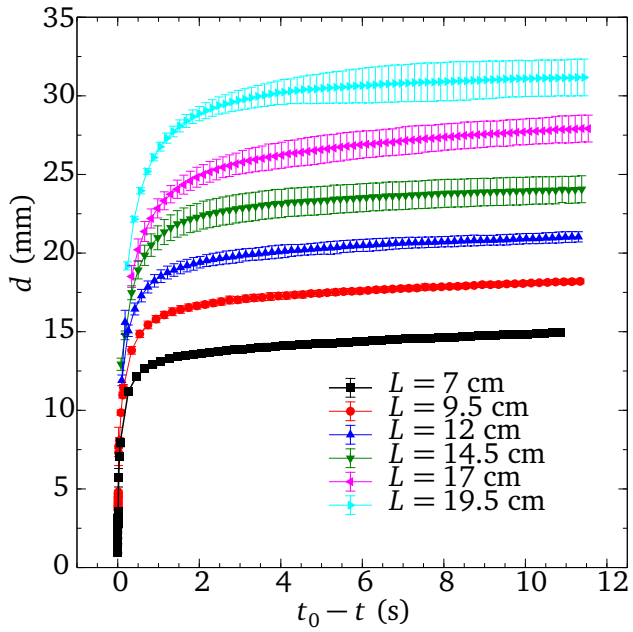

Abbildung 6.2.: Time evolution of holes in liquid layers. The plot shows the instantaneous diameter d of the hole as a function of time $(t_0 - t)$ on superhydrophobic Al surfaces. t_0 is defined as the moment when $d = 0$. All the data points are average values of five experiments with error bars representing the standard deviation. Six boxes with a side length L ranging from 7 cm to 19.5 cm have been employed [reprinted with permission from Cambridge University Press, J. Fluid Mech. 855 (2018), Lv et al. (2018)].

air using a capillary tube. Therefore, these works dealt with an artificial hole collapse, whereas the experimental procedure described here leads to a more natural hole collapse.

Figure 6.1 b) & c) can be used to explain the key factors the hole instability depends on. The 'meridional' curvature [see the cross-section in figure 6.1 c)] creates a pressure jump favoring the opening of the hole. However, the 'azimuthal' curvature or 'hoop curvature' [see the top view in figure 6.1 b)] and the hydrostatic pressure induced by gravity push the liquid to the center. The side views in figure 6.1 c) show that the liquid surface profiles are similar to each other at different instances, which indicates that the variations of the meridional curvature and the hydrostatic pressure are not pronounced. Therefore, the collapse of the liquid layer is mainly caused by the pronounced increase of the hoop curvature as additional liquid is supplied to the liquid layer.

As can be seen in side view [see figure 6.1 c) and supplementary movie 2 by Lv et al. (2018) available at `https://doi.org/10.1017/jfm.2018.680`], when the hole closes, the remaining air is divided into two parts, i.e., an air bubble remains at the surface (at $t = 1.855$ s). Subsequently, the air bubble is compressed to a pancake shape, which is very similar to the spreading of air bubbles on superhydrophobic substrates reported recently (de Maleprade et al., 2016). In the following, the air bubble disappears. However, in experiments carried out on other substrates (e.g., on Teflon) the air bubble remains, which indicates that on the Al surface the air gets transported to the micro- and nanoscopic cavities and might dissolve. Finally, the liquid film at the coalescence point grows, and the whole liquid layer reaches a uniform thickness. The thickness after hole collapse is not significantly different from the thickness before the onset of

the collapse.

In order to quantify the dynamics of the hole, the relationship between the instantaneous diameter d and time $(t_0 - t)$ for a wide range of box sizes, denoting t_0 the moment when $d = 0$, is shown in figure 6.2. The data points in the relationship between d and $(t_0 - t)$ were obtained by averaging five experiments, with corresponding error bars representing the standard deviation. Figure 6.2 clearly demonstrates the existence of two regimes, i.e., a region with a small slope and a region with a higher slope. In the former regime, since the hole remains open at a specific static diameter d when the feed is stopped, the shrinking is caused by the flow due to the pump. We refer to this situation as the hole being stable. On the contrary, in the latter regime the hole continues to close even without further feed, so the hole is unstable. The methods employed in most of the previous research only capture the latter regime, for example by removing a barrier in the central region of the liquid film (e.g., Taylor and Michael, 1973; Diez et al., 1992; Bankoff et al., 2003; Zheng et al., 2018a,b).

The universality of the above results was checked through experiments with substrates of different wettabilities, listed in table 6.1, all performed in the same square box ($L = 7$ cm). The smallest box has been chosen since the sample production is easier the smaller the samples are. The experimental results for the liquid-infused glass and Teflon substrates show a similar behavior as in figure 6.2. As already indicated, after the closure of the hole, an air bubble remains on the Teflon (see supplementary movie 3 by Lv et al. (2018) available at `https://doi.org/10.1017/jfm.2018.680`) and glass substrates.

A special focus is now given to the experimental results obtained for the time evolution of the hole on the silicon wafer (see supplementary movie 4 by Lv et al. (2018) available at `https://doi.org/10.1017/jfm.2018.680`). In figure 6.3 a), the instantaneous diameter d is plotted as a function of $(t_0 - t)$ for the square box of side length $L = 7$ cm. Owing to the high contact angle hysteresis (see table 6.1), the curve for the silicon wafer is not as smooth as for the Al surface (see figure 6.2). Before d reaches d_c, several pinning/depinning events can be observed (i.e., $(t_0 - t) \in [2, 4]$ s, $[8, 10]$ s, $[12, 14]$ s). However, after reaching the critical diameter d_c [the dashed line in figure 6.3 a) is obtained with the theoretical solution from section 6.1.2], smoother dynamics are observed. Selected frames are displayed in figure 6.3 b), showing the hole shapes on the silicon substrate in top view, indicating that the three-phase contact line deviates from a circular shape. Surprisingly, even if the contact angle hysteresis on Teflon is higher than that on a silicon wafer, a smoother evolution of the contact line was observed on Teflon (see supplementary movie 3 by Lv et al. (2018) available at `https://doi.org/10.1017/jfm.2018.680`). So far, the reasons behind this are unclear. The dynamics of a three-phase contact line, depending on the wettability of a solid substrate, is the subject of current research (Johansson and Hess, 2018; Gao et al., 2018). Common theoretical approaches (e.g., Vega et al., 2007; Ramiasa et al., 2011) dealing, among others, with contact line friction modeling, do not provide an explanation for the observed phenomenon.

6.1.2 Theoretical/numerical analysis

Due to the small volumetric flow rate at which additional liquid is fed to the liquid film inside the box, we assume the hole shrinking is a quasi-static process unless the diameter of the hole reaches a critical value $d = d_c$. Consequently, the shape of the liquid surface is solely determined

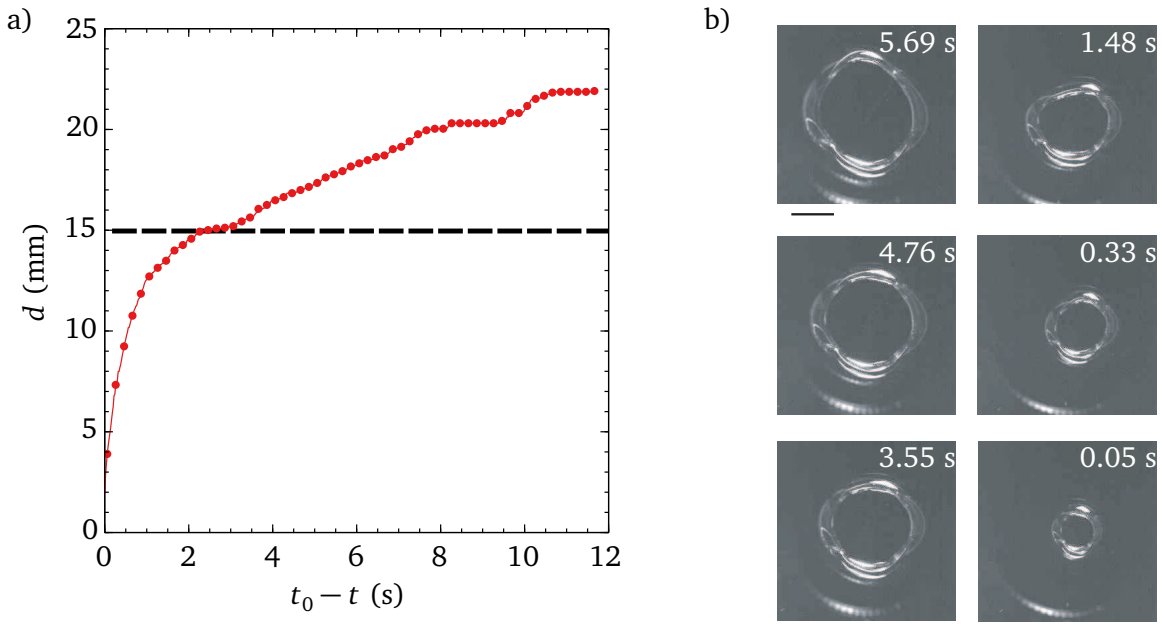

Abbildung 6.3.: Evolution of d with time $(t_0 - t)$ on a silicon wafer in a square box of $L = 7$ cm. a) The red dots are experimental results, and the dashed line is the prediction for d_c based on the asymptotic analytical solution. b) Selected frames from another experiment in top view. The scale bar represents 10 mm. The brightness (in sharp contrast to the other parts) around the three-phase contact line results from the reflection of the light source [reprinted with permission from Cambridge University Press, J. Fluid Mech. 855 (2018), Lv et al. (2018)].

through a balance of gravity and surface tension. The profile of the liquid layer is then controlled by the Young-Laplace equation, derived and discussed in section 2.2.1. It is known that analytical solutions of the Young-Laplace equation (including gravity) are limited to specific cases (Norbury et al., 2004) and therefore, numerical methods are unavoidable. However, if the slope of the liquid interface is sufficiently small in the whole domain, an asymptotic model can be derived that is based on the assumption of small contact angles between the substrate and the liquid.

Numerical solution: Custom-made approach

Considering that the contact angle between water and the box walls is 90°, such as measured for water and Plexiglas (see table 6.1), we assume on the one hand that the perturbation caused by the boundaries/edges of the box does not influence the shape of the liquid surface very much and on the other hand that the shape (square or circular) of the box does not affect the stability of the liquid layer. The latter assumption is verified with the help of full 3D numerical simulations a-posteriori. For now, we may concentrate on rotational symmetric solutions of the Young-Laplace equation that correspond to a circular hole in the center of a circular container.

For rotational symmetric menisci, the Young-Laplace equation is given in equations (2.47) - (2.49). The tangential angle φ and the arc length s are schematically shown in figure 6.4 a). Consequently,

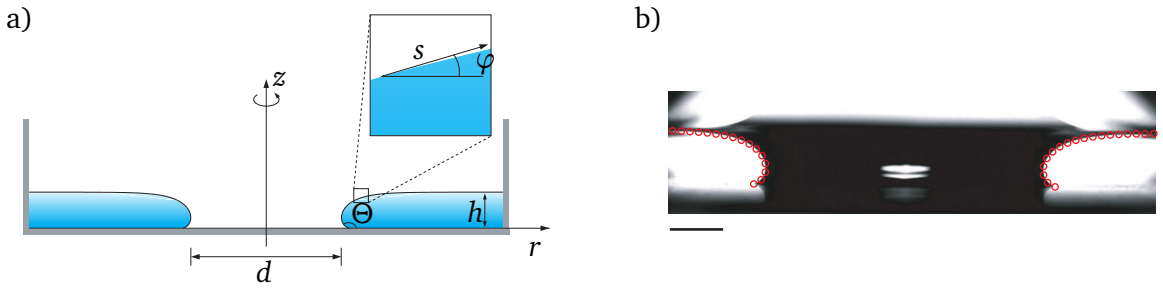

Abbildung 6.4.: a) Axisymmetric liquid layer profile shown in side view, denoting d the diameter of the hole and s the arc length along the liquid surface. As shown in the inset, the tangential angle φ is defined as $\varphi = \arctan(\mathrm{d}z/\mathrm{d}r)$. b) Comparison between the numerical result (red hollow circles) and the experimental results for a superhydrophobic Al substrate in a box ($L = 14.5$ cm) and $d = 26.1$ mm in the current frame. The scale bar represents 5 mm. Comparisons between the numerical solution and the other substrates (listed in table 6.1) is given in figure D.1 [reprinted with permission from Cambridge University Press, J. Fluid Mech. 855 (2018), Lv et al. (2018)].

the shape of the liquid interface is parametrized with its arc length s. For convenience, we find the non-dimensional form by introducing the capillary length l_c

$$\tilde{r} = \frac{r}{l_c}, \quad \tilde{z} = \frac{z}{l_c}, \quad \tilde{s} = \frac{s}{l_c}, \quad \tilde{\lambda} = \frac{\lambda\, l_c}{\gamma_{12}}, \tag{6.2}$$

and rewriting equations (2.47) - (2.49) into

$$\left(\frac{\mathrm{d}\varphi}{\mathrm{d}\tilde{s}} + \frac{\sin\varphi}{\tilde{r}}\right) = \tilde{\lambda} + \tilde{z}, \tag{6.3}$$

$$\frac{\mathrm{d}\tilde{r}}{\mathrm{d}\tilde{s}} = \cos\varphi, \tag{6.4}$$

$$\frac{\mathrm{d}\tilde{z}}{\mathrm{d}\tilde{s}} = \sin\varphi, \tag{6.5}$$

with three boundary conditions $\varphi|_{\tilde{s}=0} = \Theta$, $\tilde{r}|_{\tilde{s}=0} = \frac{\tilde{d}}{2}$ and $\tilde{z}|_{\tilde{s}=0} = 0$ at the contact line. To solve these three first-order ordinary nonlinear and coupled differential equations, a shooting method was employed. Our shooting method is based on changing the values of the two unknown parameters $\tilde{s}_{\mathrm{tot}}$ and $\tilde{\lambda}$ until the following two boundary conditions are satisfied,

$$\tilde{V}\big|_{\tilde{s}=\tilde{s}_{\mathrm{tot}}} = \tilde{V}_0, \quad \varphi|_{\tilde{s}=\tilde{s}_{\mathrm{tot}}} = 0, \tag{6.6}$$

in which $\tilde{V}_0$ is the volume of the liquid for a specific configuration (which corresponds to a specific value of $\tilde{d}$ for a static state), and $\tilde{s}_{\mathrm{tot}}$ is the total arc length. The calculations were performed using the MATLAB® function *ode45*. More precisely, by setting a hole diameter $\tilde{d}$ as well as initial values for $\tilde{\lambda}$ and $\tilde{s}_{\mathrm{tot}}$ (the initial values are typically taken from the numerical solution corresponding to a slightly smaller volume $\tilde{V}_0$) that are typically smaller than the converged result, a small value $\mathrm{d}\tilde{\lambda}$ is added to $\tilde{\lambda}$ during a loop. At a certain iteration, the numerical error increases, indicating that $\tilde{\lambda} + \mathrm{d}\tilde{\lambda}$ has exceeded the optimal value. Then, the last iteration loop

is repeated with a value $\mathrm{d}\tilde{\lambda}/2$. This overall procedure is repeated until a convergence criterion (i.e., the value of the variables at the boundaries match with the boundary conditions up to an error of 10^{-6}) for $\tilde{\lambda}$ is reached. The value s_{tot} is then chosen such that $\tilde{r}|_{\tilde{s}=\tilde{s}_{\mathrm{tot}}} = \tilde{L}/2$. This method is closely related to a one-sided interval nesting method. Figure 6.4 b) demonstrates good agreement between the theory and the experimental results. In figure D.1 in appendix D, a comparison between the experimentally and numerically obtained liquid interfaces are shown for all different substrates employed in this study. After the solutions for the surface profile have been determined, other relevant geometrical and physical quantities such as the curvature at an arbitrary point and each contribution to the total energy of the system (i.e., surface energy and gravitational energy) can also be obtained.

Numerical solution: SURFACE EVOLVER simulations

In the previous paragraph we have assumed that the exact shape of the box does not influence the validity of the results obtained with the custom-made numerical method. In order to verify this assumption, numerical simulations using the public domain finite-element software package SURFACE EVOLVER (Brakke, 1992) have been employed.

The basic concept of SURFACE EVOLVER is to minimize the energy of a surface subjected to user-defined surface tensions, external forces such as gravity and other constraints. SURFACE EVOLVER has been applied for studying various wetting phenomena (e.g., Cho et al., 2005; Kabla and Debregeas, 2007; Chou et al., 2011; Crawford et al., 2013), with excellent agreement to corresponding experimental results.

During a simulation, a partially filled square box is modeled having a pre-defined initial height. An octagonal hole is initialized at the center of the box, having an effective size, such that the initial liquid volume coincides with a predefined value. We further define the contact angles between the liquid layer and the substrate as well as between the liquid layer and the bounding walls. The initial configuration of the simulation is shown in figure 6.5 a).

The potential energy $\mathscr{E}_{\mathrm{p}}$ is defined as

$$\begin{aligned} \mathscr{E}_{\mathrm{p}} &= \mathscr{E}_{\mathrm{sf}} + \mathscr{E}_{\mathrm{g}}, && (6.7)\\ &= \big(A_{\mathrm{lg}} - A_{\mathrm{sl}}\cos(\Theta)\big)\gamma_{12} + \rho g V h_{\mathrm{c}}, && (6.8) \end{aligned}$$

in which $\mathscr{E}_{\mathrm{sf}} = \sum_i \gamma_i A_i$ and $\mathscr{E}_{\mathrm{g}}$ are the surface energy and the gravitational energy, respectively. A_{lg} and A_{sl} are the areas of the liquid-gas and solid-liquid interfaces. In equation (6.8), Young's law has been employed [see equation (2.50)]. h_{c} is the z-coordinate of the center of mass of the liquid layer. During a simulation, a volume has been specified that is smaller than a critical volume V_{c} above which the hole collapses. After the numerical solution has reached a pre-defined convergence criterion, the corresponding value of the hole diameter d can be read of. If the normalized energy difference between two steps in the loop falls below 10^{-6}, the mesh is refined. This procedure has been repeated for four times. A converged numerical solution is exemplarily shown in figure 6.5 b). Following this procedure, the dependency of the hole diameter d on the volume of the liquid film V as well as on the potential energy $\mathscr{E}_{\mathrm{p}}$ is obtained.

The purpose of these simulations is the comparison with the custom-made simulations introduced

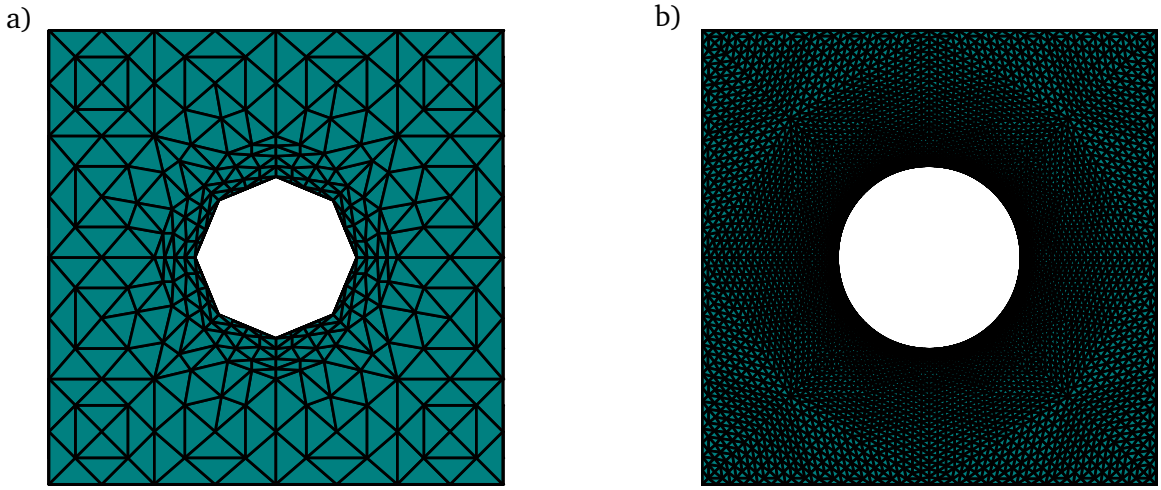

Abbildung 6.5.: Evolution of the liquid interface in a square box with $L = 14.5$ cm computed with SURFACE EVOLVER shown in top view. a) Initial profile of the liquid interface. b) Numerical result after reaching the convergence criterion.

in the previous paragraph. We therefore define the nominal potential energy $\mathscr{E}_{\mathrm{n}}$ and volume V_{n} for the results obtained with SURFACE EVOLVER via

$$\mathscr{E}_{\mathrm{n}} = \mathscr{E}_{\mathrm{p}} - (\Delta\mathscr{E}_{\mathrm{sf}} + \Delta\mathscr{E}_{\mathrm{g}}), \tag{6.9}$$

$$V_{\mathrm{n}} = V - \Delta V, \tag{6.10}$$

in which $\Delta\mathscr{E}_{\mathrm{sf}}$ and $\Delta\mathscr{E}_{\mathrm{g}}$ are defined as follows:

$$\Delta\mathscr{E}_{\mathrm{sf}} = -L^2[1-\pi/4]\gamma_{12}\cos(\Theta) - \Delta A_{lg}\gamma_{12} \tag{6.11}$$

$$\approx L^2[1-\pi/4](1-\cos(\Theta))\gamma_{12}, \tag{6.12}$$

$$\Delta\mathscr{E}_{\mathrm{g}} = \rho g(\Delta V)h_{\mathrm{ce}}, \tag{6.13}$$

$$\approx 1/2\rho g L^2 h_{\mathrm{max}}^2(1-\pi/4). \tag{6.14}$$

Here, it is assumed that outside a circular region of diameter L, the liquid surface reached a constant height h_{max}. Consequently, if the numerical results obtained by SURFACE EVOLVER [modified through equations (6.9) & (6.10)] agree well with the results obtained with the custom-made simulations, the exact shape of the box does not influence the results.

Numerical results

On the basis of the custom-made simulations, specific shapes of the liquid interface are obtained. Exemplarily in figure 6.6, a family of menisci is shown for a circular box of side length $L = 7$ cm and a contact angle of $\Theta = 120^\circ$ for various hole diameter d. During an experiment, the meniscus evolves starting with the black line in figure 6.6 towards the lighter lines. However, the static numerical solutions reveal that for small radii of the hole, the height significantly decreases, implying a decrease in the volume. As an important consequence, for a fixed volume of the liquid layer, at least two solutions of the Young-Laplace equation exist. Beside the derivation of the Young-Laplace equation as done in section 2.2.1, one can obtain the same equation

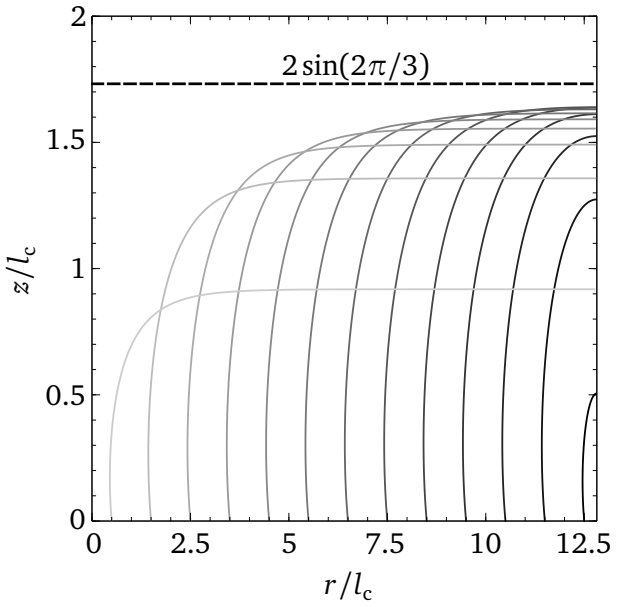

Abbildung 6.6.: Rotational symmetric liquid interface profiles obtained by the custom-made simulations for a circular box with diameter $L = 7$ cm and a contact angle of $\Theta = 120°$ and different hole diameters d. The governing equations are equations (6.3) - (6.5). The dashed line corresponds to equation (6.1) divided by l_c.

when minimizing the potential energy, typically consisting of gravitational and surface energy (Langbein, 2002; Bostwick and Steen, 2015), as already indicated in section 2.2.1. However, a solution of the Young-Laplace equation is by no means stable, i.e., a saddle point or even a maximum of the energy can be reached. Generally, the eigenvalues corresponding to the second variation of the energy shed light into the stability of the system (Langbein, 2002; Bostwick and Steen, 2015). Making use of the latter insights, Langbein (2002) proved a theorem called 'Minimum Volume Condition'. More precisely, whenever an extremum of the volume, depending on any parameter, is reached, the stability branch shows up.

Figure 6.7 shows numerical solutions obtained with the custom-made approach. In figure 6.7 a), the diameter of the hole is plotted over the volume of the liquid film for a fixed contact angle $\Theta = 180°$ and the different box sizes applied in the experiments. Independent of the size of the box, a stability branch exists that can simply be read off following the Minimum Volume Condition by Langbein (2002). Numerical solutions below the point of instability mathematically exist, but refer to a physically unobservable configuration (Moriarty and Schwartz, 1993). The maximum volume of the family of solutions increases with increasing box size. Surprisingly, as shown in figure 6.7 b) for a box size of $L = 14.5$ cm and different wettabilities, the onset of instability weakly depends on the contact angle between the liquid film and the substrate. The comparison between the custom-made simulations and the SURFACE EVOLVER simulations (hollow black circles) show good agreement, which indicates that the influence of the shape of the bounding box on the evolution of the hole is not appreciable. It is worth mentioning that a further decrease of the hole diameter in the SURFACE EVOLVER simulations led to a closure of the hole, even though the stability branch (obtained with the custom-made simulations) was not reached. A possible reason for this deviation could be the initialization of the geometry for the SURFACE EVOLVER simulations. The shape of the hole initially deviates a lot from the expected shape which might cause additional numerical perturbation during the simulation that led to

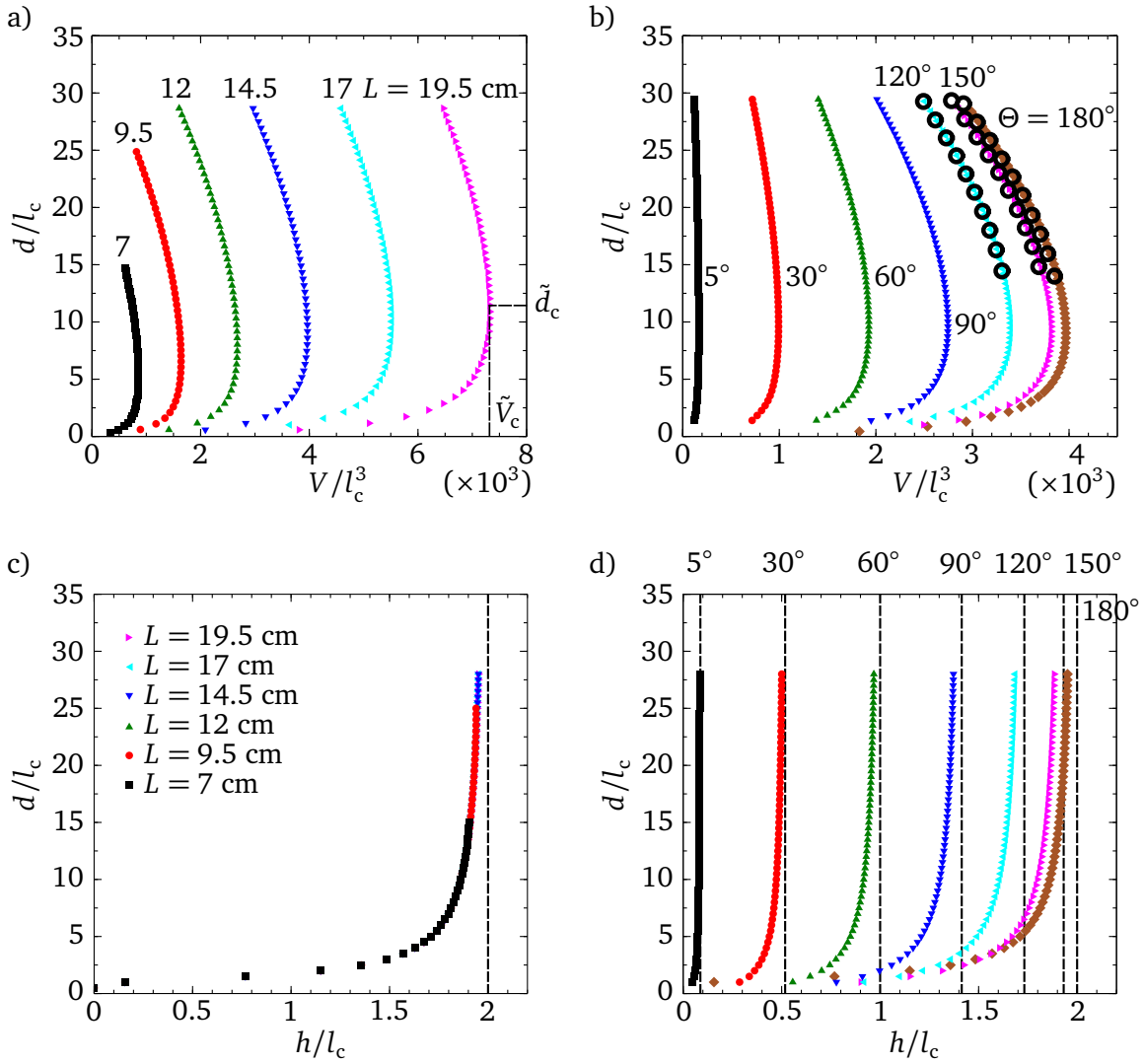

Abbildung 6.7.: Numerical solutions of equations (6.3) - (6.5) obtained with the custom-made approach. a) & b) The hole diameter d is plotted against the volume of the meniscus V for a fixed contact angle $\Theta = 180°$ and different side length of the box L [a)] and for a fixed side length of the box $L = 14.5$ cm and variable contact angles Θ [b)]. V_c and d_c denote the critical values of the volume and the hole diameter when the instability occurs [a)]. The black hollow circles in b) correspond to the numerical solution obtained with SURFACE EVOLVER. c) & d) The diameter of the hole is plotted over the maximum height of the meniscus, reached at $r = L/2$, for a fixed contact angle $\Theta = 180°$ [c)] and a variable size of the box and for a fixed box size $L = 14.5$ cm but a variable contact angle Θ [d)]. The dotted lines correspond to equation (6.1) [reprinted with permission from Cambridge University Press, J. Fluid Mech. 855 (2018), Lv et al. (2018)].

the unexpected behavior. In figure 6.7 c) and d), the diameter of the hole is plotted over the maximum height of the meniscus. The maximum height is reached at the outer boundary at $r = L/2$. In the stable branch, i.e., for sufficiently large d, the height of the liquid film changes very little, either for different box sizes or different contact angles. Therefore in contrast to the work by Taylor and Michael (1973), defining a critical height for bounded liquid layers is impractical. In the experiments, the volume of the liquid film is increased monotonously until it reaches the maximum V_c. Since the syringe pump continuously supplies liquid to the

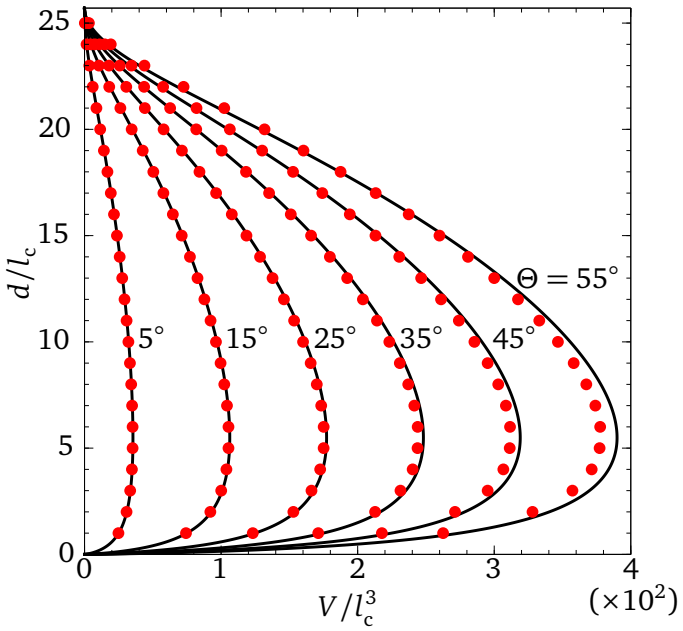

Abbildung 6.8.: Dependence of the diameter d on the volume V in dimensionless form for different contact angles in a circular box with $L = 7$ cm. The black solid lines represent the asymptotic theory, and the red dots are numerical results obtained through the custom-made approach [reprinted with permission from Cambridge University Press, J. Fluid Mech. 855 (2018), Lv et al. (2018)].

configuration, the liquid volume finally exceeds V_c, reaching a regime where no stable solution of the Young-Laplace equation exists, so the hole collapses. Furthermore, our results indicate the existence of a finite value of d_c, no matter what the size of the box or the contact angle on the substrate is. If we increase the box size beyond all limits, our results converge to the results obtained by Taylor and Michael (1973).

Asymptotic model for small contact angles

Due to the small dependency of the critical diameter on the contact angle [see figure 6.7 b)], an asymptotic solution of equations (6.3) - (6.5) is derived that is based on the assumption $\Theta \ll 1$. For sufficiently small contact angles, the following approximations are reasonably well satisfied

$$\sin\varphi \approx \varphi \approx \frac{\mathrm{d}\tilde{z}}{\mathrm{d}\tilde{r}}, \qquad \frac{\mathrm{d}\varphi}{\mathrm{d}\tilde{s}} \approx \frac{\mathrm{d}^2\tilde{z}}{\mathrm{d}\tilde{r}^2}. \tag{6.15}$$

The set of governing equations can then be rewritten as a single, linear second order ordinary differential equation

$$\frac{\mathrm{d}^2\tilde{z}}{\mathrm{d}\tilde{r}^2} + \frac{1}{\tilde{r}}\frac{\mathrm{d}\tilde{z}}{\mathrm{d}\tilde{r}} - \tilde{z} = \tilde{\lambda}. \tag{6.16}$$

Considering the boundary conditions $\tilde{z}|_{\tilde{r}=\frac{\tilde{d}}{2}} = 0$, $\tilde{z}'|_{\tilde{r}=\frac{\tilde{d}}{2}} = \tan\Theta$ and $\tilde{z}'|_{\tilde{r}=\frac{\tilde{L}}{2}} = 0$ (recall that $\tilde{\lambda}$ is a Lagrange multiplier, which is often referred to as the pressure jump across the fluid interface), an analytical solution of the above equation can be obtained,

$$\tilde{z}(\tilde{r}) = \frac{I_1(\frac{\tilde{L}}{2})\left[K_0(\tilde{r}) - K_0(\frac{\tilde{d}}{2})\right] + K_1(\frac{\tilde{L}}{2})\left[I_0(\tilde{r}) - I_0(\frac{\tilde{d}}{2})\right]}{I_1(\frac{\tilde{d}}{2})K_1(\frac{\tilde{L}}{2}) - I_1(\frac{\tilde{L}}{2})K_1(\frac{\tilde{d}}{2})} \tan\Theta, \tag{6.17}$$

where I_n is the modified Bessel function of the first kind and K_n is the Bessel function of the second kind (Magnus et al., 1966). Note that this solution has already been obtained by Moriarty and Schwartz (1993) and used by López et al. (2001). It further leads to an analytical solution for the volume V

$$\tilde{V}\left(\frac{\tilde{d}}{2}\right) = (\Gamma_1 + \Gamma_2)\pi \tan\Theta \tag{6.18}$$

with

$$\Gamma_1 = \frac{\left[\frac{1}{4}(\tilde{d}^2 - \tilde{L}^2)I_0(\frac{\tilde{d}}{2}) - \tilde{d}I_1(\frac{\tilde{d}}{2})\right]K_1(\frac{\tilde{L}}{2})}{I_1(\frac{\tilde{d}}{2})K_1(\frac{\tilde{L}}{2}) - I_1(\frac{\tilde{L}}{2})K_1(\frac{\tilde{d}}{2})}, \tag{6.19}$$

$$\Gamma_2 = \frac{\left[\frac{1}{4}(\tilde{d}^2 - \tilde{L}^2)K_0(\frac{\tilde{d}}{2}) + \tilde{d}K_1(\frac{\tilde{d}}{2})\right]I_1(\frac{\tilde{L}}{2})}{I_1(\frac{\tilde{d}}{2})K_1(\frac{\tilde{L}}{2}) - I_1(\frac{\tilde{L}}{2})K_1(\frac{\tilde{d}}{2})}. \tag{6.20}$$

To reveal the range of validity of the small-angle approximation the analytical solution is based on, we choose a circular box of diameter $L = 7$ cm. Figure 6.8 shows a series of analytical results for d vs. V (solid lines) together with the numerical solutions (red dots) for different contact angles. It becomes clear that the asymptotic solution is still accurate for contact angles up to $\Theta \approx 35°$.

The critical diameter d_c is obtained by solving $\mathrm{d}V/\mathrm{d}d = 0$, which has been done numerically. Figure 6.9 a), show the dependency of d_c on Θ in dimensionless form for box sizes ranging from 7 cm to 19.5 cm (which correspond to the lengths employed in the experiments). The dashed lines are the values of d_c obtained from the asymptotic solution, and the dots are the numerical results obtained with the custom-made approach.

Figure 6.9 a) suggests a weak contact angle dependence of d_c but a stronger dependence on the size of the box, as already indicated before. On the basis of equation (6.18) it becomes clear that the critical diameter obtained with the help of the asymptotic solution is independent of Θ. The critical diameter d_c obtained numerically decreases for larger contact angles, which indicates that the asymptotic solution represents an upper limit for d_c. Although the asymptotic result is obtained based on small contact angles, the comparison shows that it agrees well with the numerical results even for $\Theta \approx 90°$. Furthermore, it can be observed that the critical diameter decreases with increasing contact angle. For larger boxes this behavior is stronger.

Figure 6.9 b) shows the importance of considering finite box sizes. For a specific contact angle, the approach of h_c/h_∞ towards 1 becomes slower and slower with increasing L, where h_c is the film thickness at the boundary of the box in the configuration where the critical hole diameter is

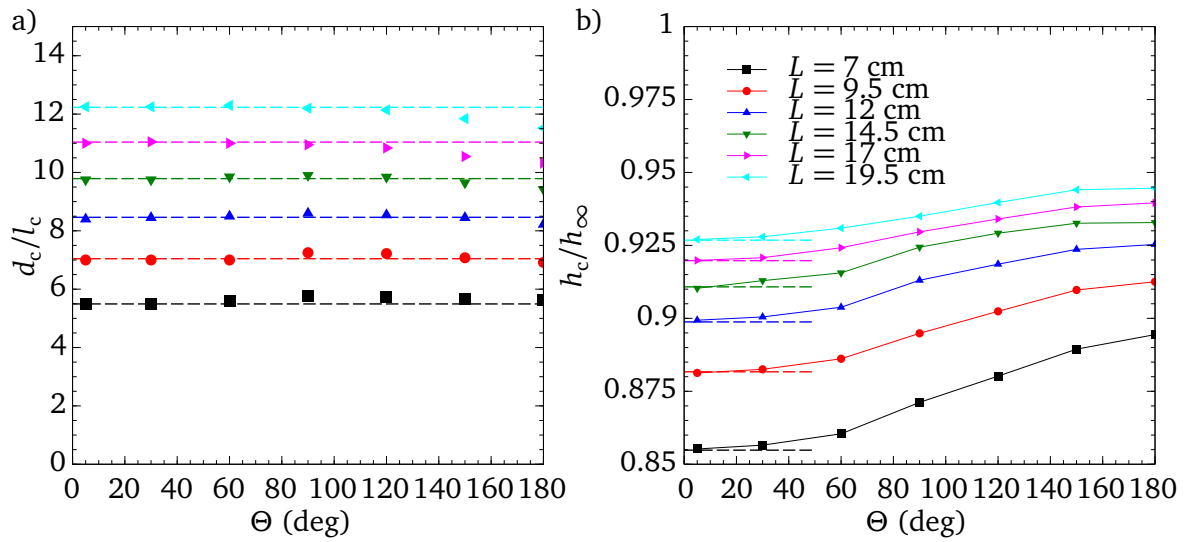

Abbildung 6.9.: a) Dependence of d_c on Θ for six different box sizes. The dashed lines represent the asymptotic result ($\Theta \ll 1$), and the symbols are numerical solutions obtained with the custom-made approach. b) Numerical results for the critical height h_c (corresponding to d_c) scaled by h_∞ as a function of the contact angle Θ. h_c is the film thickness at the boundary of the box. The dashed lines correspond to the asymptotic model [reprinted with permission from Cambridge University Press, J. Fluid Mech. 855 (2018), Lv et al. (2018)].

reached. As one example, when $\Theta = 180°$ and $L = 19.5$ cm, $h_c/h_\infty \approx 0.9476$. In other words, for obtaining values of h_c very close to h_∞, the size of the box needs to be extremely large. Simultaneously, d_c increases with increasing box size. In the limiting case, i.e., $L \to \infty$, our results converge to the results obtained by Taylor and Michael (1973).

6.1.3 Comparison between experiments and theory/numerics

Extracting the critical diameter from experiments

Since the exact value of d_c is a-priori unknown from the experimental results, a well defined procedure for the extraction of this value is required. Unfortunately, previous studies did not provide a clear description of the extraction procedure of the critical diameter (Taylor and Michael, 1973; Bankoff et al., 2003; Dijksman et al., 2015). Considering an initial hole diameter significantly larger than the capillary length, the height of the liquid film is nearly independent of the diameter of the hole [see figure 6.7 c) & d)]. Assuming a constant height given by equation (6.1), the volumetric flow rate $\mathfrak{Q}$ is given through

$$\mathfrak{Q} = -\pi l_c \sin(\Theta/2) d\dot{d}, \tag{6.21}$$

in which $\dot{d}$ represents the time derivative of d. For a given $\mathfrak{Q}$, the last equation represents a first order ordinary differential equation for the hole diameter with solution

$$d(t) = \left(d_0^2 - \frac{2\mathfrak{Q}}{\pi l_c \sin(\Theta/2)} t \right)^{1/2}, \tag{6.22}$$

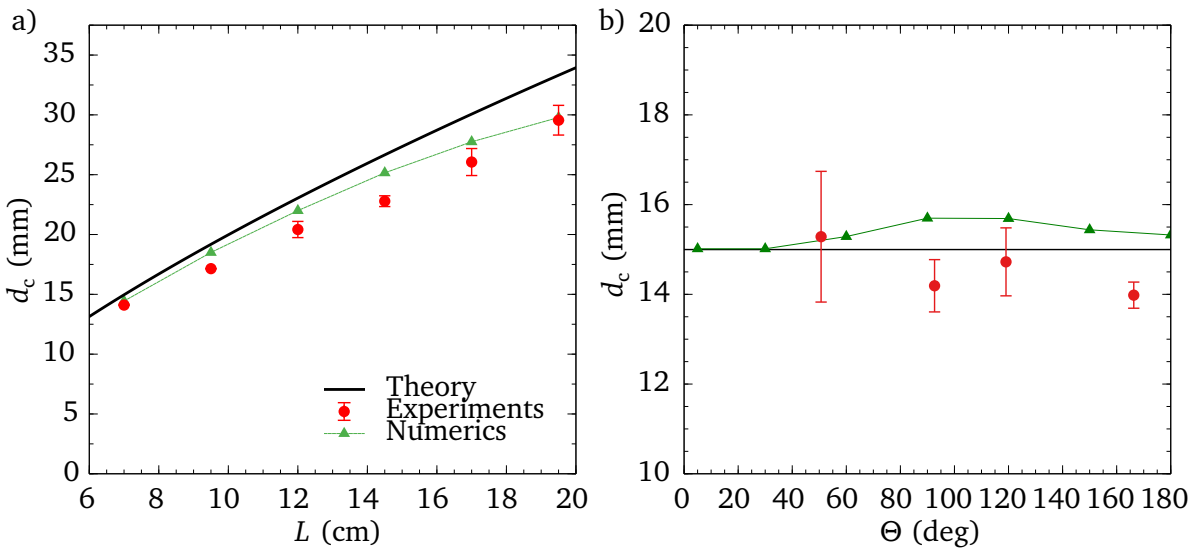

Abbildung 6.10.: a) Dependence of d_c on L on superhydrophobic Al surfaces. The experiments were performed in square boxes with $L = 7.0$ cm, 9.5 cm, 12.0 cm, 14.5 cm, 17.0 cm, and 19.5 cm. The green triangles are numerical results (in circular boxes with different box diameters L) obtained by the custom-made simulations with the green dashed line as a guide of the eye. The black solid line is the theoretical result based on an asymptotic method for small contact angles (in circular boxes with different box diameters L). b) d_c as a function of the contact angle. Four different contact angles (red dots) have been studied experimentally in the square box with $L = 7$ cm. The green triangles are numerical results. The black solid line is the asymptotic solution for d_c. All the red dots are average values of five experiments with error bars representing the standard deviation [reprinted with permission from Cambridge University Press, J. Fluid Mech. 855 (2018), Lv et al. (2018)].

in which d_0 corresponds to the initial hole diameter, representing the first hole diameter extracted from the experimental data. Since we overestimated the height throughout this modeling, the slope of $d(t)$ is clearly smaller than the slope of d over t obtained experimentally. On the basis of the solutions corresponding to the square box with $L = 7$ cm, a value ε, representing the difference between equation (6.22) and the experimental curve, is fixed in order that the experimentally and theoretically obtained results coincide. Following this approach, $\varepsilon \approx 3.74\%$ has been obtained. For the other box sizes, it is assumed that as soon as the difference between equation (6.22) and the experimentally obtained curve exceeds 3.74%, the critical diameter has been reached.

Comparison of the results

In figure 6.10 a), results obtained on superhydrophobic Al substrates in square boxes of different sizes are displayed. The red dots represent the experimental values of d_c that have been obtained as the average of five measurements, following the method explained in the previous paragraph. The green triangles are numerical results extracted from the data shown in figure 6.7 a) (i.e., the critical values d_c and V_c corresponding to the maximum volume). Even though the asymptotic model is constructed based on the assumption $\Theta \ll 1$ and cannot be justified for large contact angles a-priori, the numerical simulations suggest a weak dependence of d_c on the contact angle.

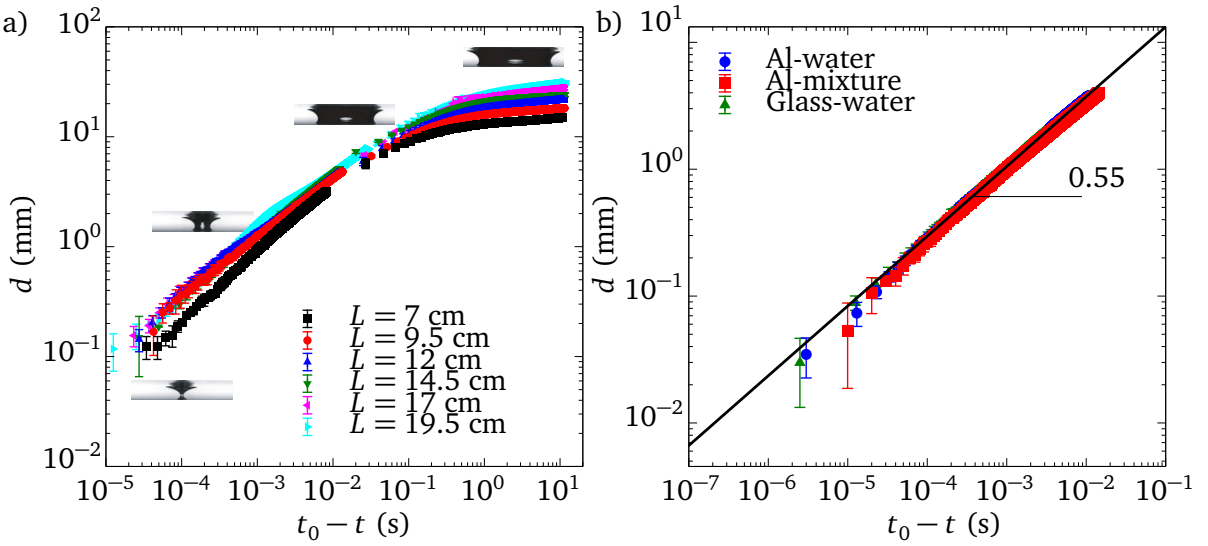

Abbildung 6.11.: Time evolution of the liquid surface around the point when the hole closes. a) Superhydrophobic Al substrates have been used in square boxes of different size. d as a function of $(t_0 - t)$ is shown in a log-log plot. b) Results on Al surfaces ($L = 7$ cm) obtained with water (red squares) and water-glycerol mixture (green triangles), together with results on liquid-infused glass ($L = 12$ cm) obtained with water (blue circles), recorded at 100 000 fps [reprinted with permission from Cambridge University Press, J. Fluid Mech. 855 (2018), Lv et al. (2018)].

Therefore, the results of the asymptotic theory are added to the plot, represented by the black solid line. Figure 6.10 a) shows that d_c increases with L. The experimental and the numerical results are consistent with each other. In spite of its inherent assumption of small contact angles, even the asymptotic method provides a reasonable approximation to the experimental data and provides an upper limit for the critical diameter as already suggested.

Figure 6.10 b) clearly shows that stable holes exist for a wide range of contact angles. Moreover, d_c is virtually independent of the contact angle, and the experimental results are consistent with the numerical and theoretical results.

6.2 Collapse dynamics

After the stability limit has been reached, a highly dynamic process sets in and the hole collapses. This section is dedicated to the dynamical behavior of the hole collapse. Starting with the discussion of the experimental results, a simplified theoretical model is introduced that captures the main physics of the dynamics. After the hole has collapsed, the thickness of the liquid column as a function of time has been recorded and theoretically explained with a simple scaling law analysis.

6.2.1 Experimental analysis

To better resolve the final moments of hole collapse, additional experiments were performed with a higher time resolution. The complete time evolution of d, starting from the initial moment when $d \gg d_c$ is shown in figure 6.11 a) as a log-log plot. High-speed imaging with mainly two different frame rates, i.e., 500 fps for the inertial collapse and 73 000 fps for the final stages

of collapse to capture, has been employed. The first set of experiments was carried out on Al superhydrophobic substrates with different box sizes. To reveal the influence of the wettability of the substrate on the dynamics of the hole collapse, two different substrates have been considered. In figure 6.11 b), data obtained with a further increased frame rate of 100 000 fps are shown: the red squares and blue dots represent experiments carried out using superhydrophobic Al plates ($L = 7$ cm) and liquid-infused glass ($L = 12$ cm), respectively, whereas the green triangles correspond to a water-glycerol mixture ($\mu \approx 2.6$ cSt) on a superhydrophobic aluminum substrate. It is interesting to note that the hole collapse predominantly obeys a scaling law

$$d \approx c_1 (t_0 - t)^{0.55} \tag{6.23}$$

similar to experimental results recently reported for converging fluid films driven by surface tension and gravitational forcing (Dijksman et al., 2015). The values for the coefficient c_1 are $c_1 \approx 0.045$ m/s$^{0.55}$ and $c_1 \approx 0.047$ m/s$^{0.55}$ for the Al and liquid-infused substrates, respectively. Such a scaling has been recognized as a result of the thin film theory by Bostwick et al. (2017), in case where capillary forces dominate over gravity. As common in thin film dynamics, the transient and convective derivatives of the velocity field have been neglected, because both are of order $O(\varepsilon^2 \mathrm{Re})$, in which $\varepsilon = H/L \ll 1$, is a perturbation parameter (see equation (C.6) in appendix C). Furthermore, their results were limited to a quasi-static hole evolution, i.e., the time dependency of the parametrization of the film height was neglected throughout their study. A rough estimation of the typical Reynolds number during the experiments leads to $\mathrm{Re} \approx 550$. For high contact angles $\varepsilon^2 \mathrm{Re}$, reflecting the importance of transient and convective terms, is in the order $O(10^0 - 10^1)$ and therefore exceeds the limit of validity of lubrication theory.

The hole collapse in our experiments is reminiscent of the final stages of the pinch-off of air bubbles in an inviscid liquid, which has been studied quite extensively. Longuet-Higgins et al. (1991) demonstrated that the pinch-off dynamics can be captured with a two-dimensional model. It shows that the inertia of the water dominates the asymptotic dynamics, so that the surface tension, viscosity and the influence of the gas may be neglected. In this limit the evolution should approximately follow the power law $d \propto t^{0.5}$, which is supported by simulations and experiments (Longuet-Higgins et al., 1991; Oguz and Prosperetti, 1993; Burton et al., 2005). Thoroddsen et al. (2007) carried out a systematic experimental study of the pinch-off of a bubble in water and found that the radius $d/2$ of the neck of the bubble shrinks with a power law behavior $(d/2) \propto t^{0.57 \pm 0.03}$ over more than two decades. Their results are in good agreement with the numerical studies of Leppinen et al. (2005), who carried out numerical simulations of the break-up of a bubble in an inviscid liquid and observed a pinch-off power law with an exponent 0.55 ± 0.01. In the analytical work by Eggers et al. (2007), the collapse of an axisymmetric cavity in a low-viscosity fluid such as water was studied, in which the surface tension, gas density and viscosity were neglected. Assuming high Reynolds numbers and a slender geometry, the authors assumed a distribution of mass sources along the axial length of the cavity. In contrast to a previous work by Gordillo et al. (2005), the axial length scale has been taken into account, showing better agreement to numerical results. Eggers et al. (2007) obtained the time-dependent scaling exponent as $\alpha \approx 1/2 + 1/\left[4\sqrt{-\ln(\tilde{t}_0 - \tilde{t})}\right]$. Based on the latter expression, a small increase of the scaling coefficient from 0.55 to 0.57 was found. These results have been verified by numerical simulations carried out by the same authors, as well as by Lu and Corvalan (2019). The results by Eggers et al. (2007) also indicate that the dynamics of inviscid bubble pinch-off is

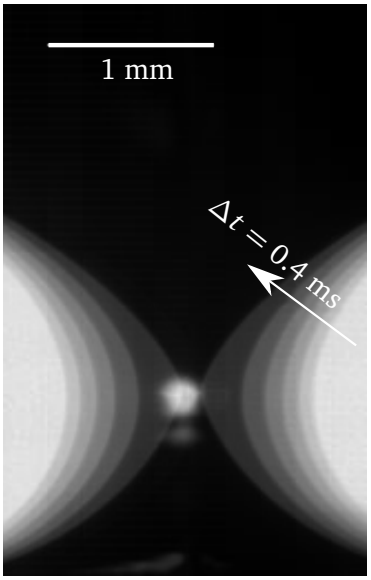

Abbildung 6.12.: Time lapse of the collapse of the hole in the last moment before the hole is closed. The flanks of different grayscale correspond to different time steps. Between two neighboring profiles the time step is $\Delta t = 0.4$ ms. In the region of the smallest diameter, pinching can be observed. The white spot at the center of the hole corresponds to a light reflection.

not universal, the exact value of the exponent weakly depends on the details of each experiment, such as the employed fluids and/or other constraints. In the theoretical model derived by Eggers et al. (2007), the only two remaining terms represent a balance of inertial forces. Therefore, a simple explanation of the scaling behavior is not possible, since scaling arguments generally require different types of driving and resisting forces. In agreement with Eggers et al. (2007), our results indicate that viscosity, the capillary forces and the presence of air inside the hole can be neglected. $d \propto (t_0 - t)^{0.55}$ is consistent with the corresponding theoretical prediction. Indeed, as shown in figure 6.12, during the collapse of the hole a pinching in the region of highest curvature can be observed. The capillary forces therefore just trigger the instability, and the final collapse is governed by inertia only. As an important consequence, if pinching at the point of highest curvature on the flanks of the hole is neglected, the scaling coefficient should lead to $\alpha = 1/2$. In the following subsection, a simplified model is derived that is in agreement with the leading-order result obtained by Eggers et al. (2007).

6.2.2 Modeling the hole closure dynamics using a simplified model

In this subsection we present a simple model to study the effects governing the hole collapse. For the sake of simplicity, we choose an approach in which we assume that the liquid film has a rectangular cross-section (see figure 6.13). This approach is feasible, since pinching is neglected throughout this subsection and the meridional curvature should play a minor role during the collapse of the hole.

The volume V of the liquid layer is constant over the time span of the hole collapse. Consequently, the volume rate caused by the syringe pump is neglected throughout this modeling. The time

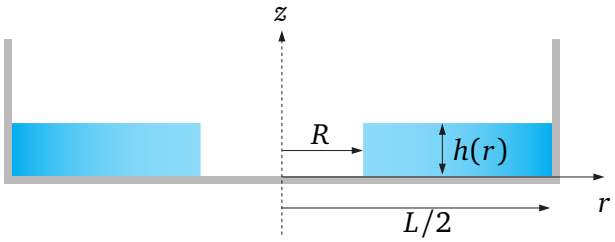

Abbildung 6.13.: Sketch of the rectangular cross-section of a liquid film in a circular container of diameter L. $R(t)$, $h[R(t)]$ are the instantaneous radius of the hole and the thickness of the liquid film, respectively. The meridional curvature [as shown in figure 6.1 c)] is neglected in this model and the contact angle Θ is therefore not geometrically captured [reprinted with permission from Cambridge University Press, J. Fluid Mech. 855 (2018), Lv et al. (2018)].

until the hole collapses is sufficiently short, to satisfy this assumption reasonable well. The height $h(R)$ of the liquid film can be expressed as

$$h(R) = \frac{V}{\pi\left[\left(\frac{L}{2}\right)^2 - R^2\right]}. \tag{6.24}$$

After integrating the continuity equation (in cylindrical coordinates) over $z \in [0, h(R)]$, we find

$$\int_0^{h(R)} \frac{1}{r}\frac{\partial}{\partial r}(r u_r)\,\mathrm{d}z + u_z[h(R)] - u_z(0) = 0, \tag{6.25}$$

in which u_r and u_z denote the radial and the vertical velocities, respectively. We neglect the influence of viscosity and therefore assume that u_r is independent of z. The vertical velocity at $z = 0$ vanishes due to the no-penetration condition at the rigid walls. By setting $u_z[h(R)] = \partial h(R)/\partial t$ and with the help of equation (6.24), we arrive at

$$u_r = \frac{R\dot{R}}{r}\left[1 - \frac{r^2 - R^2}{\left(\frac{L}{2}\right)^2 - R^2}\right]. \tag{6.26}$$

We denote the time derivative as $\dot{R} = \partial R/\partial t$. It is easy to verify that equation (6.26) indeed satisfies the no-penetration condition at the vertical wall of the container, i.e., when $r = L/2$.

The energy balance equation in absence of viscous dissipation reads

$$\frac{\partial}{\partial t}(\mathscr{E}_\mathrm{P} + \mathscr{E}_\mathrm{K}) = 0, \tag{6.27}$$

in which $\mathscr{E}_\mathrm{P}$ and $\mathscr{E}_\mathrm{K}$ are the potential and the kinetic energy, respectively. The potential energy of

our system consists of the surface energy and the gravitational energy, and can be written as

$$\begin{aligned}\mathscr{E}_{\mathrm{P}} &= \pi\left(\frac{L}{2}\right)^2\left[1-\left(\frac{R}{L/2}\right)^2\right]\gamma(1-\cos\theta)+2\pi\left(\frac{R}{L/2}\right)\frac{\gamma V}{\pi\left(\frac{L}{2}\right)\left[1-\left(\frac{R}{L/2}\right)^2\right]} \\ &+ \frac{\rho V^2 g}{2\pi\left(\frac{L}{2}\right)^2\left[1-\left(\frac{R}{L/2}\right)^2\right]}+C. \end{aligned} \tag{6.28}$$

The first two terms correspond to the surface/interfacial energy of the film, whereas the last term is the gravitational energy and C refers to a constant of no further interest ($C=0$). Here, we limit our study to the last moments of the hole collapse, i.e., when $R/(L/2)\ll 1$. By employing a Taylor series expansion and keeping only terms up to the second order in $R/(L/2)$, we obtain

$$\mathscr{E}_{\mathrm{P}} \approx \pi\left(\frac{L}{2}\right)^2\left[1-\left(\frac{R}{L/2}\right)^2\right]\gamma(1-\cos\Theta)+2\pi\left(\frac{R}{L/2}\right)\frac{\gamma V}{\pi\left(\frac{L}{2}\right)}+\frac{\rho V^2 g}{2\pi\left(\frac{L}{2}\right)^2}\left[1+\left(\frac{R}{L/2}\right)^2\right]. \tag{6.29}$$

To compute the kinetic energy of the film, the radial velocity has been evaluated at $r^{\mathrm{c}} = (L/2+R)/2$. With the help of equation (6.26) we obtain

$$u_r^{\mathrm{c}} = \frac{\left(\frac{R}{L/2}\right)\dot{R}\left(3+\frac{R}{L/2}\right)}{2\left(1+\frac{R}{L/2}\right)^2}, \tag{6.30}$$

and the corresponding kinetic energy

$$\mathscr{E}_{\mathrm{K}} = \rho V\frac{\left(\frac{R}{L/2}\right)^2\dot{R}^2\left(3+\frac{R}{L/2}\right)^2}{8\left(1+\frac{R}{L/2}\right)^4} \approx \frac{9}{8}\rho V\dot{R}^2\left(\frac{R}{L/2}\right)^2. \tag{6.31}$$

If we introduce dimensionless quantities $R/(L/2)$, t/T and $V/(L/2)^3$, with T being a characteristic time scale and inserting equations (6.29) and (6.31) into equation (6.27), we eventually get

$$1+\tilde{R}\left[\pi\frac{\cos\Theta-1}{\tilde{V}}+\mathrm{Bo}\frac{\tilde{V}}{2\pi}+\frac{9}{8}\mathrm{We}\left(\dot{\tilde{R}}^2+\tilde{R}\ddot{\tilde{R}}\right)\right]=0, \tag{6.32}$$

in which $\mathrm{Bo}=\rho g(L/2)^2/\gamma$ and $\mathrm{We}=\rho(L/2)^3/(\gamma T^2)$ are the Bond number, relating the gravitational force to the surface tension force and the Weber number relating the inertial force to the surface tension force, respectively. Since our model is limited to the situation in which the radius of the hole is small compared to the radius of the container, we choose the characteristic time $T=0.01$ s according to our experimental results from figure 6.11 a), leading to $\mathrm{Bo}\approx 708$ and $\mathrm{We}\approx 5.2\times 10^4$, for $L=14.5$ cm. We therefore consider equation (6.32) in the limit of high Weber numbers, which leads to

$$\tilde{R}\ddot{\tilde{R}}+\dot{\tilde{R}}^2=0 \tag{6.33}$$

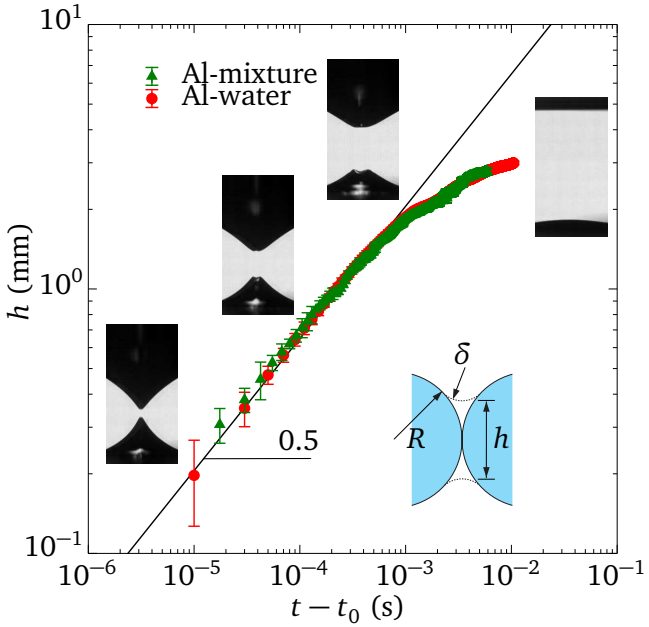

Abbildung 6.14.: Time evolution of the liquid column after hole closure. h is represented as a function of $(t - t_0)$ in a log-log plot. Each dot represents the average value of five experiments with error bars indicating the standard deviation. The red squares and green triangles represent results obtained on Al surfaces with water and a water-glycerol mixture, respectively. The solid line is the best fit to the experimental data based on the scaling law of equation (6.34). The snapshots added to specific sections of the curves give an impression of the corresponding shape of the liquid surface. The sketch shows the geometry used for the scaling analysis [reprinted with permission from Cambridge University Press, J. Fluid Mech. 855 (2018), Lv et al. (2018)].

A $\tilde{R} \propto (t_0 - t)^{\frac{1}{2}}$ scaling is obtained based on this approximation. This result coincides with the time-independent part (zeroth-order contribution) of the solution obtained by Eggers et al. (2007).

6.2.3 Evolution of the liquid column after hole collapse

When a single hole on a superhydrophobic Al surface closes, a growing liquid column separates the gas above from the gas inside the surface bubble. Finally, the liquid gets redistributed into a layer of uniform thickness to minimize the potential energy. Experimental results plotted in figure 6.14 show that the height of the liquid column h shortly after the hole has closed obeys the following scaling law

$$h \approx c_2 \left(\frac{\gamma l_c}{\rho} \right)^{\frac{1}{4}} (t - t_0)^{\frac{1}{2}}, \tag{6.34}$$

in which the unknown coefficient has been determined to be $c_2 = 3.1$ by fitting.

Compared with the hole collapse discussed in horizontal direction, the evolution of the height of the liquid column h after hole closure/bubble pinch-off has been studied to a lesser extent. Thoroddsen et al. (2007) reported that after pinch-off, the vertical separation of the air cones as a function of time obeys a power law with a fitted exponent of 0.49 ± 0.03, which is in agreement with the numerics of Leppinen et al. (2005) who found an exponent of 0.48 ± 0.05 for the

evolution of the separation length scale in the breakup of a bubble in an inviscid liquid. The closing of the hole bears a geometrical similarity to the coalescence of droplets or air bubbles (Thoroddsen et al., 2005; Ristenpart et al., 2006; Courbin et al., 2009; Bird et al., 2009; Eddi et al., 2013; Paulsen et al., 2014), which has been intensely studied in recent years. For instance, Duchemin et al. (2003) studied the inviscid coalescence of drops using a boundary integral method. They proposed a power-law scaling for the neck radius as a function of time with an exponent of 0.5. In the work of Thoroddsen et al. (2005), the growth rate of the neck formed after the coalescence of two air bubbles was measured and modeled based on a capillary/inertial balance. A scaling for the neck radius as a function of time with an exponent of 0.5, valid for a comparatively short time interval, was found. Previous results by Eggers et al. (1999) indicate that already a one-dimensional model can capture the underlying physics. The scaling law modeling shown subsequently is in close analogy to the work reported on the coalescence of drops or air bubbles. The geometry employed for the scaling law analysis is shown in the inset of figure 6.14. As known from equation (6.1), $R \propto l_c$. The balance of capillary and inertial forces for a growing neck reads $\gamma/\delta \propto \rho(h/t)^2$. Following the inset in figure 6.14, we find through geometrical considerations $\delta \propto h^2/l_c$. Finally, the scaling law from equation (6.34) is obtained.

Furthermore, we have experimentally studied the influence of viscosity on the evolution of the liquid column. With a water-glycerol mixture 2.6 times more viscous than pure water, very similar results were obtained (green triangles in figure 6.14).

6.3 Summary

In this chapter, we have studied the stability and collapse of a single circular hole in a bounded liquid film having a thickness determined through a balance of capillary and gravity forces. Experimentally, two distinguished regimes were identified, an initial quasi-stationary evolution followed by a dynamic hole collapse beyond the stability threshold. Based on theoretical models and numerical calculations, we revealed that the evolution of the hole is controlled by a critical value of the hole diameter below which no stable solution of the Young-Laplace equation exists. We have shown that the stability threshold strongly depends on the size of the box but, surprisingly, weakly depends on the contact angle between the liquid film and the substrate. This conclusion was corroborated experimentally using substrates with various sizes and wettabilities. Satisfactory agreement between the different approaches has been obtained. The contact angle hysteresis on the employed superhydrophobic and hydrophobic liquid-infused substrates is very small, which largely eliminates the uncertainties resulting from contact line friction (Taylor and Michael, 1973; Bankoff et al., 2003). However, on surfaces with higher contact angle hysteresis, shape deviations from a perfect circular hole have been obtained that mainly occur in the stable regime of the hole. For most practical applications such as coating, it is tempting to regard a liquid layer as infinitely extended. However, our results reveal that stable holes exist for finite (or bounded) configurations independent of the contact angle. The influence of the geometrical shape of the box on the critical hole diameter is, on the other hand, negligible. The latter has been shown with the use of SURFACE EVOLVER simulations.

The dynamics of hole collapse was studied using high-speed imaging. Scaling laws were identified describing the time evolution of the liquid surface during hole collapse. The collapse is governed by a time dependence $d \propto t^{0.55}$, indicating the dominance of inertial effects. Consequently,

capillary forces solely trigger the instability. The influence of viscosity was studied exemplarily by employing a water-glycerol mixture having a viscosity approximately 2.6 times that of water. A simple model was build that is consistent with the leading-order scaling coefficient obtained by Eggers et al. (2007). It was also found that the thickness of the liquid column forming after the hole has closed obeys a $h \propto t^{\frac{1}{2}}$ scaling law. A similar scaling has been observed in the context of coalescence of bubbles or droplets.

7 Collapse of multiple holes in an unbounded liquid layer

In the previous chapter, the stability and collapse of a single circular hole in a bounded liquid film having a height resulting from a balance between gravitational and surface tension forces has been studied. In particular, we have investigated the influence of the size of the box and the wettability of the substrate on the stability and collapse of a single hole. On the basis of the results of chapter 6, the investigation of the collapse of multiple holes in an infinitely extended film is the main topic of this chapter. Specifically, we aim to answer the following question: How do multiple circular holes evolve in time?

The rupture of a thin polymer film, which is applied to a solid substrate and heated above the glass transition temperature, serves as a classic example of a multi-hole formation in a thin liquid film (Karapanagiotis and Gerberich, 2005; Seemann et al., 2005; Bäumchen and Jacobs, 2009). Here, the thickness of the polymer films is of the order of $O(10^{-8})$ m and therefore small compared to the capillary length $l_c \approx O(10^{-3})$ m. Under these conditions, intermolecular forces (so-called van der Waals forces) become dominant. More specifically, for film thicknesses smaller than $O(10^{-6})$ m the interaction of atoms at the solid-liquid interface explicitly has to be taken into account (Pahlavan et al., 2018). In these cases, van der Waals forces predominantly trigger the instability and the formation of holes that grow with time. Recently, Peschka et al. (2019) studied the dewetting of a thin nanoscopic film numerically. During dewetting, the height of the rim at the flanks of the hole is typically larger than the unperturbed fluid film at large distances from a defect and unstable to geometrical perturbations that could probably lead to the formation of droplets. For two neighboring holes separated by a thin liquid ridge, the authors found an instability driven by surface tension and intermolecular forces. For thicker liquid films of the order $O(10^{-5})$ m, the formation of a single drop caused by the dewetting of a liquid film was studied by Edwards et al. (2016). The authors produced a Teflon coated, circular area of interdigitated coplanar metal stripe-arrays from which an electric field is applied underneath the droplet. Consequently when switching on an electric field, the droplet wets the substrate, due to the electrowetting-like modifications of the contact angle of the liquid puddle (Tabeling, 2005). After the electric field has been switched off, the droplet dewets the electrode until it reaches its original shape corresponding to its apparent contact angle. The dewetting of two nearly circular holes in a film of water having a thickness of $O(10^{-3})$ m, spreading above a second liquid and bounded by a rectangular container was studied by Kupershtokh et al. (2015). The authors have shown experimentally and numerically that both holes grow and finally coalesce into a single large hole. Although the collapse of multiple holes is of practical relevance, as in case of coating processes (discussed in detail in the introduction of chapter 6), this phenomenon has not yet been studied in great detail.

In the close proximity of a moving three-phase contact line, the tangential shear stresses are non-integrable, when assuming no slip between a solid and the spreading liquid, leading to an infinite energy dissipation at the three-phase contact line (e.g., De Gennes, 1985; Bonn et al.,

2009). This nonphysical behavior motivates the introduction of a cut-off length below which microscopic features play a dominant role and eventually require a modification of the no-slip boundary condition (Davis, 1980; Bonn et al., 2009; van Lengerich and Steen, 2012). In fact, numerical results obtained with molecular dynamic simulations confirm a region of near-perfect slip in the proximity of the moving three-phase contact line (e.g., Koplik et al., 1988, 1989). In addition to the two different modeling approaches already discussed in the previous chapter (slip boundary condition and precursor film), there are many other modeling approaches in the literature that have proved successful for different solid-liquid combinations. A summary of different models can be found in the work by Qian et al. (2006) and Bonn et al. (2009). As an important consequence, the underlying model of contact line motion is not universally applicable and depends on the specific substrate-fluid combination. Additionally, some authors introduced an energy dissipation attributed to the motion of the three-phase contact line modeled as proportional to the arc length and the squared contact line velocity (De Gennes, 1985; Carlson et al., 2012) superposed on the viscous dissipation in the bulk of the liquid.

Onsager (1931a,b) first noticed that many (thermodynamically) non-equilibrium configurations provide a similarity in their time evolution. His early research mainly focused on the heat conduction in an anisotropic medium. However, since then various extensions and reformulations have been made, leading to time evolution equations for many different processes. Exemplarily, the time evolution of small particles in a viscous fluid, the derivation of Stokes' equations, the flow in porous media, the diffusion of particles in dilute solutions, the magnetic relaxation of particles (Doi, 2011, 2013), the derivation of the constitutive equations for viscoelastic fluids (Zhou and Doi, 2018), as well as free surface flows have been studied on the basis of the Onsager (variational) principle, either in case of a completely wetted solid surface (Di et al., 2018) (restricted to two dimensions) or including the motion of a three-phase contact line (Qian et al., 2006).

This chapter is organized as follows: Section 7.1 describes the underlying assumptions of the theoretical modeling. The applicability of the Onsager principle for describing the motion of thin fluid films is discussed in section 7.2. Section 7.3 introduces the theoretical modeling of the collapse of multiple circular holes in an infinitely extended liquid layer on the basis of the Onsager principle. A closed form analytical expression for the potential energy is derived that, together with a heuristically model for the energy dissipation, lead to the evolution equations for the three-phase contact lines of the defects. The experimental setup as well as the experimental procedure is discussed in section 7.4. A first validation of the theoretical results on the basis of experiments is discussed in section 7.5. A summary of the results and an outlook to further studies is given in section 7.6.

7.1 Model assumptions

We consider an unbounded liquid film having a height H with N circular holes. The contact angle between the liquid film and the substrate is denoted as Θ. Following Taylor and Michael (1973), a single circular hole having a finite radius R is always unstable if the liquid film is infinitely extended. Whether a hole opens or closes strongly depends on the height of the liquid film, following the critical height given in equation (6.1). However, it is by no means clear

how multiple circular holes evolve with time. The following list of assumptions underlies the subsequent theoretical modeling:

1. The contact angle Θ between the substrate and the liquid film is small, i.e., $\Theta \ll 1$;
2. The Reynolds and capillary numbers are sufficiently small during the collapse of the holes;
3. The thickness of the liquid film H is large enough to neglect intermolecular forces.

Assumption 1 refers to the classical lubrication assumption since small contact angles imply small film heights. Following the results obtained in the previous chapter, neither the stability threshold nor the dynamics during the hole collapse strongly depends on the contact angle between the liquid layer and the solid substrate. On the basis of these results, assumption 1 might not be very restrictive. Assumption 2 is not reasonably well satisfied during a collapse of holes in a water layer. Likewise, the water-glycerol mixture employed during the experiments presented in the last chapter does not lead to a sufficient smaller Reynolds number. In addition, in case of low viscous fluids, strong surface waves are observed during the creation of the holes when employing compressed air flow (as mentioned in section 6.1.1). In order to enable a reliable experimental verification, we therefore consider liquid films having sufficiently large viscosities. Furthermore, we assume small capillary numbers during the collapse. In contrast to most of the previous works in which the collapse or opening of multiple holes have been studied, we consider film thicknesses greater than $O(10^{-6})$ m. Consequently, we assume that van der Waals forces can be neglected throughout this study (assumption 3). Additionally, all film heights considered in this chapter are beyond the critical height obtained in the previous chapter. Since we aim at comparing the theoretical results with experiments, which have been employed on finitely extended liquid films, a film height smaller than the critical height would eventually evolve the liquid film into a single stable hole configuration. On the basis of the results by Taylor and Michael (1973), this phenomenon cannot be captured with a theory assuming infinitely extended films.

7.2 From Onsager's principle towards thin film equations

During this section, the Onsager principle is introduced and applied for the derivation of the simplified governing equations describing the flow of a thin, perfectly wetting fluid film on a solid substrate. Even though, Di et al. (2018) has already derived the governing equations for a 2D thin film flow on the basis of the Onsager principle, a generalization towards 3D flows of thin films cannot be found in the literature to best of our knowledge.

Following Qian et al. (2006), the Onsager (variational) principle can be written as

$$\delta\left[\dot{\mathscr{E}}_\mathrm{d} + \dot{\mathscr{E}}_\mathrm{p}\right] = \sum_{i=1}^{N}\left(\frac{\partial \dot{\mathscr{E}}_\mathrm{d}}{\partial \dot{r}_i} + \frac{\partial \mathscr{E}_\mathrm{p}}{\partial r_i}\right)\delta \dot{r}_i = 0, \tag{7.1}$$

in which $\dot{\mathscr{E}}_\mathrm{d}$ and $\mathscr{E}_\mathrm{p} = \mathscr{E}_\mathrm{sf} + \mathscr{E}_\mathrm{g}$ are the energy dissipation (rate) and the potential energy, consisting of the surface energy and the gravitational energy, respectively. The notation δx defines the first variation of x. The set of parameters r_i and their time derivatives $\dot{r}_i$ describe the energetic displacement of a configuration from thermodynamic equilibrium (Qian et al., 2006; Doi, 2011). In agreement with assumption 2, inertial terms are neglected. Equation (7.1) effectively states

that the derivative of the energy dissipation with respect to $\dot{r}_i$ evolves as the steepest descent of the potential energy in the space of the set of the parameters r_i.

In order to shed light in the practical use of equation (7.1), the Onsager principle is now applied to derive the governing equations of motion for a perfectly wetting liquid film parameterized by a height $h(\boldsymbol{r}_\parallel, t)$, where $\boldsymbol{r}_\parallel$ contains the coordinates tangentially to the solid wall located at $z = 0$. The notation is closely related to appendix C. The presence of three-phase contact lines would probably require an extra modeling of the energy dissipation related to the motion of the contact lines. For simplicity this is not taken into account. Therefore, the energy dissipation consisting solely of viscous dissipation can be written as (Kim and Karrila, 2013)

$$\dot{\mathscr{E}}_\mathrm{d} = \frac{\mu}{2}\int_{\mathscr{V}} \left[\boldsymbol{\nabla u} + (\boldsymbol{\nabla u})^{\mathscr{T}}\right] : \left[\boldsymbol{\nabla u} + (\boldsymbol{\nabla u})^{\mathscr{T}}\right] \mathrm{d}\mathscr{V}, \tag{7.2}$$

$$\approx \frac{\mu}{2}\int_{\mathscr{V}} \left(\frac{\partial \boldsymbol{u}_\parallel}{\partial z}\right)^2 \mathrm{d}\mathscr{V}. \tag{7.3}$$

From equation (7.2) to equation (7.3), we made use of the common thin film leading-order approximation $\varepsilon = H/L \ll 1$ (see appendix C for more details). We now compute the first variation $\delta\dot{\mathscr{E}}_\mathrm{d}$ via (e.g., Komzsik, 2019)

$$\delta\dot{\mathscr{E}}_\mathrm{d} = \frac{\mathrm{d}}{\mathrm{d}\varsigma}\dot{\mathscr{E}}_\mathrm{d}(\boldsymbol{u}_\parallel + \varsigma\, \delta\boldsymbol{u}_\parallel)\bigg|_{\varsigma=0}, \tag{7.4}$$

and obtain after a short calculation

$$\delta\dot{\mathscr{E}}_\mathrm{d} = \mu\int_{\mathscr{A}} \left[\frac{\partial \boldsymbol{u}_\parallel}{\partial z}\cdot\delta\boldsymbol{u}_\parallel\right]\bigg|_{z=h} \mathrm{d}\mathscr{A} - \mu\int_{\mathscr{V}} \frac{\partial^2 \boldsymbol{u}_\parallel}{\partial z^2}\cdot\delta\boldsymbol{u}_\parallel \mathrm{d}\mathscr{V}. \tag{7.5}$$

The potential energy, on the other hand, consisting of surface and gravitational energy reads

$$\mathscr{E}_\mathrm{p} = \gamma_{12}\int_{\mathscr{A}} \sqrt{1+(\boldsymbol{\nabla}_\parallel h)^2}\mathrm{d}\mathscr{A} + \rho g\int_{\mathscr{V}} z\mathrm{d}\mathscr{V}, \tag{7.6}$$

$$\approx \gamma_{12}\int_{\mathscr{A}} 1 + \frac{(\boldsymbol{\nabla}_\parallel h)^2}{2}\mathrm{d}\mathscr{A} + \frac{\rho g}{2}\int_{\mathscr{A}} h^2\mathrm{d}\mathscr{A}, \tag{7.7}$$

in which $\sqrt{1+(\boldsymbol{\nabla}_\parallel h)^2} \approx 1 + (\boldsymbol{\nabla}_\parallel h)^2/2$ has been used, approximately valid for sufficiently thin films. Making use of the relation

$$\delta\dot{\mathscr{E}}_\mathrm{p} = \frac{\delta\mathscr{E}_\mathrm{p}}{\delta h}\delta\dot{h}, \tag{7.8}$$

we find the first variation of the potential energy with respect to the parametrization of the free fluid interface, following the style of equation (7.4), via

$$\delta\mathscr{E}_{\mathrm{p}} = \int\limits_{\mathscr{A}} \left[-\gamma_{12}\boldsymbol{\nabla}_{\parallel}^{2}h + \rho g h\right]\delta h \,\mathrm{d}\mathscr{A}, \tag{7.9}$$

or following equation (7.8):

$$\delta\dot{\mathscr{E}}_{\mathrm{p}} = \int\limits_{\mathscr{A}} \left[-\gamma_{12}\boldsymbol{\nabla}_{\parallel}^{2}h + \rho g h\right]\delta\dot{h} \,\mathrm{d}\mathscr{A}. \tag{7.10}$$

As known from the derivation of the Young-Laplace equation, in which the conservation of volume is constrained throughout the energy minimization (e.g., Myshkis et al., 1987), incompressibility has to be maintained in the present context. We therefore introduce the following constraint

$$\dot{\mathscr{L}} = -\int\limits_{\mathscr{V}} \lambda\left(\boldsymbol{\nabla}_{\parallel}\cdot\boldsymbol{u}_{\parallel} + \frac{\partial w}{\partial z}\right)\mathrm{d}\mathscr{V}, \tag{7.11}$$

with λ being a Lagrange multiplier. The term in brackets is the continuity equation from equation (C.5). However, the first variation of the latter equation is computed with respect to $\boldsymbol{u}_{\parallel}$ and w. Applying the kinematic boundary condition at fluid interfaces (e.g., Leal, 2007), i.e.,

$$w|_{z=h} = \dot{h} + \boldsymbol{u}_{\parallel}\big|_{z=h}\cdot\boldsymbol{\nabla}_{\parallel}h, \tag{7.12}$$

we eventually obtain

$$\delta\dot{\mathscr{L}} = -\int\limits_{\mathscr{A}} \lambda|_{z=h}\,\delta\dot{h} \,\mathrm{d}\mathscr{A} + \int\limits_{\mathscr{V}} \left[\boldsymbol{\nabla}_{\parallel}\lambda\cdot\delta\boldsymbol{u}_{\parallel} + \frac{\partial\lambda}{\partial z}\delta w\right]\mathrm{d}\mathscr{V}. \tag{7.13}$$

We are now in the position to apply the Onsager principle from equation (7.1) via

$$\delta\dot{\mathscr{E}}_{\mathrm{d}} + \delta\dot{\mathscr{E}}_{\mathrm{p}} + \delta\dot{\mathscr{L}} = 0, \tag{7.14}$$

and find after inserting equations (7.5), (7.10) and (7.13):

$$\begin{aligned} 0 \;=\; & \mu\int\limits_{\mathscr{A}}\left\{\left[\frac{\partial\boldsymbol{u}_{\parallel}}{\partial z}\cdot\delta\boldsymbol{u}_{\parallel}\right]\Big|_{z=h} + \left[-\gamma_{12}\boldsymbol{\nabla}_{\parallel}^{2}h + \rho g h - \lambda|_{z=h}\right]\delta\dot{h}\right\}\mathrm{d}\mathscr{A} \\ + \; & \mu\int\limits_{\mathscr{V}}\left\{\left[\boldsymbol{\nabla}_{\parallel}\lambda - \mu\frac{\partial^{2}\boldsymbol{u}_{\parallel}}{\partial z^{2}}\right]\cdot\delta\boldsymbol{u}_{\parallel} + \frac{\partial\lambda}{\partial z}\delta w\right\}\mathrm{d}\mathscr{V}. \end{aligned} \tag{7.15}$$

Following the fundamental lemma of calculus of variations (e.g., Komzsik, 2019), we finally obtain

$$\boldsymbol{\nabla}_{\parallel} p = \mu \frac{\partial^2 \boldsymbol{u}_{\parallel}}{\partial z^2}, \tag{7.16}$$

$$\frac{\partial p}{\partial z} = -\rho g, \tag{7.17}$$

$$\left.\frac{\partial \boldsymbol{u}_{\parallel}}{\partial z}\right|_{z=h} = 0, \tag{7.18}$$

$$p|_{z=h} = -\gamma_{12} \boldsymbol{\nabla}_{\parallel}^2 h, \tag{7.19}$$

where we replaced the Lagrange multiplier λ by $\lambda = p + \rho g z$, recalling that the potential of the gravitational volume forces are included in the pressure [see equation (2.8)]. Equations (7.16) and (7.17) are consistent with equations (C.9) and (C.10), when including gravity. Equations (7.18) and (7.19), on the other hand, correspond to the stress jump boundary conditions within the thin film approximation (e.g., Leal, 2007). As typical in thin film modeling, the last set of equations can be combined leading to a partial differential equation for the film height (e.g., Bostwick et al., 2017).

The forgoing deduction reveals that the Onsager principle can be applied for the modeling of thin film dynamics and could be extended to include the motion of three-phase contact lines (Qian et al., 2006).

7.3 Theoretical modeling

Although we have limited this study to the collapse of multiple circular holes in a liquid film, the potential energy will be derived for holes of arbitrary shape, as it could be relevant for further studies. During this section, the Onsager principle is applied in a slightly different way from the previous deduction but eventually leads to a set of evolution equations describing the time evolution of the collapse of multiple holes.

Due to the assumption of small capillary numbers (assumption 2), the shape of the surface of the meniscus is controlled by the Young-Laplace equation in the asymptotic limit. Consequently, the time evolution of the closing process is described as a sequence of quasi-stationary configurations.

7.3.1 The potential energy of a liquid layer with multiple holes

The main idea of the derivation of the potential energy of a liquid layer with N arbitrarily shaped holes is closely related to the work by Kralchevsky et al. (1992), where the authors computed the capillary induced forces acting on interfacial particles.

To start with, we make use of assumption 1 and simplify the Young-Laplace equation in non-dimensional form [see equation (6.16)] as follows

$$\tilde{\boldsymbol{\nabla}}^2 \tilde{h} = \tilde{h} + \tilde{\lambda}, \tag{7.20}$$

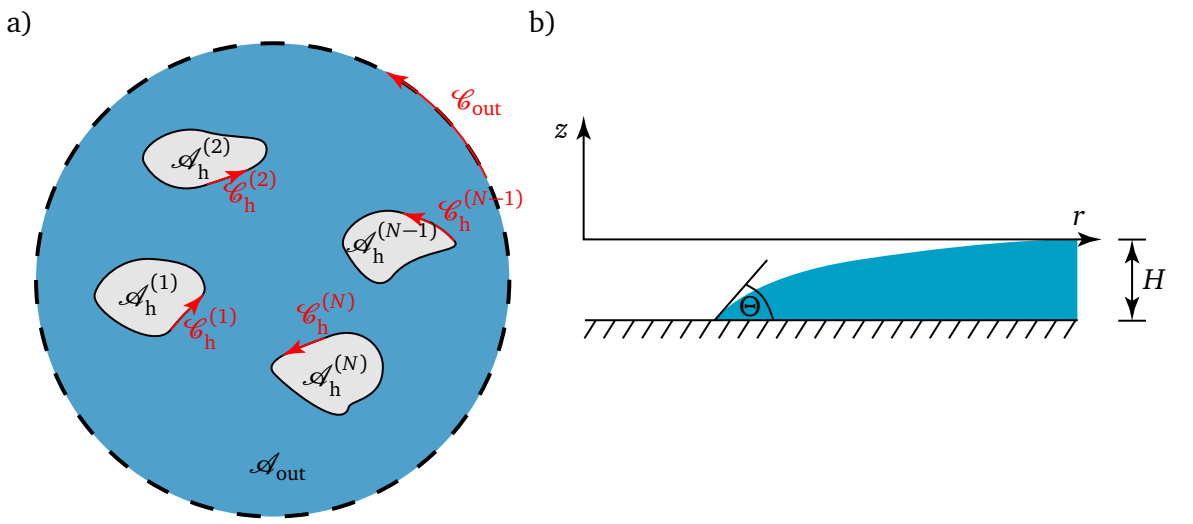

Abbildung 7.1.: Sketch of a liquid film having N arbitrarily shaped holes. a) The overall area of the configuration is subdivided into the surface wetted by the liquid layer $\mathscr{A}_{\mathrm{out}}$ and the areas of the holes $\mathscr{A}_{\mathrm{h}}^{(i)}$, with $i = 1, 2, \ldots, N$. The contours of the holes are denoted as $\mathscr{C}_{\mathrm{h}}^{(i)}$, whereas the outer contour, corresponding to the far field is denoted by $\mathscr{C}_{\mathrm{out}}$. b) Sketch of a flank of a hole in side view. Θ defines the contact angle between the substrate and the liquid layer and H refers to the height sufficiently far away from the holes, i.e., at $\mathscr{C}_{\mathrm{out}}$. The origin of the coordinate system is located at a height H above the substrate.

in which $\tilde{h}$ is the parametrization of the liquid interface (non-dimensionalized by the capillary length l_{c}) and $\tilde{\lambda}$ the Lagrange multiplier (or the pressure difference between inside and outside of the meniscus). Figure 7.1 provides a sketch of the configuration. Figure 7.1 a) introduces the notation, with $\mathscr{A}_{\mathrm{out}}$, $\mathscr{C}_{\mathrm{out}}$, $\mathscr{A}_{\mathrm{h}}^{(n)}$ and $\mathscr{C}_{\mathrm{h}}^{(n)}$ referring to the area wetted by the liquid film (i.e., the projection of the fluid interface on the substrate), the contour of the liquid film far away from all holes, the area of hole n and the corresponding contour of the three-phase contact line of hole n, respectively. Figure 7.1 b) shows the position of the coordinate system, which is located, in contrast to chapter 6, at the height of the liquid film far away from all holes, i.e., at height H above the substrate. Hereby, $\tilde{\lambda}$ refers to the pressure difference at the fluid interface in the far field where $\tilde{\boldsymbol{\nabla}}^2\tilde{h}$ and $\tilde{h}$ converge to zero. Consequently, $\tilde{\lambda} = 0$ and equation (7.20) simplifies to

$$\tilde{\boldsymbol{\nabla}}^2\tilde{h} = \tilde{h}. \tag{7.21}$$

It should be noted that the potential energy of an infinitely extended liquid film grows beyond all limits due to its infinite mass and surface area. Therefore, the presence of multiple holes does not change the potential energy of the configuration asymptotically. In order to handle this difficulty, Peschka et al. (2018) considered a large (but finite) box limiting the size of the meniscus. However, it is also possible to consider the potential energy difference $\Delta\mathscr{E}_{\mathrm{p}} = \mathscr{E}_{\mathrm{p}} - \mathscr{E}_{\mathrm{p}}^{\mathrm{healed}}$, in which $\mathscr{E}_{\mathrm{p}}$ is the potential energy of a film with N holes and $\mathscr{E}_{\mathrm{p}}^{\mathrm{healed}}$ corresponds to the energy of a film without holes but with the same (constant) height H. This approach is reasonable, since we are mainly interested in the derivative of the potential energy with respect to the set of parameters r_i [see equation (7.1)]. We will see later in this chapter that r_i correspond to the effective length-scale of the i-th hole and therefore the gradient of $\Delta\mathscr{E}_{\mathrm{p}}$ coincides to that of $\mathscr{E}_{\mathrm{p}}$, since $\mathscr{E}_{\mathrm{p}}^{\mathrm{healed}}$ is independent of r_i.

We start by computing the area differences defined in the style of the energy difference via $\Delta\mathscr{A} = \mathscr{A} - \mathscr{A}^{\text{healed}}$ and find

$$\mathrm{d}(\Delta\tilde{\mathscr{A}}_{12}) = \left[\sqrt{1+(\tilde{\boldsymbol{\nabla}}\tilde{h})^2}-1\right]\mathrm{d}.\tilde{\mathscr{A}}_{\text{out}} - \sum_{n=1}^{N}\mathrm{d}.\tilde{\mathscr{A}}_{\text{h}}^{(n)} \approx \frac{(\tilde{\boldsymbol{\nabla}}\tilde{h})^2}{2}\,\mathrm{d}.\tilde{\mathscr{A}}_{\text{out}} - \sum_{n=1}^{N}\mathrm{d}.\tilde{\mathscr{A}}_{\text{h}}^{(n)}, \tag{7.22}$$

$$\mathrm{d}(\Delta\tilde{\mathscr{A}}_{\text{S1}}) = \mathrm{d}.\tilde{\mathscr{A}}_{\text{out}} - \sum_{n=1}^{N}\mathrm{d}.\tilde{\mathscr{A}}_{\text{h}}^{(n)} - \mathrm{d}.\tilde{\mathscr{A}}_{\text{out}} = -\sum_{n=1}^{N}\mathrm{d}.\tilde{\mathscr{A}}_{\text{h}}^{(n)}, \tag{7.23}$$

$$\mathrm{d}(\Delta\tilde{\mathscr{A}}_{\text{S2}}) = \sum_{n=1}^{N}\mathrm{d}.\tilde{\mathscr{A}}_{\text{h}}^{(n)}. \tag{7.24}$$

Here, $\mathrm{d}(\Delta\tilde{\mathscr{A}}_{12})$, $\mathrm{d}(\Delta\tilde{\mathscr{A}}_{\text{S1}})$ and $\mathrm{d}(\Delta\tilde{\mathscr{A}}_{\text{S2}})$ are the incremental area between the liquid and gas, between the substrate and the liquid and the substrate and the gas, respectively. In equation (7.22), we made use of assumption 1 and expand $\sqrt{1+(\tilde{\boldsymbol{\nabla}}\tilde{h})^2} \approx 1+(\tilde{\boldsymbol{\nabla}}\tilde{h})^2/2$ in a Taylor series. Taking Young's law [see equation (2.50)] into account, we find for the incremental surface energy difference in non-dimensional form $[\Delta\tilde{\mathscr{E}}_{\text{sf}} = \Delta\mathscr{E}_{\text{sf}}/(\gamma_{12}l_{\text{c}}^2)]$

$$\mathrm{d}(\Delta\tilde{\mathscr{E}}_{\text{sf}}) = \frac{(\tilde{\boldsymbol{\nabla}}\tilde{h})^2}{2}\,\mathrm{d}.\tilde{\mathscr{A}}_{\text{out}} + (\cos(\Theta)-1)\sum_{n=1}^{N}\mathrm{d}.\tilde{\mathscr{A}}_{\text{h}}^{(n)}. \tag{7.25}$$

Following the same train-of-thought, the gravitational energy difference can be computed that leads after a short deduction into

$$\mathrm{d}(\Delta\tilde{\mathscr{E}}_{g}) = \frac{\tilde{h}^2}{2}\,\mathrm{d}.\tilde{\mathscr{A}}_{\text{out}} + \frac{\tilde{H}^2}{2}\sum_{n=1}^{N}\mathrm{d}.\tilde{\mathscr{A}}_{\text{h}}^{(n)}. \tag{7.26}$$

The sum of equations (7.25) and (7.26) lead, after integrating over $\mathrm{d}.\tilde{\mathscr{A}}_{\text{out}}$ and $\mathrm{d}.\tilde{\mathscr{A}}_{\text{h}}^{(n)}$, to the potential energy difference. The sum of the integrals of the two last terms of equations (7.25) and (7.26) represents the sum of the areas of all holes in the liquid layer. At first glance, the integration over $\mathrm{d}.\tilde{\mathscr{A}}_{\text{out}}$ requires detailed knowledge of the shape of the liquid interface. However, using the identity

$$\tilde{\boldsymbol{\nabla}}\cdot(\tilde{h}\,\tilde{\boldsymbol{\nabla}}\tilde{h}) = \left(\tilde{\boldsymbol{\nabla}}\tilde{h}\right)^2 + \tilde{h}^2, \tag{7.27}$$

the integral over $\mathrm{d}.\tilde{\mathscr{A}}_{\text{out}}$ can be transferred into a sum of contour integrals over $\tilde{\mathscr{C}}_{\text{out}}$ and all $\tilde{\mathscr{C}}_{\text{h}}^{(n)}$ by use of Green's integral theorem:

$$\int_{\tilde{\mathscr{A}}} \tilde{\boldsymbol{\nabla}}\cdot(\tilde{h}\,\tilde{\boldsymbol{\nabla}}\tilde{h})\mathrm{d}.\tilde{\mathscr{A}}_{\text{out}} = -\sum_{n=1}^{N}\oint_{\tilde{\mathscr{C}}} \boldsymbol{n}_{\text{h}}^{(n)}\cdot(\tilde{h}\,\tilde{\boldsymbol{\nabla}}\tilde{h})\,\mathrm{d}\tilde{\mathscr{C}}_{\text{h}}^{(n)} + \oint_{\tilde{\mathscr{C}}} \boldsymbol{n}_{\text{out}}\cdot(\tilde{h}\,\tilde{\boldsymbol{\nabla}}\tilde{h})\,\mathrm{d}\tilde{\mathscr{C}}_{\text{out}}. \tag{7.28}$$

The sum of the contour integrals along the three-phase contact lines of the holes has a negative sign, since $\boldsymbol{n}_{\text{h}}^{(n)}$ is defined to point into the liquid layer. Due to the choice of the location of the

coordinate origin, the last integral vanishes ($\tilde{h} \to 0$ at $\tilde{\mathscr{C}}_{\mathrm{out}}$). Therefore, we find for the potential energy difference

$$\Delta\tilde{\mathscr{E}}_{\mathrm{p}} = \Delta\tilde{\mathscr{E}}_{\mathrm{sf}} + \Delta\tilde{\mathscr{E}}_{\mathrm{g}}, \tag{7.29}$$

$$= -\frac{1}{2}\sum_{n=1}^{N}\oint_{\mathscr{C}} \boldsymbol{n}_{\mathrm{h}}^{(n)} \cdot (\tilde{h}\,\tilde{\boldsymbol{\nabla}}\tilde{h})\,\mathrm{d}\tilde{\mathscr{C}}_{\mathrm{h}}^{(n)} + \left(\frac{\tilde{H}}{2} + \cos(\Theta) - 1\right)\sum_{n=1}^{N}\int_{\mathscr{A}} \mathrm{d}\tilde{\mathscr{A}}_{\mathrm{h}}^{(n)}. \tag{7.30}$$

Assuming a homogeneous contact angle on the substrate, equation (7.30) can further be simplified. At the three-phase contact line, the following conditions are applied

$$\tilde{h}\big|_{\tilde{\mathscr{C}}_{\mathrm{h}}^{(n)}} = -\tilde{H}, \qquad \tilde{\boldsymbol{\nabla}}\tilde{h}\cdot\boldsymbol{n}_{\mathrm{h}}^{(n)}\Big|_{\tilde{\mathscr{C}}_{\mathrm{h}}^{(n)}} = \tan(\Theta), \qquad \forall n = 1, 2, \ldots, N. \tag{7.31}$$

Inspired by equation (6.1), we may rewrite the height $\tilde{H} = \kappa\sin(\Theta/2)$, with $\kappa \in R_0^+$, and according to the Taylor expansion up to the second order in the contact angle Θ, we find

$$\Delta\tilde{\mathscr{E}}_{\mathrm{p}} = \frac{\Theta^2}{4}\left\{\kappa\sum_{n=1}^{N}\oint_{\mathscr{C}} \mathrm{d}\tilde{\mathscr{C}}_{\mathrm{h}}^{(n)} + \frac{\kappa^2-4}{2}\sum_{n=1}^{N}\int_{\mathscr{A}} \mathrm{d}\tilde{\mathscr{A}}_{\mathrm{h}}^{(n)}\right\}. \tag{7.32}$$

Remarkably, the potential energy difference solely depends on the contact angle between the liquid layer and the substrate, the height of liquid film, the circumference of the three-phase contact lines of the holes and on the area of the holes. The potential energy of a liquid film with N holes of arbitrary shape can therefore be computed without a detailed knowledge of the geometrical shape of the fluid interface. In case of N circular holes, the last equation simplifies to

$$\Delta\tilde{\mathscr{E}}_{\mathrm{p}} = \frac{\Theta^2\pi}{2}\left\{\kappa\sum_{n=1}^{N}\tilde{R}_n + \frac{\kappa^2-4}{4}\sum_{n=1}^{N}\tilde{R}_n^2\right\}. \tag{7.33}$$

Apart from the temporal evolution of a liquid film, we can also apply equation (7.33) to obtain the critical film height for a single circular hole for verification purposes, i.e., a comparison with the results obtained by Taylor and Michael (1973). In contrast to their work, we limit ourselves to small contact angles. Taylor and Michael (1973) found that every hole closes (opens) if the height of the liquid film is larger (smaller) than the height given in equation (6.1). A stability limit is reached, if the energy difference between a liquid film with and without a hole vanishes, leading to the following critical height

$$\kappa = \frac{2\left(\sqrt{1+\tilde{R}^2}-1\right)}{\tilde{R}}, \tag{7.34}$$

which, if $\tilde{R} \to \infty$, leads to $\kappa = 2$. However, the latter result does not provide any insight on whether the hole closes or opens. When computing the derivative of equation (7.33) with respect to $\tilde{R}$ and inserting $\kappa = 2 + \beta$ with $|\beta| \ll 1$, we obtain after linearizing around β

$$\frac{\partial \Delta \tilde{\mathscr{E}}_\mathrm{p}}{\partial \tilde{R}} = \frac{\partial \tilde{\mathscr{E}}_\mathrm{p}}{\partial \tilde{R}} = 2\pi \left(2 + \beta(1 + 2\tilde{R})\right). \tag{7.35}$$

Consequently, if $\beta > 0$, a circular hole closes, whereas $\beta < 0$ leads to an opening of the hole, in agreement with the results obtained by Taylor and Michael (1973).

For a later use, we also obtain the critical height of a liquid film with N circular holes as

$$\kappa = \frac{2\left(\sqrt{\left\{\sum_{n=1}^{N} \tilde{R}_n\right\}^2 + \left\{\sum_{n=1}^{N} \tilde{R}_n^2\right\}^2} - \sum_{n=1}^{N} \tilde{R}_n\right)}{\sum_{n=1}^{N} \tilde{R}_n^2}. \tag{7.36}$$

7.3.2 Modeling the energy dissipation in a film with N holes

The energy dissipation in a liquid film containing N-holes in general requires the solution of the thin film equations including a suitable model for contact line motion. However, to make full use of the derivation of the previous subsection, we aim at modeling the energy dissipation from a different perspective. It is known that the energy dissipation related to a translating sphere (translational velocity $\boldsymbol{U}$) reads $\dot{\mathscr{E}}_\mathrm{d} = 6\pi\mu a \boldsymbol{U}^2$ in the Stokes flow limit (e.g., Kim and Karrila, 2013). The energy dissipation related to the motion of a single three-phase contact line has been modeled as $\dot{\mathscr{E}}_\mathrm{d} = 2\pi\mu_\mathrm{TCL} R \dot{R}^2$ (De Gennes, 1985; Carlson et al., 2012), in which μ_TCL denotes a constant (related to an effective viscosity) that takes a role of a fitting parameter. In both examples, the energy dissipation related to a creeping flow is proportional to the square of the velocity. Hereinafter, we assume that the overall energy dissipation for a configuration consisting of multiple circular three-phase contact lines can be written in the form

$$\dot{\mathscr{E}}_\mathrm{d} = \frac{1}{2} \sum_{m=1}^{N} \sum_{n=1}^{N} \Gamma_{mn} \dot{R}_n^2, \tag{7.37}$$

in which $\boldsymbol{\Gamma}$ is a $N \times N$ tensor containing pre-factors (unit: viscosity × length) related to the (overall) energy dissipation which we denote as dissipation tensor. The extra diagonal elements, i.e., Γ_{ij} with $i \neq j$, thereby describe the energy dissipation between two neighboring holes i and j, whereas the diagonal elements Γ_{ii} represent the energy dissipation corresponding to the i-th hole alone. The elements from $\boldsymbol{\Gamma}$, however, depend on the modeling approach of the contact line motion and can, exemplarily, depend on R_i. It is worth mentioning that the energy dissipation due to the contact line motion should be restricted to the close vicinity. Therefore, the extra diagonal elements of $\boldsymbol{\Gamma}$ are probably dominated by viscous dissipation in the bulk, if neighboring holes are separated largely enough. However, in agreement with the Onsager reciprocal relation, $\boldsymbol{\Gamma}$ should be symmetric (and positive definite, i.e., all eigenvalues are positive)

(Onsager, 1931a,b) and does therefore contain $N(N+1)/2$ independent elements. Translated to the current configuration, the symmetry of $\mathbf{\Gamma}$ states that the dissipation created by hole i acting on hole j is the same as the energy dissipation from j on i. However, when assuming that the three-phase contact lines are separated far enough to neglect hydrodynamic interaction, $\mathbf{\Gamma}$ takes a diagonal form, in which in general, all diagonal elements could potentially depend on R_i and therefore have different values varying with time. For now, we assume that all diagonal elements are independent on R_i and coincide to a single constant $\Gamma > 0$. As shown in the next section, this approach leads to a decoupled temporal evolution of the hole radii, and to the following energy dissipation

$$\dot{\mathscr{E}}_{\mathrm{d}} = \frac{1}{2}\Gamma \sum_{n=1}^{N} \dot{R}_n^2. \tag{7.38}$$

Consequently, for the collapse of multiple holes in an infinitely extend film, the radii R_i take the role of the set of parameters in the Onsager principle.

7.3.3 The evolution equation for a liquid film with N circular holes

Following equation (7.1), the derivative of the energy dissipation with respect to $\dot{R}_i$ leads to

$$\frac{\partial \dot{\mathscr{E}}_{\mathrm{d}}}{\partial \dot{R}_i} = \Gamma \dot{R}_i, \quad \forall i \in (1,\ldots,N). \tag{7.39}$$

In non-dimensional form, where the variables are denoted by a tilde, the above equation can be rewritten into

$$\frac{\partial \dot{\tilde{\mathscr{E}}}_{\mathrm{d}}}{\partial \dot{\tilde{R}}_i} = \frac{\Theta^2 \pi}{2} \frac{\partial \tilde{R}_i}{\partial \tilde{t}}, \tag{7.40}$$

where $\tilde{t} = t/T$, with the characteristic time scale $T = \Gamma l_{\mathrm{c}} \Theta^2 \pi / (2\gamma_{12})$.

The derivative of the potential energy $\tilde{\mathscr{E}}_{\mathrm{p}}$ with respect to $\tilde{R}_i$ on the basis of equation (7.33) is found to read

$$\frac{\partial \tilde{\mathscr{E}}_{\mathrm{p}}}{\partial \tilde{R}_i} = \frac{\Theta^2 \pi}{2} \left(\kappa + \frac{\kappa^2 - 4}{2} \tilde{R}_i \right). \tag{7.41}$$

Employing the Onsager principle [following equation (7.1)] leaves us with the following, remarkably simple evolution equation

$$\frac{\partial \tilde{R}_i}{\partial \tilde{t}} = -\left(\kappa + \frac{\kappa^2 - 4}{2} \tilde{R}_i \right), \quad \forall i \in (1,\ldots,N). \tag{7.42}$$

For $\kappa = 2$, the analytical solution of equation (7.42) leads to a $\tilde{R}_i \propto \tilde{t}$ scaling law, such as reported for the opening of a hole in a very viscous film (Redon et al., 1991). For $\kappa \neq 2$, on the other hand, the analytical solution reads

$$\tilde{R}_i = \exp\left(-\frac{1}{2}\tilde{t}(\kappa^2-4)\right)\frac{2\kappa\left[1-\exp\left(\frac{1}{2}\tilde{t}(\kappa^2-4)\right)\right]+\tilde{R}_i^0(\kappa^2-4)}{\kappa^2-4}, \tag{7.43}$$

in which $\tilde{R}_i^0$ is the initial radius of hole i.

7.4 Experimental analysis

A small number of experiments have been performed in order to provide a first validation of the theoretical modeling. This section contains the introduction of the experimental setup and a discussion of the experimental procedure.

7.4.1 Experimental setup & procedure

The experimental setup largely coincides to that shown in figure 6.1 a). In contrast to chapter 6, we have limited ourselves to a single square box of side length of $L = 12$ cm. This comparably small box has been employed because of the increasing difficulty when producing larger substrates. Furthermore, the high-speed camera in the original setup has been replaced with a SLR camera (Nikon D810) and the recording speed was 60 fps. The experiments have been recorded in top view.

In order to minimize the effect of contact line pinning, the experiments have been carried out on superhydrophobic Al substrates, following the procedure described by Song et al. (2012). Even though the theoretical model is derived on the basis of the small contact angle assumption, the results of the previous chapter indicate that the contact angle does not play a major role during the collapse of a single hole. Additionally, it was planned to perform experiments on surface modified hydrophilic silicone wafers. The procedure reported by Kaneko et al. (2019) (based on a sol-gel coating) provides excellent sliding properties with remarkably low contact angle hysteresis $\Delta\Theta \approx 5°$ and therefore ensures a better comparability to the theoretical model. However, the production of the comparably large surfaces is challenging, since it requires a cleaning by either oxygen plasma treatment or peroxymonosulfuric acid (known as Piranha acid). Oxygen plasma treatment of the samples was not possible due to the large size of the substrates and the comparably small chamber size of the oxygen plasma device available in our laboratories. Peroxymonosulfuric acid is very hazardous and since a large volume is required (due to the large substrates), the chemical treatment is very dangerous. Until now, it has not been possible to become familiar with the safe use of peroxymonosulfuric acid.

In order to satisfy assumption 2 reasonably well during the experiments and in order to reduce surface waves observable during the creation of the holes, a water-glycerol mixture with a viscosity of approximately 40 times of that of water has been employed. All relevant material properties of the water-glycerol mixture are given in table 7.1. It should be noted that the wetting properties of the mixture are comparable to those of pure water which are given in table 6.1.

During an experiment, a fixed volume of $V = 70$ ml water-glycerol mixture was filled into the

Parameter	Value	Method
Viscosity: μ in cSt	37.812 ± 0.369	Brookfield DV-III ULTRA
Density: ρ in g/cm^3	1.19	Reference
Surface tension: γ_{12} in dyne/cm	67.5	Reference
Advancing contact angle: Θ_a in deg.	165.38 ± 2.257	Krüss DSA 100

Tabelle 7.1.: Relevant material properties of the water-glycerol mixture. Each measured value is the average of ten experiments with standard deviation. The advancing contact angle has been measured on the superhydrophobic Al substrate following the droplet sliding method described in section 6.1.1. The values for the density and surface tension have been taken from Glycerine Producers' Association and others (1963).

box. A liquid volume of $V = 70$ ml leads to an effective height close to the critical height obtained in the previous chapter. After the creation of a uniform film, three nearly circular holes have been created with nitrogen jets. The three holes have been aligned in the form of a right-angled triangle where the center of the holes have a minimum distance of about 5 cm. Right after the nitrogen jet has been stopped, the recording started and the time evolution of all holes has been captured. By employing a custom-made MATLAB® code, circles have been fitted to the experimentally obtained hole radii at every time step.

7.5 Comparison between theory and experiments

In contrast to the theory, the experiments have been performed on liquid films of finite lateral extension. Consequently, the critical film height differs from that of an infinitely extended liquid film, as shown in figure 6.9 b). The comparability between these two approaches is ensured by defining a correction constant to the critical height given in equation (7.36).

By employing the numerical method discussed in section 6.1.2, the critical volume V_c of a liquid film in a circular box of radius $R = L/2$ and a contact angle of $\Theta_a = 165°$ is found to read $V_c = 3483.01 \cdot l_c^3$, with $l_c \approx 2.40$ mm (following the material constants from table 7.1). Consequently, the critical height of the liquid film in absence of a hole is found via

$$\tilde{h}_T = \frac{\tilde{V}_c}{\pi \frac{\tilde{L}^2}{4}} \approx 1.7807. \tag{7.44}$$

The height is non-dimensionalized with the capillary length l_c. The height of a liquid film in a square box of side-length $L = 12$ cm, corresponding to a volume of $V = 70$ ml and in absence of holes reaches

$$\tilde{h}_E = \frac{\tilde{V}}{\tilde{L}^2} \approx 2.0216. \tag{7.45}$$

Consequently, the experimental conditions ensure a collapse of the holes since the height of the liquid film is about 13% larger than the critical value. The ratio of both heights is used as a comparability factor to the critical height given in equation (7.36). We may set

$$\kappa \to \kappa\, \delta_h, \quad \text{with} \quad \delta_h = \frac{\tilde{h}_{\mathrm{E}}}{\tilde{h}_{\mathrm{T}}} \approx 1.1353. \tag{7.46}$$

To compare the results between theory and experiments, we concentrate on the relative evolution of the hole radii and therefore do not consider the exact temporal development of each individual hole. Thereby, the energy dissipation constant Γ does not need to be computed. In other words, the trajectories of the hole radii can be validated without a detailed knowledge of the energy dissipation.

Figure 7.2 shows a comparison of five different experiments with the theory in which the trajectories of the hole radii are compared with the theoretical results [with a corrected height following equation (7.46)]. Figure 7.2 a) shows a 3D plot of the comparison, whereas the 2D projections of a) are given in b), c) and d). For graphical reasons, all radii have been normalized with the initial radius of the largest hole $R_{\max}$ in the experiments. For the given set of parameters it can be observed that smaller holes close faster than larger ones, clearly in agreement with physical intuition. Theory and experiments agree satisfyingly well, even though, the theory was derived under the assumption of small contact angles and infinitely extended liquid layers. The weak dependence of the results on the contact angle is in agreement with the results obtained in chapter 6. It is worth mentioning that the theory does not contain any artificial (or nonphysical) fitting parameter in order to achieve satisfying agreement with the experiments.

7.6 Summary & Outlook

In summary, we have studied the collapse of multiple circular holes in an infinitely extended liquid layer assuming a small contact angle between the liquid layer and the substrate. Based on the Onsager principle, the thin film equations have been derived in absence of three-phase contact lines that motivated the usability of this principle in the present context. The potential energy for a liquid film with N holes of arbitrary shape has been obtained which solely depends on the physical conditions at the three-phase contact lines of the holes. By neglecting the hydrodynamic interaction between different holes, a simple expression for the energy dissipation has been postulated from which the trajectories of the hole radii have been derived independent of the exact value of the energy dissipation. The main advantage of the theoretical model is that it does not require the solution of the thin film equation in order to predict the collapse of multiple holes. Even though the experimental results provide a satisfying agreement with the theory, further experimental validation is still required, including a variation of the liquid volume, the wetting properties of the substrates and probably also the lateral extension of the liquid layer. Consequently, the study of the collapse of multiple holes described in this chapter is still in its fledgling stages.

Apart from a more detailed experimental verification, many other extensions of this work are conceivable. For a sufficient small height of the liquid film, the opening of multiple holes could be studied following the approach outlined in this chapter. Existing experiments, focusing on

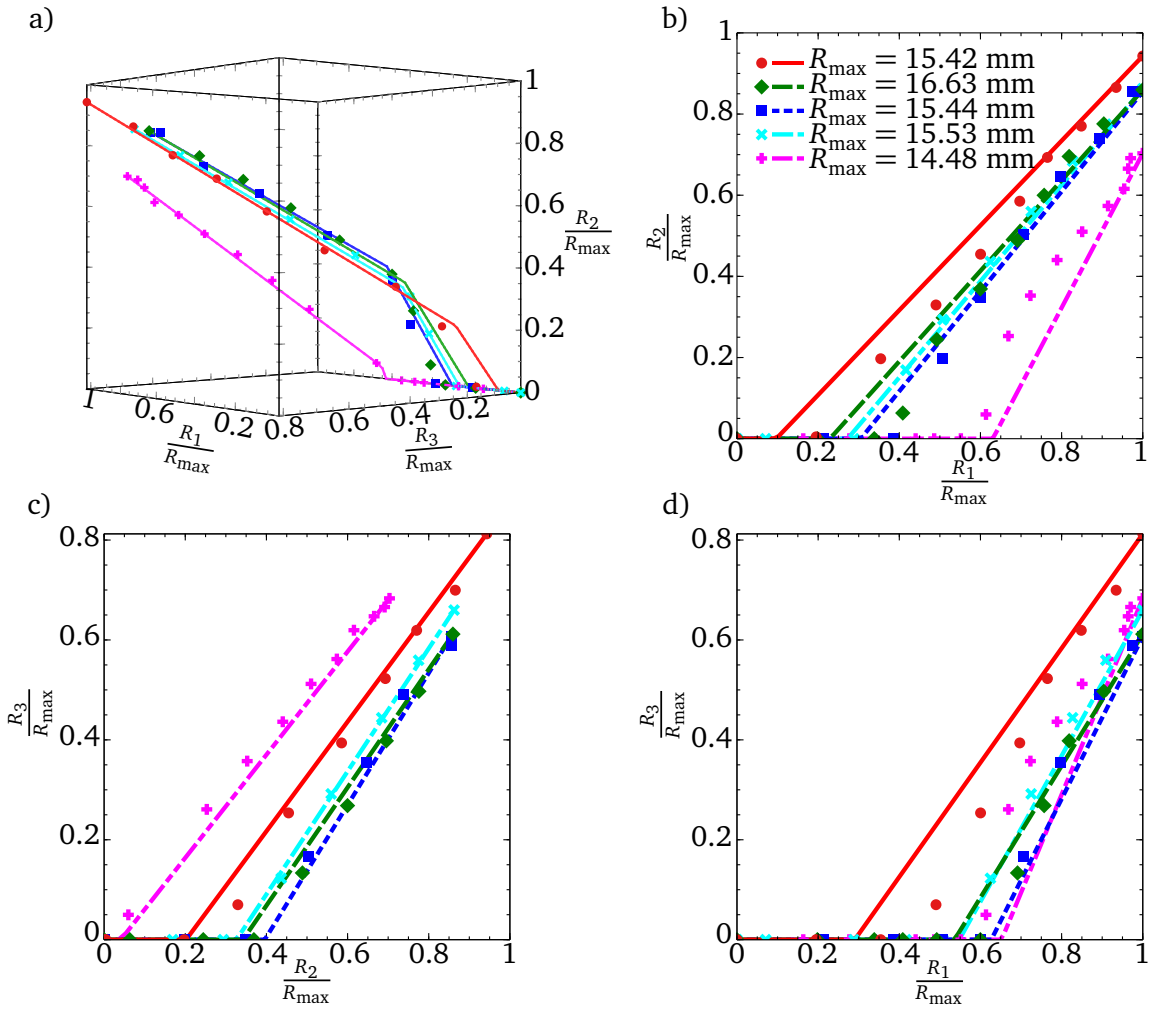

Abbildung 7.2.: Comparison between theory (lines) and experiments (symbols) for five different maximum hole radii $R_{\max}$ showing the time evolution of three different hole radii depending on each other. R_1 and R_3 corresponds to the largest and smallest initial hole, respectively. The theoretical results correspond to equation (7.43) with κ given in equation (7.36) multiplied by δ_h defined in equation (7.46). a) 3D plot of the three different hole radii. The subfigures b), c) and d) are 2D projections of the results given in a).

the evolution of multiple holes in a liquid film, have been performed with liquid film heights for which intermolecular forces become dominant (Karapanagiotis and Gerberich, 2005; Seemann et al., 2005; Bäumchen and Jacobs, 2009). Experiments, validating the theoretical prediction on the expansion of holes in thicker films, are therefore required. Furthermore, the general validity of the expression for the potential energy may encourage extending the current work towards the collapse of multiple holes of arbitrary shape. Hereby, a new modeling of the energy dissipation is required, taking the exact shape of the three-phase contact line into account. When expanding the exact shape of the three-phase contact line into a Fourier series, the number of elements of the energy dissipation tensor $\mathbf{\Gamma}$ would increase significantly, since every partial sum of the Fourier series would have a corresponding entry in $\mathbf{\Gamma}$ as well as entries for the interaction between different frequencies. Furthermore, the interaction of two holes could be computed on the basis of the thin film equations by employing bipolar coordinates (e.g., Happel and Brenner,

2012). Additionally, numerical simulations of the thin film equations could hopefully provide further insight into the temporal evolution of deformed holes.

8 Concluding remarks

The aim of the present work was to investigate the influence of different boundary configurations on the dissipation and stability of flows at low Reynolds numbers. Specifically, this study was concerned with the transport of single interfacial particles driven by an externally applied electric field, the increase of the energy dissipation due to the presence of multiple spherical interfacial particles, the hydrodynamic shielding of an obstacle in narrow channels with the help of electro-osmotic flow, the stability and collapse of a single hole in bounded liquid layers as well as the collapse of multiple holes in an infinitely extended liquid layer.

The motion of weakly charged interfacial particles, attached to a chargeless fluid interface separating two fluids having a large viscosity and permittivity ratio and subjected to a weak electric field was studied theoretically in chapter 3. The computation of the translational velocity, depending on the thickness of the electric double layer, the contact angle between the particle and the fluid interface and on the applied electric field, was the main goal of this chapter. It was shown that arbitrary shaped particles attached to flat fluid interfaces have the same electrophoretic mobility as long as the Debye layer thickness is asymptotically small (Smoluchowski limit). Furthermore, the translation of these particles does not lead to an interfacial deformation in the leading order, independent on the Debye layer thickness. In case of spherical interfacial particles, the electrophoretic mobility has been computed for arbitrary Debye lengths. Just as for bulk particles, the dependency of the electrophoretic mobility on the exact shape of the particle increases the more the electric double layer thickness varies from the Smoluchowski limit, which in this context indicates that the wetting properties become more dominant. More specifically, it was observed that hydrophobic particles have a higher electrophoretic mobility than hydrophilic particles. However, in case of spherical interfacial particles, the interfacial deformation induced by the charge of the particle has been obtained and found to be closely related to the thickness of the electric double layer forming at the surface portion immersed in the fluid with the higher permittivity. In contrast to the electrophoretic mobility, the interfacial deformation is independent on the contact angle between the particle and the fluid interface in the first-order contact angle perturbation, even in case of thick electric double layers. The theoretical results have been validated with full 3D numerical simulations. Interfacial electrophoresis enables the separation of Janus particles that is not always possible in the bulk, especially in case of different Janus particles that carry the same average ζ-potential.

The impact of the presence of multiple spherical interfacial particles on the energy dissipation has been discussed in chapter 4. Under the assumption of a sufficiently dilute interfacial suspension, in which hydrodynamic interactions can be neglected, the effective interfacial viscosities have been computed. The contact angle between the particles and the fluid interface has a significant influence on both interfacial viscosities, with its influence on the dilatational viscosity being larger than on the shear viscosity. Similar to a suspension of bulk particles, the presence of particles attached to an incompressible fluid interface lead to an effectively compressible behavior of the interface. The theoretical second-order results agree very well with previous semi-analytical results over a broad range of contact angles. In order to make full use of the theoretical results

in numerical simulations, a model for the effective interfacial tension of particle decorated fluid interfaces has been derived. As an example of application of our theory, the instability of a particle-laden liquid jet has been discussed. It has been found that even a small number of interfacial particles have a stabilizing effect on the liquid cylinder.

The focus of chapter 5 was on the shielding of a charged obstacle from an applied pressure driven flow. On the basis of the Hele-Shaw approximation and suitable shaped ζ-potential distributions at the upper and lower wall of the channel, an electro-osmotic flow can be induced such that the pressure force acting on the arbitrarily shaped obstacle is identically zero. The exact strength of the electro-osmotic flow that enables the shielding of an object was determined and depends on the strength of the applied electric field, on the ζ-potential of the annulus and on its lateral extension. For a slightly deformed circular obstacle, the reshape of the ζ-potential annulus has been computed and validated with the help of 2D numerical simulations. When parameterizing the obstacle using Fourier series, the required shape of the ζ-potential annulus is determined by the same number of terms in the Fourier series expansion as the obstacle and thus also by the same number of shape perturbation frequencies. However, the amplitude of the parametrization of the annulus is proportional to that of the obstacle, whereas the amplitudes corresponding to higher frequencies decay faster than those of small frequencies.

In chapter 6, the stability and collapse of holes in bounded liquid layers has been studied experimentally, numerically and theoretically. A stability branch has been obtained that strongly depends on the lateral extension of the liquid film, whereas the dependency on the contact angle is rather weak. Good agreement between experimental and numerical results has been obtained. Furthermore, the dynamics of hole collapse has been investigated. It has been found that the hole collapse predominantly obeys a scaling law, resulting from a balance of inertial forces (transient and convective contributions). In the final moment before the hole closes, pinching at the flanks of the hole was observed. A simple model has been developed to capture the main physics of the hole collapse. Right after the hole has been closed, a liquid column develops and grows in time. This dynamic process can be understood as a balance of inertial and surface tension forces providing a scaling law that agrees well with the experiments.

As an extension of chapter 6, the collapse of multiple circular holes in a thin liquid layer has been studied theoretically in chapter 7. It has been demonstrated that the potential energy of a thin liquid layer solely depends on the constitution at the three-phase contact line. With the help of the Onsager (variational) principle, an evolution equation has been derived that allows the computation of the time evolution of multiple holes in an infinitely extended liquid film. Experiments, employed on finitely extended liquid layers having a large contact angle, have been compared to the theoretical prediction and satisfying agreement has been obtained, despite the theory being derived based on the small contact angle assumption.

All results of this work provide insights into the relevance of boundary configurations on the motion and energy dissipation related to interfacial particles, the ability of shielding an object in a shallow channel, as well as on the stability of multiphase configurations. General conclusions on whether the influence of a certain boundary configuration significantly affects the global properties of a flow, cannot be made. Owing to the abundance of different boundary configurations, each specific system requires detailed investigation and thus provides a wealth of further possible studies.

Appendices

A Simplification of the governing equations of electrophoresis

The aim of this appendix is the simplification of the governing equations of electrophoresis on the basis of the assumptions from section 3.1, starting with equations (2.2), (2.7), (2.17), (2.25) and (2.26). In order to avoid carrying unnecessary subscripts and superscripts throughout this derivation, the simplification of the equations is proceeded assuming a particle suspended in a bulk consisting of a single, incompressible and Newtonian fluid. Transferring the resulting equations towards a two-phase configuration is provided subsequently.

To start with, we expand all variables in the governing equations into an equilibrium (superscript s 'static') and perturbation (superscript d 'dynamic') contribution, following O'Brien and White (1978). The equilibrium configuration corresponds to a non-moving charged particle dispersed in the bulk of a fluid in absence of an applied electric field. Consequently, the effect of the presence of the applied electric field is solely present in the perturbation variables. We may set

$$p = p^s + p^d, \tag{A.1}$$
$$\Psi = \psi^s + \psi^d, \tag{A.2}$$
$$n_i = n_i^s + n_i^d. \tag{A.3}$$

When inserting the latter expansions in the governing equations and making use of assumption 1 (from chapter 3) that leads to negligence of all products of variables corresponding to the perturbation state, we find

$$-\nabla p^s - \mathfrak{z} e(n_+^s - n_-^s)\nabla\psi^s = 0, \tag{A.4}$$
$$\epsilon\nabla^2\psi^s = -\mathfrak{z} e(n_+^s - n_-^s), \tag{A.5}$$
$$\nabla\cdot\left(\nabla n_i^s + n_i^s\frac{\mathfrak{z}_i e}{k_B T}\nabla\psi^s\right) = 0, \tag{A.6}$$
$$\nabla\cdot\boldsymbol{u} = 0, \tag{A.7}$$
$$-\nabla p^d + \mu\nabla^2\boldsymbol{u} - \mathfrak{z} e(n_+^d - n_-^d)\nabla\psi^s - \mathfrak{z} e(n_+^s - n_-^s)\nabla\psi^d = 0, \tag{A.8}$$
$$\epsilon\nabla^2\psi^d = -\mathfrak{z} e(n_+^d - n_-^d), \tag{A.9}$$
$$\nabla\cdot\left(n_i^s\boldsymbol{u} - D\left[\nabla n_i^d + n_i^s\frac{\mathfrak{z}_i e}{k_B T}\nabla\psi^d + n_i^d\frac{\mathfrak{z}_i e}{k_B T}\nabla\psi^s\right]\right) = 0. \tag{A.10}$$

Equations (A.4) - (A.6) refer to the equilibrium state, whereas equations (A.7) - (A.10) correspond to the perturbation state. In the following two subsections, a further simplification of the equations of equilibrium and perturbed state is discussed individually.

Equilibrium (static) state

In absence of an external electric field, the distribution of ions around the particle is solely determined through a balance of electrostatic migration and diffusion [see equation (A.6)]:

$$\boldsymbol{\nabla} \ln n_i^s + \frac{\mathfrak{z}_i e}{k_B T} \boldsymbol{\nabla} \psi^s = 0, \tag{A.11}$$

$$\boldsymbol{\nabla} \left(\ln n_i^s + \frac{\mathfrak{z}_i e}{k_B T} \psi^s \right) = 0, \tag{A.12}$$

$$\Rightarrow n_i^s = C_i e^{-\frac{\mathfrak{z}_i e}{k_B T} \psi^s}. \tag{A.13}$$

In the latter derivation, we have used the identity $\boldsymbol{\nabla} \ln n_i^s = \boldsymbol{\nabla} n_i^s / n_i^s$. C_i is a constant which has to be determined using appropriate boundary conditions. The distortion of the ion distribution from an equilibrium value n_i^∞ due to the presence of the particle is assumed to decay at sufficiently large distances from the particle. Since we solely consider symmetric electrolytes, such as NaCl ($\mathfrak{z} = 1$) dissolved in water, it follows that $n_+^\infty = n_-^\infty = n^\infty$ (by electroneutrality). Consequently, the ion distribution reads in the static state

$$n_i^s = n^\infty e^{-\frac{\mathfrak{z}_i e}{k_B T} \psi^s}, \; i = +, -. \tag{A.14}$$

Inserting of the latter equation into equation (A.5), the Poisson-Boltzmann equation is obtained (e.g., Masliyah and Bhattacharjee, 2006):

$$\epsilon \boldsymbol{\nabla}^2 \psi^s = 2 \mathfrak{z} e n^\infty \sinh \left(\frac{\mathfrak{z} e}{k_B T} \psi^s \right). \tag{A.15}$$

Analytical solutions of the Poisson-Boltzmann equation are limited to one dimensional ion screenings (Behrens and Borkovec, 1999), approximations are therefore unavoidable. We rewrite the latter equation in dimensionless form by introducing $\tilde{\psi}^s = \psi^s / \Psi_{\mathscr{P}}$ and $\tilde{\boldsymbol{\nabla}} = a \boldsymbol{\nabla}$, with $\Psi_{\mathscr{P}}$ and a denoting the electrostatic potential at the surface of the particle and a characteristic length of the particle, respectively. It is worth mentioning that in spirit of section 2.6, we could have used the ζ-potential instead of the electrostatic potential at the surface of the particle for non-dimensionalization purposes. However, in order to be consistent with literature, we use the scaled surface potential for now (e.g., Masliyah and Bhattacharjee, 2006; Hunter, 2013). In dimensionless form, equation (A.15) reads

$$\tilde{\boldsymbol{\nabla}}^2 \tilde{\psi}^s = \frac{2 a^2 \mathfrak{z} e n^\infty}{\Psi_{\mathscr{P}} \epsilon} \sinh \left(\frac{\mathfrak{z} e \Psi_{\mathscr{P}}}{k_B T} \tilde{\psi}^s \right). \tag{A.16}$$

If the scaled surface potential is small (assumption 2) $\mathfrak{z} e \Psi_{\mathscr{P}} / (k_B T) \ll 1$ (or $|\Psi_{\mathscr{P}}| \ll 25$ mV at room temperature), it follows that $\sinh(x) \approx x + O(x^3)$ and equation (A.16) simplifies to (in dimensional form)

$$\boldsymbol{\nabla}^2 \psi^s = \kappa^2 \psi^s, \tag{A.17}$$

$$\text{with} \quad \kappa = \sqrt{\frac{2 \mathfrak{z}^2 e^2 n^\infty}{\epsilon k_B T}}. \tag{A.18}$$

The linearization of the right-hand side of equation (A.15) is commonly known as the Debye-Hückel approximation (e.g., Masliyah and Bhattacharjee, 2006). The range of validity corresponding to the Debye-Hückel approximation is discussed in section 3.4.1. κ, defined in equation (A.18), is the inverse Debye length. For a 1 mM NaCl-water solution, the Debye length is of order $\kappa^{-1} \approx O(10^{-8})$ m. The momentum balance from equation (A.4) determines the osmotic (equilibrium) pressure:

$$\boldsymbol{\nabla} p^s - \epsilon \kappa^2 \psi^s \boldsymbol{\nabla} \psi^s = 0, \tag{A.19}$$

$$\boldsymbol{\nabla} \left(p^s - \epsilon \frac{\kappa^2}{2} (\psi^s)^2 \right) = 0, \tag{A.20}$$

$$\Rightarrow p^s = \epsilon \frac{\kappa^2}{2} (\psi^s)^2. \tag{A.21}$$

From equation (A.20) to (A.21) we have used that the osmotic pressure decays to zero at sufficient large distances from the particle.

Therefore, by solving the linearized Poisson-Boltzmann equation, all variables describing the equilibrium state are known.

Perturbation (dynamic) state

Analogously to the previous subsection, we start with the ionic transport equation as shown in equation (A.10). For now, we introduce the following dimensionless quantities: $\tilde{\boldsymbol{\nabla}} = a\boldsymbol{\nabla}$, $\tilde{\boldsymbol{u}} = \boldsymbol{u}/U$, $\tilde{n}_i^k = n_i^k / n^\infty$ ($k = s, d$ and $i = +, -$), $\tilde{\psi}^d = \psi^d / \Psi_{\mathscr{D}}$ and $\tilde{\psi}^s = \psi^s / \Psi_{\mathscr{D}}$. Equation (A.10) then reads

$$\tilde{\boldsymbol{\nabla}} \cdot \left(\mathrm{Pe}\, \tilde{n}_i^s \tilde{\boldsymbol{u}} - \left[\tilde{\boldsymbol{\nabla}} \tilde{n}_i^d + \frac{\jmath_i e \Psi_{\mathscr{D}}}{k_B T} \left(\tilde{n}_i^s \tilde{\boldsymbol{\nabla}} \tilde{\psi}^d + \tilde{n}_i^d \tilde{\boldsymbol{\nabla}} \tilde{\psi}^s \right) \right] \right) = 0, \text{ with } \mathrm{Pe} = \frac{Ua}{D}. \tag{A.22}$$

Pe is the Péclet number, defined as the ratio between the convective and the diffusive ion transport. The first term, proportional to Pe describes the convective motion of ions relative to the moving particle, which results in a transport of ions to the back of the particle (with respect to the direction of the motion of the particle).

A typical velocity with which a spherical polystyrene particle ($a \approx O(10^{-7} - 10^{-6})$ m) attached to an interface between a 1 mM NaCl solution [$D \approx O(10^{-9})$ m^2/s (Vitagliano, 1956)] and air translates, due to the presence of an applied electric field of order $E \approx O(10^2 - 10^3)$ V/m, is $U \approx O(10^{-5} - 10^{-4})$ m/s (Lee and Li, 2006; Zhang et al., 2018), leading to Pe $\approx O(10^{-2})$. It is worth it mentioning that the experimentally obtained velocities by Lee and Li (2006) and Zhang et al. (2018) are a superposition of the electrophoretic motion of the particle and an induced electroosmotic flow of the electrolyte and therefore $U \approx O(10^{-5} - 10^{-4})$ m/s probably overestimates the electrophoretic velocity of the particle. It will be shown in the course of chapter 3 that the electrophoretic velocity of an interfacial particle is proportional to its ζ-potential (in the phase of the higher permittivity) and the applied electric field E_∞, which, recalling assumptions 1 & 2, indeed leads to a small velocity of the particle, thus implying Pe $\ll 1$. Moreover, the results obtained by Wiersema et al. (1966) show that the convective ion transport mainly influences a

Debye layer thickness range of $0.2 < \kappa a < 50$ in case of a spherical particle suspended in a bulk fluid [a discussion on the impact of the Péclet number in electro-osmotic flows can be found in the work by Squires and Bazant (2004)]. On the basis of the previous discussion, we may limit ourselves to the asymptotic limit: $\mathrm{Pe} \to 0$.

In agreement with the Debye-Hückel approximation used in the previous subsection, we may expand all variables in the scaled surface potential, exemplary such as

$$\tilde{\psi}^s \approx \tilde{\psi}^{s,0} + \frac{\mathfrak{z} e \Psi_{\mathscr{D}}}{k_B T} \tilde{\psi}^{s,1}, \tag{A.23}$$

$$\tilde{\psi}^d \approx \tilde{\psi}^{d,0} + \frac{\mathfrak{z} e \Psi_{\mathscr{D}}}{k_B T} \tilde{\psi}^{d,1}. \tag{A.24}$$

We obtain the following equations:

$$\tilde{\boldsymbol{\nabla}}^2 \tilde{n}_i^{d,0} = 0, \tag{A.25}$$

$$\tilde{\boldsymbol{\nabla}}^2 \tilde{n}_i^{d,1} + \mathrm{sgn}(\mathfrak{z}_i) \tilde{\boldsymbol{\nabla}} \cdot \left[\tilde{n}_i^{s,0} \tilde{\boldsymbol{\nabla}} \tilde{\psi}^{d,0} + \tilde{n}_i^{d,0} \tilde{\boldsymbol{\nabla}} \tilde{\psi}^{s,0} \right] = 0. \tag{A.26}$$

Equation (A.25) and (A.26) correspond to the zeroth- and first-order expansion in the scaled potential, respectively. The function $\mathrm{sgn}(x)$ is the sign function that returns the sign of x. The perturbation of the ion concentration from equilibrium $\tilde{n}_i^d$ should decay to zero far away from the particle, in order to ensure the electroneutrality condition i.e., $\tilde{n}_i^d\big|_{r\to\infty} = 0$. Furthermore, no ions can penetrate into the surface of the particle which is mathematically described by a vanishing gradient of $\tilde{n}_i^{d,0}$ normal to the surface of the particle. The solution of the Laplace equation, satisfying both boundary conditions, clearly reads $\tilde{n}_i^{d,0} = 0$. Further, we have from equation (A.14): $\tilde{n}_i^s \approx 1 - \mathrm{sgn}(\mathfrak{z}_i)(\mathfrak{z} e \Psi_{\mathscr{D}})/(k_B T)\tilde{\psi}^{s,0}$. Thus, equation (A.26) can be written as

$$\tilde{\boldsymbol{\nabla}}^2 (\tilde{n}_+^{d,1} + \tilde{n}_-^{d,1}) = 0. \tag{A.27}$$

A suitable boundary condition on the surface of the particle is $\tilde{\boldsymbol{\nabla}} \tilde{n}_i^{d,1} \cdot \boldsymbol{n} = -\mathrm{sgn}(\mathfrak{z}_i) \tilde{\boldsymbol{\nabla}} \tilde{\psi}^{d,0} \cdot \boldsymbol{n}$, ensuring that no ions can penetrate the surface of the particle. Translated to the differential equation (A.27), we have $\tilde{\boldsymbol{\nabla}}(\tilde{n}_+^{d,1} + \tilde{n}_-^{d,1}) \cdot \boldsymbol{n} = 0$. Furthermore, when assuming that the gradient of the electrostatic potential in normal direction to the surface of the particle is zero (to be further discussed in section 3.1.1), a zero-gradient boundary condition is observed for both $\tilde{n}_i^{d,1}$ independently. As already discussed, at large distances from the particle the perturbation of the ion concentration should decay to zero. Thus we have $\tilde{n}_+^{d,1} = -\tilde{n}_-^{d,1}$.

Inserting the expanded variables into the Poisson equation and neglecting all terms of second order, we find

$$\tilde{\boldsymbol{\nabla}}^2 \tilde{\psi}^{d,0} = -\frac{1}{2} (\kappa a)^2 (\tilde{n}_+^{d,1} - \tilde{n}_-^{d,1}), \tag{A.28}$$

$$\tilde{\boldsymbol{\nabla}}^2 \tilde{\psi}^{d,1} = 0. \tag{A.29}$$

By making use of equations (A.26) and (A.28), we obtain

$$\tilde{\boldsymbol{\nabla}}^2(\tilde{n}_+^{d,1}-\tilde{n}_-^{d,1})=(\kappa a)^2(\tilde{n}_+^{d,1}-\tilde{n}_-^{d,1}). \tag{A.30}$$

When taking the boundary conditions into account, we find $\tilde{n}_+^{d,1}=\tilde{n}_-^{d,1}=0$. Consequently, the electrostatic potential $\tilde{\psi}^d$ is determined by the solution of the Laplace equation. The resulting set of simplified governing equations, are similar to these by Henry (1931). In contrast to Henry (1931), who postulated that the electrostatic potential can be written as a superposition of two potentials, one describing the electric double layer and the other the applied electric field, we have, starting with the general governing equations of electrophoresis, i.e., equations (2.2), (2.7), (2.17), (2.25) and (2.26), derived the same simplified set of equations.

The preceding derivation cannot be found in literature which could be the reason for misunderstandings about the applicability and physical correctness of Henry's solution (Henry, 1931). For example, Masliyah and Bhattacharjee (2006) suggest to introduce the chemical potential as a perturbation variable instead of the electrostatic potential, which finally leads to the same electrophoretic mobility. The derivation of the simplified set of equations, as performed in this appendix, clearly illustrates the complexity of the problem and the necessity of the underlying assumptions in the present context.

The governing equations hold for both phases $l=1,2$, independently. When employing the notation $\psi=\psi^s$ and $\phi=\psi^d$ [following Henry (1931)], the governing equations given in equations (3.2) - (3.6) are obtained.

In section 2.1.1, we have argued that the electrostatic volume force density can be written as the divergence of the Maxwell stress tensor. When introducing the Maxwell stress tensors $\boldsymbol{\sigma}_M^s$ and $\boldsymbol{\sigma}_M^d$ corresponding to an equilibrium and perturbed state, it is straightforward to prove that

$$\boldsymbol{\sigma}_{M,l}^s=\epsilon_l\left(\boldsymbol{\nabla}\psi_l\boldsymbol{\nabla}\psi_l-\frac{1}{2}\boldsymbol{\nabla}\psi_l\cdot\boldsymbol{\nabla}\psi_l\boldsymbol{I}\right), \tag{A.31}$$

$$\boldsymbol{\sigma}_{M,l}^d=\epsilon_l(\boldsymbol{\nabla}\phi_l\boldsymbol{\nabla}\psi_l+\boldsymbol{\nabla}\psi_l\boldsymbol{\nabla}\phi_l-\boldsymbol{\nabla}\phi_l\cdot\boldsymbol{\nabla}\psi_l\boldsymbol{I}), \tag{A.32}$$

fulfills

$$\boldsymbol{\nabla}\cdot\boldsymbol{\sigma}_{M,l}^s=\epsilon_l\boldsymbol{\nabla}^2\psi_l\boldsymbol{\nabla}\psi_l,\quad \boldsymbol{\nabla}\cdot\boldsymbol{\sigma}_{M,l}^d=\epsilon_l\boldsymbol{\nabla}^2\psi_l\boldsymbol{\nabla}\phi_l. \tag{A.33}$$

The subscript l refers to both fluid phases $l=1,2$.

B Solution of the Stokes equations for a slightly deformed sphere in pure straining flow

In this appendix, the solution of the Stokes equations together with the boundary condition from equation (4.15) is derived on the basis of Lamb's general solution (e.g., see section 2.3 and Happel and Brenner, 2012). Although, our main interest are mirror-fused particles, we keep the calculation as general as possible, i.e., we use the parametrization of an arbitrary slightly deformed sphere, as given in equation (2.63). According to section 2.4, we may limit our analysis to the first-order solution in the perturbation parameter β.

Equation (4.15) reads for a slightly deformed sphere in the first order of β

$$\boldsymbol{u}|_{r_{\mathscr{P}}} = -\boldsymbol{\mathfrak{E}} \cdot \frac{\boldsymbol{r}}{r} a \left[1 + \beta f(\theta, \varphi)\right]. \tag{B.1}$$

The velocity field can be expanded in a perturbation series via

$$\boldsymbol{u} = \sum_{n=0}^{\infty} \beta^n \boldsymbol{u}^{(n)}. \tag{B.2}$$

Correspondingly, every velocity field $\boldsymbol{u}^{(n)}$ has to satisfy the Stokes equations. Following the outline from section 2.4, the following boundary conditions are obtained

$$\boldsymbol{u}^{(0)}\big|_{r=a} = -\boldsymbol{\mathfrak{E}} \cdot \frac{\boldsymbol{r}}{r} a, \tag{B.3}$$

$$\boldsymbol{u}^{(1)}\big|_{r=a} = -a f(\theta, \varphi) \left(\boldsymbol{\mathfrak{E}} \cdot \frac{\boldsymbol{r}}{r} + \left. \frac{\partial \boldsymbol{u}^{(0)}}{\partial r} \right|_{r=a} \right). \tag{B.4}$$

The former boundary condition refers to a sphere in a pure straining flow, for which the solution is readily known (e.g., Guazzelli and Morris, 2011):

$$\boldsymbol{u}^{(0)} = -\frac{5a^3}{2} \frac{\boldsymbol{r}\,(\boldsymbol{r} \cdot \boldsymbol{\mathfrak{E}} \cdot \boldsymbol{r})}{r^5} - \frac{a^5}{2} \left(\frac{\boldsymbol{\mathfrak{E}} \cdot \boldsymbol{r} + \boldsymbol{r} \cdot \boldsymbol{\mathfrak{E}}}{r^5} - \frac{5\boldsymbol{r}\,(\boldsymbol{r} \cdot \boldsymbol{\mathfrak{E}} \cdot \boldsymbol{r})}{r^7} \right), \tag{B.5}$$

$$p^{(0)} = -5\mu a^3 \frac{\boldsymbol{r} \cdot \boldsymbol{\mathfrak{E}} \cdot \boldsymbol{r}}{r^5}. \tag{B.6}$$

Equation (B.4) then leads to

$$\boldsymbol{u}^{(1)}\big|_{r=a} = 5a f(\theta, \varphi) \left(\frac{(\boldsymbol{r} \cdot \boldsymbol{\mathfrak{E}} \cdot \boldsymbol{r})}{r^3} \boldsymbol{r} - \boldsymbol{\mathfrak{E}} \cdot \frac{\boldsymbol{r}}{r} \right). \tag{B.7}$$

According to section 2.3 and equations (2.57) - (2.59), the following three equations are expanded in surface spherical harmonics

$$\sum_{n=1}^{\infty} X_n = \frac{\boldsymbol{r}}{r} \cdot \boldsymbol{u}^{(1)}\big|_a = 0, \tag{B.8}$$

$$\sum_{n=1}^{\infty} Y_n = -r\boldsymbol{\nabla} \cdot \left(\boldsymbol{u}^{(1)}\big|_a\right) = 5a\left(\boldsymbol{\nabla}(f(\theta,\varphi)) \cdot \boldsymbol{\mathfrak{E}} \cdot \boldsymbol{r} - 3f(\theta,\varphi)\frac{\boldsymbol{r}\cdot\boldsymbol{\mathfrak{E}}\cdot\boldsymbol{r}}{r^2}\right), \tag{B.9}$$

$$\sum_{n=1}^{\infty} Z_n = \boldsymbol{r} \cdot \boldsymbol{\nabla} \times \left(\boldsymbol{u}^{(1)}\big|_a\right) = 5a\left(\boldsymbol{\mathfrak{E}} \cdot \frac{\boldsymbol{r}}{r}\right) \cdot \boldsymbol{\nabla} \times (f(\theta,\varphi)\boldsymbol{r}). \tag{B.10}$$

It follows directly that $X_n = 0$, $\forall n$. We now expand $f(\theta,\varphi) = \sum_{k=0}^{\infty} f_k$ in an infinite sum of surface spherical harmonics $[f_k = f_k(\theta,\varphi)]$ and define

$$\sum_{n=1}^{\infty} {}_kY_n = 5a\left(\boldsymbol{\nabla}(f_k) \cdot \boldsymbol{\mathfrak{E}} \cdot \boldsymbol{r} - 3f_k\frac{\boldsymbol{r}\cdot\boldsymbol{\mathfrak{E}}\cdot\boldsymbol{r}}{r^2}\right), \tag{B.11}$$

$$\sum_{n=1}^{\infty} {}_kZ_n = 5a\left(\boldsymbol{\mathfrak{E}} \cdot \frac{\boldsymbol{r}}{r}\right) \cdot \boldsymbol{\nabla} \times (f_k\boldsymbol{r}), \tag{B.12}$$

with the following relations

$$\sum_{k=0}^{\infty}\sum_{n=1}^{\infty} {}_kY_n = \sum_{n=1}^{\infty} Y_n, \tag{B.13}$$

$$\sum_{k=0}^{\infty}\sum_{n=1}^{\infty} {}_kZ_n = \sum_{n=1}^{\infty} Z_n. \tag{B.14}$$

It can be shown that for every fixed value of k, only a finite number of terms in the sums of equations (B.11) and (B.12) are non-vanishing. After some algebra, the following relations are obtained

$${}_kY_n = \begin{cases} \frac{5ak(k-2)}{8k^2-2}\boldsymbol{\mathfrak{E}} : \left[4\boldsymbol{\nabla}(f_k)\boldsymbol{r} + 2(k-2)f_k\frac{\boldsymbol{rr}}{r^2} + \frac{2}{k}r^2\boldsymbol{\nabla}\boldsymbol{\nabla}(f_k)\right], & n = k-2 \\ \frac{30a}{8k(k+1)-6}\boldsymbol{\mathfrak{E}} : \left[\boldsymbol{\nabla}(f_k)\boldsymbol{r} - k(k+1)f_k\frac{\boldsymbol{rr}}{r^2} + r^2\boldsymbol{\nabla}\boldsymbol{\nabla}(f_k)\right], & n = k \\ \frac{5a(k+1)(k+3)}{4k(k+2)+3}\boldsymbol{\mathfrak{E}} : \left[2\boldsymbol{\nabla}(f_k)\boldsymbol{r} - (k+3)f_k\frac{\boldsymbol{rr}}{r^2} - \frac{1}{k+1}r^2\boldsymbol{\nabla}\boldsymbol{\nabla}(f_k)\right], & n = k+2 \\ 0, & \text{else,} \end{cases} \tag{B.15}$$

$${}_kZ_n = \begin{cases} \frac{5a}{2k+1}\left[k\left(\boldsymbol{\mathfrak{E}}\cdot\frac{\boldsymbol{r}}{r}\right)\cdot(\boldsymbol{\nabla}(f_k)\times\boldsymbol{r}) + r\boldsymbol{\mathfrak{E}} : \boldsymbol{\nabla}(\boldsymbol{\nabla}(f_k)\times\boldsymbol{r})\right], & n = k-1 \\ \frac{5a}{2k+1}\left[(k+1)\left(\boldsymbol{\mathfrak{E}}\cdot\frac{\boldsymbol{r}}{r}\right)\cdot(\boldsymbol{\nabla}(f_k)\times\boldsymbol{r}) \right. \\ \left. -r\boldsymbol{\mathfrak{E}} : \boldsymbol{\nabla}(\boldsymbol{\nabla}(f_k)\times\boldsymbol{r})\right], & n = k+1 \\ 0, & \text{else.} \end{cases} \tag{B.16}$$

These identities can be verified in two steps: (i) The sum of all non-zero contributions on the right-hand side of equations (B.15) and (B.16) have to be equal to the right-hand sides of

equations (B.11) and (B.12), (ii) Since ${}_kY_n$ and ${}_kZ_n$ are surface spherical harmonics, it follows that $\boldsymbol{\nabla}^2(r^n\lambda_n)=0\ \forall n$, with $\lambda_n = {}_kY_n,\ {}_kZ_n$.

Using equations (B.15) and (B.16) we may rewrite equations (2.60) - (2.62) by replacing n with k for all non-vanishing contributions

$$
\begin{aligned}
{}_kp_{-(k-1)} &= \frac{5(k-2)k(2k-5)}{2(k-1)(4k^2-1)}\mu\left(\frac{a}{r}\right)^{k-1}\boldsymbol{\mathfrak{E}}:\Big[4\boldsymbol{\nabla}(f_k)\boldsymbol{r}+2(k-2)f_k\frac{\boldsymbol{r}\boldsymbol{r}}{r^2} \\
&\quad +\frac{2}{k}r^2\boldsymbol{\nabla}\boldsymbol{\nabla}f_k\Big], && \text{(B.17)}\\
{}_kp_{-(k+1)} &= \frac{15}{2k^2+5k+3}\mu\left(\frac{a}{r}\right)^{k+1}\boldsymbol{\mathfrak{E}}:\Big[\boldsymbol{\nabla}(f_k)\boldsymbol{r}-k(k+1)f_k\frac{\boldsymbol{r}\boldsymbol{r}}{r^2} \\
&\quad +r^2\boldsymbol{\nabla}\boldsymbol{\nabla}f_k\Big], && \text{(B.18)}\\
{}_kp_{-(k+3)} &= \frac{5(k+1)}{2k+1}\mu\left(\frac{a}{r}\right)^{k+3}\boldsymbol{\mathfrak{E}}:\Big[2\boldsymbol{\nabla}(f_k)\boldsymbol{r}-(k+3)f_k\frac{\boldsymbol{r}\boldsymbol{r}}{r^2} \\
&\quad -\frac{1}{k+1}r^2\boldsymbol{\nabla}\boldsymbol{\nabla}f_k\Big], && \text{(B.19)}\\
{}_k\phi_{-(k-1)} &= \frac{5k(k-2)a^2}{4(k-1)(4k^2-1)}\left(\frac{a}{r}\right)^{k-1}\boldsymbol{\mathfrak{E}}:\Big[4\boldsymbol{\nabla}(f_k)\boldsymbol{r}+2(k-2)f_k\frac{\boldsymbol{r}\boldsymbol{r}}{r^2} \\
&\quad +\frac{2}{k}r^2\boldsymbol{\nabla}\boldsymbol{\nabla}f_k\Big], && \text{(B.20)}\\
{}_k\phi_{-(k+1)} &= \frac{15a^2}{(k+1)(8k(k+1)-6)}\left(\frac{a}{r}\right)^{k+1}\boldsymbol{\mathfrak{E}}:\Big[\boldsymbol{\nabla}(f_k)\boldsymbol{r}-k(k+1)f_k\frac{\boldsymbol{r}\boldsymbol{r}}{r^2} \\
&\quad +r^2\boldsymbol{\nabla}\boldsymbol{\nabla}f_k\Big], && \text{(B.21)}\\
{}_k\phi_{-(k+3)} &= \frac{5(k+1)a^2}{8k(k+2)+6}\left(\frac{a}{r}\right)^{k+3}\boldsymbol{\mathfrak{E}}:\Big[2\boldsymbol{\nabla}(f_k)\boldsymbol{r}-(k+3)f_k\frac{\boldsymbol{r}\boldsymbol{r}}{r^2} \\
&\quad -\frac{1}{k+1}r^2\boldsymbol{\nabla}\boldsymbol{\nabla}f_k\Big], && \text{(B.22)}\\
{}_k\chi_{-k} &= \frac{5a}{2k^3-k^2-k}\left(\frac{a}{r}\right)^{k}\Big[k\left(\boldsymbol{\mathfrak{E}}\cdot\frac{\boldsymbol{r}}{r}\right)\cdot(\boldsymbol{\nabla}(f_k)\times\boldsymbol{r}) \\
&\quad +r\boldsymbol{\mathfrak{E}}:\boldsymbol{\nabla}(\boldsymbol{\nabla}(f_k)\times\boldsymbol{r})\Big], && \text{(B.23)}\\
{}_k\chi_{-(k+2)} &= \frac{5a}{2k^3+7k^2+7k+2}\left(\frac{a}{r}\right)^{k+2}\Big[(k+1)\left(\boldsymbol{\mathfrak{E}}\cdot\frac{\boldsymbol{r}}{r}\right)\cdot(\boldsymbol{\nabla}(f_k)\times\boldsymbol{r}) \\
&\quad -r\boldsymbol{\mathfrak{E}}:\boldsymbol{\nabla}(\boldsymbol{\nabla}(f_k)\times\boldsymbol{r})\Big]. && \text{(B.24)}
\end{aligned}
$$

The pressure up to first order in β is then found via

$$
\begin{aligned}
p_0 &= {}_kp_{-(k+3)}\big|_{k=0}, && \text{(B.25)}\\
p_1 &= {}_kp_{-(k+1)}\big|_{k=1} + {}_kp_{-(k+3)}\big|_{k=1}, && \text{(B.26)}\\
p_2 &= {}_kp_{-(k+1)}\big|_{k=2} + {}_kp_{-(k+3)}\big|_{k=2}, && \text{(B.27)}\\
p_k &= {}_kp_{-(k-1)} + {}_kp_{-(k+1)} + {}_kp_{-(k+3)},\ \text{if } k>2, && \text{(B.28)}\\
p^{(1)} &= \sum_{k=0}^{\infty}p_k. && \text{(B.29)}
\end{aligned}
$$

Following the same strategy, we find for the velocity field $\boldsymbol{u}$ in the first order in β:

$$\boldsymbol{u}_0 = \boldsymbol{\nabla}\times\left(\boldsymbol{r}\ {}_k\chi_{-(k+2)}\big|_{k=0}\right)+\boldsymbol{\nabla}\left({}_k\phi_{-(k+3)}\big|_{k=0}\right)+\frac{1}{2\mu}\boldsymbol{r}\ {}_kp_{-(k+3)}\big|_{k=0}, \tag{B.30}$$

$$\begin{aligned}\boldsymbol{u}_1 = {}&\boldsymbol{\nabla}\times\left(\boldsymbol{r}\ {}_k\chi_{-(k+2)}\big|_{k=1}\right)+\boldsymbol{\nabla}\left({}_k\phi_{-(k+3)}\big|_{k=1}+{}_k\phi_{-(k+1)}\big|_{k=1}\right)\\&+\frac{1}{2\mu}r^2\boldsymbol{\nabla}\left({}_kp_{-(k+1)}\big|_{k=1}-\frac{1}{15}\ {}_kp_{-(k+3)}\big|_{k=1}\right)\\&+\frac{2}{\mu}\boldsymbol{r}\left({}_kp_{-(k+1)}\big|_{k=1}+\frac{2}{15}\ {}_kp_{-(k+3)}\big|_{k=1}\right),\end{aligned} \tag{B.31}$$

$$\begin{aligned}\boldsymbol{u}_2 = {}&\boldsymbol{\nabla}\times\left[\boldsymbol{r}\left({}_k\chi_{-(k+2)}\big|_{k=2}+{}_k\chi_{-k}|_{k=2}\right)\right]\\&+\boldsymbol{\nabla}\left({}_k\phi_{-(k-1)}\big|_{k=2}+{}_k\phi_{-(k+3)}\big|_{k=2}+{}_k\phi_{-(k+1)}\big|_{k=2}\right)\\&-\frac{r^2}{28\mu}\boldsymbol{\nabla}\left({}_k\phi_{-(k+3)}\big|_{k=2}\right)+\frac{1}{2\mu}\boldsymbol{r}\left({}_kp_{-(k+1)}\big|_{k=2}+\frac{5}{14}\ {}_kp_{-(k+3)}\big|_{k=2}\right),\end{aligned} \tag{B.32}$$

$$\begin{aligned}\boldsymbol{u}_k = {}&\boldsymbol{\nabla}\times\left[\boldsymbol{r}\left({}_k\chi_{-(k+2)}+{}_k\ \chi_{-k}\right)\right]+\boldsymbol{\nabla}\left({}_k\phi_{-(k-1)}+{}_k\ \phi_{-(k+3)}+{}_k\ \phi_{-(k+1)}\right)\\&-\frac{(k-4)}{2(k-2)(2(k-2)-1)\mu}r^2\boldsymbol{\nabla}\left({}_kp_{-(k-1)}\right)-\frac{(k-2)}{2k(2k-1)\mu}r^2\boldsymbol{\nabla}\left({}_kp_{-(k+1)}\right)\\&-\frac{k}{2(k+2)(2(k+2)-1)\mu}r^2\boldsymbol{\nabla}\left({}_kp_{-(k+3)}\right)\\&+\boldsymbol{r}\frac{k-1}{(k-2)(2(k-2)-1)\mu}\ {}_kp_{-(k-1)}+\boldsymbol{r}\frac{(k+1)}{k(2k-1)\mu}\ {}_kp_{-(k+1)}\\&\boldsymbol{r}\frac{k+3}{(k+2)(2(k+2)-1)\mu}\ {}_kp_{-(k+3)},\ \text{if } k>2,\end{aligned} \tag{B.33}$$

$$\boldsymbol{u}^{(1)} = \sum_{k=0}^{\infty}\boldsymbol{u}_k. \tag{B.34}$$

Equations (B.17) - (B.34) represent the first-order solution of the Stokes equations. The stresslet can be calculated in its most general form for Lamb's general solution and reads (Kim and Karrila, 2013)

$$\mathscr{S} = -\frac{2\pi}{3}\boldsymbol{\nabla}\boldsymbol{\nabla}\left(r^5p_{-3}\right). \tag{B.35}$$

With the help of the foregoing derivations, we rewrite the $O(\beta)$ contribution to the latter equation as

$$\mathscr{S}^{(1)} = -\frac{2\pi}{3}\boldsymbol{\nabla}\boldsymbol{\nabla}\left[r^5\left({}_kp_{-(k-1)}\big|_{k=4}+{}_kp_{-(k+1)}\big|_{k=2}+{}_kp_{-(k+3)}\big|_{k=0}\right)\right]. \tag{B.36}$$

Inserting equations (B.17) - (B.19), we find after a cumbersome but rather straightforward calculation

$$\begin{aligned}\mathscr{S}^{(1)} = {}&20\pi\mu a^3\left(f_0\boldsymbol{\mathfrak{E}}-\frac{1}{21}\left(\boldsymbol{\nabla}\boldsymbol{\nabla}\left(r^2f_2\right):\boldsymbol{\mathfrak{E}}\right)\boldsymbol{I}\right.\\&+\frac{1}{14}\left(\boldsymbol{\mathfrak{E}}\cdot\boldsymbol{\nabla}\boldsymbol{\nabla}\left(r^2f_2\right)+\boldsymbol{\nabla}\boldsymbol{\nabla}\left(r^2f_2\right)\cdot\boldsymbol{\mathfrak{E}}\right)\\&\left.-\frac{1}{189}\boldsymbol{\nabla}\boldsymbol{\nabla}\boldsymbol{\nabla}\boldsymbol{\nabla}\left(r^4f_4\right):\boldsymbol{\mathfrak{E}}\right).\end{aligned} \tag{B.37}$$

It should be noted that the latter equation holds for an arbitrary slightly deformed sphere. Interestingly, compared to the force and torque acting on a slightly deformed sphere in pure translation and rotation [see equations (4.27) and (4.31)] which are determined by f_0 and f_2, the stresslet requires more detailed information of the shape of the particle, reflected in the term containing f_4.

C Simplification of the governing equations in Hele-Shaw channels

In this appendix, the governing equations of fluid motion inside a Hele-Shaw channel are derived on the basis of the assumptions from section 5.1. We introduce the following notation $\boldsymbol{u} = \boldsymbol{u}_\parallel + w\boldsymbol{e}_z$, in which the velocity vector is decomposed in parallel and normal components with respect to lower and upper channel wall [see figure 5.1 a)]. The following dimensionless variables are introduced

$$\tilde{\boldsymbol{r}}_\parallel = \frac{\boldsymbol{r}_\parallel}{a},\ \tilde{z} = \frac{z}{H}, \tilde{\boldsymbol{u}}_\parallel = \frac{\boldsymbol{u}_\parallel}{U_\parallel},\ \tilde{w} = \frac{w}{W},\ \tilde{p} = \frac{p}{P},\ \tilde{t} = \frac{t}{T},\ \tilde{\boldsymbol{\nabla}}_\parallel = a\boldsymbol{\nabla},\ \frac{\partial}{\partial \tilde{z}} = H\frac{\partial}{\partial z}. \tag{C.1}$$

The governing equations of fluid motion, i.e., equations (2.2) & (2.6), in absence of Maxwell stresses, then read

$$\frac{U_\parallel}{a}\tilde{\boldsymbol{\nabla}}_\parallel \cdot \tilde{\boldsymbol{u}}_\parallel + \frac{W}{H}\frac{\partial \tilde{w}}{\partial \tilde{z}} = 0, \tag{C.2}$$

$$\frac{\rho U_\parallel}{T}\left(\frac{\partial \tilde{\boldsymbol{u}}_\parallel}{\partial \tilde{t}} + \frac{T}{a/U_\parallel}\tilde{\boldsymbol{u}}_\parallel \cdot \tilde{\boldsymbol{\nabla}}_\parallel \tilde{\boldsymbol{u}}_\parallel + \frac{T}{H/W}\tilde{w}\frac{\partial \tilde{\boldsymbol{u}}_\parallel}{\partial \tilde{z}}\right) = -\frac{P}{a}\tilde{\boldsymbol{\nabla}}_\parallel \tilde{p} + \frac{\mu U_\parallel}{a^2}\left(\tilde{\boldsymbol{\nabla}}_\parallel^2 \tilde{\boldsymbol{u}}_\parallel + \frac{a^2}{H^2}\frac{\partial^2 \tilde{\boldsymbol{u}}_\parallel}{\partial \tilde{z}^2}\right), \tag{C.3}$$

$$\frac{\rho W}{T}\left(\frac{\partial \tilde{w}}{\partial \tilde{t}} + \frac{T}{a/U_\parallel}\tilde{\boldsymbol{u}}_\parallel \cdot \tilde{\boldsymbol{\nabla}}_\parallel \tilde{w} + \frac{T}{H/W}\tilde{w}\frac{\partial \tilde{w}}{\partial \tilde{z}}\right) = -\frac{P}{H}\frac{\partial \tilde{p}}{\partial \tilde{z}} + \frac{\mu W}{a^2}\left(\tilde{\boldsymbol{\nabla}}_\parallel^2 \tilde{w} + \frac{a^2}{H^2}\frac{\partial^2 \tilde{w}}{\partial \tilde{z}^2}\right). \tag{C.4}$$

We now make use of assumption 1 and set $H/a = \varepsilon$, in which ε is a small number $\varepsilon \ll 1$. In order to balance the terms in the continuity equation (C.2), it further follows that $W/U_\parallel = \varepsilon$. The characteristic time scale is chosen to match the transient and convective derivatives of the velocity field: $T = a/U_\parallel$. Furthermore, the characteristic pressure is set as $P = \mu U_\parallel/(a\varepsilon^2)$ in order to keep the driving term present in equation (C.3). Introducing the Reynolds number $\mathrm{Re} = \rho U_\parallel a/\mu$ leads us to

$$\tilde{\boldsymbol{\nabla}}_\parallel \cdot \tilde{\boldsymbol{u}}_\parallel + \frac{\partial \tilde{w}}{\partial \tilde{z}} = 0, \tag{C.5}$$

$$\varepsilon^2 \mathrm{Re}\left(\frac{\partial \tilde{\boldsymbol{u}}_\parallel}{\partial \tilde{t}} + \tilde{\boldsymbol{u}}_\parallel \cdot \tilde{\boldsymbol{\nabla}}_\parallel \tilde{\boldsymbol{u}}_\parallel + \tilde{w}\frac{\partial \tilde{\boldsymbol{u}}_\parallel}{\partial \tilde{z}}\right) = -\tilde{\boldsymbol{\nabla}}_\parallel \tilde{p} + \varepsilon^2 \tilde{\boldsymbol{\nabla}}_\parallel^2 \tilde{\boldsymbol{u}}_\parallel + \frac{\partial^2 \tilde{\boldsymbol{u}}_\parallel}{\partial \tilde{z}^2}, \tag{C.6}$$

$$\varepsilon^4 \mathrm{Re}\left(\frac{\partial \tilde{w}}{\partial \tilde{t}} + \tilde{\boldsymbol{u}}_\parallel \cdot \tilde{\boldsymbol{\nabla}}_\parallel \tilde{w} + \tilde{w}\frac{\partial \tilde{w}}{\partial \tilde{z}}\right) = -\frac{\partial \tilde{p}}{\partial \tilde{z}} + \varepsilon^4 \tilde{\boldsymbol{\nabla}}_\parallel^2 \tilde{w} + \varepsilon^2 \frac{\partial^2 \tilde{w}}{\partial \tilde{z}^2}. \tag{C.7}$$

In the leading order ($\varepsilon = 0$) the equations simplify to

$$\tilde{\boldsymbol{\nabla}}_\parallel \cdot \tilde{\boldsymbol{u}}_\parallel + \frac{\partial \tilde{w}}{\partial \tilde{z}} = 0, \tag{C.8}$$

$$\tilde{\boldsymbol{\nabla}}_\parallel \tilde{p} = \frac{\partial^2 \tilde{\boldsymbol{u}}_\parallel}{\partial \tilde{z}^2}, \tag{C.9}$$

$$\frac{\partial \tilde{p}}{\partial \tilde{z}} = 0. \tag{C.10}$$

Since $\tilde{p}$ is virtually independent on $\tilde{z}$, equation (C.9) can be integrated and we find

$$\tilde{\boldsymbol{u}}_{\parallel} = \frac{1}{2}\tilde{\boldsymbol{\nabla}}_{\parallel}\tilde{p}\left(\tilde{z}^2 - \tilde{z}\right) + \tilde{\boldsymbol{u}}_{\parallel}\Big|_{\tilde{z}=1}\tilde{z} + \tilde{\boldsymbol{u}}_{\parallel}\Big|_{\tilde{z}=0}(1-\tilde{z}), \tag{C.11}$$

in which $\tilde{\boldsymbol{u}}_{\parallel}\big|_{\tilde{z}=0}$ and $\tilde{\boldsymbol{u}}_{\parallel}\big|_{\tilde{z}=1}$ are the boundary conditions of the velocity field at the lower and upper wall. The depth-averaged velocity $\langle\tilde{\boldsymbol{u}}_{\parallel}\rangle_H$ can be found when computing the integral of equation (C.11) over the depth of the channel. Thereby we obtained equation (5.2). However, when inserting equation (5.2) into equation (C.8) and integrating again over the depth of the channel equation (5.1) is achieved.

D Comparison between the custom-made numerical simulations and the experimentally observed menisci

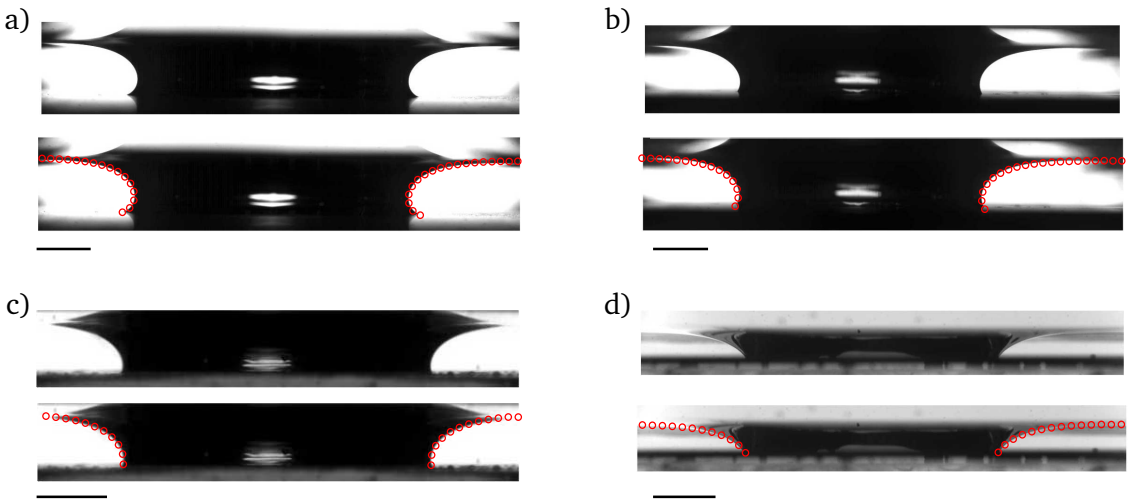

Abbildung D.1.: Comparison of the experimentally and numerically obtained liquid profiles. The numerical data were obtained as described in section 6.1.2 and are represented as hollow red circles. In each sub-figure, the upper frame is the original experimental image at a certain moment, before the instability sets in. The lower one shows the comparison. The corresponding substrates are: a) Superhydrophobic Al substrate with $\Theta_a = 167.5°$, $L = 14.5$ cm, $d = 26.1$ mm. b) Teflon substrate with $\Theta_a = 125.6°$, $L = 14.5$ cm, $d = 24.1$ mm. c) Liquid infused glass substrate with $\Theta_a = 97.6°$, $L = 14.5$ cm, $d = 23.2$ mm. d) Silicon wafer with $\Theta_a = 55.9°$, $L = 7$ cm, $d = 20.8$ mm. The scale bars represent 5 mm [reprinted with permission from Cambridge University Press, J. Fluid Mech. 855 (2018), Lv et al. (2018)].

Bibliography

M. Ahmadzadehtalatapeh and M. Mousavi. A Review on the Drag Reduction Methods of the Ship Hulls for Improving the Hydrodynamic Performance. *Int. J. Marit. Technol.*, 4:51–64, 2015.

R. A. Alberty. An introduction to electrophoresis: Part I: Methods and calculations. *J. Chem. Educ.*, 25(8):426, 1948. doi: 10.1021/ed025p426.

H. Altenbach. *Kontinuumsmechanik*. Springer Berlin Heidelberg, 2012.

A. Ashori. Wood-plastic composites as promising green-composites for automotive industries! *Bioresour. Technol.*, 99(11):4661–4667, 2008. doi: 10.1016/j.biortech.2007.09.043.

P. Aussillous and D. Quéré. Liquid marbles. *Nature*, 411(6840):924–927, 2001. doi: 10.1038/35082026.

R. Aveyard, B. P. Binks, J. H. Clint, P. D. I. Fletcher, T. S. Horozov, B. Neumann, V. N. Paunov, J. Annesley, S. W. Botchway, D. Nees, A. W. Parker, A. D. Ward, and A. N. Burgess. Measurement of Long-Range Repulsive Forces between Charged Particles at an Oil-Water Interface. *Phys. Rev. Lett.*, 88(24):246102, 2002. doi: 10.1103/PhysRevLett.88.246102.

R. Aveyard, B. P. Binks, and J. H. Clint. Emulsions stabilised solely by colloidal particles. *Adv. Colloid Interface Sci.*, 100:503–546, 2003. doi: 10.1007/978-3-642-04417-5_2.

R.-E. Avrămescu, M.-V. Ghica, C. Dinu-Pîrvu, D. I. Udeanu, and L. Popa. Liquid Marbles: From Industrial to Medical Applications. *Molecules*, 23(5):1120, 2018. doi: 10.3390/molecules23051120.

A. Bandopadhyay and S. Hardt. Stability of horizontal viscous fluid layers in a vertical arbitrary time periodic electric field. *Phys. Fluids*, 29(12):124101, 2017. doi: 10.1063/1.4999429.

S. G. Bankoff, M. F. G. Johnson, M. J. Miksis, R. A. Schluter, and P. G. Lopez. Dynamics of a dry spot. *J. Fluid Mech.*, 486:239-259, 2003. doi: 10.1017/S0022112003004634.

S. Barany. Electrophoresis in strong electric fields. *Adv. Colloid Interface Sci.*, 147:36–43, 2009. doi: 10.1016/j.cis.2008.10.006.

G. K. Batchelor. The stress system in a suspension of force-free particles. *J. Fluid Mech.*, 41(3):545–570, 1970. doi: 10.1017/S0022112070000745.

G. K. Batchelor. Brownian diffusion of particles with hydrodynamic interaction. *J. Fluid Mech.*, 74(1):1–29, 1976. doi: 10.1017/S0022112076001663.

G. K. Batchelor. The effect of Brownian motion on the bulk stress in a suspension of spherical particles. *J. Fluid Mech.*, 83(1):97–117, 1977. doi: 10.1017/S0022112077001062.

G. K. Batchelor. *An introduction to fluid mechanics*. Cambridge University press, 2000.

G. K. Batchelor and J. T. Green. The determination of the bulk stress in a suspension of spherical particles to order c^2. *J. Fluid Mech.*, 56(3):401–427, 1972. doi: 10.1017/S0022112072002435.

O. Bäumchen and K. Jacobs. Slip effects in polymer thin films. *J. Phys. Condens. Matter*, 22(3): 033102, 2009. doi: 10.1088/0953-8984/22/3/033102.

J. C. Baygents and D. A. Saville. Electrophoresis of drops and bubbles. *J. Chem. Soc. Faraday Trans.*, 87(12):1883–1898, 1991. doi: 10.1039/FT9918701883.

S. H. Behrens and M. Borkovec. Exact Poisson-Boltzmann solution for the interaction of dissimilar charge-regulating surfaces. *Phys. Rev. E - Stat. Physics, Plasmas, Fluids, Relat. Interdiscip. Top.*, 60(6):7040–7048, 1999. doi: 10.1103/PhysRevE.60.7040.

A. Belousov and M. Belousova. Dynamics and viscosity of 'a'a and pahoehoe lava flows of the 2012-2013 eruption of Tolbachik volcano, Kamchatka (Russia). *Bull. Volcanol.*, 80(1), 2018. doi: 10.1007/s00445-017-1180-2.

B. P. Binks. Particles as surfactants - similarities and differences. *Curr. Opin. Colloid Interface Sci.*, 7(1-2):21–41, 2002. doi: 10.1016/S1359-0294(02)00008-0.

J. C. Bird, W. D. Ristenpart, A. Belmonte, and H. A. Stone. Critical Angle for Electrically Driven Coalescence of Two Conical Droplets. *Phys. Rev. Lett.*, 103(16):164502, 2009. doi: 10.1103/PhysRevLett.103.164502.

B. Blocken, T. van Druenen, Y. Toparlar, F. Malizia, P. Mannion, T. Andrianne, T. Marchal, G.-J. Maas, and J. Diepens. Aerodynamic drag in cycling pelotons: New insights by CFD simulation and wind tunnel testing. *J. Wind Eng. Ind. Aerodyn.*, 179:319–337, 2018. doi: 10.1016/j.jweia.2018.06.011.

G. Böhme. *Strömungsmechanik nichtnewtonscher Fluide*. Springer-Verlag, 2013.

M. P. Boneva, N. C. Christov, K. D. Danov, and P. A. Kralchevsky. Effect of electric-field-induced capillary attraction on the motion of particles at an oil-water interface. *Phys. Chem. Chem. Phys.*, 9(48):6371-6384, 2007. doi: 10.1039/b709123k.

G. Boniello, C. Blanc, D. Fedorenko, M. Medfai, N. B. Mbarek, M. In, M. Gross, A. Stocco, and M. Nobili. Brownian diffusion of a partially wetted colloid. *Nat. Mater.*, 14(9):908–911, 2015. doi: 10.1038/nmat4348.

D. Bonn, J. Eggers, J. Indekeu, J. Meunier, and E. Rolley. Wetting and spreading. *Rev. Mod. Phys.*, 81(2):739–805, 2009. doi: 10.1103/RevModPhys.81.739.

F. Booth. The Cataphoresis of Spherical, Solid Non-Conducting Particles in a Symmetrical Electrolyte. *Proc. R. Soc. A Math. Phys. Eng. Sci.*, 203(1075):514–533, 1950. doi: 10.1098/rspa.1950.0154.

E. Bormashenko, R. Pogreb, Y. Bormashenko, A. Musin, and T. Stein. New Investigations on Ferrofluidics: Ferrofluidic Marbles and Magnetic-Field-Driven Drops on Superhydrophobic

Surfaces. *Langmuir*, 24(21):12119–12122, 2008. doi: 10.1021/la802355y.

E. Bormashenko, R. Pogreb, R. Balter, O. Gendelman, and D. Aurbach. Composite non-stick droplets and their actuation with electric field. *Appl. Phys. Lett.*, 100(15):151601, 2012. doi: 10.1063/1.3702568.

E. Bormashenko, A. Musin, G. Whyman, Z. Barkay, A. Starostin, V. Valtsifer, and V. Strelnikov. Revisiting the surface tension of liquid marbles: Measurement of the effective surface tension of liquid marbles with the pendant marble method. *Colloids Surfaces A Physicochem. Eng. Asp.*, 425:15–23, 2013. doi: 10.1016/j.colsurfa.2013.02.043.

J. B. Bostwick and P. H. Steen. Stability of Constrained Capillary Surfaces. *Annu. Rev. Fluid Mech.*, 47:539–568, 2015. doi: 10.1146/annurev-fluid-010814-013626.

J. B. Bostwick, J. A. Dijksman, and M. Shearer. Wetting dynamics of a collapsing fluid hole. *Phys. Rev. Fluids*, 2(1):014006, 2017. doi: 10.1103/PhysRevFluids.2.014006.

J. V. Boussinesq. Sur l'existence d'une viscosité superficielle, dans la mince couche de transition séparant un liquide d'un autre fluide contigu. *J. Ann. Chim. Phys.*, 29:349 – 357, 1913.

E. Boyko, S. Rubin, A. D. Gat, and M. Bercovici. Flow patterning in Hele-Shaw configurations using non-uniform electro-osmotic slip. *Phys. Fluids*, 27(10):102001, 2015. doi: 10.1063/1.4931637.

J. F. Brady, A. S. Khair, and M. Swaroop. On the bulk viscosity of suspensions. *J. Fluid Mech.*, 554:109-123, 2006. doi: 10.1017/S0022112006009438.

K. A. Brakke. The Surface Evolver. *Exp. Math.*, 1(2):141–165, 1992. doi: 10.1080/10586458.1992.10504253.

H. Brenner. The Stokes resistance of a slightly deformed sphere. *Chem. Eng. Sci.*, 19(8):519–539, 1964. doi: 10.1016/0009-2509(64)85045-4.

H. Brenner. *Interfacial Transport Processes and Rheology*. Elsevier, 1991.

H. Brenner and R. G. Cox. The resistance to a particle of arbitrary shape in translational motion at small Reynolds numbers. *J. Fluid Mech.*, 17(4):561–595, 1963. doi: 10.1017/S002211206300152X.

E. N. Brodskaya and V. V. Zakharov. Computer simulation study of the surface polarization of pure polar liquids. *J. Chem. Phys.*, 102(11):4595–4599, 1995. doi: 10.1063/1.469507.

A. Bühl. Über die Potentialdifferenz in der Doppelschicht an der Oberfläche einfacher Elektrolyte und des reinen Wassers. *Ann. Phys.*, 389(18):211–244, 1927. doi: 10.1002/andp.19273891803.

E. W. Burkholder and J. F. Brady. Nonlinear microrheology of active Brownian suspensions. *Soft Matter*, 2020. doi: 10.1039/C9SM01713E.

J. C. Burton, R. Waldrep, and P. Taborek. Scaling and Instabilities in Bubble Pinch-Off. *Phys. Rev. Lett.*, 94(18):184502, 2005. doi: 10.1103/PhysRevLett.94.184502.

J. W. Bush and D. L. Hu. Walking on water: Biolocomotion at the Interface. *Annu. Rev. Fluid Mech.*, 38:339–369, 2006. doi: 10.1146/annurev.fluid.38.050304.092157.

W. E. Byerly. *An elementary treatise on Fourier's series: and spherical, cylindrical, and ellipsoidal harmonics, with applications to problems in mathematical physics*. Dover Publications, 1893. ISBN 0486495469.

A. Carlson, G. Bellani, and G. Amberg. Contact line dissipation in short-time dynamic wetting. *EPL (Europhysics Letters)*, 97(4):44004, 2012. doi: 10.1209/0295-5075/97/44004.

A. Castellanos. *Electrohydrodynamics*. Springer Vienna, Vienna, 1998. ISBN 978-3-211-83137-3.

M. Chaplin. Theory vs Experiment: What is the Surface Charge of Water? *WATER*, 1 (1):1–28, 2009. doi: 10.14294/WATER.2009.2.

G. Chen, P. Tan, S. Chen, J. Huang, W. Wen, and L. Xu. Coalescence of Pickering Emulsion Droplets Induced by an Electric Field. *Phys. Rev. Lett.*, 110(6):064502, 2013. doi: 10.1103/PhysRevLett.110.064502.

Y.-S. Cho, G. R. Yi, J.-M. Lim, S.-H. Kim, V. N. Manoharan, D. J. Pine, and S.-M. Yang. Self-Organization of Bidisperse Colloids in Water Droplets. *J. Am. Chem. Soc.*, 127(45):15968–15975, 2005. doi: 10.1021/ja0550632.

T. Chou. Geometry-Dependent Electrostatics near Contact Lines. *Phys. Rev. Lett.*, 87(10):106101, 2001. doi: 10.1103/PhysRevLett.87.106101.

T.-H. Chou, S.-J. Hong, Y.-E. Liang, H.-K. Tsao, and Y.-J. Sheng. Equilibrium Phase Diagram of Drop-on-Fiber: Coexistent States and Gravity Effect. *Langmuir*, 27(7):3685–3692, 2011. doi: 10.1021/la2000969.

K. Ciunel, M. Armélin, G. H. Findenegg, and R. von Klitzing. Evidence of Surface Charge at the Air/Water Interface from Thin-Film Studies on Polyelectrolyte-Coated Substrates. *Langmuir*, 21(11):4790–4793, 2005. doi: 10.1021/la050328b.

A. Cogotti. Experimental techniques for the aerodynamic development of convertible cars. *SAE Tech. Pap.*, No. 920347:183–201, 1992. doi: 10.4271/920347.

L. Courbin, J. C. Bird, M. Reyssat, and H. A. Stone. Dynamics of wetting: from inertial spreading to viscous imbibition. *J. Phys. Condens. Matter*, 21(46):464127, 2009. doi: 10.1088/0953-8984/21/46/464127.

R. G. Cox. The dynamics of the spreading of liquids on a solid surface. Part 1. Viscous flow. *J. Fluid Mech.*, 168:169–194, 1986. doi: 10.1017/S0022112086000332.

R. G. Cox and H. Brenner. Effect of finite boundaries on the Stokes resistance of an arbitrary particle Part 3. Translation and rotation. *J. Fluid Mech.*, 28(2):391-411, 1967. doi: 10.1017/S0022112067002150.

D. J. Coyle, C. W. Macosko, and L. E. Scriven. The fluid dynamics of reverse roll coating. *AIChE J.*, 36(2):161–174, 1990. doi: 10.1002/aic.690360202.

R. V. Craster and O. K. Matar. Dynamics and stability of thin liquid films. *Rev. Mod. Phys.*, 81(3): 1131–1198, 2009. doi: 10.1103/RevModPhys.81.1131.

T. J. Craven, J. M. Rees, and W. B. Zimmerman. On slip velocity boundary conditions for electroosmotic flow near sharp corners. *Phys. Fluids*, 20(4):043603, 2008. doi: 10.1063/1.2906344.

S. Crawford, S. K. Lim, and S. Gradečak. Fundamental Insights into Nanowire Diameter Modulation and the Liquid/Solid Interface. *Nano Lett.*, 13(1):226–232, 2013. doi: 10.1021/nl3039019.

P. Creux, J. Lachaise, A. Graciaa, J. K. Beattie, and A. M. Djerdjev. Strong specific hydroxide ion binding at the pristine oil/water and air/water interfaces. *J. Phys. Chem. B*, 113(43): 14146–14150, 2009. doi: 10.1021/jp906978v.

T. N. Crouch, D. Burton, Z. A. LaBry, and K. B. Blair. Riding against the wind: a review of competition cycling aerodynamics. *Sport. Eng.*, 20(2):81–110, 2017. doi: 10.1007/s12283-017-0234-1.

K. D. Danov and P. A. Kralchevsky. Electric forces induced by a charged colloid particle attached to the water-nonpolar fluid interface. *J. Colloid Interface Sci.*, 298(1):213–231, 2006a. doi: 10.1016/j.jcis.2005.12.037.

K. D. Danov and P. A. Kralchevsky. Reply to Comment on Electrodipping Force Acting on Solid Particles at a Fluid Interface. *Langmuir*, 22(2):848–849, 2006b. doi: 10.1021/la051489i.

K. D. Danov, P. A. Kralchevsky, and M. P. Boneva. Electrodipping Force Acting on Solid Particles at a Fluid Interface. *Langmuir*, 20(15):6139–6151, 2004. doi: 10.1021/la0497090.

K. D. Danov, P. A. Kralchevsky, and M. P. Boneva. Shape of the capillary meniscus around an electrically charged particle at a fluid interface: Comparison of theory and experiment. *Langmuir*, 22(6):2653–2667, 2006. doi: 10.1021/la052749z.

S. H. Davis. Moving contact lines and rivulet instabilities. Part 1. The static rivulet. *J. Fluid Mech.*, 98(2):225–242, 1980. doi: 10.1017/S0022112080000110.

M. De Corato and V. Garbin. Capillary interactions between dynamically forced particles adsorbed at a planar interface and on a bubble. *J. Fluid Mech.*, 847:71–92, 2018. doi: 10.1017/jfm.2018.319.

P. G. De Gennes. Wetting: Statics and dynamics. *Rev. Mod. Phys.*, 57(3):827–863, 1985. doi: 10.1103/RevModPhys.57.827.

P.-G. de Gennes, F. Brochard-Wyart, and D. Quéré. *Capillarity and wetting phenomena*. Springer, 2003.

H. de Maleprade, C. Clanet, and D. Quéré. Spreading of Bubbles after Contacting the Lower Side of an Aerophilic Slide Immersed in Water. *Phys. Rev. Lett.*, 117(9):094501, 2016. doi: 10.1103/PhysRevLett.117.094501.

G. Debregéas, P.-G. de Gennes, and F. Brochard-Wyart. The Life and Death of "Bare" Viscous Bubbles. *Science*, 279(5357):1704–1707, 1998. doi: 10.1126/science.279.5357.1704.

Á. V. Delgado, F. González-Caballero, R. J. Hunter, L. K. Koopal, and J. Lyklema. Measurement and interpretation of electrokinetic phenomena. *J. Colloid Interface Sci.*, 309(2):194–224, 2007. doi: 10.1016/j.jcis.2006.12.075.

Y. Di, X. Xu, J. Zhou, and M. Doi. Thin film dynamics in coating problems using Onsager principle. *Chinese Phys. B*, 27(2):024501, 2018. doi: 10.1088/1674-1056/27/2/024501.

E. Dickinson. Food emulsions and foams: Stabilization by particles. *Curr. Opin. Colloid Interface Sci.*, 15:40–49, 2010. doi: 10.1016/j.cocis.2009.11.001.

J. A. Diez, R. Gratton, and J. Gratton. Self-similar solution of the second kind for a convergent viscous gravity current. *Phys. Fluids A Fluid Dyn.*, 4(6):1148–1155, 1992. doi: 10.1063/1.858233.

J. A. Dijksman, S. Mukhopadhyay, C. Gaebler, T. P. Witelski, and R. P. Behringer. Obtaining self-similar scalings in focusing flows. *Phys. Rev. E*, 92(4):043016, 2015. doi: 10.1103/PhysRevE.92.043016.

M. Doi. Onsager's variational principle in soft matter. *J. Phys. Condens. Matter*, 23(28):284118, 2011. doi: 10.1088/0953-8984/23/28/284118.

M. Doi. *Soft matter physics*. Oxford University Press, 2013.

P. Dommersnes and J. Fossum. Surface structuring of particle laden drops using electric fields. *Eur. Phys. J. Spec. Top.*, 225(4):715–728, 2016. doi: 10.1140/epjst/e2016-60013-9.

K. D. Dorfman. DNA electrophoresis in microfabricated devices. *Rev. Mod. Phys.*, 82(4):2903–2947, 2010. doi: 10.1103/RevModPhys.82.2903.

A. Dörr and S. Hardt. Line tension and reduction of apparent contact angle associated with electric double layers. *Phys. Fluids*, 26(8):082105, 2014. doi: 10.1063/1.4892621.

A. Dörr and S. Hardt. Driven particles at fluid interfaces acting as capillary dipoles. *J. Fluid Mech.*, 770:5–26, 2015. doi: 10.1017/jfm.2015.129.

A. Dörr, S. Hardt, H. Masoud, and H. A. Stone. Drag and diffusion coefficients of a spherical particle attached to a fluid-fluid interface. *J. Fluid Mech.*, 790:607–618, 2016. doi: 10.1017/jfm.2016.41.

L. Duchemin, J. Eggers, and C. Josserand. Inviscid coalescence of drops. *J. Fluid Mech.*, 487: 167-178, 2003. doi: 10.1017/S0022112003004646.

C. Duprat and H. A. Stone. *Fluid-Structure Interactions in Low-Reynolds-Number Flows*. Royal Society of Chemistry, 2015.

A. Eddi, K. G. Winkels, and J. H. Snoeijer. Influence of Droplet Geometry on the Coalescence of Low Viscosity Drops. *Phys. Rev. Lett.*, 111(14):144502, 2013. doi: 10.1103/PhysRevLett.111.144502.

A. Edwards, R. Ledesma-Aguilar, M. I. Newton, C. Brown, and G. McHale. Not spreading in reverse: The dewetting of a liquid film into a single drop. *Sci. Adv.*, 2(9):1–11, 2016. doi: 10.1126/sciadv.1600183.

J. Eggers, J. R. Lister, and H. A. Stone. Coalescence of liquid drops. *J. Fluid Mech.*, 401:293–310, 1999. doi: 10.1017/S002211209900662X.

J. Eggers, M. A. Fontelos, D. Leppinen, and J. H. Snoeijer. Theory of the Collapsing Axisymmetric Cavity. *Phys. Rev. Lett.*, 98(9):094502, 2007. doi: 10.1103/PhysRevLett.98.094502.

A. Eifert, D. Paulssen, S. N. Varanakkottu, T. Baier, and S. Hardt. Simple Fabrication of Robust Water-Repellent Surfaces with Low Contact-Angle Hysteresis Based on Impregnation. *Adv. Mater. Interfaces*, 1(3):1300138, 2014. doi: 10.1002/admi.201300138.

M. Eigenbrod and S. Hardt. The effective shear and dilatational viscosities of a particle-laden interface in the dilute limit. *J. Fluid Mech.*, 903, A26, 2020. doi: 10.1017/jfm.2020.627.

M. Eigenbrod, F. Bihler, and S. Hardt. Electrokinetics of a particle attached to a fluid interface: Electrophoretic mobility and interfacial deformation. *Phys. Rev. Fluids*, 3(10):103701, 2018. doi: 10.1103/PhysRevFluids.3.103701.

A. Einstein. Eine neue Bestimmung der Moleküldimensionen. *Ann. Phys.*, 324(2):289–306, 1906. doi: 10.1002/andp.19063240204.

N. Eshtiaghi, J. J. Liu, and K. P. Hapgood. Formation of hollow granules from liquid marbles: Small scale experiments. *Powder Technol.*, 197(3):184–195, 2010. doi: 10.1016/j.powtec.2009.09.013.

X. Fan, Z. Zhang, G. Li, and N. Rowson. Attachment of solid particles to air bubbles in surfactant-free aqueous solutions. *Chem. Eng. Sci.*, 59(13):2639–2645, 2004. doi: 10.1016/j.ces.2004.04.001.

H. Faxén. Der Widerstand gegen die Bewegung einer starren Kugel in einer zähen Flüssigkeit, die zwischen zwei parallelen Wänden eingeschlossen ist. *Ann. Phys.*, 373(10):89–119, 1922.

M. Fixman. Charged macromolecules in external fields. I. The sphere. *J. Chem. Phys.*, 72(9):5177–5186, 1980. doi: 10.1063/1.439753.

C. L. Flurer. Analysis of antibiotics by capillary electrophoresis. *Electrophoresis*, 20(15-16):3269–3279, 1999. doi: 10.1002/elps.1150181233.

M. Flury and S. Aramrak. Role of air-water interfaces in colloid transport in porous media: A review. *Water Resour. Res.*, 53:5247–5275, 2017. doi: 10.1002/2017WR020597.

L. Foret and A. Würger. Electric-Field Induced Capillary Interaction of Charged Particles at a Polar Interface. *Phys. Rev. Lett.*, 92(5):058302, 2004. doi: 10.1103/PhysRevLett.92.058302.

D. R. Foss and J. F. Brady. Structure, diffusion and rheology of Brownian suspensions by Stokesian Dynamics simulation. *J. Fluid Mech.*, 407:167–200, 2000. doi: 10.1017/S0022112099007557.

F. E. Fox and G. D. Rock. Compressional Viscosity and Sound Absorption in Water at Different Temperatures. *Phys. Rev.*, 70(1-2):68–73, 1946. doi: 10.1103/PhysRev.70.68.

J. B. Freund. Numerical Simulation of Flowing Blood Cells. *Annu. Rev. Fluid Mech.*, 46(1):67–95, 2014. doi: 10.1146/annurev-fluid-010313-141349.

A. N. Frumkin. Note on B. Kamieński's paper: The nature of the electric potential at the free surface of aqueous solutions. *Electrochim. Acta*, 2(4):351–354, 1960. doi: 10.1016/0013-4686(60)80031-X.

R. Gahoual, A. Beck, E. Leize-Wagner, and Y.-N. Francois. Cutting-edge capillary electrophoresis characterization of monoclonal antibodies and related products. *J. Chromatogr. B*, 1032:61–78, 2016. doi: 10.1016/j.jchromb.2016.05.028.

P. Galatola and J.-B. Fournier. Capillary force acting on a colloidal particle floating on a deformed interface. *Soft Matter*, 10(13):2197–2212, 2014. doi: 10.1039/C3SM52622D.

H.-M. Gao, Z.-Y. Lu, H. Liu, Z.-Y. Sun, and L.-J. An. Orientation and surface activity of Janus particles at fluid-fluid interfaces. *J. Chem. Phys.*, 141(13):134907, 2014. doi: 10.1063/1.4897185.

N. Gao, F. Geyer, D. W. Pilat, S. Wooh, D. Vollmer, H. J. Butt, and R. Berger. How drops start sliding over solid surfaces. *Nat. Phys.*, 14(2):191–196, 2018. doi: 10.1038/nphys4305.

Y. Gao and D. Li. Translational motion of a spherical particle near a planar liquid-fluid interface. *J. Colloid Interface Sci.*, 319(1):344–352, 2008. doi: 10.1016/j.jcis.2007.11.052.

A. D. Gat, I. Frankel, and D. Weihs. A higher-order Hele-Shaw approximation with application to gas flows through shallow micro-channels. *J. Fluid Mech.*, 638:141–160, 2009. doi: 10.1017/S002211200999125X.

R. Gatignol and R. Prud'homme. *Mechanical and thermodynamical modeling of fluid interfaces*. World Scientific, 2001.

Q. Ge, Z. Liu, Y. Bai, D. Zhang, P. Yu, and Z. Lu. Emulsion PCR-based method to detect Y chromosome microdeletions. *Anal. Biochem.*, 367(2):173–178, 2007. doi: 10.1016/j.ab.2007.05.008.

H. Giesekus. *Phänomenologische Rheologie: Eine Einführung*. Springer-Verlag, 2011.

D. Gilberg and N. S. Trudinger. *Elliptic Partial Differential Equations of Second Order*. Springer, 2015. ISBN 978-3-642-61798-0.

Glycerine Producers' Association and others. *Physical properties of glycerine and its solutions*. Glyerine Producers' Association, 1963.

J. M. Gordillo, A. Sevilla, J. Rodríguez-Rodríguez, and C. Martínez-Bazán. Axisymmetric Bubble Pinch-Off at High Reynolds Numbers. *Phys. Rev. Lett.*, 95(19):194501, 2005. doi: 10.1103/PhysRevLett.95.194501.

A. Graciaa, G. Morel, P. Saulner, J. Lachaise, and R. Schechter. The ζ-Potential of Gas Bubbles. *J. Colloid Interface Sci.*, 172(1):131–136, 1995. doi: 10.1006/jcis.1995.1234.

E. Guazzelli and J. F. Morris. *A Physical Introduction to Suspension Dynamics*. Cambridge University press, 2011.

J. Happel and H. Brenner. *Low Reynolds number hydrodynamics: with special applications to particulate media*. Springer Science & Business Media, 2012.

D. J. Harrison, A. Manz, Z. Fan, H. Luedi, and H. M. Widmer. Capillary electrophoresis and sample injection systems integrated on a planar glass chip. *Anal. Chem.*, 64(17):1926–1932, 1992. doi: 10.1021/ac00041a030.

S. M. R. Hassan, T. Islam, M. Ali, and M. Q. Islam. Numerical Study on Aerodynamic Drag Reduction of Racing Cars. *Procedia Eng.*, 90:308–313, 2014. doi: 10.1016/j.proeng.2014.11.854.

D. C. Henry. The Cataphoresis of Suspended Particles. Part I. The Equation of Cataphoresis. *Proc. R. Soc. A Math. Phys. Eng. Sci.*, 133(821):106–129, 1931. doi: 10.1098/rspa.1931.0133.

R. Hill and G. Power. Extremum principles for slow viscous flow and the approximate calculation of drag. *Q. J. Mech. Appl. Math.*, 9(3):313–319, 1956. doi: 10.1093/qjmam/9.3.313.

E. J. Hinch and L. G. Leal. The effect of Brownian motion on the rheological properties of a suspension of non-spherical particles. *J. Fluid Mech.*, 52(4):683–712, 1972. doi: 10.1017/S002211207200271X.

E. J. Hinch and L. G. Leal. Rotation of small non-axisymmetric particles in a simple shear flow. *J. Fluid Mech.*, 92(03):591, 1979. doi: 10.1017/S002211207900077X.

D. Huang, C. Cottin-Bizonne, C. Ybert, and L. Bocquet. Massive Amplification of Surface-Induced Transport at Superhydrophobic Surfaces. *Phys. Rev. Lett.*, 101(6):064503, 2008. doi: 10.1103/PhysRevLett.101.064503.

J. S. Huang and R. Varadaraj. Colloid and interface science in the oil industry. *Curr. Opin. Colloid Interface Sci.*, 1(4):535–539, 1996. doi: 10.1016/S1359-0294(96)80124-5.

E. Hückel. Die Kathaphorese der Kugel. *Phys. Z.*, 25:204 – 210, 1924.

R. J. Hunter. *Zeta potential in colloid science: principles and applications*. Academic Press, 2 edition, 2013.

N. S. Hush. The Free Energies of Hydration of Gaseous Ions. *Aust. J. Chem.*, 1(4):480–493, 1948. doi: 10.1071/CH9480480.

J. D. Jackson. *Classical Electrodynamics*. John Wiley & Sons, 2007.

G. B. Jeffery. The Motion of Ellipsoidal Particles Immersed in a Viscous Fluid. *Proc. R. Soc. A Math. Phys. Eng. Sci.*, 102(715):161–179, 1922. doi: 10.1098/rspa.1922.0078.

P. Johansson and B. Hess. Molecular origin of contact line friction in dynamic wetting. *Phys. Rev. Fluids*, 3:074201, 2018. doi: 10.1103/PhysRevFluids.3.074201.

A. Kabla and G. Debregeas. Quasi-static rheology of foams. Part 1. Oscillating strain. *J. Fluid Mech.*, 587:23–44, 2007. doi: 10.1017/S0022112007007264.

S. Kaneko, C. Urata, T. Sato, R. Hönes, and A. Hozumi. Smooth and Transparent Films Showing Paradoxical Surface Properties: The Lower the Static Contact Angle, the Better the Water Sliding Performance. *Langmuir*, 35(21):6822–6829, 2019. doi: 10.1021/acs.langmuir.9b00206.

I. S. Kang and L. G. Leal. Small-amplitude perturbations of shape for a nearly spherical bubble in an inviscid straining flow (steady shapes and oscillatory motion). *J. Fluid Mech.*, 187:231–266, 1988. doi: 10.1017/S0022112088000412.

I. Karapanagiotis and W. W. Gerberich. Polymer film rupturing in comparison with leveling and dewetting. *Surf. Sci.*, 594(1-3):192–202, 2005. doi: 10.1016/j.susc.2005.07.023.

S. M. Kathmann, I.-F. W. Kuo, and C. J. Mundy. Electronic Effects on the Surface Potential at the Vapor-Liquid Interface of Water. *J. Am. Chem. Soc.*, 131(47):17522–17522, 2009. doi: 10.1021/ja908142d.

H. J. Keh and J. L. Anderson. Boundary effects on electrophoretic motion of colloidal spheres. *J. Fluid Mech.*, 153:417–439, 1985. doi: 10.1017/S002211208500132X.

H. J. Keh and T. H. Hsieh. Electrophoresis of a colloidal sphere in a spherical cavity with arbitrary zeta potential distributions and arbitrary double-layer thickness. *Langmuir*, 24(2):390–398, 2008. doi: 10.1021/la702399u.

A. S. Khair. Diffusiophoresis of colloidal particles in neutral solute gradients at finite Péclet number. *J. Fluid Mech.*, 731:64–94, 2013. doi: 10.1017/jfm.2013.364.

J. Y. Kim and B. J. Yoon. Electrophoretic Motion of a Slightly Deformed Sphere with a Nonuniform Zeta Potential Distribution. *J. Colloid Interface Sci.*, 251(2):318–330, 2002. doi: 10.1006/jcis.2002.8359.

S. Kim and S. J. Karrila. *Microhydrodynamics: principles and selected applications*. Courier Corporation, 2013.

B. J. Kirby and E. F. Hasselbrink. Zeta potential of microfluidic substrates: 2. Data for polymers. *Electrophoresis*, 25(2):203–213, 2004. doi: 10.1002/elps.200305755.

S. F. Kistler and P. M. Schweizer. *Liquid Film Coating*. Springer Netherlands, Dordrecht, 1997. ISBN 978-94-010-6246-6.

E. Klodzinska, M. Szumski, E. Dziubakiewicz, K. Hrynkiewicz, E. Skwarek, W. Janusz, and B. Buszewski. Effect of zeta potential value on bacterial behavior during electrophoretic separation. *Electrophoresis*, 31(9):1590–1596, 2010. doi: 10.1002/elps.200900559.

L. Komzsik. *Applied calculus of variations for engineers*. CRC Press, 2019.

J. Koplik, J. R. Banavar, and J. F. Willemsen. Molecular dynamics of Poiseuille flow and moving contact lines. *Phys. Rev. Lett.*, 60(13):1282–1285, 1988. doi: 10.1103/PhysRevLett.60.1282.

J. Koplik, J. R. Banavar, and J. F. Willemsen. Molecular dynamics of fluid flow at solid surfaces. *Phys. Fluids A Fluid Dyn.*, 1(5):781–794, 1989. doi: 10.1063/1.857376.

P. A. Kralchevsky, V. N. Paunov, I. B. Ivanov, and K. Nagayama. Capillary meniscus interaction between colloidal particles attached to a liquid-fluid interface. *J. Colloid Interface Sci.*, 151(1): 79–94, 1992. doi: 10.1016/0021-9797(92)90239-I.

L. I. Krishtalik. The Surface Potential of Solvent and the Intraphase Pre-existing Potential. *Russ. J. Electrochem.*, 44(1):43–49, 2008. doi: 10.1134/S1023193508010072.

A. L. Kupershtokh, E. V. Ermanyuk, and N. V. Gavrilov. The Rupture of Thin Liquid Films Placed on Solid and Liquid Substrates in Gravity Body Forces. *Commun. Comput. Phys.*, 17(5): 1301–1319, 2015. doi: 10.4208/cicp.2014.m340.

E. T. Lagally, C. A. Emrich, and R. A. Mathies. Fully integrated PCR-capillary electrophoresis microsystem for DNA analysis. *Lab Chip*, 1(2):102, 2001. doi: 10.1039/b109031n.

H. Lamb. *Statics*. Cambridge University Press, 1916.

H. Lamb. *Hydrodynamics*. University Press, 1945.

L. D. Landau and E. M. Lifschitz. *Fluid Mechanics*. 1987.

D. Langbein. *Capillary surfaces: Shape-stability-dynamics, in particular under weightlessness*. Springer-Verlag Berlin Heidelberg, 2002.

C.-B. Laurell. Quantitative estimation of proteins by electrophoresis in agarose gel containing antibodies. *Anal. Biochem.*, 15(1):45–52, 1966. doi: 10.1016/0003-2697(66)90246-6.

L. G. Leal. *Advanced transport phenomena: fluid mechanics and convective transport processes*. Cambridge University press, 2007.

J. Léandri and A. Würger. Trapping energy of a spherical particle on a curved liquid interface. *J. Colloid Interface Sci.*, 405:249–255, 2013. doi: 10.1016/j.jcis.2013.04.024.

C.-C. Lee. The charge conserving Poisson-Boltzmann equations: Existence, uniqueness, and maximum principle. *J. Math. Phys.*, 55(5):051503, 2014. doi: 10.1063/1.4878492.

J. S. Lee and Y. C. Fung. Stokes flow around a circular cylindrical post confined between two parallel plates. *J. Fluid Mech.*, 37(4):657–670, 1969. doi: 10.1017/S0022112069000796.

J. S. H. Lee and D. Li. Electroosmotic flow at a liquid-air interface. *Microfluid. Nanofluidics*, 2(4): 361–365, 2006. doi: 10.1007/s10404-006-0084-9.

D. Leppinen, J. Lister, and J. Eggers. Capillary pinch-off of inciscid fluids at varying density ratios: the bubble limit. *Bull. Am. Phys. Soc*, 50:63 (Abstract only), 2005.

K. Leung. Surface Potential at the Air-Water Interface Computed Using Density Functional Theory. *J. Phys. Chem. Lett.*, 1(2):496–499, 2010. doi: 10.1021/jz900268s.

S. Lim and K. H. Ahn. Rheological properties of oil paints and their flow instabilities in blade coating. *Rheol. Acta*, 52(7):643–659, 2013. doi: 10.1007/s00397-013-0717-3.

S. V. Lishchuk. Effective surface dilatational viscosity of highly concentrated particle-laden interfaces. *Phys. Rev. E*, 90(5):053005, 2014. doi: 10.1103/PhysRevE.90.053005.

S. V. Lishchuk. Dilatational viscosity of dilute particle-laden fluid interface at different contact angles. *Phys. Rev. E*, 94(6):063111, 2016. doi: 10.1103/PhysRevE.94.063111.

S. V. Lishchuk and I. Halliday. Effective surface viscosities of a particle-laden fluid interface. *Phys. Rev. E*, 80:1–7, 2009. doi: 10.1103/PhysRevE.80.016306.

Y. W. Liu, S. Pennathur, and C. D. Meinhart. Electrophoretic mobility of a spherical nanoparticle in a nanochannel. *Phys. Fluids*, 26(11):112002, 2014. doi: 10.1063/1.4901330.

Y. W. Liu, S. Pennathur, and C. D. Meinhart. Electrophoretic mobility of spherical particles in bounded domain. *J. Colloid Interface Sci.*, 461:32–38, 2016. doi: 10.1016/j.jcis.2015.08.039.

M. Longuet-Higgins, B. R. Kerman, and K. Lunde. The release of air bubbles from an underwater nozzle. *J. Fluid Mech.*, 230:365–390, 1991. doi: 10.1121/1.2029902.

P. G. López, M. J. Miksis, and S. G. Bankoff. Stability and evolution of a dry spot. *Phys. Fluids*, 13 (6):1601–1614, 2001. doi: 10.1063/1.1369607.

H. A. Lorentz. A general theorem concerning the motion of a viscous fluid and a few consequences derived from it. *Zittingsverlag Akad. Wet. Amsterdam*, 5:168–175, 1896.

J. Lu and C. M. Corvalan. Dynamical transitions during the collapse of inertial holes. *Sci. Rep.*, 9 (1):14649, 2019. doi: 10.1038/s41598-019-50956-w.

C. Lv, M. Eigenbrod, and S. Hardt. Stability and collapse of holes in liquid layers. *J. Fluid Mech.*, 855:1130–1155, 2018. doi: 10.1017/jfm.2018.680.

T. M. MacRobert. *Spherical Harmonics: An Elementary Treatise on Harmonic Functions with Applications*. Dover, 1947.

W. Magnus, F. Oberhettinger, and R. P. Soni. *Formulas and Theorems for the Special Functions of Mathematical Physics*. Springer, 3 edition, 1966.

Malvern Instruments Ltd. Zetasizer Nano User Manual. Technical Report 11, Worcestershire, 2013.

S. Mandal, A. Bandopadhyay, and S. Chakraborty. Effect of interfacial slip on the cross-stream migration of a drop in an unbounded Poiseuille flow. *Phys. Rev. E*, 92(2):023002, 2015. doi: 10.1103/PhysRevE.92.023002.

A. Manz, D. J. Harrison, E. M. J. Verpoorte, J. C. Fettinger, A. Paulus, H. Lüdi, and H. M. Widmer. Planar chips technology for miniaturization and integration of separation techniques into monitoring systems. *J. Chromatogr. A*, 593(1-2):253–258, 1992. doi: 10.1016/0021-9673(92)80293-4.

D. Mark, S. Haeberle, G. Roth, F. von Stetten, and R. Zengerle. Microfluidic lab-on-a-chip platforms: requirements, characteristics and applications. *Chem. Soc. Rev.*, 39(3):1153–1182, 2010. doi: 10.1039/b820557b.

A. Martínez-Calvo and A. Sevilla. Temporal stability of free liquid threads with surface viscoelasticity. *J. Fluid Mech.*, 846:877–901, 2018. doi: 10.1017/jfm.2018.293.

H. Maru and D. T. Wasan. Dilatational viscoelastic properties of fluid interfaces-II: Experimental study. *Chem. Eng. Sci.*, 34(11):1295 – 1307, 1979. doi: 10.1016/0009-2509(79)80021-4.

J. H. Masliyah and S. Bhattacharjee. *Electrokinetic and colloid transport phenomena*. John Wiley & Sons, 2006.

H. Masoud and H. A. Stone. The reciprocal theorem in fluid dynamics and transport phenomena. *J. Fluid Mech.*, 879:P1, 2019. doi: 10.1017/jfm.2019.553.

E. C. Mbamala and H. H. von Grünberg. Effective interaction of a charged colloidal particle with an air-water interface. *J. Phys. Condens. Matter*, 14(19):4881, 2002. doi: 10.1088/0953-8984/14/19/313.

G. McHale and M. I. Newton. Liquid marbles: principles and applications. *Soft Matter*, 7(12):5473–5481, 2011. doi: 10.1039/c1sm05066d.

M. Megens and J. Aizenberg. Like-charged particles at liquid interfaces. *Nature*, 424:246102, 2003. doi: 10.1038/4241014b.

Y. Mei, G. Li, P. Moldenaers, and R. Cardinaels. Dynamics of particle-covered droplets in shear flow: unusual breakup and deformation hysteresis. *Soft Matter*, 12(47):9407–9412, 2016. doi: 10.1039/C6SM02031C.

J. Mewis and N. J. Wagner. *Colloidal Suspension Rheology*. Cambridge University Press, 2012.

M. Montemor. Functional and smart coatings for corrosion protection: A review of recent advances. *Surf. Coatings Technol.*, 258:17–37, 2014. doi: 10.1016/j.surfcoat.2014.06.031.

J. Moriarty and L. Schwartz. Dynamic Considerations in the Closing and Opening of Holes in Thin Liquid Films. *J. Colloid Interface Sci.*, 161(2):335–342, 1993. doi: 10.1006/jcis.1993.1475.

F. A. Morrison. Electrophoresis of a particle of arbitrary shape. *J. Colloid Interface Sci.*, 34(2): 210–214, 1970. doi: 10.1016/0021-9797(70)90171-2.

S. Mueller, E. W. Llewellin, and H. M. Mader. The rheology of suspensions of solid particles. *Proc. R. Soc. A Math. Phys. Eng. Sci.*, 466(2116):1201–1228, 2010. doi: 10.1098/rspa.2009.0445.

A. D. Myshkis, V. G. Babskii, N. D. Kopachevski, L. A. Slobozhanin, and A. D. Tyuptsov. *Low-Gravity Fluid Mechanics*. Springer-Verlag Berlin Heidelberg, 1987.

I. Nejati, M. Dietzel, and S. Hardt. Exploiting cellular convection in a thick liquid layer to pattern a thin polymer film. *Appl. Phys. Lett.*, 108(5):051604, 2016. doi: 10.1063/1.4940366.

P. Neužil, S. Giselbrecht, K. Länge, T. J. Huang, and A. Manz. Revisiting lab-on-a-chip technology for drug discovery. *Nat. Rev. Drug Discov.*, 11(8):620–632, 2012. doi: 10.1038/nrd3799.

M. I. Newton, D. L. Herbertson, S. J. Elliott, N. J. Shirtcliffe, and G. McHale. Electrowetting of liquid marbles. *J. Phys. D. Appl. Phys.*, 40(1):20–24, 2007. doi: 10.1088/0022-3727/40/1/S04.

T. Ngai and S. A. F. Bon. *Particle-stabilized emulsions and colloids*. Royal Society of Chemistry, 2014. ISBN 978-1-84973-881-1.

M. G. Nikolaides, A. R. Bausch, M. F. Hsu, A. D. Dinsmore, M. P. Brenner, and D. A. Weitz. Electric-field-induced capillary attraction between like-charged particles at liquid interfaces. *Nature*, 420(6913):299–301, 2002. doi: 10.1038/nature01113.

J. Norbury, G. C. Sander, and C. F. Scott. Corner solutions of the Laplace-Young equation. *Q. J. Mech. Appl. Math.*, 60(1):1–16, 2004. doi: 10.1093/qjmamj/hbh020.

B. K. Nunnally and K. Yao. The use of capillary electrophoresis in vaccines. *Anal. Lett.*, 40(4): 615–627, 2007. doi: 10.1080/00032710701241966.

R. W. O'Brien and L. R. White. Electrophoretic mobility of a spherical colloidal particle. *J. Chem. Soc. Faraday Trans. 2*, 74:1607–1626, 1978. doi: 10.1039/f29787401607.

M. Oettel, A. Domínguez, and S. Dietrich. Comment on Electrodipping Force Acting on Solid Particles at a Fluid Interface. *Langmuir*, 22(2):846–847, 2006. doi: 10.1021/la0514260.

H. N. Oguz and A. Prosperetti. Dynamics of bubble growth and detachment from a needle. *J. Fluid Mech.*, 257:111–145, 1993. doi: 10.1017/S0022112093003015.

C. J. Ojiako, R. Cimpeanu, H. Bandulasena, R. Smith, and D. Tseluiko. Deformation and dewetting of liquid films under gas jets. 2020. Pre-print available under: `http://arxiv.org/abs/2001.06632`.

L. Onsager. Reciprocal Relations in Irreversible Processes. I. *Phys. Rev.*, 37(4):405–426, 1931a. doi: 10.1103/PhysRev.37.405.

L. Onsager. Reciprocal Relations in Irreversible Processes. II. *Phys. Rev.*, 38(12):2265–2279, 1931b. doi: 10.1103/PhysRev.38.2265.

J. T. G. Overbeek. Theorie der Elektrophorese - Der Relaxationseffekt. *Kolloid-Beihefte*, 54(7-9): 287–364, 1943. doi: 10.1007/BF02556774.

J. F. Padday. The Profiles of Axially Symmetric Menisci. *Philos. Trans. R. Soc. London . Ser. A*, 269 (1197):265–293, 1971. doi: 10.1098/rsta.1971.0031.

A. A. Pahlavan, L. Cueto-Felgueroso, A. E. Hosoi, G. H. McKinley, and R. Juanes. Thin films in partial wetting: stability, dewetting and coarsening. *J. Fluid Mech.*, 845:642–681, 2018. doi: 10.1017/jfm.2018.255.

M. Paluch. Surface potential at the water-air interface. *Ann. Univ. Mariae Curie-Sklodowska, Sect. AA–Chemia*, 70(2), 2016. doi: 10.17951/aa.2015.70.2.1

F. Paratore, V. Bacheva, G. V. Kaigala, and M. Bercovici. Dynamic microscale flow patterning using electrical modulation of zeta potential. *Proc. Natl. Acad. Sci.*, 116(21):10258–10263, 2019a. doi: 10.1073/pnas.1821269116.

F. Paratore, E. Boyko, G. V. Kaigala, and M. Bercovici. Electroosmotic Flow Dipole: Experimental Observation and Flow Field Patterning. *Phys. Rev. Lett.*, 122(22):224502, 2019b. doi: 10.1103/PhysRevLett.122.224502.

V. I. Parfenyuk. Surface Potential at the Gas - Aqueous Solution Interface. *Colloid J.*, 64(5): 588–595, 2002. doi: 10.1023/A:1020614010528.

B. J. Park, T. Brugarolas, and D. Lee. Janus particles at an oil-water interface. *Soft Matter*, 7(14): 6413, 2011. doi: 10.1039/c1sm05460k.

J. Park, J. R. Youn, and Y. S. Song. Hydrodynamic Metamaterial Cloak for Drag-Free Flow. *Phys. Rev. Lett.*, 123(7):074502, 2019. doi: 10.1103/PhysRevLett.123.074502.

J. Y. Park and R. C. Advincula. Nanostructuring polymers, colloids, and nanomaterials at the air-water interface through Langmuir and Langmuir-Blodgett techniques. *Soft Matter*, 7(21): 9829–9843, 2011. doi: 10.1039/c1sm05750b.

J. D. Paulsen, R. Carmigniani, A. Kannan, J. C. Burton, and S. R. Nagel. Coalescence of bubbles and drops in an outer fluid. *Nat. Commun.*, 5(1):3182, 2014. doi: 10.1038/ncomms4182.

J. R. Peaudecerf, J. R. Landel, R. E. Goldstein, and P. Luzzatto-Fegiz. Traces of surfactants can severely limit the drag reduction of superhydrophobic surfaces. *Proceeding Natl. Acad. Sci.*, 114(28):7254–7259, 2017. doi: 10.1073/pnas.1702469114.

A. Persat, R. D. Chambers, and J. G. Santiago. Basic principles of electrolyte chemistry for microfluidic electrokinetics. Part I: Acid-base equilibria and pH buffers. *Lab Chip*, 9(17): 2437–2453, 2009a. doi: 10.1039/b906465f.

A. Persat, M. E. Suss, and J. G. Santiago. Basic principles of electrolyte chemistry for microfluidic electrokinetics. Part II: Coupling between ion mobility, electrolysis, and acid-base equilibria. *Lab Chip*, 9(17):2454, 2009b. doi: 10.1039/b906468k.

D. Peschka, S. Bommer, S. Jachalski, R. Seemann, and B. Wagner. Impact of energy dissipation on interface shapes and on rates for dewetting from liquid substrates. *Sci. Rep.*, 8(1):13295, 2018. doi: 10.1038/s41598-018-31418-1.

D. Peschka, S. Haefner, L. Marquant, K. Jacobs, A. Münch, and B. Wagner. Signatures of slip in dewetting polymer films. *Proc. Natl. Acad. Sci.*, 116(19):9275–9284, 2019. doi: 10.1073/pnas.1820487116.

J. T. Petkov, N. D. Denkov, K. D. Danov, O. D. Velev, R. Aust, and F. Durst. Measurement of the Drag Coefficient of Spherical Particles Attached to Fluid Interfaces. *J. Colloid Interface Sci.*, 172 (1):147–154, 1995. doi: 10.1006/jcis.1995.1237.

Y. A. Pishchalnikov, O. A. Sapozhnikov, M. R. Bailey, J. C. Williams, R. O. Cleveland, T. Colonius, L. A. Crum, A. P. Evan, and J. A. McAteer. Cavitation bubble cluster activity in the breakage of kidney stones by lithotripter shockwaves. *J. Endourol.*, 17(7):435–446, 2003. doi: 10.1089/089277903769013568.

M. N. Popescu, G. Oshanin, S. Dietrich, and A.-M. Cazabat. Precursor films in wetting phenomena. *J. Phys. Condens. Matter*, 24(24):243102, 2012. doi: 10.1088/0953-8984/24/24/243102.

T. Qian, X.-P. Wang, and P. Sheng. A variational approach to moving contact line hydrodynamics. *J. Fluid Mech.*, 564:333, 2006. doi: 10.1017/S0022112006001935.

J. Ralston and S. S. Dukhin. The interaction between particles and bubbles. *Colloids Surfaces A Physicochem. Eng. Asp.*, 151(1-2):3–14, 1999. doi: 10.1016/S0927-7757(98)00642-6.

A. Ramachandran and A. S. Khair. The dynamics and rheology of a dilute suspension of hydrodynamically Janus spheres in a linear flow. *J. Fluid Mech.*, 633:233–269, 2009. doi: 10.1017/S0022112009007472.

M. Ramiasa, J. Ralston, R. Fetzer, and R. Sedev. Contact Line Friction in Liquid-Liquid Displacement on Hydrophobic Surfaces. *J. Phys. Chem. C*, 115(50):24975–24986, 2011. doi: 10.1021/jp209140a.

A. Ramos. *Electrokinetics and electrohydrodynamics in microsystems*. Springer Science & Business Media, 2011.

C. Redon, F. Brochard-Wyart, and F. Rondelez. Dynamics of dewetting. *Phys. Rev. Lett.*, 66(6): 715–718, 1991. doi: 10.1103/PhysRevLett.66.715.

L. D. Reed and F. A. Morrison. Hydrodynamic interactions in electrophoresis. *J. Colloid Interface Sci.*, 54(1):117–133, 1976. doi: 10.1016/0021-9797(76)90291-5.

N. Ressler. Two-dimensional electrophoresis of protein antigens with an antibody containing buffer. *Clin. Chim. Acta*, 5(6):795–800, 1960. doi: 10.1016/0009-8981(60)90111-X.

F. Riegels. Zur Kritik des Hele-Shaw-Versuchs. *ZAMM-Journal Appl. Math. Mech. für Angew. Math. und Mech.*, 18(2):95–106, 1938. doi: 10.1002/zamm.19380180202.

W. D. Ristenpart, P. M. McCalla, R. V. Roy, and H. A. Stone. Coalescence of Spreading Droplets on a Wettable Substrate. *Phys. Rev. Lett.*, 97(6):064501, 2006. doi: 10.1103/PhysRevLett.97.064501.

R. Rusconi, S. Lecuyer, N. Autrusson, L. Guglielmini, and H. A. Stone. Secondary Flow as a Mechanism for the Formation of Biofilm Streamers. *Biophys. J.*, 100(6):1392–1399, 2011. doi: 10.1016/j.bpj.2011.01.065.

P. Saulnier, J. Lachaise, G. Morel, and A. Graciaa. Zeta potential of air bubbles in surfactant solutions. *J. Colloid Interface Sci.*, 182(2):395–399, 1996. doi: 10.1006/jcis.1996.0479.

N. Savva and S. Kalliadasis. Dynamics of moving contact lines: A comparison between slip and precursor film models. *EPL*, 94(6):64004, 2011. doi: 10.1209/0295-5075/94/64004.

M. Schäfer. *Numerik im Maschinenbau*. Springer-Verlag, 2013.

R. B. M. Schasfoort, S. Schlautmann, J. Hendrikse, and A. Van Den Berg. Field-effect row control for microfabricated fluidic networks. *Science*, 286(5441):942–945, 1999. doi: 10.1126/science.286.5441.942.

O. Schnitzer and E. Yariv. Strong-field electrophoresis. *J. Fluid Mech.*, 701:333–351, 2012a. doi: 10.1017/jfm.2012.161.

O. Schnitzer and E. Yariv. Macroscale description of electrokinetic flows at large zeta potentials: Nonlinear surface conduction. *Phys. Rev. E*, 86(2):021503, 2012b. doi: 10.1103/PhysRevE.86.021503.

O. Schnitzer and E. Yariv. Nonlinear electrophoresis at arbitrary field strengths: small-Dukhin-number analysis. *Phys. Fluids*, 26(12):122002, 2014. doi: 10.1063/1.4902331.

O. Schnitzer, I. Frankel, and E. Yariv. Electrophoresis of bubbles. *J. Fluid Mech.*, 753:49–79, 2014. doi: 10.1017/jfm.2014.350.

C. Schönecker and S. Hardt. Electro-osmotic flow along superhydrophobic surfaces with embedded electrodes. *Phys. Rev. E*, 89(6):063005, 2014. doi: 10.1103/PhysRevE.89.063005.

C. Schönecker, T. Baier, and S. Hardt. Influence of the enclosed fluid on the flow over a microstructured surface in the Cassie state. *J. Fluid Mech.*, 740(1):168–195, 2014. doi: 10.1017/jfm.2013.647.

B. Schroyen, C.-P. Hsu, L. Isa, P. Van Puyvelde, and J. Vermant. Stress Contributions in Colloidal Suspensions: The Smooth, the Rough, and the Hairy. *Phys. Rev. Lett.*, 122(21):218001, 2019. doi: 10.1103/PhysRevLett.122.218001.

D. Schwartz and C. R. Cantor. Separation of yeast chromosome-sized DNAs by pulsed field gradient gel electrophoresis. *Cell*, 37(1):67–75, 1984. doi: 10.1016/0092-8674(84)90301-5.

H.-R. Schwarz. *Methode der finiten Elemente*. Springer Verlag, 47 edition, 2013.

L. Scriven. Dynamics of a fluid interface Equation of motion for Newtonian surface fluids. *Chem. Eng. Sci.*, 12(2):98–108, 1960. doi: 10.1016/0009-2509(60)87003-0.

R. Seemann, S. Herminghaus, C. Neto, S. Schlagowski, D. Podzimek, R. Konrad, H. Mantz, and K. Jacobs. Dynamics and structure formation in thin polymer melt films. *J. Phys. Condens. Matter*, 17(9):S267–S290, 2005. doi: 10.1088/0953-8984/17/9/001.

S. Senchenko and H. J. Keh. Thermophoresis of a slightly deformed aerosol sphere. *Phys. Fluids*, 19(3):1–12, 2007. doi: 10.1063/1.2712902.

O. Séro-Guillaume and M. Er-Riani. Domain perturbation method and shape of a bubble in a uniform flow of an inviscid liquid. *Eur. J. Mech. B/Fluids*, 18(6):991–1003, 1999. doi: 10.1016/S0997-7546(99)00125-9.

R. K. Shah, H. C. Shum, A. C. Rowat, D. Lee, J. J. Agresti, A. S. Utada, L.-Y. Chu, J.-W. Kim, A. Fernandez-Nieves, C. J. Martinez, and D. Weitz. Designer emulsions using microfluidics. *Mater. Today*, 11(4):18–27, 2008. doi: 10.1016/S1369-7021(08)70053-1.

A. Sharma and E. Ruckenstein. Energetic criteria for the breakup of liquid films on nonwetting solid surfaces. *J. Colloid Interface Sci.*, 137(2):433–445, 1990. doi: 10.1016/0021-9797(90)90418-N.

J. S. Sharp. Resonant properties of sessile droplets; contact angle dependence of the resonant frequency and width in glycerol/water mixtures. *Soft Matter*, 8(2):399–407, 2012. doi: 10.1103/PhysRevFluids.3.074201.

V. Shilov, S. Barany, C. Grosse, and O. Shramko. Field-induced disturbance of the double layer electro-neutrality and non-linear electrophoresis. *Adv. Colloid Interface Sci.*, 104(1-3):159–173, 2003. doi: 10.1016/S0001-8686(03)00040-X.

R. N. Shimizu and N. R. Demarquette. Evaluation of surface energy of solid polymers using different models. *J. Appl. Polym. Sci.*, 76(12):1831–1845, 2000. doi: 10.1002/(SICI)1097-4628(20000620)76:12<1831::AID-APP14>3.0.CO;2-Q.

A. A. Shugai, S. L. Carnie, D. Y. C. Chan, and J. L. Anderson. Electrophoretic Motion of Two Spherical Particles with Thick Double Layers. *J. Colloid Interface Sci.*, 191(2):357–371, 1997. doi: 10.1006/jcis.1997.4921.

A. Sierou and J. F. Brady. Accelerated Stokesian Dynamics simulations. *J. Fluid Mech.*, 448:115–146, 2001. doi: 10.1017/S0022112001005912.

M. Singh, H. M. Haverinen, P. Dhagat, and G. E. Jabbour. Inkjet Printing-Process and Its Applications. *Adv. Mater.*, 22(6):673–685, 2010. doi: 10.1002/adma.200901141.

J. C. Slattery, L. Sagis, and E. S. Oh. *Interfacial transport phenomena*. Springer Science & Business Media, 2007.

J.-L. Song, W.-J. Xu, X. Liu, Y. Lu, and J. Sun. Electrochemical machining of super-hydrophobic Al surfaces and effect of processing parameters on wettability. *Appl. Phys. A*, 108(3):559–568,

2012. doi: 10.1007/s00339-012-6927-1.

T. M. Squires and M. Z. Bazant. Induced-charge electro-osmosis. *J. Fluid Mech.*, 509(509): 217–252, 2004. doi: 10.1017/S0022112004009309.

J. Stachurski and M. Michalek. The zeta potential of emulsion droplets of the aliphatic hydrocarbons in aqueous solutions. *Colloids and Surfaces*, 15:255–259, 1985. doi: 10.1016/0166-6622(85)80076-7.

O. Stern. Zur Theorie der elektrolytischen Doppelschicht. *Zeitschrift für Elektrochemie*, 30: 508–516, 1924. doi: 10.1002/bbpc.192400182.

J. J. Stickel and R. L. Powell. Fluid Mechanics and Rheology of Dense Suspensions. *Annu. Rev. Fluid Mech.*, 37(1):129–149, 2005. doi: 10.1146/annurev.fluid.36.050802.122132.

F. H. Stillinger and A. Ben-Naim. Liquid-Vapor Interface Potential for Water. *J. Chem. Phys.*, 47 (11):4431–4437, 1967. doi: 10.1063/1.1701649.

A. Stocco, B. Chollet, X. Wang, C. Blanc, and M. Nobili. Rotational diffusion of partially wetted colloids at fluid interfaces. *J. Colloid Interface Sci.*, 542:363–369, 2019. doi: 10.1016/j.jcis.2019.02.017.

S. A. Suarez, R. F. Gibson, C. T. Sun, and S. K. Chaturvedi. The influence of fiber length and fiber orientation on damping and stiffness of polymer composite materials. *Exp. Mech.*, 26(2): 175–184, 1986. doi: 10.1007/BF02320012.

P. Tabeling. *Introduction to Microfluidics*. OUP Oxford, 2005.

M. Takahashi. ζ Potential of Microbubbles in Aqueous Solutions: Electrical Properties of the Gas-Water Interface. *J. Phys. Chem. B*, 109(46):21858–21864, 2005. doi: 10.1021/jp0445270.

Y. Takamura, H. Onoda, H. Inokuchi, S. Adachi, A. Oki, and Y. Horiike. Low-voltage electroosmosis pump for stand-alone microfluidics devices. *Electrophoresis*, 24(12):185–192, 2003. doi: 10.1002/elps.200390012.

G. I. Taylor and D. H. Michael. On making holes in a sheet of fluid. *J. Fluid Mech.*, 58(4):625–639, 1973. doi: 10.1017/S0022112073002375.

M. Teubner. The motion of charged colloidal particles in electric fields. *J. Chem. Phys.*, 76(11): 5564–5573, 1982. doi: 10.1063/1.442861.

B. D. Texier, K. Piroird, D. Quéré, and C. Clanet. Inertial collapse of liquid rings. *J. Fluid Mech.*, 717, 2013. doi: 10.1017/jfm.2013.15.

A. B. Theberge, F. Courtois, Y. Schaerli, M. Fischlechner, C. Abell, F. Hollfelder, and W. T. S. Huck. Microdroplets in Microfluidics: An Evolving Platform for Discoveries in Chemistry and Biology. *Angew. Chemie Int. Ed.*, 49(34):5846–5868, 2010. doi: 10.1002/anie.200906653.

B. W. Thompson. Secondary flow in a Hele-Shaw cell. *J. Fluid Mech.*, 31(2):379–395, 1968. doi: 10.1017/S0022112068000212.

S. T. Thoroddsen, T. G. Etoh, K. Takehara, and N. Ootsuka. On the coalescence speed of bubbles. *Phys. Fluids*, 17(7):071703, 2005. doi: 10.1063/1.1965692.

S. T. Thoroddsen, T. G. Etoh, and K. Takehara. Experiments on bubble pinch-off. *Phys. Fluids*, 19 (4):042101, 2007. doi: 10.1063/1.2710269.

A. Tiselius. A new apparatus for electrophoretic analysis of colloidal mixtures. *Trans. Faraday Soc.*, 33:524, 1937. doi: 10.1039/tf9373300524.

J. Toro-Mendoza, G. Rodriguez-Lopez, and O. Paredes-Altuve. Brownian diffusion of a particle at an air/liquid interface: the elastic (not viscous) response of the surface. *Phys. Chem. Chem. Phys.*, 19(13):9092–9095, 2017. doi: 10.1039/C6CP07442A.

C. Tropea. Optical Particle Characterization in Flows. *Annu. Rev. Fluid Mech.*, 43(1):399–426, 2011. doi: 10.1146/annurev-fluid-122109-160721.

R. Truesdell, A. Mammoli, P. Vorobieff, F. van Swol, and C. J. Brinker. Drag Reduction on a Patterned Superhydrophobic Surface. *Phys. Rev. Lett.*, 97(4):044504, 2006. doi: 10.1103/PhysRevLett.97.044504.

P. Tsai, J. Lou, Y.-Y. He, and E. Lee. Electrophoresis of a spherical particle normal to an air-water interface. *Electrophoresis*, 31(20):3363–3371, 2010. doi: 10.1002/elps.201000012.

H. B. van Lengerich and P. H. Steen. Energy dissipation and the contact-line region of a spreading bridge. *J. Fluid Mech.*, 703:111–141, 2012. doi: 10.1017/jfm.2012.199.

M. J. Vega, C. Gouttière, D. Seveno, T. D. Blake, M. Voué, J. De Coninck, and A. Clarke. Experimental Investigation of the Link between Static and Dynamic Wetting by Forced Wetting of Nylon Filament. *Langmuir*, 23(21):10628–10634, 2007. doi: 10.1021/la701390m.

M. Versluis, B. Schmitz, A. van der Heydt, and D. Lohse. How Snapping Shrimp Snap: Through Cavitating Bubbles. *Science*, 289(5487):2114–2117, 2000. doi: 10.1126/science.289.5487.2114.

O. Vesterberg. History of electrophoretic methods. *J. Chromatogr. A*, 480(C):3–19, 1989. doi: 10.1016/S0021-9673(01)84276-X.

O. Vesterberg. A short history of electrophoretic methods. *Electrophoresis*, 14(1):1243–1249, 1993. doi: 10.1002/elps.11501401188.

A. Viallat and M. Abkarian. *Dynamics of Blood Cell Suspensions in Microflows*. CRC Press, 2020.

V. Vitagliano, and P. A. Lyons. Diffusion coefficients for aqueous solutions of sodium chloride and barium chloride. *J. Am. Chem. Soc.*, 78(8):1549–1552, 1956. doi: 10.1021/ja01589a011.

O. V. Voinov. Hydrodynamics of wetting. *Fluid Dyn.*, 11(5):714–721, 1976. doi: 10.1007/BF01012963.

H. von Helmholtz. *Wissenschaftliche Abhandlungen von Hermann von Helmholtz*. Johann Ambrosius Barth, 1882.

M. von Smoluchowski. Contribution to the theory of electro-osmosis and related phenomena. *Bull. Int. Acad. Sci. Cracovie*, 3:184–199, 1903.

S. Wall. The history of electrokinetic phenomena. *Curr. Opin. Colloid Interface Sci.*, 15(3): 119–124, 2010. doi: 10.1016/j.cocis.2009.12.005.

C. Wang, M. Li, Y. Song, X. Pan, and D. Li. Electrokinetic motion of a spherical micro particle at an oil-water interface in microchannel. *Electrophoresis*, 39(5-6):807–815, 2018. doi: 10.1002/elps.201700289.

Y. Wang and M. Oberlack. A thermodynamic model of multiphase flows with moving interfaces and contact line. *Contin. Mech. Thermodyn.*, 23(5):409–433, 2011. doi: 10.1007/s00161-011-0186-9.

Y. Weng, F. F. Delgado, S. Son, T. P. Burg, S. C. Wasserman, and S. Manalis. Mass sensors with mechanical traps for weighing single cells in different fluids. *Lab Chip*, 11(24):4174, 2011. doi: 10.1039/c1lc20736a.

F. M. White and I. Corfield. *Viscous fluid flow*. New York: McGraw-Hill, vol. 3 edition, 2006.

P. H. Wiersema, A. L. Loeb, and J. T. G. Overbeek. Calculation of the electrophoretic mobility of a spherical colloid particle. *J. Colloid Interface Sci.*, 22(1):78–99, 1966. doi: 10.1016/0021-9797(66)90069-5.

S. K. Wilson and B. R. Duffy. An asymptotic analysis of small holes in thin fluid layers. *J. Eng. Math.*, 30(4):445–457, 1996. doi: 10.1007/BF00049245.

J. Wu and G.-H. Ma. Recent Studies of Pickering Emulsions: Particles Make the Difference. *Small*, 12(34):4633–4648, 2016. doi: 10.1002/smll.201600877.

C. Yang, T. Dabros, D. Li, J. Czarnecki, and J. H. Masliyah. Measurement of the Zeta Potential of Gas Bubbles in Aqueous Solutions by Microelectrophoresis Method. *J. Colloid Interface Sci.*, 243(1):128–135, 2001. doi: 10.1006/jcis.2001.7842.

S. Yang, F. Guo, B. Kiraly, X. Mao, M. Lu, K. Leong, and T. J. Huang. Microfluidic synthesis of multifunctional Janus particles for biomedical applications. *Lab Chip*, 12(12):2097, 2012. doi: 10.1039/c2lc90046g.

E. Yariv. An asymptotic derivation of the thin-Debye-layer limit for electrokinetic phenomena. *Chem. Eng. Commun.*, 197(1):3–17, 2009. doi: 10.1080/00986440903076590.

S.-N. Yin, C.-F. Wang, Z.-Y. Yu, J. Wang, S.-S. Liu, and S. Chen. Versatile Bifunctional Magnetic-Fluorescent Responsive Janus Supraballs Towards the Flexible Bead Display. *Adv. Mater.*, 23 (26):2915–2919, 2011. doi: 10.1002/adma.201100203.

J. Zhang, Y. Song, and D. Li. Electrokinetic motion of a spherical polystyrene particle at a liquid-fluid interface. *J. Colloid Interface Sci.*, 509:432–439, 2018. doi: 10.1016/j.jcis.2017.09.020.

L. Zhang, Y. Zhong, D. Cha, and P. Wang. A self-cleaning underwater superoleophobic mesh for oil-water separation. *Sci. Rep.*, 3(1):2326, 2013. doi: 10.1038/srep02326.

X. Zhang, H. Lhuissier, C. Sun, and D. Lohse. Surface Nanobubbles Nucleate Microdroplets. *Phys. Rev. Lett.*, 112(14):144503, 2014. doi: 10.1103/PhysRevLett.112.144503.

Z. Zheng, M. A. Fontelos, S. Shin, M. C. Dallaston, D. Tseluiko, S. Kalliadasis, and H. A. Stone. Healing capillary films. *J. Fluid Mech.*, 838:404–434, 2018a. doi: 10.1017/jfm.2017.777.

Z. Zheng, M. A. Fontelos, S. Shin, and H. Stone. Universality in the nonlinear leveling of capillary films. *Phys. Rev. Fluids*, 3(3):032001, 2018b. doi: 10.1103/PhysRevFluids.3.032001.

J. Zhou and M. Doi. Dynamics of viscoelastic filaments based on Onsager principle. *Phys. Rev. Fluids*, 3(8):084004, 2018. doi: 10.1103/PhysRevFluids.3.084004.

List of Symbols

Latin Symbols

Symbol	Dimension	Meaning
a	m	Characteristic length of a particle
a_i	-	Fourier coefficients related to $\cos(i\varphi)$
$\mathfrak{a}$	m	Radius of an ion
A or $\mathscr{A}$	m^2	Area, interface or surface
$\mathscr{A}_h^{(n)}$	m^2	Area of hole n
$\mathscr{A}_\mathscr{P}$	m^2	Surface of a particle
$\mathscr{A}_\infty$	m^2	Enclosing surface corresponding to $r \to \infty$
b_i	-	Fourier coefficients related to $\sin(i\varphi)$
$\mathscr{B}$	-	Body suspended in a fluid
c	m/s	Speed of sound
c_i	$m/s^{0.55}$ or -	Fitting parameters referring to scaling laws
$C_i^{(j)}$	-	Coefficients related to the effective surface viscosities or Fourier coefficients
$\mathscr{C}$	m	Contour
$\mathscr{C}_h^{(n)}$	m	Contour of hole n
d	m	Diameter of a circular hole
d_c	m	Critical hole diameter
d_i	-	Fourier coefficients related to $\cos(i\varphi)$
$\mathrm{d}\mathscr{V}$	m^3	Infinitesimal volume element
$\mathrm{d}(\partial\mathscr{V})$	m^2	Infinitesimal surface element of $\mathrm{d}\mathscr{V}$
D	m/s^2	Diffusion coefficient
$\boldsymbol{e}_i$	-	Unit vector in i-direction
E or E_∞	kg m/(A s^3)	Magnitude of the electric field strength
$\boldsymbol{E}$	kg m/(A s^3)	Electric field strength
$\mathscr{E}_k$	kg m^2/s^2	Kinetic energy
$\mathscr{E}_g$	kg m^2/s^2	Gravitational energy
$\mathscr{E}_p$	kg m^2/s^2	Potential energy
$\mathscr{E}_{sf}$	kg m^2/s^2	Surface energy
$\dot{\mathscr{E}}_d$	kg m^2/s^3	Energy dissipation
$\mathfrak{E}$	1/s	Rate of strain tensor
f	-	Arbitrary function
$\boldsymbol{f}$	kg/(m^2 s^2)	Volume force density
$\boldsymbol{f}_g$	kg/(m^2 s^2)	Volume force density corresponding to gravity
$\boldsymbol{f}_M$	kg/(m^2 s^2)	Volume force density corresponding to Maxwell forces
$\mathscr{F}$	kg m/s^2	Hydrodynamic force
$\mathscr{F}_{SF}$	kg m/s^2	Surface tension force
$\mathscr{F}_c$	kg m/s^2	Coulomb force

Symbol	Dimension	Meaning
$\mathscr{F}_{\mathscr{S}}$	kg m/s^2	Force acting on a flat fluid interface
$\mathscr{F}_{\mathfrak{p}}$	kg/s^2	Force per height acting on an obstacle in absence of EOF
g	-	Arbitrary function or gravitational constant
$\boldsymbol{g}$	m/s^2	Vector containing the gravity constant
h or H	m	Height
h_{c}	m	Critical height of the meniscus or height of the center of mass
h_∞	m	Height of a liquid puddle
h_i	-	Fourier coefficients related to $\sin(i\varphi)$
h_{T}	m	Critical height of a bounded, uniform liquid layer
h_{E}	m	Height of a uniform liquid film in a square box
$h_{\max}$	m	Maximum height of a liquid layer
$\mathfrak{h}$	m	Correction of the height proportional to Ce
H_n	-	Solid spherical harmonic of order n
$\mathscr{H}$	1/m	Mean curvature
$\boldsymbol{I}$	-	Identity tensor
$\boldsymbol{j}_i$	1/(m^2 s)	Ionic flux of species i
$\boldsymbol{j}_i^d$	1/(m^2 s)	Diffusion flux of species i
$\boldsymbol{j}_i^m$	1/(m^2 s)	Electrostatic migration flux of species i
k	-	Arbitrary function or wave number
K	-	Summation limit
K_i^j	-	Fourier coefficients
L	m	Characteristic length or length of a box
l_{c}	m	Capillary length
$\boldsymbol{m}$	-	Tangential vector along an intersection curve
n_i	1/m^3	Number density of species i
n_i^∞	1/m^3	Number density of species i in equilibrium
$\boldsymbol{n}$	-	Normal vector
N	-	Number of particles
$\mathscr{O}$	-	Origin of a coordinate system
p	kg/(m s^2)	Thermodynamic pressure
P	kg/(m s^2)	Characteristic pressure
p^s	kg/(m s^2)	Equilibrium pressure
p^d	kg/(m s^2)	Perturbation pressure
p_n	-	Solid spherical harmonics of order n
$p^\star$	kg/(m s^2)	Pressure including gravity
$\mathfrak{p}$	kg/(m s^2)	Pressure in Hele-Shaw cell in absence of EOF
q	A s/m^3	Charge density
$q_{\mathscr{S}}$	A s/m^2	Surface charge density
Q_i	A s	Point charge
$\mathfrak{Q}$	m^3/s	Volumetric flow rate
r	m	Length of position vector
r_a	m	Characteristic length of the ζ-potential annulus
r_i	m	Set of parameters, describing energetic displacement from equilibrium

Symbol	Dimension	Meaning
$\boldsymbol{r}$	m	Position vector
$\boldsymbol{r}_{\mathscr{P}}$	m	Parametrization of the surface of a particle
$\boldsymbol{r}_{\mathscr{O}}$	m	Parametrization of the surface of an obstacle
$\boldsymbol{r}_{\mathscr{A}}$	m	Parametrization of the ζ-potential annulus
$\boldsymbol{R}$	-	Rotation tensor
R	m	Radius of a hole
$R_{\max}$	m	Maximum radius of a hole in experiments
s	m	Arc length
s_{tot}	m	Total arc length
$\boldsymbol{s}$	-	Vector orthogonal to $\boldsymbol{n}$ and $\boldsymbol{m}$
$\mathscr{S}$	kg m^2/s^2	Stresslet
t	s	Time
t_0	s	Time when the hole is closed, i.e., $d = 0$
$\boldsymbol{t}_i$	-	Tangential vector in i-direction
T	K or s	Temperature or characteristic time scale
$\mathscr{T}$	kg m^2/s^2	Hydrodynamic torque
$\mathscr{T}_{\mathscr{S}}$	kg m^2/s^2	Torque acting on a flat fluid interface
$\boldsymbol{u}$	m/s	Velocity vector
$\boldsymbol{u}_{\parallel}$	m/s	Velocity vector tangential to a rigid wall
$\boldsymbol{u}_i$	m/s	Velocity of species i or fluid i
$\boldsymbol{u}^{\mathscr{S}}$	m/s	Interfacial velocity vector
U	m/s	Characteristic velocity
$U_{\parallel}$	m/s	Characteristic velocity in tangential direction to a rigid wall
$\boldsymbol{U}^{\infty}$	m/s	Constant velocity vector
$\boldsymbol{U}(\boldsymbol{r})$	m/s	Arbitrary velocity vector
$\boldsymbol{U}^{\text{eff}}$	m/s	Effective translational velocity
$\boldsymbol{V}$	m/s	Arbitrary velocity at the surface of a sphere
$\mathscr{V}$ or V	m^3	Volume
V_{c}	m^3	Critical volume of the liquid layer
$\mathscr{V}_{\mathscr{F}}$	m^3	Volume of a fluid
$\mathscr{V}_{\mathscr{P}}$	m^3	Volume of a particle
$\mathscr{V}_{\mathscr{B}}$	m^3	Total volume of the bulk
$\mathscr{V}_{\mathscr{S}}$	m^3	Total volume of bulk portion 1 and fluid interface
w	m/s	Velocity component in normal direction with respect to a rigid wall
W	m/s	Characteristic velocity in normal direction with respect to a rigid wall
$\mathscr{W}_i$	-	Boundary of the computational domain
X_n	-	Surface spherical harmonic
Y_n	-	Surface spherical harmonic
Y_m^n	-	Surface spherical harmonic
Z_n	-	Surface spherical harmonic
$\mathfrak{z}$	-	Valency

Greek Symbols

Symbol	Dimension	Meaning
α_i	deg.	Euler angles
β	-	Perturbation parameter
β_L	m	Height of each volume portion in Gaussian pillbox
$\dot{\gamma}$	1/s	Shear rate
γ_{ij}	kg/s^2	Surface/Interfacial tension between phase i and phase j
$\gamma^{\mathscr{S}}$	kg/s^2	Effective surface tension of a particle-laden interface
Γ_i	-	Abbreviations or surface
δ	m	Radius of curvature
δ_{h}	-	Comparability factor
ϵ	A^{2}s^4/(kg m^3)	Permittivity
ε	-	Height to length ratio or difference between experimental and numerical obtained results
$\dot{\epsilon}$	1/s	Strain rate
ζ	kg m^2/(A s^3)	Zeta potential
η	A s^2/kg	Electrophoretic mobility
θ	deg.	Polar angle in spherical coordinates
Θ	deg.	Contact angle
Θ_a	deg.	Advancing contact angle
Θ_r	deg.	Receding contact angle
$\Delta\Theta$	deg.	Contact angle hysteresis
ϑ	deg.	Azimuthal angle in cylindrical coordinates
κ	-	Height coefficient related to the liquid-puddle height
κ^{-1}	m	Debye length
$\kappa^{\mathscr{S}}$	kg/s	Surface dilatational viscosity
λ or λ_i	kg/(m s^2) or -	Lagrange multiplier
μ	kg/(m s)	Shear viscosity
μ_{E}	kg/(m s)	Einstein viscosity
$\mu^{\mathscr{S}}$	kg/s	Surface shear viscosity
$\mathbf{\Pi}$	kg/(m s^2)	Total stress tensor
ρ	kg/m^3	Density
ϱ	m	Radial coordinate in cylindrical coordinates
$\boldsymbol{\sigma}$	kg/(m s^2)	Hydrodynamic stress tensor
$\boldsymbol{\sigma}_{\mathscr{I}}$	kg/(m s^2)	Isotropic part of hydrodynamic stress tensor
$\boldsymbol{\sigma}_{\mathscr{D}}$	kg/(m s^2)	Deviatoric part of hydrodynamic stress tensor
$\boldsymbol{\sigma}^{\mathscr{S}}$	kg/(m^2 s^2)	Surface stress tensor
$\boldsymbol{\sigma}^{\mathscr{S}}_{\mathscr{D}}$	kg/(m^2 s^2)	Deviatoric part of the surface stress tensor
$\boldsymbol{\sigma}_{\mathrm{M}}$	kg/(m s^2)	Maxwell stress tensor
$\langle\boldsymbol{\sigma}\rangle_{\mathscr{V}}$	kg/(m s^2)	Volume averaged stress tensor
$\Sigma^{\mathscr{P}}_{\mathscr{B}}$	kg m^2/s^2	Particle excess stress in the bulk
φ	deg.	Azimuthal angle in spherical/cylindrical coordinates or slope angle of the meniscus
ϕ	kg/(A s^3) or -	Perturbation electrostatic potential or surface concentration of interfacial particles

Symbol	Dimension	Meaning
$\phi_{\mathcal{V}}$	-	Volume concentration of particles
ϕ_L	-	Surface concentration of interfacial particles defined by Lishchuk and Halliday (2009)
ϕ_n	-	Solid spherical harmonic of order n
χ	-	Arbitrary function
χ_n	-	Solid spherical harmonic of order n
ψ	kg/(A s^3) or m^2/s	Equilibrium electrostatic potential or stream function
$\boldsymbol{\psi}$	m^2/s	Vector of the stream function
Ψ	kg/(A s^3)	Electrostatic potential
$\Psi_{\mathscr{P}}$	kg/(A s^3)	Potential at the surface of a particle
Ψ_{d}	kg/(A s^3)	Stern potential
ω	-	Growth rate
$\boldsymbol{\omega}$	1/s	Rotational velocity
$\boldsymbol{\Omega}^{\infty}$	1/s	Constant rotational velocity
$\boldsymbol{\Omega}^{\mathrm{eff}}$	1/s	Effective rotational velocity

Dimensionless Numbers

Symbol	Definition	Meaning
Bo	$\rho g L^2/\gamma_{12}$	Bond number: Ratio of gravitational forces and surface tension forces
$\mathrm{B}_{\mu^{\mathscr{S}}}$	$\mu^{\mathscr{S}}/(\mu L)$	Shear Boussinesq number: Ratio of surface shear viscosity and shear viscosity in the bulk
$\mathrm{B}_{\kappa^{\mathscr{S}}}$	$\kappa^{\mathscr{S}}/(\mu L)$	Dilatational Boussinesq number: Ratio of surface dilatational viscosity and shear viscosity in the bulk
Ca	$\mu U/\gamma_{12}$	Capillary number: Ratio of viscous forces and capillary forces
Ce	$\epsilon\zeta^2/(L\gamma_{12})$	Electric capillary number: Ratio of electrostatic forces and capillary forces
Ma	U/c	Mach number: Ratio of flow velocity and speed of sound
Pe	Ua/D	Peclèt number: Ratio of convective transport and diffusive transport
Re	$\rho UL/\mu$	Reynolds number: Ratio of inertial forces and viscous forces
We	$\rho L^3/(\gamma_{12}T^2)$	Weber number: Ratio between inertial forces and surface tension forces
Λ	$\epsilon\zeta E_{\infty}/(\mu U_{\mathrm{ext}})$	Ratio between electro-osmotic flow and viscous flow

Physical Constants

Symbol	Meaning	Dimension	Value
e	Elementary charge	A s	$1.60217662 \times 10^{-19}$
g	Graviational constant	m/s^2	9.81
k_B	Boltzmann constant	m^2 kg/(s^2 K)	$1.38064852 \times 10^{-23}$

List of Figures

List of Tables